Tesi di Dottorato

Development and application of advanced numerical techniques for the analysis of optical data of turbulent flames

Tutore: Prof. Gaetano Continillo   **Candidato: Simone Lombardi**

Coordinatore del Dottorato:
Prof. Fabio Bozza

Acknowledgement

My most sincere thanks go to my tutor, Professor Gaetano Continillo at University of Sannio, who constantly has conveyed a part of his spirit of adventure towards the research of the most innovative topics and has given me the extraordinary opportunity to spend a part of my doctoral period at University of Cambridge. Particularly, I would like to thank him for his extraordinary humanity shown in many moments.

I would like to express my appreciation to Professor Epaminondas Mastorakos (University of Cambridge) for accepting me as visiting student in his research group, for the hospitality and above all for the wonderful experience of research done under his supervision.

I would like to express the most sincere thanks to Dr. Bianca Maria Vaglieco and her research group of C.N.R. - Istituto Motori of Naples, for the experimental work on optically accessible engine and particularly for the kindness that I have received.

I want to express sincere gratitude to my friend, Professor Katarzyna Bizon, now at Cracow University of Technology, for her support to the research activities, for her friendship and for all the moments spent together.

Moreover, I would like to thank the POLIGRID project for the financial support given during these years.

Lastly, I would like to lovely thank my family for all their love and faithful support received and in particular way during the final stages of this PhD.

Contents

List of Figures

Chapter 1

Summary

Turbulent flames (premixed, partially premixed and non-premixed) are widely employed in the majority of practical combustion systems such as internal combustion engines, ramjet, turbine engines, boilers, furnaces, etc. Understanding the phenomena underlying turbulent combustion is essential in order to improve the performance of the combustion systems.

Both experiments and numerical simulations are used to study turbulent flames. Nowadays, optical diagnostic is surely one of the most common techniques employed to study the turbulent combustion processes that occur in various combustion systems. Besides, the development of faster and faster optical diagnostic techniques during the last years has allowed to investigate better and better the flames of various combustion systems. Consequently, these techniques, as so the advanced numerical simulations (DNS, LES), generate a huge amount of data that cannot be processed with classical numerical techniques of analysis. Despite having more data is certainly better than having less, the huge amount of data poses new challenges. Particularly, processing of such data to extract any useful information requires the development of new numerical techniques for the data analysis.

This thesis is focused on the development and application of advanced numerical techniques for the analysis of images from turbulent flames. Particularly, the main techniques developed are based on Proper Orthogonal Decomposition (POD), Independent Component Analysis (ICA), Dynamic Mode Decomposition (DMD) and Optical Flow (OF). These techniques were applied to flame images from optically accessible engines (ICE), Spark Ignition and Diesel engines, and from bluff-body swirl spray burners.

The main scope of this thesis is the application of new advanced numerical techniques for the analysis of images from turbulent flames. With regards to the applications to images from optically accessible engines, the specific objectives are: (i) to apply POD and ICA in order to extract the dominant features of the flames; (ii) to examine the cycle-to-cycle variations in terms of both global measures and dominant features (ICA and/or POD modes) of the flames; (iii) to estimate and analyse the apparent motion field of the flame during the propagation in a port fuel injection spark-ignition engine. With regards to the applications to 2D images from bluff-body swirl spray burner, the instability condition known as blow-off is investigated by means of POD analysis. Blow-off occurs when the local supply velocity of the reactant is greater than the flame speed. This phenomenon is the main cause for which turbine generators, which operate in a fuel-lean burning mode (low NOx emission), trip offline. The specific objectives are: (i) to examine differences in the flame behaviour far from and close to extinction conditions; (ii) to reveal the dominant flame structures just before blow-off; (iii) to reveal differences and similarities among the different liquid fuels used; (iv) to study the statistical behaviour of the POD Modes, in terms of coherent and incoherent components, when the condition of blow-off is approached.

1.0.1 Organization and contributions

Chapter 2 consists of a literature review, followed by brief mathematical descriptions of Proper Orthogonal Decomposition, Independent Component Analysis, Dynamic Mode Decomposition and Optical Flow.

Chapter 3 deals with the description of the experimental tests and numerical analysis of images of combustion from optically accessible engines. Specifically, Section 3.1.1 reports the description of the experimental apparatus and tests concerning a port-fuel injection spark-ignition engine operating under two different fuel injection strategies. Section 3.1.2 reports the analysis of the cycle-to-cycle variations in terms of global quantities (in-cylinder pressure, integral luminosity and centroid of luminosity). Sections 3.1.3 and 3.1.4 report respectively on the application of POD and ICA for the analysis of cycle-to-cycle variations in terms of dominant features (POD modes and independent components). Section 3.2.3 reports on the application of ICA to images of combustion that occurs in an optically accessible diesel engine. It is shown how ICA is able to extract the independent combustion phenomena that occur in an engine combustion chamber.

Chapter 4 is focused on the POD analysis of images of OH*(chemiluminescence) and OH-PLIF of swirling spray flames far from and at extinction. The analysis permits to extract the dominant features of the flames and information on their dynamics. To this aim, the dynamics of the dominant modes of the flames is analysed through the Fourier analysis of the POD coefficients. Section 4.2.3 reports the description of the experimental apparatus and the operating conditions investigated. Section 4.4 reports on the formulation of POD and on two methods for the analysis of the coherent and incoherent components. Moreover, the definition of two new energy spectra based on the coherent and incoherent analysis is proposed.

Section 4.5 reports on the POD analysis for flames of n-dodecane, n-decane, n-

hepthane and ethanol, for operating conditions far and close to blow-off. In this section, the dominant features of the flames are shown and their dynamics are studied through the Fourier analysis of the POD coefficients. Section 4.6 reports on the analysis of the statistical behaviour of the flame, in terms of its coherent (non-Gaussian) and incoherent (Gaussian) component, for flames far and close to blow-off. This analysis has suggested a criterion to identify the blow-off condition from the stable conditions.

Chapter 5 reports an application of Dynamic Mode Decomposition to PIV measurements of high Reynolds and high swirl number flow, in order to extract the dominant dynamics - in terms of frequency and growth rate - of the turbulent flow investigated. The conclusions of this work are reported in Chapter 6.

The work reported in this thesis has already produced the following publications:

1. Bizon, K., Lombardi, S., Continillo, G., Mancaruso,E. and Vaglieco, B.M. (2012). Analysis of Diesel engine combustion using imaging and independent component analysis. Proceedings of the Combustion Institute, Available online 26 August 2012, ISSN 1540-7489.

2. Bizon, K., Lombardi, S., Continillo, G. & Vaglieco, B.M. (2012). Analysis of the independent components from images of transient reactive flows. Proceedings of the XXXV Meeting of the Italian Section of the Combustion Institute, 10-12 October 2012, Milano, Italy

3. Bizon, K., Continillo, G., Lombardi, S. & Vaglieco, B. M. (2013). Independent Component Analysis of transient reactive flows in optically accessible SI and Diesel engines. The 24th ICDERS (International Colloquium on the Dynamics of Explosions and Reactive Systems), 28 July - 2 August 2013,

Taipei, Taiwan.

4. Lombardi, S., Bizon, K., Continillo, G., Mancaruso, E. & Vaglieco, B. M. (2013). Dynamics of spectral emissions in HCCI combustion. International Conference on Engines & Vehicles, 15-19 September 2013, Capri, Napoli (Italy).

5. Bizon, K., Continillo, G., Lombardi, S., Mancaruso, E., Sementa, P. & Vaglieco, B. M. (2013). Independent Component Analysis if combustion images in optically accessible SI and Diesel engines. International Conference on Engines & Vehicles, 15-19 September 2013, Capri, Napoli (Italy).

6. K. Bizon, G. Continillo, S. Lombardi, E. Mancaruso, P. Sementa, B.M. Vaglieco, Independent Component Analysis applied to combustion images in transparent engines, Ingineria Automobilului 8:7-11, 2014.

7. K. Bizon, G. Continillo, S. Lombardi, E. Mancaruso, P. Sementa, B.M. Vaglieco, Decomposition methods in engine research, Joint Meeting of French and Italian Section IFRF and the Combustion Institute, Pisa, Italia, 23-24 April 2014.

8. K. Bizon, G. Continillo, S. Lombardi, P. Sementa, B.M. Vaglieco, Independent Component Analysis of combustion images from a Spark Ignition optical engine, submitted to Combustion and Flame.

9. K. Bizon, G. Continillo, S. Lombardi, P. Sementa, B.M. Vaglieco, Application of Independent Component Analysis for the study of flame dynamics and cyclic variation in spark ignition engines, accepted to the 9th Mediterranean Combustion Symposium, Rhodes, Greece, 7-11 June 2015.

10. S. Lombardi, K. Bizon, A. Coghe, F. Cozzi, G. Continillo, DMD analysis of experimental PIV data of a swirled jet, submitted to The 25th ICDERS

(International Colloquium on the Dynamics of Explosions and Reactive Systems), Leeds, UK, 2-7 August 2015.

11. S. Lombardi, R. Yuan, G. Continillo, E. Mastorakos, Proper Orthogonal Decomposition analysis of an n-decane swirling spray flame at extinction, accepted to Ninth Mediterranean Combustion Symposium, Rhodes, Greece, 7-11 June 2015.

Chapter 2

Numerical techniques for the analysis of optical data obtained from turbulent flames

This chapter is focused on the numerical techniques for the analysis of optical data obtained from turbulent (premixed and non-premixed) flame. Specifically, the techniques reported in this chapter are: Proper Orthogonal Decomposition (POD), Independent Component Analysis (ICA), Dynamic Mode Decomposition (DMD) and Optical Flow (OF) method.

POD, ICA and DMD are modal decomposition techniques. A modal decomposition technique takes a set of data and it computes from set of modes, or characteristic features. The meaning of the modes, on the particular type of decomposition used. POD extracts the set of modes so that they capture the most amount of energy. ICA determines the set of modes so that all modes (features) are mutually statistically independent from each other. DMD extracts the modes (dynamic modes) that describes the dominant dynamics of the set of data. Differently, Optical Flow is a technique that allows to estimate the apparent motion field starting

from two or more consecutive images.

2.1 Proper Orthogonal Decomposition

Proper orthogonal decomposition (POD) is a powerful technique presented by Lumley (1967) for data analysis and model reduction (ROM). POD has the purpose to extract the dominant features contained in a given set of data, which represent in some way the state of the system under study. Particularly, POD provides optimal set of basis functions starting from a ensemble of data (called snapshots) originated by experiments or numerical simulations, so that they represent as better as possible the dominant (coherent) features (or information) captured by the entire set of data. The basis functions are called in various ways such as modes, empirical eigenfunctions, empirical basis functions, proper orthogonal modes (POD modes), or basis functions; in this dissertation, the basis functions shall be called POD modes. Basically, POD allows to express the entire ensemble of data, which was employed to estimate POD modes, as linear combination of such basis functions and proper coefficients, that are properly called POD coefficients. It has been used in many application of various scientific fields, as a result it has assumed different forms such as Principal Component Analysis (PCA), Karhunen-Loéve (KL) transform, and singular value decomposition (SVD).The connections and the equivalence of these methods have been discussed in paper presented by Wu et al. (2003).

PCA is a statistical technique which purposes to identify the most important uncorrelated components (principal components, PCs) present within an ensemble of data obtained by multivariate observations. The underlying idea of PCA is to find a compact and uncorrelated representation of the data that captures the most

amount of variance present into the observations. KL decomposition has taken the name of the two scientists, Karhunen and Loéve, which independently developed a theory regarding the optimal series expansions of continuous-time stochastic process (Webb, 2002). In other words, KL decomposition can be considered as the extension of PCA to the case of infinite dimensional spaces, such as the space of the continuous-time functions. In the last, SVD can be seen as the extension of the eigenvalues decomposition to non-square matrices. Since that SVD is much more general than the eigenvalue decomposition and intimately relates to the matrix rank and reduced-rank least-squares approximation, it is a very important and fundamental working tool in many areas such as matrix theory, linear systems, statistics, and signal analysis (Scharf, 1991; Trefethen, 1997).

There are many applications of POD in the context of reduction of models of reacting flow system (Bizon and Continillo, 2009, 2012). Other applications concern the data (or image) compression in order to over come issues connected with data storage and transmission.

Nowadays, POD is one of the most famous techniques in the research fields of the fluid mechanics and combustion. In fact, it is employed both to carry out the data analysis and model order reduction in contexts of combustion and fluid mechanics. Since the aims of this dissertation are focused on the study of turbulent flames, an overview on the state of the art about the POD applications in turbulence and combustion, will be presented in the next subsection. Subsequently, the mathematical formulation shall be discussed for both continuous and discrete cases.

2.1.1 POD Review

POD is becoming more and more, a popular tool for the study of turbulent flows and turbulent flames. Lumley (1967) was the first to introduce this technique to

study the coherent features in inhomogeneous turbulence. Berkooz et al. (1993) presented a review on the role of POD for the analysis of turbulent flows; wherein the POD strengths, about the data analysis and reduction of models in fluid mechanics, are highlighted. Although, this review was made more than twenty years ago, its contents are still of interest for the researcher in the field of turbulence and combustion. In fact, Berkooz et al. (1993) have underlined the issues about the understanding of the underlying processes of the turbulence. In the context of the analysis of experimental data, Liu (1988) was one of first researchers to observe coherent features into flows at high Reynolds number. The term *coherent structure* denotes the organized spatial features that systematically appear with a given temporal coherence. Usually, the coherent structures of a turbulent field correspond to phenomena of large scale, instead *incoherent structures* correspond to those of small scale. Moreover, Berkooz et al. (1993) highlight that POD offers a rational method for the extraction of coherent structures. During the last twenty years, many researchers have observed coherent features during experiments carried out at high Reynolds number.

Glauser and George (1992) have employed various techniques to resolve issues connected to the application of multipoint measurements of turbulent flows. Particularly, they proposed a method based on POD to determine the criteria of spatial sampling, that is the criteria to choose the number of probes and their spatial locations without information losses, to investigate *inhomogeneous turbulent flows*. These flows are of great importance because most engineering flows are strongly inhomogeneous in one or more directions. Indeed, it is sufficient to think of flows that occur into many modern devices such as engines, burners, chemical-process devices, and so on, that require a complex geometry to make flows homogeneous. Besides, the authors highlight that, in case of homogeneous and periodic flows, spatial sampling criteria based on Fourier decomposition can be employed as well.

Indeed, if the flow fields are homogeneous and periodic, POD and Fourier decomposition will be equivalent along the direction of homogeneity and stationary.

Bonnet et al. (1994) has proposed a complementary technique based on POD and Linear Stochastic Estimation (LSE) to reconstruct turbulent velocity fields and to identify large-scale structures. This method was shown to be very useful because it requires only two simultaneous measurements of the velocity in order to reconstruct the entire turbulent velocity field. Bonnet and Delville (2001) have also written a review dedicated to methods for the analysis of coherent structures (conditional averages, filtering techniques, wavelets, LSE, POD, etc.) in various turbulent flows (such as jets, mixing layers and boundary layers), and the links between these methods and mathematical models employed in turbulence (RANS, LES, SDM, etc.).

Gordeyev and Thomas (2000) employed POD to extract and investigate the large-scale coherent structures in the similarity region of a planar turbulent jet. Moreover, the self-similarities of POD eigenfunctions were analysed and scaling laws were found for both POD eigenvalues and eigenvectors. This analysis was obviously carried out in the region of the flow where the flow field is guaranteed to have self-similarity. Moreover, POD has also permitted to individuate two POD modes (spatial features), a symmetric mode with respect to the jet profile centreline and an antisymmetric mode, that may be the cause of instability of the flow.

Citriniti and Greorge (2000) employed POD to extract the coherent, or large-scale, structures in a high Reynolds fully developed, turbulent axisymmetric shear layer generated by a round jet. Particularly, it was shown that meaningful physical structures (large ring vortices) were captured by the first POD modes. Subsequently, POD coefficients were used to analyse the dynamic behaviours (time scales) of the most meaningful modes in order to understand the underlying mixing mechanisms induced by the interaction between round jet nozzle and air jet. In addition, the

ability of POD to filter out the small-scale turbulent fluctuations, which obscure
the view of the large structures, was shown as well.

Ito et al. (2001) investigated the vortex shedding behind a cylinder in a fully de-
veloped pipe flow by means of anemometric measurements. Velocity field data
were analysed by using POD coupled to *wavelets analysis*. Therefore, wavelets
analysis was carried out on POD coefficients to analyse the dynamic behaviour
of the investigated phenomena, focusing on the periodic phenomena connected to
vortex shedding process. Additionally, the POD modes were classified according
to the entropy of the corresponding POD coefficients.

During the last decade, POD was widely employed to analyse data provided
from advanced measurement techniques, such as *particle image velocimetry* (PIV),
which provides high-resolution spatial-temporal information, and large-eddy sim-
ulations. Consequently, various extensions of POD have been developed in order
to extract *information of interest*. One of these extensions is known as *extended
POD*, which was firstly used to study a jet-interaction in an internal combustion
engines. Subsequently, an accurate description of extended POD was presented
by Borèe (2003), wherein this method is proposed as a tool for the analysis of
correlated events in turbulent flows. Basically, extended POD allows to estimate
POD modes in the entire domain starting from POD modes obtained from data
relative to only one subdomain. Moreover, it is also possible to use it to study the
correlation of any physical quantity (e.g., pressure) with any scalar or vector field
(e.g., velocity field). An accurate description about extended POD will presented
in a subsequent section.

The flow around bluff body, a device employed in engineering flows to produce
vortexes, was analysed by means of PIV measurements and POD (Oudheusden
et al., 2005). Particularly, an appropriate version of POD was proposed and used
in order to extract the vortex-shedding phase of velocity fields, which were acquired

at asynchronous low frequency respect to the vortex cycles. The authors were focused on understanding the underlying physics of vortex formation and shedding processes. Everson and Sirovich (1995) presented an iterative-algorithm based on POD for the recovery and reconstruction of spatio-temporal missing data. This method is known as *Gappy POD*. During the last years, gappy POD was widely employed to recover and reconstruct the missing data obtained from PIV measurements. Therefore, Murray and Ukeiley (2007) applied gappy POD in order to recover and reconstruct the spatio-temporal missing data obtained from PIV measurements of a subsonic cavity flow. This application is very useful because data missing is a phenomenon that occurs frequently, above all for high-speed measurements of optical data.

Farge et al. (1999) used POD to decompose a turbulent flow, obtained by direct numerical simulation (DNS), in two orthogonal components: an organized coherent flow (non-Gaussian) and a random incoherent flow (Gaussian). He found that the small scale flow contained still coherent structures, since the velocity PDF was stretched exponential, while the incoherent flow was structureless, and its velocity PDF was Gaussian. Bizon et al. (2009b) proposed a method based on POD for the reconstruction of information in between consecutive measurements of flame images taken from an optically accessible internal combustion engine. A filtering approach, based on POD and statistical moments, was proposed and used to extract the mean, coherent (non Gaussian) and incoherent (Gaussian) components of the fluctuation of the luminosity from combustion processes in engines (Bizon et al., 2009a). Furthermore, Bizon et al. (2010b) proposed a *Coefficient of Variation* defined on the POD coefficients as measure of the cyclic variability of the morphologic features of the flames. For systems having a dominant periodicity, as in thermoacoustically-excited flames, POD has also been used to reveal typical flame shapes and their connection with the acoustics (Davis et al., 2013) and the

flow (Stöhr et al., 2012). POD has also been applied to chemiluminescence images to study the blow-off dynamics of stratified premixed flames (Kopp-Vaughan et al., 2013) and vortex shedding (Kostka et al., 2012). In simulations, POD has been used to represent DNS data (Frouzakis et al., 2000; Danby and Echekki, 2006) and for analysis of LES data (Duwig and Fureby, 2007).

In the next section, the mathematical description of POD will be discussed.

2.1.2   POD: mathematical description

In this section, the formulation proposed by Holmes (1996) will be followed. Suppose an ensemble of M snapshots of scalar fields $\{u^k\}_{k=1}^M$, each being a function $u = u(x)$ defined on the domain $0 \leq x \leq 1$. Furthermore, it is assumed that the u's belong to an inner product space: the linear, infinite-dimensional Hilbert space $L^2([0,1])$, of square integrable functions with inner product:

$$(f,g) = \int_0^1 f(x)g(x)dx \tag{2.1}$$

and the *induced norm*

$$\|f\| = (f,f)^2 \tag{2.2}$$

POD permits to obtain an optimal basis $\{\phi(x)\}_{j=1}^\infty$ for the data set in the sense that the finite-dimensional representations of the form

$$u_N(x) = \sum_{j=1}^N c_j\phi_j(x) \tag{2.3}$$

describes the members of the ensemble better than a representation of the same dimension in any other basis. In mathematical words, this statement of optimality means that the basis function ϕ should be chosen such that the mean square error between the data u and the its projection onto ϕ is minimized, that is:

$$\min_{\phi \in L_2([0,1])} \left\langle \left\| u - \frac{(u,\phi)}{\|\phi\|^2}\phi \right\|^2 \right\rangle \tag{2.4}$$

where $\langle \cdot \rangle$ denotes averaging operation commutative with the spatial integral.

This optimization problem is equivalent to maximizing the averaged projection of u onto ϕ, namely:

$$\max_{\phi \in L_2([0,1])} \frac{\langle |(u, \phi)|^2 \rangle}{\|\phi\|^2} \tag{2.5}$$

where $|\cdot|$ denotes the absolute value. Since that it is desirable to have the basis $\phi_j(x)$ orthonormal, the problem (2.5) is subject to the constraint $\|\phi\|^2 = 1$. The corresponding function for this constrained variation problem is

$$J[\phi] = \langle |(u, \phi)|^2 \rangle - \lambda(\|\phi\|^2 - 1) \tag{2.6}$$

The extremum is reached when the functional derivative vanish for all variations $\phi + \delta \psi \in L^2([0,1]), \delta \in \mathbb{R}$. After few mathematical manipulation (Holmes, 1996) such condition of optimality reduces the problem to the following integral eigenvalue problem:

$$\int_0^1 \langle u(x)u(x') \rangle \phi(x')dx' = \lambda \phi(x) \tag{2.7}$$

Let R denote the linear operator of the autocorrelation function defined by

$$R \equiv \langle u(x)u(x') \rangle \tag{2.8}$$

Consequently, problem (2.7) can be written as

$$R\phi = \lambda \phi \tag{2.9}$$

Thus, the optimal basis is given by the eigenfunctions $\{\phi_j\}$ of the autocorrelation function that is only defined from the empirical data u. The basis functions are called *empirical eigenfunctions*, or *POD modes*.

The modal coefficients c_j that appear in Eq. (2.3) are determined by the projection of the empirical data onto POD modes:

$$c_j = (u, \phi_j) \tag{2.10}$$

Moreover, each eigenfunction ϕ_j is associated with the corresponding eigenvalues λ_j, and since the autocorrelation function is defined non-negative, this implies that eigenvalues λ_j are strictly positive, namely $\lambda_j \geq 0$ for all j. Therefore, we may order the eigenvalues $\lambda_j \geq \lambda_{j+1}$ and define the energy fraction captured by the k-th eigenfunction as

$$e_k = \frac{\lambda_k}{\sum_j \lambda_j} \qquad (2.11)$$

and the cumulative energy of the first K eigenfunctions as

$$E_{K,POD} = \frac{\sum_{j=1}^{K} \lambda_j}{\sum_j \lambda_j} \qquad (2.12)$$

The function of the cumulative energy on K is called *cumulative energy spectrum based on POD*. Usually, in many practical applications the fields depend on four variables, three spatial and one temporal. Therefore, it is necessary to generalize the integral equation (2.7) to functions of more than one variable and to vector-valued functions $\mathbf{u}(\mathbf{x}, t)$ by using a appropriate Hilbert spaces and inner products. Following the example proposed by (Holmes, 1996), for experiments performed in a one-dimensional spatial domain $0 \leq x \leq 1$ over times of duration T, one simply considers the problem in the space $L^2([0,1] \times [0,T])$ with inner product defined as double integral over x and t. As a consequence, the POD representation of the field $u(x,t)$ assumes the following form:

$$u(x,t) = \sum_j c_j(t) \phi_j(x) \qquad (2.13)$$

It is interesting to observe that the POD representation allows to separate the temporal and spatial features: POD modes depend only on the space variable x, whereas POD coefficients depends only on the time variable t. This last property is widely used in this thesis in order to extract useful information on the investigated phenomena

2.1.3   POD: discrete formulation and the method of Sirovich

In practical applications, numerical or experimental observations $\{u_k(x)\}_{k=1}^M$ are discretized both in space and time. Let $\mathbf{x} = (x_1, \ldots, x_N)$ be the discretization of the spatial domain, and $\mathbf{t} = (t_1, \ldots, t_M)$ the discretization of the temporal domain; where the subscripts N ad M are respectively the size of the discretized spatial and temporal domains.

The entire set of observations can be represented by the *matrix of snapshots* $\mathbf{U}$ defined by

$$\mathbf{U} \equiv \begin{pmatrix} u(x_1, t_1) & \ldots & u(x_1, t_M) \\ \vdots & \ddots & \vdots \\ u(x_N, t_1) & \ldots & u(x_N, t_M) \end{pmatrix} \tag{2.14}$$

hence, in the discrete case, the autocorrelation function of Eq. (2.8) is replaced by the spatial autocorrelation matrix

$$\mathbf{R} = \frac{1}{M}\mathbf{U}\mathbf{U}^T \tag{2.15}$$

of dimension $N \times N$. Therefore, the POD modes ϕ_j having the same dimension N as the discretization of the spatial domain can be found by solving the eigenvalue problem

$$\mathbf{R}\phi = \lambda\phi \tag{2.16}$$

In the cases when the dimension of the discretized spatial domain is high, the matrix $\mathbf{R}$ can become too large for the machine capacity and/or too expensive in terms of computational cost for solving the eigenvalue problem (2.16). For example, in the case of POD application to a set of images having resolution 400×400 pixels, the dimension of the discretized spatial domain is 160000, the spatial correlation matrix dimension is 160000×160000. Hence, it is impossible to solve the eigenvalues problem (2.16) due to the high dimensionality of $\mathbf{R}$.

Fortunately, Sirovich (1987) proposed a method that allows, in case of $N \gg M$, to reduce an $N \times N$ eigenvalue problem to an $M \times M$ eigenvalue problem. This method, called *method of snapshots*, is based on the assumption that the POD modes ϕ_j can be written as a linear combination of the snapshots:

$$\phi_j = \sum_{i=1}^{M} b_j(t_i) \mathbf{u}(\mathbf{x}, t_i) \tag{2.17}$$

the coefficients $\mathbf{b}_j$ being given by solution of the new eigenvalue problem

$$\mathbf{Cb} = \lambda \mathbf{b} \tag{2.18}$$

where $\mathbf{C}$ is the *temporal correlation matrix* defined as:

$$\mathbf{C} = \frac{1}{M} \mathbf{U}^T \mathbf{U} \tag{2.19}$$

It is clear that the dimension of the eigenvalue problem (2.18) depends on the number of snapshots. From a statistical point of view, Eqs (2.15) and (2.19) are equivalent to the biased estimators of the corresponding correlation matrix. Usually, in case of experimental data, the unbiased estimator of the correlation matrix is used

$$\mathbf{C} = \frac{1}{M-1} \mathbf{U}^T \mathbf{U} \tag{2.20}$$

because it provides a more accurate estimate.

In the analysis of turbulent flows and flames, POD is usually carried on data centred around the mean component, namely on the fluctuation of the field of interest. Hence, the POD representation of the field is given by

$$\widetilde{u}(x,t) = u(x,t) - \overline{u}(x) = \sum_{i=1}^{M} c_i(t)\phi_i(x) \tag{2.21}$$

Hence, the correlation matrix of the data centred on the mean component is given by

$$\mathbf{C} = \frac{1}{M-1}(\mathbf{U} - \overline{\mathbf{U}})^T(\mathbf{U} - \overline{\mathbf{U}}) = \frac{1}{M-1}\widetilde{\mathbf{U}}^T\widetilde{\mathbf{U}} \tag{2.22}$$

which is well-known as covariance matrix. This formulation should be used when the investigated phenomenon can be considered statistically stationary.

2.2   Independent component analysis

Independent component analysis (ICA) is a statistical and computational technique to extract the hidden factors that underlie sets of random variables, measurements, or signals. In ICA model is assumed that the observed multivariate data are generated by linear or non-linear mixtures of some unknown *latent variables*, so called sources, and the mixing system unknown as well. Under particular hypotheses, ICA methods aim to extract the signal sources starting from the multivariate data acquired (*observations*), namely without prior knowledge the physical system (mixing system). These latent variables are often called *independent components* (ICs) or *factors.*

ICA was introduced for the first time in early 1980s in the context of neural network modeling. Later, the development of much more efficient algorithms and the growth of computing power have allowed to extend ICA to various fields of research such as signal processing, image processing and analysis, information theory, probability theory, etc. The first applications of ICA dealt with the so-called cocktail party problem (Hyvärinen and Oja, 2000), in which ICA was employed to determine individual speech waveforms from their mixtures. Therefore, ICA methods are of great interest in blind source separation (BSS) problems, where the main aim is the extraction of signal sources (input signal) of a system starting from multivariate data time-series of the output signals. Particularly in the engine context, ICA has been used to identify the source signals related to independent mechanical events from acoustic measurements (Albarbar et al., 2010) and vibration signals (Liu et al., 2008). Another example of ICA application in combustion

can be found in the paper by Tan et al. (2012), where the method was applied to identify the fuel type in power plants from flame oscillation signals. Recently, Bizon et al. (2013) introduced application of ICA to flame images of the combustion process that occurs inside the combustion chamber of an optically-accessible diesel engine.

Next sections, ICA and BSS concepts will be firstly introduced through the description of the *"cocktail party"* problem. Subsequently, ICA will be rigorously presented.

2.2.1 Cocktail party problem

Consider three people are speaking (source signals) in the same room, where three microphones are placed in different locations. Each microphone will record a mixture (observed signals) of the three voices with different weights.

For sake of simplicity of exposition, denote by $x_1(t)$, $x_2(t)$ and $x_3(t)$ the observed signals, which are the amplitudes of the recorded signals at time t, and by $s_1(t)$, $s_2(t)$ and $s_3(t)$ the source signals. The observed signals, $x_i(t)$, are also called *mixtures* because they are the weighted sums of the sources, $s_i(t)$, where the weight coefficients, or mixing weights, depend on the distances between the sources (people) and the sensors (microphones):

$$x_1(t) = a_{11}s_1(t) + a_{12}s_2(t) + a_{13}s_3(t)$$
$$x_2(t) = a_{21}s_1(t) + a_{22}s_2(t) + a_{23}s_3(t) \qquad (2.23)$$
$$x_3(t) = a_{31}s_1(t) + a_{32}s_2(t) + a_{33}s_3(t)$$

The mixing weights a_{ij} are assumed constant and unknown, since their knowledge would require all the properties of the physical mixing system, that could be extremely difficult in general. Furthermore, the source signals $s_i(t)$ are unknown as well, since the actual problem is that the signal sources $s_i(t)$ cannot be directly

recorded.

Suppose that number of sensors equals the number of sources, and that the coefficients a_{ij} form an invertible matrix. Thus, there exists a matrix $\mathbf{W}$ with coefficients w_{ij}, such that the source signals can be separated as:

$$
\begin{aligned}
s_1(t) &= w_{11}x_1(t) + a_{12}x_2(t) + a_{13}x_3(t) \\
s_2(t) &= w_{21}x_1(t) + a_{22}x_2(t) + a_{23}x_3(t) \\
s_3(t) &= w_{31}x_1(t) + a_{32}x_2(t) + a_{33}x_3(t)
\end{aligned}
\tag{2.24}
$$

Thus, the cocktail party problem regards the estimation of elements w_{ij} of $\mathbf{W}$ only from observations $x_i(t)$. A surprisingly solution to this problem is provided by considering the source signals to be *statistically independent* and *not gaussian*. These assumptions are enough to estimate the coefficients w_{ij}, so that the signals

$$
\begin{aligned}
y_1(t) &= w_{11}x_1(t) + a_{12}x_2(t) + a_{13}x_3(t) \\
y_2(t) &= w_{21}x_1(t) + a_{22}x_2(t) + a_{23}x_3(t) \\
y_3(t) &= w_{31}x_1(t) + a_{32}x_2(t) + a_{33}x_3(t)
\end{aligned}
\tag{2.25}
$$

are statistically independent and correspond to the sources $s_i(t)$, apart from an arbitrary multiplicative scalar constant. Therefore, the estimates $y_i(t)$ are known as *independent components* of the observations $x_i(t)$.

In order to clarify the ICA concept, a numerical example is reported here. Consider the waveforms in Fig. 2.1 of the observations $x_i(t)$ generated by linear combination of source signals $s_i(t)$ previously generated (Fig. 2.2), and random coefficients a_{ij}, which form a mixing matrix $\mathbf{A}$ with full-rank. Subsequently, the independent components $y_i(t)$ were directly estimated from the observations $x_i(t)$ by using the FastICA algorithm. It is possible to see as the estimated independent components correspond to the source signals that were used in generating the
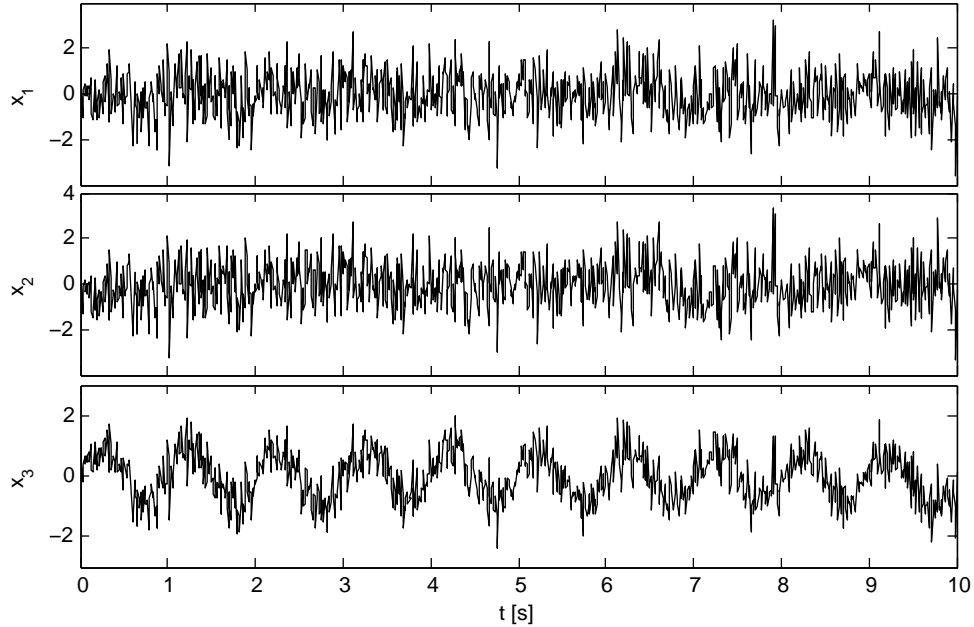
Figure 2.1: The observed signals that are assumed to be mixtures of some under-lying source signals.

mixtures $x_i(t)$.

2.2.2   ICA: generative model

Given a set of m temporal signal mixtures $x_1(t), \ldots, x_n(t)$ measured over $t = 1, \ldots, T$ and generated by linear combination of n random variables $s_1(t), \ldots, s_n(t)$:

$$x_i = a_{i1}s_1(t) + a_{i2}s_2(t) + \cdots + a_{in}s_{in}(t), \quad \text{for all } i = 1, \ldots, n \qquad (2.26)$$

where a_{ij} are the mixing coefficients. By definition, the s_i are statistically mutually independent. Hence, it is clear that ICA is based on a generative model, since the observed data are generated by a process of mixing of the source components s_i.
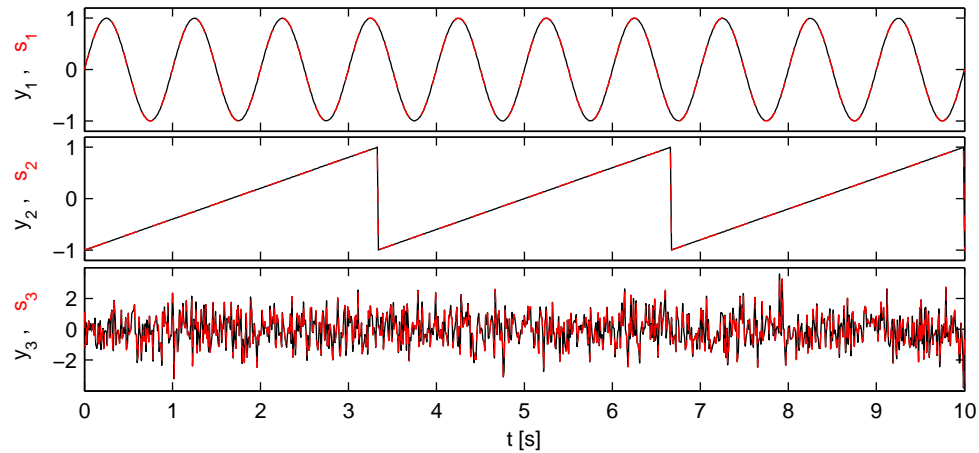
Figure 2.2: Comparison between the estimates of the independent components y_i and actual signal sources s_i.

Recall that in this model, both the independent components, s_i, and the mixing coefficients a_{ij} are unknown. Moreover, the time index t that was used in the previous section has been eliminated, because in the rigorous definition of the ICA model the mixtures x_i as well as the ICs s_i are assumed to be random variables, instead of time signals or time series.

Usually, the matrix-vector notation is used to express the sums of Eq. 2.26. Thus, let $\mathbf{x}$ denote the random vector of mixtures $x_1, \ldots, x_n$, let $\mathbf{s}$ denote the random vector of the signal, and let $\mathbf{A}$ denote the mixing matrix with elements a_{ij}, that is

$$\mathbf{A} = \begin{pmatrix} a_{11} & a_{12} & \ldots & a_{1n} \\ a_{21} & a_{22} & \ldots & a_{2n} \\ \vdots & \vdots & \ddots & \vdots \\ a_{n1} & a_{n2} & \ldots & a_{nn} \end{pmatrix} \tag{2.27}$$

Using this vector-matrix notation, the generative model can be written as

$$\mathbf{x} = \mathbf{A}\mathbf{s} \tag{2.28}$$

It is sometimes useful to write Eq. 2.28 as

$$\mathbf{x} = \sum_{i=1}^{n} \mathbf{a}_i s_i \tag{2.29}$$

where $\mathbf{a}_i$ denotes the i-th column of $\mathbf{A}$.

The solution of the ICA problem consists of estimating both $\mathbf{A}$ and $\mathbf{s}$ when only $\mathbf{x}$ is observed, provided that the observers collecting the mixtures are independent. In the basic model defined by Eq. (2.28), the number of observed mixtures is assumed to be equal to the number of the underlying independent sources, hence the mixing matrix $\mathbf{A}$ is invertible, and the model can be rewritten as:

$$\mathbf{s} = \mathbf{W}\mathbf{x} \tag{2.30}$$

The problem, as stated, poses a number of interesting theoretical issues, related to concepts as identifiability, separability, and uniqueness (Eriksson and Koivunen, 2004). Indeed, it makes sense to search for both an unknown matrix $\mathbf{W}$ and set of sources if there is some warranty of existence and uniqueness of the inverse formulation (2.30) related to problem (2.28), and Ref. [30] indicates conditions for such warranty. Assuming existence and uniqueness of the solution of Eq. (2.28), we can approach the problem by an estimation procedure, searching a linear transformation $\mathbf{W} = \mathbf{A}^{-1}$ in such a way that the linear combination $\mathbf{y}$

$$\mathbf{y} = \mathbf{W}\mathbf{x} \tag{2.31}$$

is the optimal estimation of the independent source signals $\mathbf{s}$.

2.2.3   Assumptions and ambiguities of ICA

In order to extract the independent components, we here make the following assumptions:

1. the independent components are assumed statistically independent;

2. the independent components must have non gaussian distributions;

3. for simplicity, the mixing matrix is square and invertible.

The first assumption is the basis principle of ICA. Given n random variables $y_1, y_2, \ldots, y_n$, they are *independent* if information in y_i does not give information on y_j for $i \neq j$. Formally, the concept of independence can be defined by means of the probability density functions (*pdf*). Denote by $p(y_1, y_2 \ldots, y_n)$ the joint probability density function of the n random variables y_i, and by $p_i(y_i)$ the marginal pdf of y_i. Then, the n random variables $y_1, y_2, \ldots, y_n$ are said *statistically independent* if and only if the joint pdf is factorizable in the product of the n marginal pdfs, that is:

$$p(y_1, y_2, \ldots, y_n) = p_1(y_1)p_2(y_2)\ldots p_n(y_n) \tag{2.32}$$

In relation to the second assumption, if the observed variables have gaussian distributions, ICA cannot to separate the independent Gaussian components (Hyvärinen and Oja, 2000). As a consequence, many applications of ICA consider a rejection component, wherein the effects of all the gaussian sources are rejected. This can also be seen as a filtering of the gaussian components.

In relation to the third assumption, it is assumed that the number of independent components is equal to the number of observable mixtures. In some cases, this assumptions can be relaxed, as it will be explained later.

The ICA generative model (Eq. 2.28) contains the following ambiguities:

- *ICA cannot determine the variance (energies) of the independent components.* This is due to the unknowing of both the mixing matrix $\mathbf{A}$ and the vector of the source signal $\mathbf{s}$. Therefore, any scalar multiplier, α_i, in one of the sources s_i could always be eliminated by dividing the corresponding column of $\mathbf{a}_i$ of $\mathbf{A}$ by the same scalar, that is

$$\mathbf{x} = \sum_i \left(\frac{1}{\alpha_i}\mathbf{a}_i\right)(s_i\alpha_i) \tag{2.33}$$

As a result, it may be useful to fix the magnitudes of the independent components so that they assume unit variance $E\{s_i^2\} = 1$ (the operator $E\{\cdot\}$ denotes the statistical mean). Then, in the ICA methods the mixing matrix will be adapted to take into account this constraint. It it possible to note that this still leaves the *ambiguity of sign*. Indeed, each independent component could be multiplied by -1 without influencing the model. Fortunately, this ambiguity is insignificant in most applications.

- *ICA does not provide a natural order of independent components*. This is again due to the unknowing of both **A** and **s**. Indeed, it is possible to change the order of the terms in the sum Eq. (2.29) without loosing information on the sources.

2.2.4 Preprocessing for ICA: centering and whitening

In order to obtain good estimates of the independent components from ICA algorithms, the observable data (mixtures) should be preprocessed by *centering* and *whitening*.

Centering is used to have both observable data and independent components with zero mean, since such preprocessing simplifies theory and algorithms a lot. This is made by subtracting the sample mean from the observable mixtures. Formally, this means that the original mixtures, $\mathbf{x}'$, are preprocessed by

$$\mathbf{x} = \mathbf{x}' - E\{\mathbf{x}'\} \tag{2.34}$$

As a result, the independent components **s** have zero mean as well, since $E\{\cdot\}$ is a linear operator, hence the mixing matrix remains the same after the centering of the mixture variables, that is:

$$E\{\mathbf{s}\} = \mathbf{A}^{-1} E\{\mathbf{x}\} \tag{2.35}$$

After estimation of the mixing matrix and of the independent components for the zero-mean data, the subtracted mean can be reconstructed by adding $\mathbf{A}^{-1}E\{\mathbf{x}'\}$ to the centred independent components.

The second step of the preprocessing procedure is given by *whitening* the observable data. Whitening consists of applying a linear transform to observable data (mixtures) so that its components are uncorrelated and have unit variance. This is suggested by the fact that uncorrelatedness is a weak form of independence. In other words, independence implies uncorrelatedness, but the reverse is not true. Let y_1 and y_2 be two random variables: they are said uncorrelated if their covariance are zero, namely

$$cov\{y_1, y_2\} = E\{y_1 y_2\} - E\{y_1\}E\{y_2\} = 0 \tag{2.36}$$

Let $\mathbf{y}$ be a random vector: it is said to be *white*, if its covariance matrix equals the identity matrix, that is

$$E\{\mathbf{y}\mathbf{y}^T\} = \mathbf{I} \tag{2.37}$$

Consequently, an observed data vector $\mathbf{x}$ can be transformed into a white zero.mean $\mathbf{z}$, by multiplying it by some matrix $\mathbf{V}$

$$\mathbf{z} = \mathbf{V}\mathbf{x} \tag{2.38}$$

One of the most popular methods for whitening is based on the eigenvalue decomposition of the covariance matrix

$$\mathbf{C} = E\{\mathbf{x}\mathbf{x}^T\} = \mathbf{E}\boldsymbol{\Lambda}\mathbf{E}^T \tag{2.39}$$

where $\mathbf{E} = (\mathbf{e_1}, \mathbf{e_2}, \ldots, \mathbf{e_n})$ is the matrix of the eigenvectors of the covariance matrix, whereas $\boldsymbol{\Lambda} = diag(\lambda_1, \lambda_2, \ldots, \lambda_n)$ is the diagonal matrix of the eigenvalues of $\mathbf{C}$. Now, whitening can be done by the whitening matrix:

$$\mathbf{V} = \boldsymbol{\Lambda}^{-1/2}\mathbf{E}^T \tag{2.40}$$

Now, applying the whitening transform $\mathbf{V}$ to the mixture variables $\mathbf{x}$ of the ICA model (Eq. (2.28))

$$\mathbf{z} = \boldsymbol{\Lambda}^{-1/2}\mathbf{E}^T\mathbf{x} = \mathbf{V}\mathbf{x} = \mathbf{V}\mathbf{A}\mathbf{s} = \widetilde{\mathbf{A}}\mathbf{s} \tag{2.41}$$

It is easy to see as the new mixing matrix $\widetilde{\mathbf{A}}$ coming out from whitening $\mathbf{x}$, is *orthogonal*, that is

$$E\{\mathbf{z}\mathbf{z}^T\} = \widetilde{\mathbf{A}}\widetilde{\mathbf{A}}^T = \mathbf{I} \tag{2.42}$$

This means that whitening the observable data before applying ICA, restricts the search for the mixing matrix to the space of orthogonal matrices. Instead, having to estimate n^2 parameters, which are the elements of the original matrix $\mathbf{A}$, it is sufficient to estimate the orthogonal mixing matrix $\widetilde{\mathbf{A}}$, which contains $(n-1)n/2$ degrees of freedom. Since whitening is a simple procedure and allows to reduce the complexity of the problem, it is strongly recommended to make it before doing ICA.

2.2.5   Non-Gaussianity as guideline for the independence

As previously mentioned, the assumption of non-Gaussianity of the sources is essential for solving the ICA problem. Therefore, Hyvarinen (1999) proposed an ICA algorithm based on maximizing non-Gaussianity as a measure of statistical independence. Indeed, the *central limit theorem* (CLT) establishes that the sum of independent and identically distributed (i.i.d.) random variables tends to a Gaussian distribution. Thus, the sum of even two independent random variables is usually more Gausssian than each of the original variables.

Observing CLT and ICA assumptions, the independent components could be found by searching an unmixing matrix $\mathbf{W}$ that maximizes the non-Gaussianity of the independent components. Therefore, one quantitative measure of non-Gaussianity is necessary. There are various ways to measure the non-Gaussianity

of a random variable. One of the most common ways to is excess kurtosis, *kurt*:

$$kurt(y) = E\{y^4\} - 3\left(E\{y^2\}^2\right) \qquad (2.43)$$

Remember that all of the random variables here are normalized to zero mean (centering) and unit variance (whitening). Recall that for a Gaussian random variable, kurtosis is 3. Therefore, it is possible to use, as a measure of non-Gaussianity, the excess kurtosis. Specifically, the excess kurtosis is zero for a Gaussian random variable, and for most non-Gaussian random variables, excess kurtosis is nonzero.

In this work, the independent components are estimated by using the FastICA algorithm. FastICA is a fixed-point algorithm that estimates the unmixing matrix by maximizing the absolute value of the kurtosis.

2.2.6   Number of independent components

In some cases, the number of underlying structures n to be determined is known beforehand to be much smaller than the number m of mixtures available, thus making **A** a non-square matrix, whose inverse cannot be defined. One solution is to reduce the rank of the data during the whitening phase, by applying SVD (or POD) (Wu et al., 2003) and using only the leading n eigenvectors and eigenvalues (where $n \ll m$). When performing the transformation described by Eq. (2.40), this results in taking, from matrix **Λ**, only the submatrix consisting of the first n rows and columns, and from matrix **E** only the first n columns, respectively.

Usually, however, the number of independent sources is unknown. In this case it is still advisable to seek a chosen, relatively low number of sources, that are mathematically identifiable and interpretable from the physical point of view. Alternatively, one can determine the independent components directly from a high dimensional data set and then identify dominant components that can well rep-

resent the data. The weak point of this second approach is that, unlike with the POD method, there exists no natural ordering of the independent components, thus dominant components cannot be identified unless an order relation is defined, which is somewhat arbitrary. This can be readily done (Wu et al., 2006), for example by calculating the norms of the columns of the mixing matrix $\mathbf{A}$ and then ordering the s_i according to the norm of the corresponding columns, or use a measure of the non-gaussianity of the components. Here we employ one of the ordering criteria presented by Wu et al. (2006), i.e. the one based on the mean square error (MSE) of the low-dimensional representation of the original data in terms of components. In particular, it can be shown that a set of components $\mathbf{s}(t) = (s_1, ... s_n)^T$ can be ordered as follows:

$$\sum_{t=1}^{T} \sum_{i=1}^{m} a_{i1}^2 Var(s_1(t)) \geq \sum_{t=1}^{T} \sum_{i=1}^{m} a_{i2}^2 Var(s_2(t)) \geq \cdots \geq \sum_{t=1}^{T} \sum_{i=1}^{m} a_{in}^2 Var(s_n(t))$$

$$(2.44)$$

Eq.(2.44) implies that, when increasing the number of components considered, larger optimal sets of components are always supersets of the smaller optimal sets, that is:

$$S_{opt}^p \subset S_{opt}^{p+1} \qquad p = 1, \ldots, n-1 \tag{2.45}$$

where S_{opt}^p is the set of p dominant components in according to the order established by Eq. (2.44).

2.2.7   ICA: image applications

As previously mentioned, in the classical application of ICA, each of n temporal signal mixtures is measured over T time steps, and n temporal source signals are recovered as $\mathbf{y} = \mathbf{Wx}$, where each source signal is independent over time from every other source signal.

When we consider a sequence of images (Stone, 2004), each image consists of a

Sources

Mixtures

Independent Components

POD modes
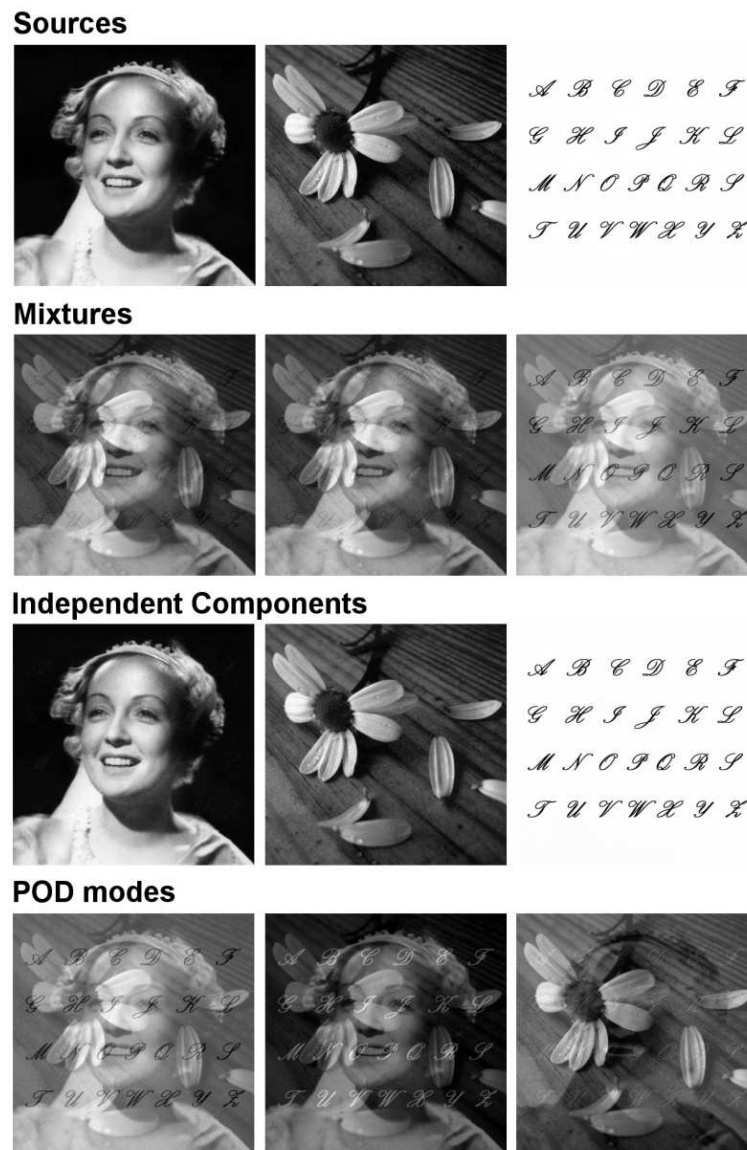
Figure 2.3: Independent source images, artificial mixtures of images, and images mixtures.

set of pixels, and ICA can be used in one of the two complementary to extract either temporal source signals using temporal ICA (tICA), or spatial source signals using spatial ICA (sICA). tICA produces a set of mutually independent temporal sequences and a corresponding set of unconstrained images, i.e. no restriction

is imposed on the mutual properties of the images: they simply characterize the contribution of each independent source signal to the observed one. Instead, sICA determines mutually independent images and a corresponding set of unconstrained temporal sequences.

Regarding the images, the concepts of mixing and separation are illustrated with an artificial example in Figure 2.3. In other words, this example shows the extension of the cocktail-party problem to images. A set of three independent source images is chosen and multiplied by the mixing matrix $\mathbf{A}$ (with randomly generated elements) in order to generate mixture images. Then, ICA is applied by maximizing the independence over space as a function of the matrix $\mathbf{W}$, so that signals y can be determined, being an estimation of the source signals s. The separation performance of ICA, starting from the mixtures, is striking. On the contrary, POD is unable to identify the three independent components. Source images in the example are: a stunning smile of Grethe Gerda Kornstädt, stage name Dita Parlo, from the motion picture "L'Atalante" (1932), by J. Vigo; a popular photograph of a trampled-on flower; and an alphabet written with Palace Script MT font.

2.3   Dynamic Mode Decomposition

Dynamic Mode Decomposition (DMD) is a recent analysis technique presented at a 2008 conference by Schmid and Sesterhenn, readily received and employed by many researchers in the fields of both fluid dynamics and combustion. The first article accepted was published by Rowley et al. (2009) only a year later. Schimd et al. published their first article on DMD in 2010 (Schmid, 2010). The articles by Rowley and Schimd are the most important works on this topic, and represent

the starting points for the study of this analysis technique. However, it must be noted that the theoretical approaches followed by Rowely and Schimd, differ quite a bit in the way they consider DMD.

The work presented by Rowley et al. (2009) is based on the theory of Koopman spectral analysis, which is based on an infinite-dimensional linear operator, called *Koopman operator*, associated with the full nonlinear system. In particular, the technique proposed by Rowley is based on the spectral decomposition of complex nonlinear flows into modes, called *Koopman modes*, determined from the spectral decomposition of the Koopman operator of the system. Koopman modes are associated with a particular state of the system, and may be estimated directly from a set of snapshots (either numerical or experimental) by means of a particular version of the standard Arnoldi algorithm. Each Koopman mode is associated with a particular *Koopman eigenvalue.* These eigenvalues provide information on the dynamic of the system in terms of frequency and growth rate connected to a particular feature relative to corresponding Koopman mode. Since the Arnoldi method proposed by Rowley et al. (2009) for the computations of the Koopman modes, is identical to DMD proposed by Schmid and Sesterhenn, Rowley et al. (2009) regard DMD as a particular algorithm that provides an approximation of the spectral decomposition of the Koopman operator.

On the contrary, the paper by (Schmid, 2010) focuses directly on DMD. In this paper, DMD is thought as a generalization of global stability analysis; furthermore, in this paper is shown that DMD is also valid for the analysis of nonlinear systems (nonlinear flows). Specifically, in the case of linearized systems (or linearized flow), DMD analysis and global stability analysis provide the same results; for a nonlinear system (or nonlinear flow), DMD provides the features of the linear tangent approximation to the underlying flow and the corresponding information on the dynamic behaviour (frequency and growth rate) captured by the set of data

(snapshots).

The differing interpretations found in these two articles could make confusion regarding the difference between Koopman modes and DMD modes. Indeed, the two terms can be interchanged. In fact, both Koopman and DMD analysis are based on the same algorithms, and the differences depend only on the theoretical framework in which the results are interpreted. A nice review on spectral Koopman spectral analysis (or DMD) was written by Mezić (2013). In the rest of this dissertation, we shall follow the same discussion and terminology proposed by Schmid (2010). In this section, a brief review is presented about the recent DMD applications in the field of turbulence and combustion, followed by a mathematical description of DMD.

2.3.1   Applications of DMD analysis

Dynamic Mode Decomposition is a powerful technique in order to extract useful information about the dynamics of a system starting from experimental or simulation data. Specifically, it permits to extract spatial modes (spatial features) from a given data set (snapshots), and to associate to each mode a unique frequency and growth rate (temporal feature). In the last years, many researchers have employed DMD to extract and describe the underlying phenomena from sets of data obtained by particle image velocimetry (PIV) experiments and large eddy simulations (LES). Schmid et al. (2011) applied DMD to Schlieren snapshots of a helium (passive scalar) jet and to time-resolved PIV-measurements of an unforced and harmonically forced jet, to analyse the physical mechanisms of the fluid flow in terms of spatial features and corresponding frequencies. Seena and Sung (2011) used DMD to carry out global stability analysis on cavity flow at high Reynolds numbers, in order to extract the features of the flow field that may be related to flow instability. Tirunagari et al. (2012) applied DMD to analyse LES data of sub-

sonic jets in order to understand better the mixing of fuel and oxidiser. Sakowitz et al. (2013) analysed the flow field in an internal combustion (IC) engine manifold by processing the data obtained by large eddy simulations to extract the spatial features associated to characteristic frequencies of the engine.

Aoki et al. (2015) analysed the acoustic instabilities and the dynamics of a hydrogen-air turbulent swirling flame in a cuboid combustor by applying DMD on DNS data. Particularly, the interaction between the pressure and heat release fields was investigated in terms of dynamic modes.

2.3.2   DMD: mathematical description

In this section, we follow the same mathematical description made by Schmid (2010) on the DMD. Given a snapshot sequence obtained by experiments or simulations, $\mathbf{v_i}$, it is possible to organize the data into following matrix $\mathbf{V}_j^N$

$$\mathbf{V}_j^N = \{\mathbf{v}_j, \mathbf{v}_{j+1}, \mathbf{v}_{j+2}, ..., \mathbf{v}_N\} \tag{2.46}$$

where the subscript denotes the first snapshot of the sequence, while the superscript denotes the last snapshots of the sequence. Only two sequence shall be used for the mathematical description of DMD, that is:

$$\mathbf{V}_1^{N-1} = \{\mathbf{v}_1, \mathbf{v}_2, \mathbf{v}_3, ..., \mathbf{v}_{N-1}\} \tag{2.47a}$$

$$\mathbf{V}_2^N = \{\mathbf{v}_2, \mathbf{v}_3, \mathbf{v}_4, ..., \mathbf{v}_N\} \tag{2.47b}$$

Besides, an ordered sequence of snapshots is considered separated by a constant sampling time Δt. In the case of experimental data, a preprocessing could be necessary in order to increase the *signal-to-noise ratio* (SNR), or equivalently to reduce the amount of noise present in the set of data.

The main idea of the DMD is to assume the existence of a constant linear mapping $\mathbf{A}$ that connects the snapshot $\mathbf{v}_i$ to the subsequent snapshot $\mathbf{v}_{i+1}$, that is,

$$\mathbf{v_{i+1}} = \mathbf{A}\mathbf{v_i} \tag{2.48}$$

and that this mapping is (approximately) the same over the entire observation time $[0, (N-1)\Delta t]$. If the set of data are generated by a nonlinear process, this assumption is equivalent to a linear tangent approximation of the system. In the particular case that the data are generated by a linear system, no assumption is made by assuming a constant linear mapping. In any case, the assumption of a constant linear mapping between the snapshots will permit to write the i-th snapshot, $\mathbf{v}_i$, as

$$\mathbf{v}_i = \mathbf{A}\mathbf{v}_{i-1} = \mathbf{A}^2\mathbf{v}_{i-2} = \mathbf{A}^3\mathbf{v}_{i-3} = ... = \mathbf{A}^{i-1}\mathbf{v}_1 \tag{2.49}$$

As a result, the entire sequence of the snapshots $\mathbf{V}_1^N$ can be formulated as a Krylov sequence (Greenbaum, 1997),

$$\mathbf{V}_1^N = \left\{ \mathbf{v}_1, \mathbf{A}\mathbf{v}_1, \mathbf{A}^2\mathbf{v}_1, ..., \mathbf{A}^{N-1}\mathbf{v}_1 \right\} \tag{2.50}$$

Hence, the main objective of DMD is to extract the dynamic characteristic (eigenvalues, eigenvectors, pseudoeigenvalues, energy amplification, resonance behaviour) of the dynamic process described by the linear mapping matrix $\mathbf{A}$ based on the sequence $\mathbf{V}_1^N$. About the influence of the number of snapshots on the dynamic features of the underlying physical process investigated, it is logical to think that the number of snapshots increases, the data sequence better captures the main dominant features of the dynamical system (underlying physical process). Therefore, it is reasonable to assume that there exists a critical number of snapshots, say N, beyond which the vector components of $\mathbf{V}_1^N$ become linearly dependent. In other words, adding further snapshots $\mathbf{v}_i$ to the data sequence will not contribute further information about the dynamic dominant features of the system investigated. In mathematical words, when this limit is approached, the N-th snapshots can be thought as linear combination of the N-1 previous linearly independent snapshots, that is

$$\mathbf{v}_N = a_1\mathbf{v}_1 + a_2\mathbf{v}_2 + ... + a_{N-1}\mathbf{v}_{N-1} + \mathbf{r} \tag{2.51}$$

or equivalently, in matrix form:

$$\mathbf{v}_N = \mathbf{V}_1^{N-1}\mathbf{a} + \mathbf{r} \tag{2.52}$$

where $\mathbf{a}^T = \{a_1, a_2, ..., a_{N-1}\}$ and $\mathbf{r}$ are respectively the vector of the coefficients and the of residuals. Following the approach proposed by Ruhe (1984), it is possible to write:

$$\mathbf{A}\mathbf{V}_N^{N-1} = \mathbf{V}_2^N = \mathbf{V}_1^{N-1}\mathbf{S} + \mathbf{r}\mathbf{e}_{N-1}^T \tag{2.53}$$

where $\mathbf{e}_{N-1} \in \mathbb{R}^{N-1}$ is the unit vector.

Looking at the elements of the matrix $\mathbf{S}$,

$$\mathbf{S} = \begin{pmatrix} 0 & & & & a_1 \\ 1 & 0 & & & a_2 \\ & \ddots & \ddots & & \vdots \\ & & 1 & 0 & a_{N-2} \\ & & & 1 & a_{N-1} \end{pmatrix} \tag{2.54}$$

it can be seen as this matrix is of *companion* type to the linear representation in Eq.2.51. Moreover, the only unknowns in $\mathbf{S}$ are the coefficients $\{a_1, a_2, ..., a_{N-1}\}$ of the linear combination of Eq. (2.51); namely, the coefficients of the representation of the last snapshot $\mathbf{v}_N$ as linear combination of the previous N-1 snapshots $\{\mathbf{v}_1, \mathbf{v}_2, ..., \mathbf{v}_{N-1}\}$. Since the eigenvalues of $\mathbf{S}$, also known as the Ritz values, approximate some eigenvalues of $\mathbf{A}$, various DMD algorithm have been developed to estimate the matrix $\mathbf{S}$ in a way that the norm (usually L_2-norm) of the residual vector is minimized. In other words, as the residual $\mathbf{r}$ becomes smaller and smaller, the eigenvalues of $\mathbf{S}$ approximate better and better the eigenvalues of $\mathbf{A}$. Thus, DMD can also be considered as an optimization problem with the following objective function:

$$\mathbf{S} = \arg\min_{\mathbf{M}} \left\| \mathbf{V}_2^N - \mathbf{V}_1^{N-1}\mathbf{M} \right\| \tag{2.55}$$

with $\mathbf{M} \in \mathbb{R}^{(N-1)\times(N-1)}$.

2.3.3 DMD Algorithms

In this section will be presented the main DMD algorithms employed for the analysis of experimental data. Few algorithms are grouped in the work by Richecoeur et al. (2012). Particularly, in this subsection two main algorithms will be presented:

1. DMD algorithm based on QR-decomposition;

2. DMD algorithm based on singular value decomposition (SVD).

DMD algorithm based on QR-decomposition. The matrix $\mathbf{S}$ is computed as follows: the last snapshot of a given sequence is expressed as a linear combination of the N previous snapshots (see Eq. 2.51). Under the assumption that the matrix $\mathbf{V}_1^{N-1}$ has full rank, the solution vector of the coefficients a_i that minimize the L_2-norm of the residual vector (Eq. 2.51), namely the least-squares solution, is given by:

$$\mathbf{a} = \mathbf{R}^{-1}\mathbf{Q}^H \mathbf{v}_N \tag{2.56}$$

where the matrices $\mathbf{Q}$ and $\mathbf{R}$ are given by QR-decomposition of the snapshot sequence $\mathbf{V}_1^{N-1} = \mathbf{QR}$, and $\mathbf{Q}^H$ is the complex conjugate transpose of $\mathbf{Q}$. Hence, the companion matrix $\mathbf{S}$ can be obtained as

$$\mathbf{S} = \mathbf{R}^{-1}\mathbf{Q}^H \mathbf{V}_2^N \tag{2.57}$$

and its spectral decomposition

$$\mathbf{S}\mathbf{y}_i = \mu_i \mathbf{y}_i \tag{2.58}$$

where $\mathbf{y_1}$ and μ_i are respectively the i-th eigenvector and eigenvalue (they are typically complex and conjugate) of $\mathbf{S}$. Each dynamic mode (DM_i), ϕ_i, is obtained

by projection of $\mathbf{V}_1^{N-1}$ onto the eigenvector $\mathbf{y}_i$, namely:

$$\phi_i = \mathbf{V}_1^{N-1}\mathbf{y}_i \qquad i = \{1, 2, ..., N-1\} \tag{2.59}$$

The information about the dynamic of each mode, in terms of frequency f_i and growth rate σ_i , are provided by the eigenvalues μ_i of the companion matrix $\mathbf{S}$ through the following relationships:

$$\sigma_i = \log\left(\mathrm{Re}(\mu_i)\right)/\Delta t \tag{2.60a}$$

$$f_i = \log\left(\mathrm{Im}(\mu_i)\right)/2\pi\Delta t \tag{2.60b}$$

whereas the amplitude of the i-th dynamic mode is given by its L_2-norm, $\|\phi_i\|_{L_2}$. In addition, the ensemble of all Ritz values of $\mathbf{S}$ takes the name of dynamic mode spectrum. The DMD method based on QR-decomposition is summarised in Algorithm 1, where $\mathbf{D}$ is the diagonal matrix of the eigenvalues μ_i of $\mathbf{S}$. In accordance with standard convention reported in Algorithm 1, the dynamic mode spectrum is often logarithmically mapped onto plane complex as:

$$\lambda_i = \log(\mu_i)/\Delta t \tag{2.61}$$

Besides, it is important to highlight that at no step in Algorithm 1 the explicit form of the system matrix $\mathbf{A}$ (Eq. 2.48) appears. As a result, the dynamic modes and the dynamic mode spectrum are both computed by using only the ensemble of data (snapshots) collected. The most important property of this method is the ability to extract the underlying dynamics of a system using only few snapshots of the system, i.e. without assuming any model of the underlying physical system. In mathematical words, this means that $\mathbf{A}$ is assumed to be a *free-matrix* (Schmid, 2010).

DMD algorithm based on SVD. Even though the method based on QR-decomposition is mathematically correct and it is often employed to prove the

---

Algorithm 1: DMD algorithm based on QR-decomposition (Schmid et al., 2011)

Data: a sequence of n snapshots $\{\mathbf{v}_1, \mathbf{v}_2, \ldots, \mathbf{v}_N\}$ sampled with fixed sampling time Δt;

Output: dynamic mode spectrum λ_i and associated dynamic modes ϕ_i with $\{i =, 2, \ldots, N-1\}$

$\mathbf{V}_1^{N-1} = \{\mathbf{v}_1, \mathbf{v}_2, \ldots, \mathbf{v}_{N-1}\}$

$\mathbf{V}_2^{N} = \{\mathbf{v}_2, \mathbf{v}_3, \ldots, \mathbf{v}_N\}$

$[\mathbf{Q}, \mathbf{R}] = qr(\mathbf{V}_1^{N-1}, 0)$

$\mathbf{S} = \mathbf{R}^{-1}\mathbf{Q}^H\mathbf{V}_2^N$

$[\mathbf{Y}, \mathbf{D}] = eig(\mathbf{S})$

$\lambda_i = \log{(\mathbf{D}_{ii})}/\Delta t$

$\phi_i = \mathbf{V}_1^{N-1}\mathbf{y}_i$

---

properties of convergence of a full Arnoldi method, in practical applications Algorithm 1 yields an ill-conditioned companion matrix and is not able to extract more than one or two dynamic modes. This is particularly true in the case of experimental data, which are corrupted by noise and other uncertainties. Therefore, Schmid (2010) has proposed a more robust algorithm based on singular value decomposition (SVD), which can also be employed for the analysis of experimental data. The robustness is achieved by carrying out a singular value decomposition of the sequence data snapshot matrix $\mathbf{V}_1^{N-1}$,

$$\mathbf{V}_1^{N-1} = \mathbf{U}\boldsymbol{\Sigma}\mathbf{W}^H \tag{2.62}$$

where matrix $\mathbf{U}$ contains the spatial structures, matrix $\mathbf{W}$ contains the temporal features , matrix $\mathbf{S}$ contains the singular values and superscript H denotes the

Hermitian transpose. Since SVD and POD are equivalent, it is possible to show that matrix $\mathbf{U}$ corresponds to the POD modes, matrix $\mathbf{W}$ corresponds to the POD coefficients, and the singular values correspond to the energies of the POD modes. Substituting Eq. (2.62) into Eq. (2.53) and rearranging the resulting expression, the *full* matrix $\widetilde{\mathbf{S}}$ is obtained as

$$\mathbf{U}^H \mathbf{A} \mathbf{U} = \mathbf{U}^H \mathbf{V_2}^N \mathbf{W} \mathbf{\Sigma}^{-1} = \widetilde{\mathbf{S}} \tag{2.63}$$

Besides, it is clear that matrix $\widetilde{\mathbf{S}}$ is obtained via a similarity transform of $\mathbf{S}$, hence $\mathbf{S}$ and $\widetilde{\mathbf{S}}$ have the same eigenvalues. Since matrix $\mathbf{U}$ contains the POD modes of the matrix of snapshots $\mathbf{V}_1^{N-1}$, it is interesting to note as the matrix $\widetilde{\mathbf{S}}$ represents the projection of the POD modes $\mathbf{U}$ onto with structured shifted over one time step Δt, expressed as $\mathbf{A} \mathbf{U}$. The computation of matrix $\widetilde{\mathbf{S}}$ as $\mathbf{U}^H \mathbf{A} \mathbf{U}$ is only possible by numerical simulation where, given the initial conditions, the system matrix $\mathbf{A}$ is known over the first time-step; in the case of experiments, such expression cannot be employed. Therefore, matrix $\widetilde{\mathbf{S}}$ has to be computed from the sequence of snapshots.

A further advantage of this method regards the potentiality to extract the dynamic modes when the matrix of snapshots $\mathbf{V}_1^{N-1}$ is rank-deficient (or nearly so), due to the occurrence of linearly dependent snapshots within the sequence, that causes an ill-conditioned companion matrix $\mathbf{S}$. Specifically, this problem is overcome by employing a truncated SVD representation of $\mathbf{V}_1^{N-1}$ obtained by the parts of $\mathbf{U}$, $\mathbf{W}$ and $\mathbf{\Sigma}$ corresponding to singular values smaller than threshold (or the first M largest singular values that capture a fixed amount of energy). Let $\widetilde{\mathbf{U}}$, $\widetilde{\mathbf{W}}$ and $\widetilde{\mathbf{\Sigma}}$ be the matrices of the truncated SVD representation of $\mathbf{V}_1^{N-1}$, the companion matrix based on truncated SVD is given by

$$\widetilde{\mathbf{S}} = \widetilde{\mathbf{U}}^H \mathbf{V_2}^N \widetilde{\mathbf{W}} \widetilde{\mathbf{\Sigma}}^{-1} \tag{2.64}$$

Similar to Algorithm 1, frequency and growth rate of each dynamic mode are

---

Algorithm 2: SVD-based DMD algorithm (Schmid, 2010)

Data: a sequence of n snapshots $\{\mathbf{v}_1, \mathbf{v}_2, \ldots, \mathbf{v}_N\}$ sampled with fixed

sampling time Δt;

Output: dynamic mode spectrum λ_i and associated dynamic modes ϕ_i

with $\{i =, 2, \ldots, N-1\}$

$\mathbf{V}_1^{N-1} = \{\mathbf{v}_1, \mathbf{v}_2, \ldots, \mathbf{v}_{N-1}\}$

$\mathbf{V}_2^{N} = \{\mathbf{v}_2, \mathbf{v}_3, \ldots, \mathbf{v}_N\}$

$\mathbf{U\Sigma W}^H = \mathbf{V}_1^{N-1}$ *(Singular Value Decomposition)*

$\widetilde{\mathbf{S}} = \mathbf{U}^H \mathbf{V_2}^N \mathbf{W\Sigma}^{-1}$

$[\mathbf{Y}, \mathbf{D}] = eig(\widetilde{\mathbf{S}})$

$\lambda_i = \log\left(\mathbf{D}_{ii}\right)/\Delta t$

$\phi_i = \mathbf{U}\mathbf{y}_i$

---

provided from Eqs. (2.60). Finally, this method is summarised in Algorithm 2.

2.4   Optical flow

In the last decades, the study of techniques for the estimation of the motion field
from a sequence of images has been of great interest to fluid mechanics and com-
puter vision communities. This topic of research is also of great interest for scien-
tists in the fields of meteorology and oceanography, where satellite images provide
information for the estimation of cloud motion and ocean currents. One of the
numerical techniques, which allow to extract information on the motion field from
a sequence of images, is based on the concept of *Optical Flow.*

Optical flow was introduced in the context of computer vision, and regards *appar-
ent visual motion* between the observer (e.g. camera, eyes, etc.) and the objects

of the scene. Specifically, optical flow is defined as the apparent motion of the brightness patterns (Horn and Schunck, 1981). In the ideal case, where the brightness of the object does not change, the optical flow will correspond to the relative motion field between the objects and the observer.

Similarly to the intrusive PIV, in applications of fluid mechanics, the non-intrusive optical flow technique aims at estimating the velocity field from an image sequence. Therefore, it is worth discussing the main dissimilarities between these two techniques.

PIV is the most common and used technique in laboratories to extract the velocity field of a fluid from image sequences. It requires the use of a tracer particles sufficiently small, so that it may be presumed that the particles faithfully follow the flow, and laser pulses that illuminate the particles inside the flow. The images of the tracer particles are acquired in two consecutive instances by a camera. Then, the motion field can be retrieved by searching the local displacement that maximizes the cross correlation between two interrogation windows collocated in each of the two images. Nevertheless, several limiting factors influence this method. It has proved to be efficient when satisfying various criteria related to tracer particle density or to the local gradient of the studied flow. The first limiting factor is related to size of the interrogation window. Indeed, if such window is chosen too small, cross-correlation peaks might not occur; if it is chosen too large, particles in the window might have different motions due to local inhomogeneities of the flow; because PIV method estimates a single velocity vector representing the motion majority of the particles present in the interrogation window. In both cases, due to the size of the interrogation window, the estimation of the velocity field might be either too noisy (interrogation window size is too small), or too smooth (interrogation window size is too big), or even incorrect. Another limiting factor is connected to the use of tracer particles. Consequently, PIV method cannot be

used in all those applications where tracer particles cannot be employed (e.g. meteorology, oceanography, high temperature, reacting flows).

Despite that the optical flow methods are less popular than PIV in applications of fluid mechanics, because they are more sensitive to noise and imaging conditions they are becoming more and more interesting during the last years. Optical flow methods perform more efficiently in dense estimation of velocity field from image sequence, because they do not use interrogation windows. Besides, unlike PIV methods, optical flow methods have the potentiality to include various physical constraints (Barron et al., 1994). Indeed, Chen et al. (2015) have proposed a new formulation of optical flow for the 2D incompressible turbulent flows, based on the coupling of the equation of optical flow and the continuity equation of 2D incompressible flow.

In this dissertation, the optical flow method will be employed in order to estimate the motion field associated to the propagation of the flame front during the kernel period of the combustion process that occurs within the combustion chamber of a spark-ignition engine.

In the next section, the optical flow constraint equation will be reported.

2.4.1 Optical flow estimation

The usual assumption behind optical flow is the well-known brightness conservation (Horn and Schunck, 1981), namely the changes of the brightness in the image sequence are due only to motion. Let $I(x, y, t)$ be the brightness intensity at the point (x, y) at time t; the balance equation for the brightness, commonly called optical-flow constraint equation, is given by:

$$\frac{\mathrm{d}}{\mathrm{d}t}I(x, y, t) = \frac{\partial}{\partial t}I(x, y, t) + \nabla I(x, y, t) \cdot \mathbf{u}(x, y, t) = 0 \qquad (2.65)$$

where $\mathbf{u}(x,y,t) = [u_x(t), u_y(t)]^T \equiv [\mathrm{d}x/\mathrm{d}t, \mathrm{d}y/\mathrm{d}t]^T$ is the optical flow field, $I(x,y,t)$ is the intensity of the image as a function of time and space, and $\nabla I(x,y,t) = [\partial I/\partial x, \partial I/\partial y]^T$ is the gradient of the intensity of the image.

Let I_x, I_y and I_t be respectively the abbreviations for the partial derivatives of the intensity of the image respect with x, y and t, the optical flow constraint equation (Eq. (2.65)) can be written as:

$$I_t + I_x u_x + I_y u_y = 0 \tag{2.66}$$

This equation describes the constraint on the local flow velocity, which is illustrated in Fig. 2.4. Writing Eq. (2.66) in another way,

$$(I_x, I_y) \cdot (u_x, u_y) = -I_t \tag{2.67}$$

it can be noted as the component of the movement in the direction of the image intensity gradient (I_x, I_y) is equal to

$$\frac{-I_t}{\sqrt{I_x^2 + I_y^2}} \tag{2.68}$$

Since the unknowns of Eq. (2.66) are the components u_x and u_y of the vector $\mathbf{u}$, namely the flow field; this balance equation provides only one linear constraint. As a result, it is clear that Eq. (2.66) is not sufficient to specify completely the flow field $\mathbf{u}$. This is usually known as the "*aperture problem*" of optical flow algorithms. In order to obtain a uniqueness of the solution, it is necessary to regularize by imposing an *additional smoothness constraint*. One first way to express the additional constraint is to minimize the square of the magnitude of the gradient of the optical flow velocity, that is

$$(\partial u_x/\partial x)^2 + (\partial u_x/\partial y)^2 \quad \text{and} \quad (\partial u_y/\partial x)^2 + (\partial u_y/\partial y)^2 \tag{2.69}$$
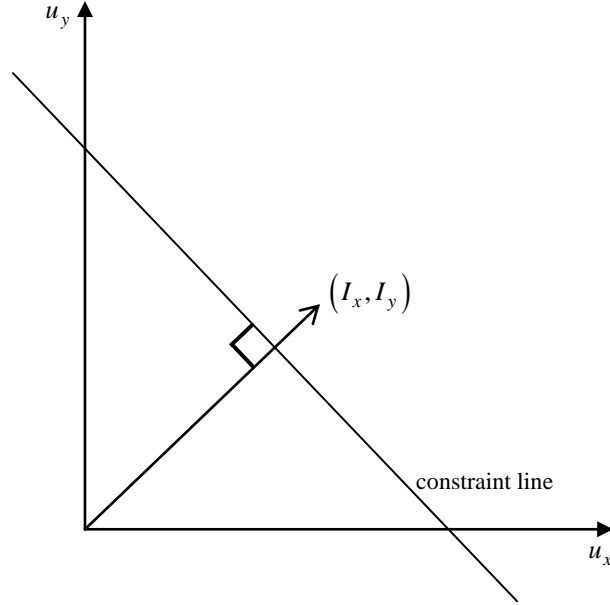
Figure 2.4: Representation of the image brightness equation constraint the optical flow (adapted from Horn and Schunck (1981)).

Another additional smoothness constraint employed in order to regularize the optical flow problem is the sum of the square of the Laplacians of the components u_x and u_y of the optical flow field,

$$\nabla^2 u_x = \frac{\partial^2 u_x}{\partial x^2} + \frac{\partial^2 u_x}{\partial y^2} \quad \text{and} \quad \nabla^2 u_y = \frac{\partial^2 u_y}{\partial x^2} + \frac{\partial^2 u_y}{\partial y^2} \tag{2.70}$$

In this thesis, the regularization form based on Eq. (2.69) is employed to carry out the analysis. Therefore, the optical flow is estimated via minimization of the sum of the errors in the equation of balance of image brightness,

$$\varepsilon_a = I_x u_x + I_y u_y + I_t \tag{2.71}$$

and of the regularization term of Eq. (2.69),

$$\varepsilon_b = \left(\frac{\partial u_x}{\partial x}\right)^2 + \left(\frac{\partial u_x}{\partial y}\right)^2 + \left(\frac{\partial u_y}{\partial x}\right)^2 + \left(\frac{\partial u_y}{\partial y}\right)^2 \tag{2.72}$$

Hence, the optical flow estimation can be found by minimizing the total error ε_{tot}

$$\varepsilon_{tot} = \iint \left(\alpha^2 \varepsilon_a^2 + \varepsilon_b^2 \right) \mathrm{d}x \mathrm{d}y \tag{2.73}$$

Now, it is possible to formulate the following optimization problem for the estimation of the optical flow,

$$\widehat{\mathbf{u}}(x, y, t) = \arg \min_{\mathbf{u}(x,y,t)} \iint \left(\alpha^2 \varepsilon_a^2 + \varepsilon_b^2 \right) \mathrm{d}x \mathrm{d}y \tag{2.74}$$

where $\widehat{\mathbf{u}}(x, y, t)$ denotes the estimation of the optical flow. Besides, during the numerical implementation of the optimization problem, all differential operators (partial derivative and gradient) are approximated by finite differences.

Chapter 3

Analysis of flame images in ICEs

This chapter illustrates the analysis conducted on flame images by employing the numerical techniques presented in the previous chapter. Particularly, the analysis were done in order to study and to characterize the cycle-to-cycle variations of a port-fuel injection spark ignition engine and a diesel engine. The numerical techniques used in this chapter are POD, ICA and optical flow.

3.1 Spark ignition engine

This section reports the analysis of 2D cycle-resolved images of combustion-related luminosity collected in a port-fuel injection spark ignition (PFI SI) optically accessible engine for two injection strategies (closed valve, open valve). The description of the experimental apparatus and the investigated operating conditions are reported in section 3.1.1. Particularly, for both injection strategies, the cyclic variations phenomena are firstly studied via a standard statical approach on the global quantities (in-cylinder pressure, global luminosity and centroid of luminosity) (Section 3.1.2). Section 3.1.3 reports the results of the application of Proper Orthogonal Decomposition (POD) to acquired images for the extraction of the

dominant features of the luminosity field emitted by the flames. Indeed, the POD modes have permitted to identify the zones of the combustion chamber wherein the higher variations of the flames occur. In addition, the coefficient of variation based on the POD coefficients, proposed by Bizon et al. (2010b), was employed in order to quantify the cyclic variations in terms of both luminous intensity and morphology of the flames. Section 3.1.4 discusses the application of Independent Component Analysis (ICA) to the set of images acquired.

The method of ICA is employed for the identification of the independent components which describe underlying patterns of the combustion process. The determined components together with the corresponding time dependent coefficients are employed to investigate the spatio-temporal evolution of the luminous combustion during a single cycle and over a number of cycles. It is demonstrated that ICA applied to single cycle permits to extract independent structures, clearly separated in time, and related to the spatial distribution in the high luminosity zone. The corresponding coefficients are clearly correlated with the integral flame luminosity and characterize time evolution of the combustion pattern in the chamber. The analysis over several cycles shows that independent components carry information about the dominant morphology of the cyclic variations. Finally, Section 3.1.5 reports the application of optical flow technique to determine the motion field of the flame front during propagation. Such technique allows to obtain information on the flame front motion without the use of intrusive technique as PIV. All of proposed procedures are promising in terms of new insight in the non-intrusive the analysis of combustion processes.

3.1.1 SI Engine: Experimental apparatus

The optically accessible single cylinder spark ignition (SI) engine is equipped with the cylinder head of a small Port Fuel Injection (PFI) gasoline engine, having four
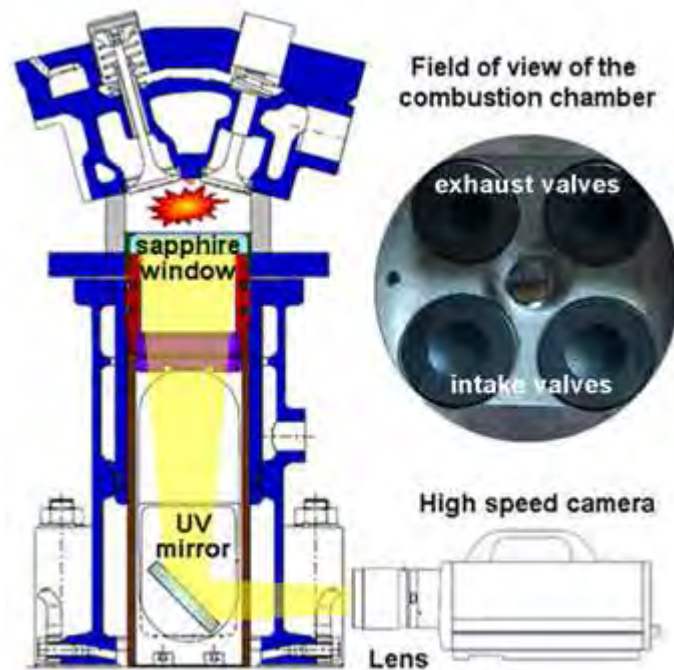
Figure 3.1: Scheme of optical engine and field of view of the combustion chamber.

valves and a centrally located spark plug. The specifications of the engine are reported in Table 3.1. Figure 3.1 reports a sketch of the optical apparatus and the bottom field view of the combustion chamber. A commercial 3-holes injector is used, with the injection pressure set at 3.5 bar. A quartz pressure transducer is flush-installed in the region between intake and exhaust valves. Combustion pressure measurements are performed for all operating conditions. The engine piston is flat and made transparent by means of a sapphire window. An elongated piston arrangement is used, together with unlubricated Teflon-bronze composite piston rings in the optical section, to avoid contamination of the window by lubricating oil. Combustion is detected through the wide sapphire window located in the piston. Images are reflected by a 45° inclined UV-visible mirror located at bottom of the engine, and conveyed towards the optical detection assembly. The latter is

made of a 78 mm focal length, f/3.8 UV Nikon objective, followed by a fast CMOS camera characterized by a sensor of 20 μm pixel size, 12-bit ADC. The spectral range spans from 400 to 900 nm. A camera region of interest is selected (360×360 pixel) to obtain the best match between spatial and temporal resolution, allowing for a spatial resolution around 0.127 mm/pixel and a frame rate of 7200 fps. The exposure time is fixed at 100 μs. AVL Indimodul records the TTL signal from the camera along with the signal acquired by the pressure transducer. It is possible in this way to record the crank angles at which the optical data are collected.

Table 3.1: Specifications of the single cylinder SI engine.

Displacement [cm^3]	250
Bore [mm]	72
Stroke [mm]	60
Connecting rod [mm]	130
Compression ratio	10.5:1

All of the tests are performed at steady state, 3000 rpm and wide open throttle. The intake air pressure and the temperature are set at 1000 mbar and 298 K, respectively. Fuel injection always takes place in the intake manifold. Two different fuel injection timings are adopted (Table 3.2), i.e. injection when the intake valves are closed (CV, 0 CAD) and injection when the intake valves are open (OV, 300 CAD). The engine is fuelled with commercial gasoline at a stoichiometric equivalence ratio as measured by an exhaust lambda sensor. To operate at maximum brake torque conditions, the spark timing is set at -22 CAD. The engine is stabilized for about 10 seconds before starting data acquisition.

Table 3.2: Engine operating conditions.

Case	Intake valves	Speed [rpm]	SOS [CAD]	DOI [CAD]	EOI [CAD]
CV	closed	3000	-22	135	0
OV	open	3000	-22	135	-300

3.1.2 Cycle-to-cycle variations analysis via global indexes

A selection of flame images detected at different crank-angles for the both CV and OV operating conditions are reported in Figure 3.2 and 3.3.It can be noted strong differences in the morphology of the flame front during the stage of propagation of flame (-2 CAD and 0.5 CAD). Moreover, the combustion of fuel drops appears as high luminosity spots. Besides, it can be also noted a strong difference in the luminosity and morphology of the flames between the closed valve and open valve conditions due to the different amount of the fuel film deposited on the intake ports during the intake stroke. In the closed-valve condition the deposits flow onto the surfaces of the cylinder head and valves in the chamber during intake causing higher flame intensity. These diffusion controlled flames persist well after the normal combustion event, because the oxygen is not completely consumed after the flame front propagation. The cycle variation of the luminosity field of the flames is well visible by observing the captured flames. In this section, the cycle variation analysis is carried out through the study of the following global parameters: integral luminosity, pressure, and luminosity centroid. The study was carried out on 22 consecutive cycles at 80 values of the crank angle.

Denote by I_g the integral luminosity computed as space integral of the acquired luminosity field (image), the analysis is focused on computing of the coefficient of
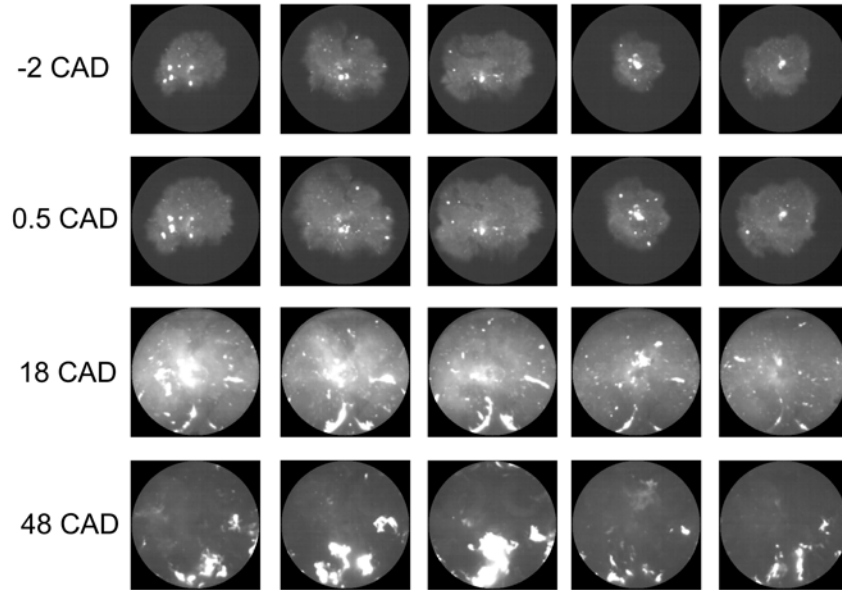
Figure 3.2: A selection of flame images detected at different crank-angles for 5 consecutive cycles (closed valve injection).

variation (CoV) for the global indexes, defined as:

$$\text{CoV} = \frac{\sigma}{\mu} \tag{3.1}$$

where μ is the mean and σ is the standard deviation considered at each value of the crank angle.

Figure 3.4 reports the CoV of the in cylinder pressure for both operating conditions investigated. It can be noted as open valve injection produces both higher mean and standard deviation values as compared to closed valve injection strategy. It can be noted that the open valve injection strategy produces higher cyclic variation in terms of pressure CoV , over the entire range of crank angle, as compared to closed valve injection. Since the highest values of both $\mu_{pressure}$ and $\sigma_{pressure}$ occur in presence of knocking, it is possible to say that the OV operating condition has higher knock than CV operating condition.

Figure 3.5 reports the scatter plots and average cycle of the integral luminosity for
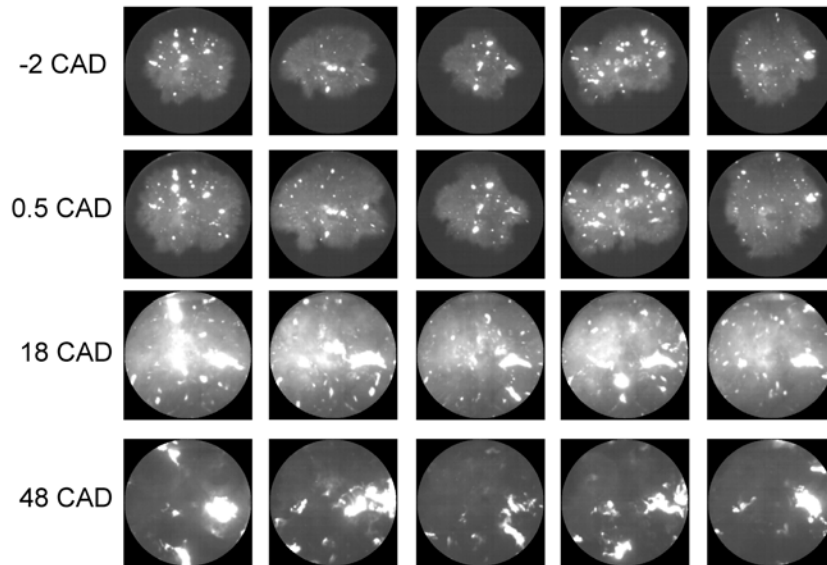
Figure 3.3: A selection of flame images detected at different crank-angles for 5 consecutive cycles (open valve injection)

all detected cycles. It can be observed that the dispersion of the integral luminosity is higher during after the normal combustion, namely during the combustion of the fuel film deposited on the intake valves. Focusing on the average cycle of the integral luminosity (solid line), it can be observed that the OV condition si characterized by higher luminosity as compared to CV condition. For CV operating conditions, after 50 CAD the average integral luminosity is roughly constant due to the diffusive combustion of the fuel film deposited on the intake valves. Conversely, for the OV operating condition, the average integral luminosity (solid line) follows the pressure cycle. Figure 3.6 reports the CoVs of the integral luminosity for both CV and OV operating conditions. It can be noted that both operating conditions show a CoV peak close to the top dead center. Precisely, they occur in correspondence of the same crank angles of the CoV peaks regarding the pressure cycles.
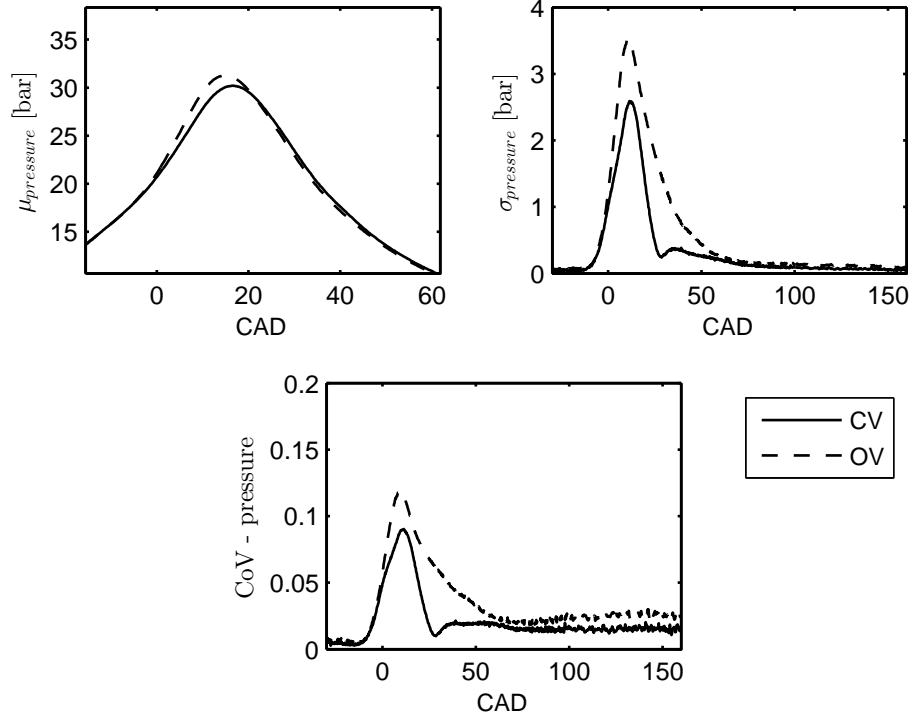
Figure 3.4: Mean ($\mu_{pressure}$), standard variation ($\sigma_{pressure}$) and CoV of the pressure in cylinder for the CV(solid line) and OV(dash line) operating conditions.

Besides, the CoV of I_g shows an increase during the diffusive combustion of the fuel film deposited on the intake valves. Conversely, the CoV of the pressure during the stage of the diffusion-controlled combustion is very small. This means that the combustion of the film fuel deposited on the intake valve has a little influence over the pressure cycle. Nevertheless, this combustion stage is important in terms of pollution emissions. For both operating conditions, during the flame front propagation (normal combustion), the CoV of the integral luminosity increases over the crank angle due to the influence of turbulence on the front flame. After the normal combustion (premixed combustion), at the beginning of the expansion stroke, the CoV tends to follow the CoV of the pressure cycle (Fig. 3.4)
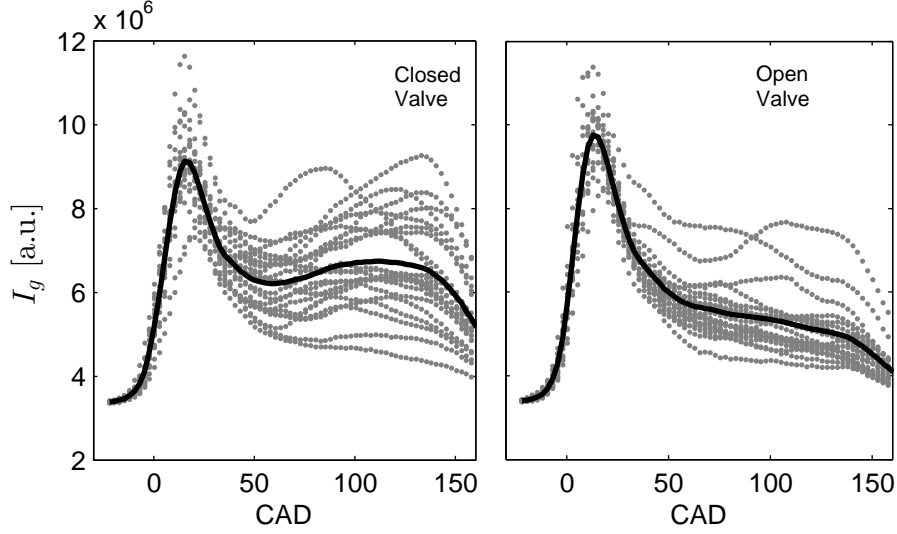
Figure 3.5: Scatter plot of the instantaneous integral luminosity (dots) and corresponding average cycle (solid line).

until 50.5 CAD and 20.5 CAD respectively for CV and OV operating conditions. Subsequently, we observe the increase of CoV for both operating conditions due to diffusion-controlled combustion of the fuel film deposited on the intake valves. In this stage, it can be noted that the CV operating condition is characterized by CoV values of I_g higher than that of the OV operating condition. Thus, in terms of integral luminosity, the CV operating condition is characterized by more intense cycle variations as compared to that of the OV operating condition. Observing average integral luminosity cycles (Fig. 3.5) and the corresponding CoVs (3.6), it is possible to say that the higher value of the CoV occurs in correspondence of high values of the integral luminosity connected to the diffusion flames close to the intake valves.

The distribution of flame light through the chamber is investigated via the luminosity centroid, $\mathbf{C}$, proposed by Bizon et al. (2010a):

$$\mathbf{C} = \frac{\int I(\mathbf{r})\mathbf{r}d\mathbf{r}}{\int I(\mathbf{r})d\mathbf{r}} \qquad (3.2)$$

where $\mathbf{C} = [X_C, Y_C]$ is the coordinate vector of the luminosity centroid; $\mathbf{r}$ is the vector position, with origin in the geometric centre of the combustion chamber, of the pixel of luminous intensity $I(\mathbf{r})$. Then, for each frame the luminosity centroid can be determined and then plotted for the entire cycle. It also possible to define the eccentricity of the luminosity centroid as the modulus of the vector $\mathbf{C}$:

$$E_C = \|\mathbf{C}\| \tag{3.3}$$

Figure 3.7 shows the luminosity centroid during a combustion cycle for CV and OV operating conditions. It can be noted as the luminosity centroid moves to intake valves in both operating conditions. Figures 3.8 and 3.9 report the scatter plots and the average values of the coordinates X_C and Y_C of $\mathbf{C}$ respectively for CV and OV conditions. For both operating conditions, it can be noted that the luminosity centroid shows relevant displacements from the combustion chamber center after 50 CAD, namely when the diffusion flames occur inside of the combustion
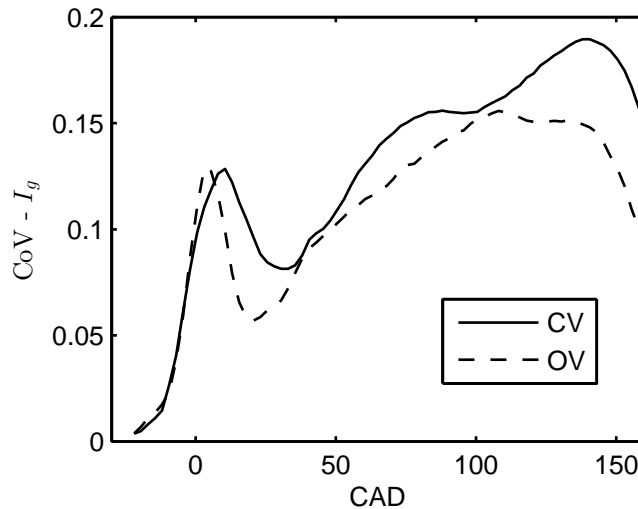
Figure 3.6: CoV of the integral luminosity for CV(solid line) and OV(dash line) operating conditions.

cycle. The dispersion of the luminosity centroid (scatter plots) is maximum during the diffusion-controlled combustion.

Focusing on average values of X_C and Y_C (solid line), a non-symmetrical behaviour of the luminosity centroid is noted for both operating conditions. Indeed, for the CV operating condition, the displacement of the luminosity centroid from the centre of the combustion chamber occurs along the y-axis; more precisely, the centroid moves towards the intake valves due to the persistent high luminous intensity diffusion flames. Instead, for OV operating condition, the displacement of the luminosity centroid occurs along the x-axis: this is due to luminosity spots that present a non symmetrical distribution in combustion chamber.

Figure 3.10 reports the standard variations for the coordinates of **C**. It can be noted that the cycle variations of the luminosity centroid are more intense for the OV operating condition than CV operating condition. This can be connected to the strong randomness of the amount of fuel deposited on the intake valves during the intake stroke. It is interesting to study the cycle variations in terms of eccen-
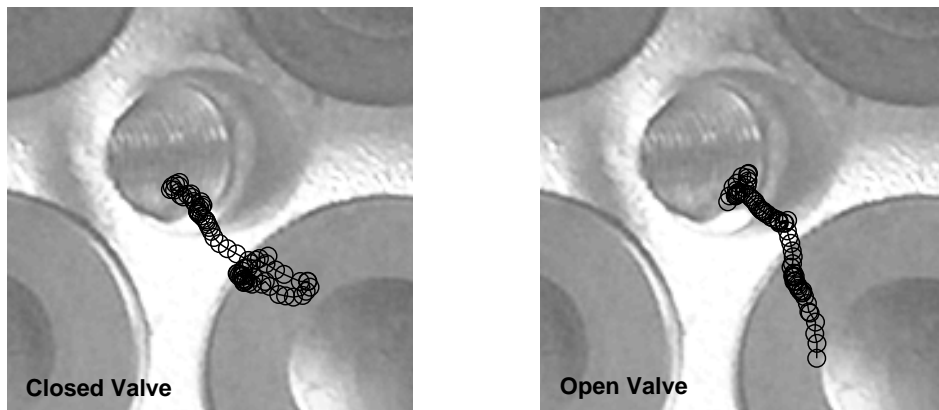
Figure 3.7: CoV of the integral luminosity for CV(solid line) and OV(dash line) operating conditions.
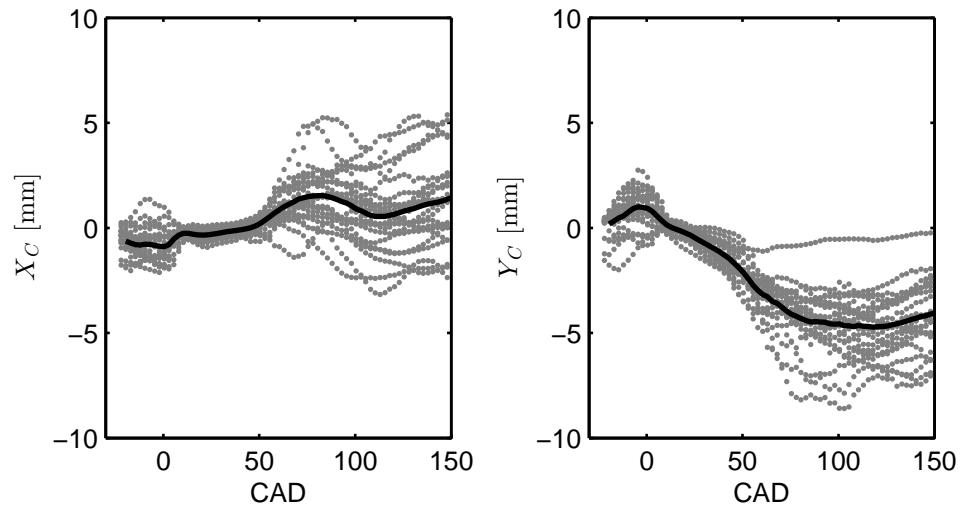
Figure 3.8: CV operating condition. Scatter plots of luminosity centroid coordinates (dots) and mean coordinates (solid line) at each crank angle.
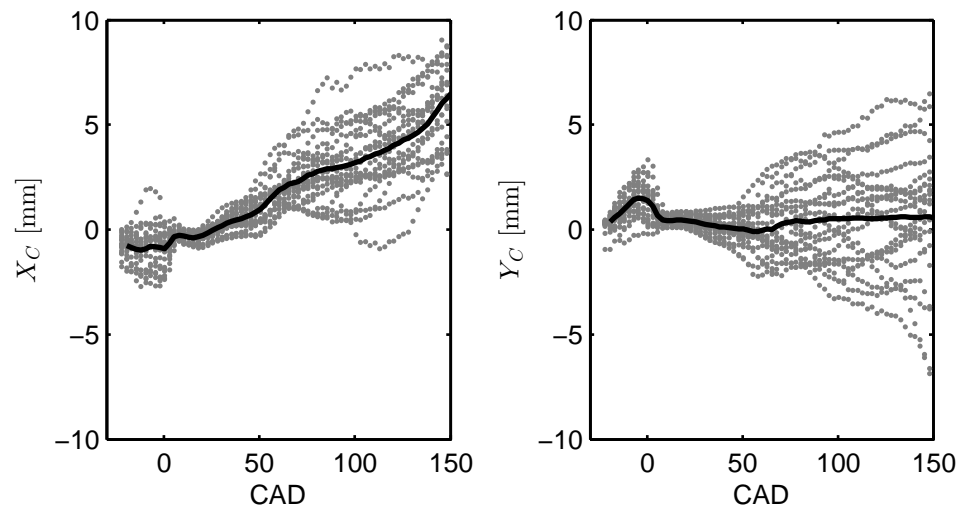
Figure 3.9: OV operating condition. Scatter plots of luminosity centroid coordinates (dots) and mean coordinates (solid line) at each crank angle.

of E_C at each crank angle investigated during the cycle-resolved acquisitions. For both operating conditions, the highest values of eccentricity occur after 50 CAD,

namely in presence of diffusion-controlled flames. Besides, observing the scatter plots of the eccentricity, more once it can be noted that the highest cycle variations of E_C occur roughly after 50 CAD as well.

Now, focusing on the mean of E_C calculated over the cycles (Figure 3.11 (solid line)), it is possible to highlight the differences and similarities between the CV and OV operating conditions. For both operating conditions, it is possible to note a similar trend between the operating conditions before 8 CAD due to similar behaviours of the flame front propagation, in terms of E_C. Indeed, for both operating conditions, the positive peaks of the mean eccentricity at top dead center are roughly of 2 mm. The two operating conditions show relevant differences of mean eccentricities after 50 CAD, where the diffusive flame appear. Here, for the CV operating conditions, the mean eccentricity increases until to stabilize around 5 mm. On the contrary, for the OV operating conditions, the mean eccentricity assumes a monotonically increasing trend (after 50 CAD) due to the diffusive com-
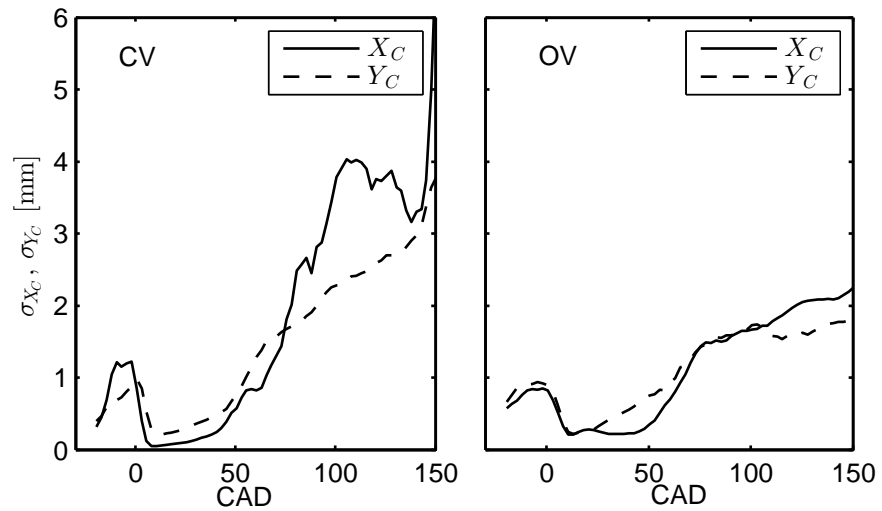
Figure 3.10: Standard variations of the luminosity centroid coordinates for CV (left side) and OV (right side) operating conditions.
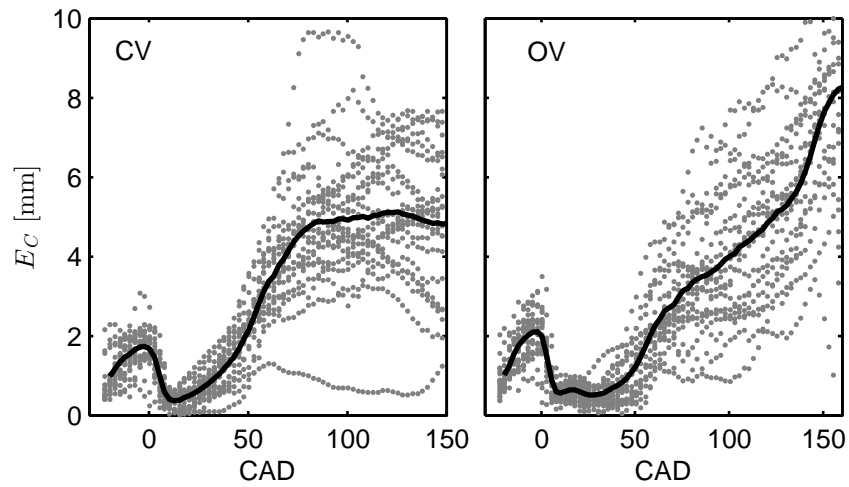
Figure 3.11: Scatter plots of luminosity centroid coordinates (dots) and mean coordinates (solid line) at each crank angle for the CV (left side) and OV (right side) operating conditions.
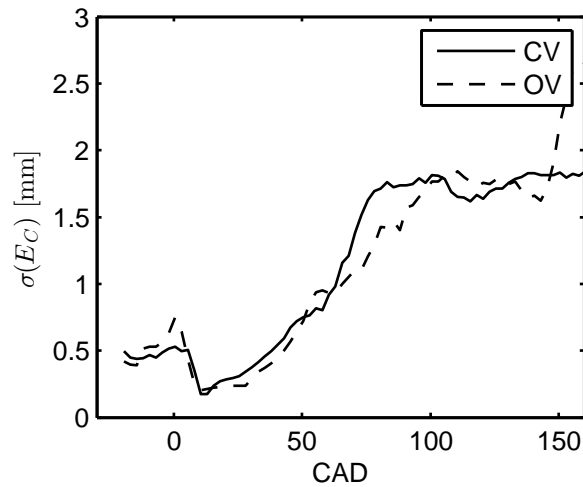
Figure 3.12: Standard variation of the eccentricity of the luminosity centroid for CV (solid line) and OV (dash line).

bustion of fuel pockets localized close to cylinder wall.

The cycle variations can be studied in terms of eccentricity of the luminosity

centroid at each crank angle. As a consequence, Figure 3.12 reports the standard variations of E_c at each crank angle for both the operating conditions. Recalling that E_C is a global index of the location in combustion chamber of the flames, it can be seen as the two operating conditions have similar behaviour in terms of standard variation of E_C. Precisely, for both the operating conditions, the standard variation of E_C is about 0.5 mm around the top dead center. Next, it increases until it stabilizes around 2 mm. Once more, the increase of the standard variation of a global index is due to the diffusion-controlled flames due to both fuel film deposited on the intake valves, and fuel liquid pockets localized near chamber walls.

In conclusion, the study of the statistics (μ,σ and CoV) of the global indexes has provided useful information on the cycle-to-cycle variations in a port-fuel injection spark ignition engines. Particularly, the study has allowed to characterize the cycle-cycle variations at each crank angle in terms of pressure, luminous intensity and luminosity centroid. As a result, the CV operating conditions is characterized by higher cycle-to-cycle variations than OV operating. The analysis does not provide any information on the cycle-to-cycle variations of the flames in terms of morphology. As a consequence, in the next subsection, the cycle-to-cycle variations are analysed using Proper Orthogonal Decomposition.

3.1.3   POD application to cycle-to-cycle variations analysis

In this section, the cycle-to-cycle variations analysis is carried out by employing the method based on POD proposed by Bizon et al. (2009b). This method is based on the definition of the coefficient of variation of the POD coefficients. Subsequently, Bizon et al. (2010b) proposed an numerical example to clarify the ability of such CoV to detect the cycle-to-cycle variations of the morphology of the flame investigated. More details of POD method are reported in Section 2.1.

$$U = \begin{bmatrix} \begin{bmatrix} u_1(x_1) \\ u_1(x_2) \\ \vdots \\ u_1(x_N) \end{bmatrix} & \begin{bmatrix} u_2(x_1) \\ u_2(x_2) \\ \vdots \\ u_2(x_N) \end{bmatrix} & \cdots & \begin{bmatrix} u_M(x_1) \\ u_M(x_2) \\ \vdots \\ u_M(x_N) \end{bmatrix} \end{bmatrix}$$
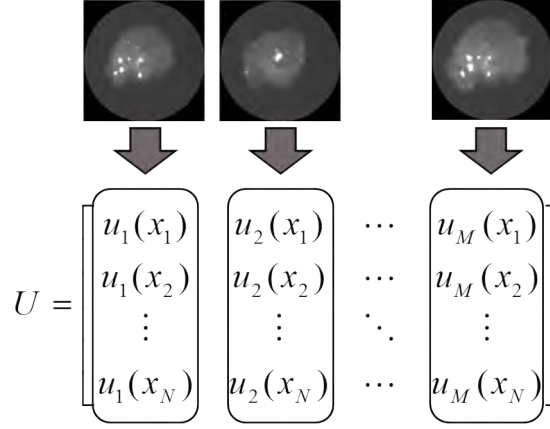
Figure 3.13: Matrix of snapshots made up by images.

Since the POD algorithm requires a 2D matrix of snapshots, it is necessary to convert each collected image. In order to carry out POD analysis, it is necessary to transform each collected image, which is a 2D matrix, from matrix form to vector form via lexicographic ordering of the pixels (Figure 3.13). For the cycle-to-cycle variations analysis, at each crank angle the matrix of the snapshots is made up by images of consecutive cycles.

In this section, the application of POD to optical data is illustrated before showing the results of the cycle-to-cycle variations analysis. Precisely, the cycle-to-cycle variations is provided via POD analysis of the ensemble of images collected at same crank angle for various consecutive cycles. Thus, let M be the number of consecutive cycles, and N the number of pixels of the images acquired, the matrix of the snapshots (Eq. 3.1.3) $N \times M$ is given by

$$\mathbf{U} = \begin{pmatrix} u_{1,1} & \cdots & u_{1,M} \\ \vdots & \ddots & \vdots \\ u_{N,1} & \cdots & u_{N,M} \end{pmatrix} = [\mathbf{u}_1, \mathbf{u}_2, \ldots \mathbf{u}_M]$$

where the element $u_{i,j}$ is the pixel value at the location of the i-th pixel at the j-th cycle, and $\mathbf{u}_j$ is the column vector obtained by lexicographic ordering of the image

acquired at j-th cycle. Since the set of data is made up by images (360×360 pixels) collected at 80 different crank angles for 20 consecutive cycles, the dimension of $\mathbf{U}$ is 129600×22. Thus, the dimension of the spatial discretization is much higher than number of snapshots ($N \gg M$), hence it is possible to apply the method of Sirovich (see Section 2.1.3) in order to come over the computational complexity due to eigenvalue computing.

Now, at each crack angle,the images are centred by subtracting the mean component, and POD is subsequently performed. Therefore, the image acquired at the j-th cycle can be expressed by sum of the mean component $\overline{\mathbf{u}}$, sometimes called mode 0, a linear combination of POD coefficients, c, and POD modes ϕ,

$$\mathbf{u_j} = \overline{\mathbf{u}} + \sum_{i=1}^{M} c_{ij}\phi_{\mathbf{i}} = c_0\phi_{\mathbf{0}} + \sum_{i=1}^{M} c_{ij}\phi_{\mathbf{i}} \tag{3.4}$$

where $c_0 = \|\overline{\mathbf{u}}\|_{L_2}$ is the L_2-norm of the mean component, ϕ_0 is the normalized mean component. Besides, in the case of data, the POD coefficients have all null mean over cycles, namely

$$\overline{c}_i = \frac{1}{M} \sum_{j=1}^{M} c_{ij} = 0 \qquad i = 1, 2, \ldots, M \tag{3.5}$$

Figures 3.14 and 3.15 show the mean component and the first four most energetic (or informative) POD modes, in absolute value, at various crank angles for the CV and OV operating conditions, respectively. POD modes are reported in absolute value in order to highlight the relevant morphological features. At -2 CAD and 5 CAD, for both operating conditions, it can be noted that the mean components and the first POD modes show morphological features that can be associated to the flame front propagation and the diffusive combustion; whereas, the other POD modes show morphological features that can be associated to diffusion combustion around scattered fuel pockets. At 18 CAD, for CV operating condition, the first 3 POD modes show dominant features that can be associated to the beginning of

the diffusion-controlled combustion of the fuel film deposited on the intake valve. Later, at 43 and 88 CAD, the first POD mode highlights well the dominant feature of the combustion localized near the intake valves, which are localized at the bottom of all figures reported in this section. For OV operating condition, both mode 1 at 43 CAD and modes 1-3 at 88 CAD show features of flames localized near cylinder wall, precisely on the right side of the images reported in Fig. 3.15. This suggests that, far from top dead center, the diffusion flames are localized near the cylinder wall. All considerations done here about the collocation of the diffusion flames far from the top dead center for the CV and OV injection strategies, seem in good agreement with what done in the previous section. Now, recalling the definition of energy captured by a single POD mode and the cumulative energy spectrum (see Section 2.1), it may be interesting to study the dissimilarities between the two operating condition in terms of energies (or amount of information) captured by POD modes. Therefore, Figures 3.16 reports the energy spectra and energy cumulative spectra based on POD (see Section 2.1). Since the decomposition has been carried out on centred data, these spectra do not take in account the contribution associated with the mean component. As a result, these spectra provide information about the percentage of total information associated, and captured by the k-th mode (e_k) and the first k modes. At -2 CAD, the CV operating condition is characterized by the fact that the first POD modes capture a higher amount of energy. Given that the first POD modes are associated to the large scale features and the energy e_k represents also the percentage of total variance captured by k-th mode (Lumley, 2007), this suggests that, around the top dead center, the CV operating condition is characterized by fluctuations of large scale more intense than the OV operating condition. Once more, this may prove an increasing of the cycle-to-cycle variations.

Since POD allows to extract the dominant features from a set of data, in our case
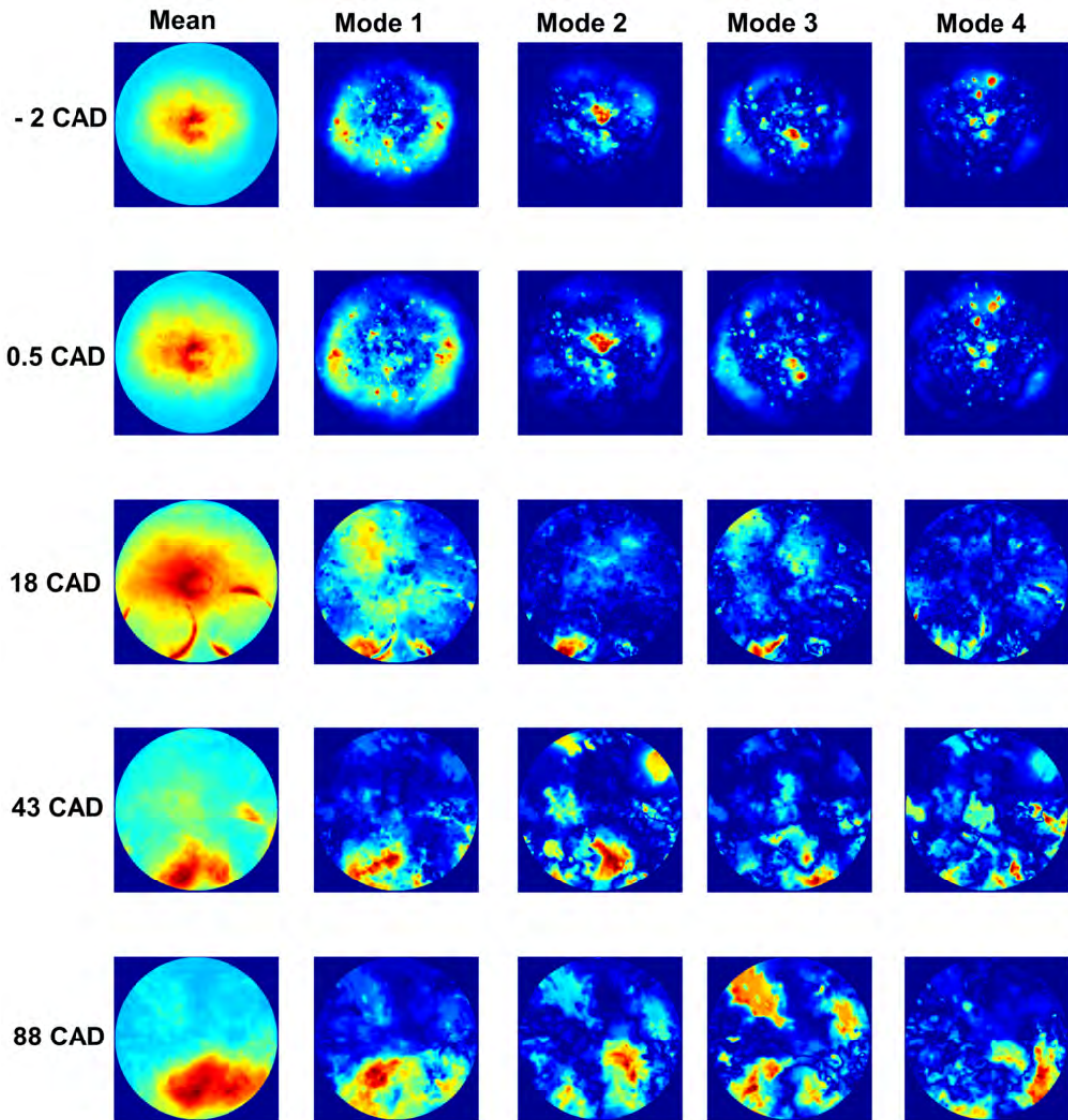
Figure 3.14: The first 5 most energetic POD modes (absolute value) at various crank angles (CV operating condition).
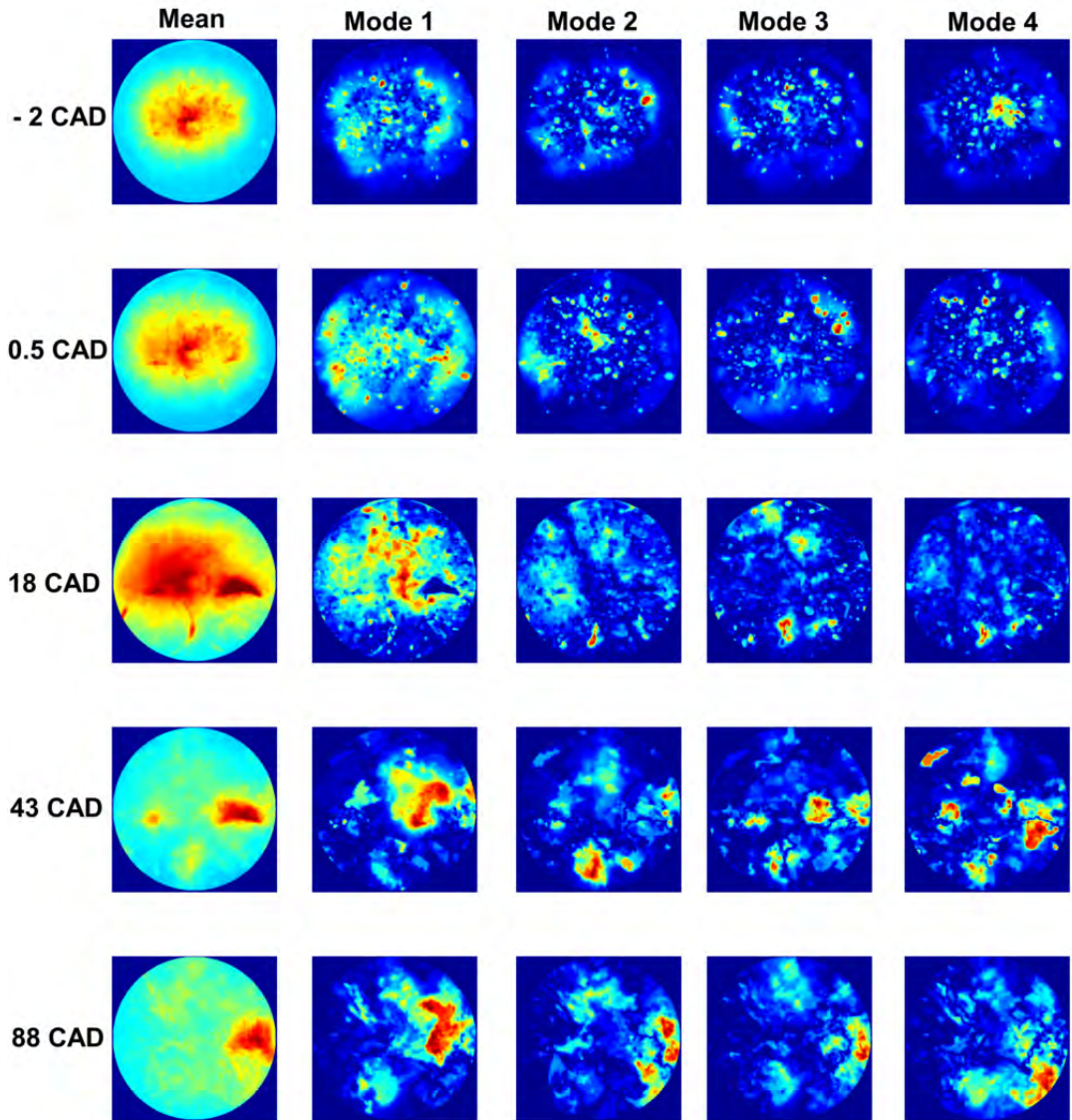
Figure 3.15: The first 5 most energetic POD modes (absolute value) in value absolute at various crank angles (OV operating condition).
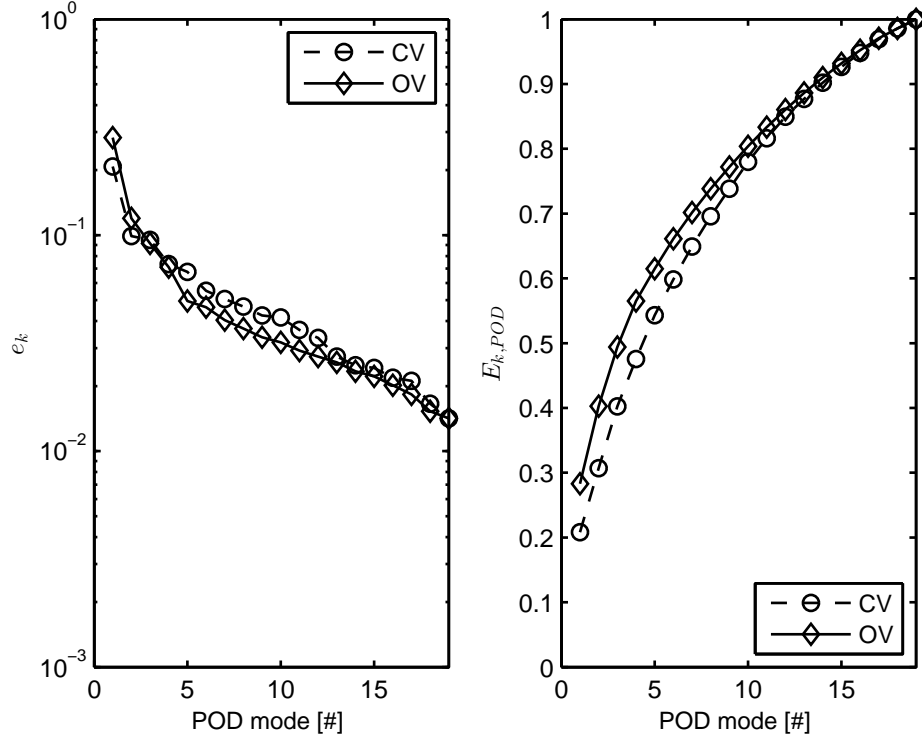
Figure 3.16: Energy POD spectra (left side) and cumulative energy spectra (right side) for both CV and OV operating conditions at -2 CAD.

the dominant morphological features of the flames, Bizon et al. (2010b) proposed a new definition of the Coefficient of Variation based on POD, which expresses not just the cycle variation of the global luminosity signal, but also contains information about the spatial distribution of the luminosity field. Therefore, in the case of POD carried out on centred data, CoV based on POD proposed by Bizon et al. (2010b) can be simplified in the following form,

$$\text{CoV}_{POD} = \sqrt{\frac{\sum_{i=1}^{M}(\overline{c_i^2} - \overline{c}_i^2)}{c_0^2}} = \sqrt{\frac{\sum_{i=1}^{M}\overline{c_i^2}}{c_0^2}} \tag{3.6}$$

where $\overline{c_i^2}$ is given by

$$\overline{c_i^2} = \frac{1}{M}\sum_{j=1}^{M} c_{ij}^2 \tag{3.7}$$
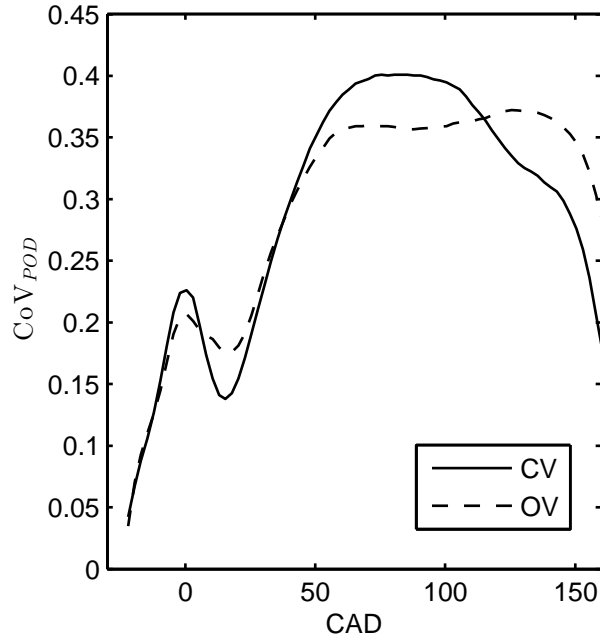
Figure 3.17: CoV_{POD} for CV operating condition (dot line) and OV operating condition (dash line).

It can be noted how such CoV depends only on the POD coefficients, which capture the temporal information contained in the ensemble of the data analysed. Here, expression in Eq. (3.6) has been applied to each of the groups of images obtained at each crack angle for both the operating conditions. Consequently, such analysis provides a single value for CoV at each crank angle.

Figure 3.17 reports the CoV_{POD} for both CV and OV operating conditions investigated. For both operating conditions, during the period of the flame front propagation it is possible to observe a linearly increasing trend of CoV_{POD} until it attains a peak around the top dead center. Once more, that is due to the kinematic interaction between turbulent eddies and the flame front (corrugated flamelets). At the top dead center, it is possible to note that the CV operating condition has a CoV_{POD} higher than that of the OV operating condition. This

means that the closed valve injection shows higher cycle-to-cycle variations at top dead center. At about 15 CAD, for both operating conditions, CoV_{POD}s show a minimum. Indeed, at this crank angle, the flame front is very close to the cylinder wall, then the minimum of CoV_{POD} suggest that the extinction of the flame front occurs in a rather abrupt manner for both operating conditions.

For the CV operating condition, after 15 CAD, CoV_{POD} increases until it reaches a value of about 0.4 at 60 CAD, as a result of the beginning of the diffusion-controlled combustion due to fuel film deposited on the intake valves. Subsequently, it assumes an approximately constant high values until about 110 CAD at its maximum value. This behaviour is due to the strong irregularities of the diffusion-controlled combustion, where both morphology and luminous intensity of the flame assume a strongly irregular behaviour.

For the OV operating condition, after 15 CAD, CoV_{POD} increases until it reaches about 0.35 at 60 CAD. In this case, the increase of CoV is due to occurrence of the diffusion flames localized near the cylinder wall, as it was previously shown. Then, until about 130 CAD, the CoV_{POD} assumes an approximately constant trend as a result of the strong irregularities of the diffusion flames, in terms of both luminous intensity and morphology. It can be noted that the CV operating condition is characterized by higher CoV_{POD}. Therefore, closed valve injection strategy exhibits higher cycle variations.

Moreover, CoV_{POD} has shown higher values than that reported by CoV for the global indexes (Figures 3.6 and 3.4). This is explained by the fact that CoV_{POD} takes in account the morphological variations as well. Finally, POD has allowed to extract the dominant features of the luminosity field emitted by flames. Besides, it has allowed to study the cycle-to-cycle variations in terms of morphology and luminous intensity. The dominant features, in terms of flame patterns (mean and first 4 POD modes), have allowed to highlight the zones of combustion chamber

where the flames that cause the cyclic variability phenomena take place.

3.1.4 ICA application to flame images from SI engine

This is section is organized in three parts. Firstly, a numerical example of ICA application is provided in order to clarify and show the capability of ICA for the identification and separation of independent events for an observed transient phenomenon. The second part regards the employ of ICA methods for the analysis of transient phenomena that occur during the combustion phase of the SI engine described in the previous section. We shall call this analysis "single-cycle". The third part will be focused on the application of ICA methods for the analysis of the cycle-to-cycle variations.

ICA: artificial example. Two independent images were created and multiplied by two time courses (Figure 3.18, top) to create temporal sequences of images, then mixed to generate the image mixtures (Figure 3.18, center). Then, ICA is applied to the created mixture, to estimate independent images and corresponding time courses (Figure 3.18, bottom). The separation performance of ICA is impressive: the values of 2D correlation coefficients for the first pair i.e. image source s1 and its estimate y_1 is high as 0.9999, while for the second pair - s_2 and y_2 - it is equal to 0.9994. Similarly high correlation values characterize the corresponding pairs of the time courses and their estimates.

Experimental result. A number of images sequences from consecutive fired cycles were collected using a high speed camera. Figures 3.19 and 3.20 show a selection of the images collected, at 2.5 CAD increment, during the combustion phase, for two cycles employing CV and OV injection strategy, respectively. In both cases, the premixed flame front, ignited at 22 CAD, spreads quickly through-
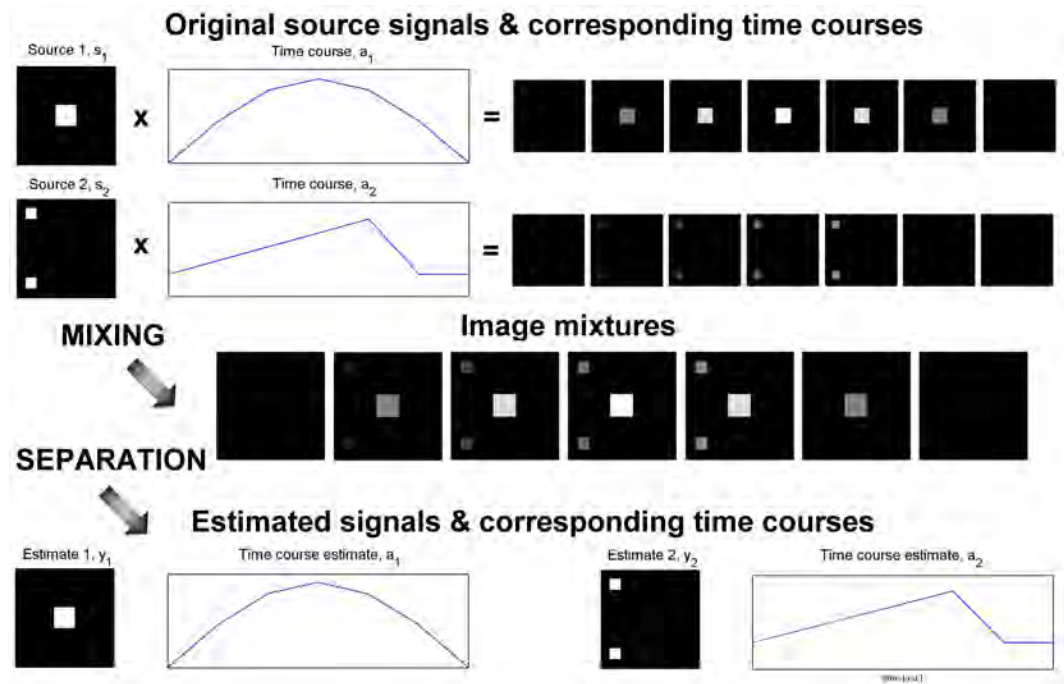
Figure 3.18: Scheme of optical engine and field of view of the combustion chamber.

out the combustion chamber with radial progression. During the spread and afterwards, diffusion flames establish around and between intake valve seats. Intense diffusion flames are also visible later elsewhere in the chamber, due to the ignition of the fuel film deposited on the cylinder walls, and to the gas motion from intake to exhaust. Such flames produce soot (rich zones), whereas chamber regions containing a lean mixture cannot sustain flame propagation and, hence, are responsible for unburned hydrocarbon emissions.

Figure 3.21 compares the in-cylinder pressure and integral luminosity for the same two cycles. In both cases, it can be observed that the angular location of luminosity and pressure peaks is found at around 20 CAD. The Open Valve injection strategy produces slightly higher pressure and luminosity peaks.
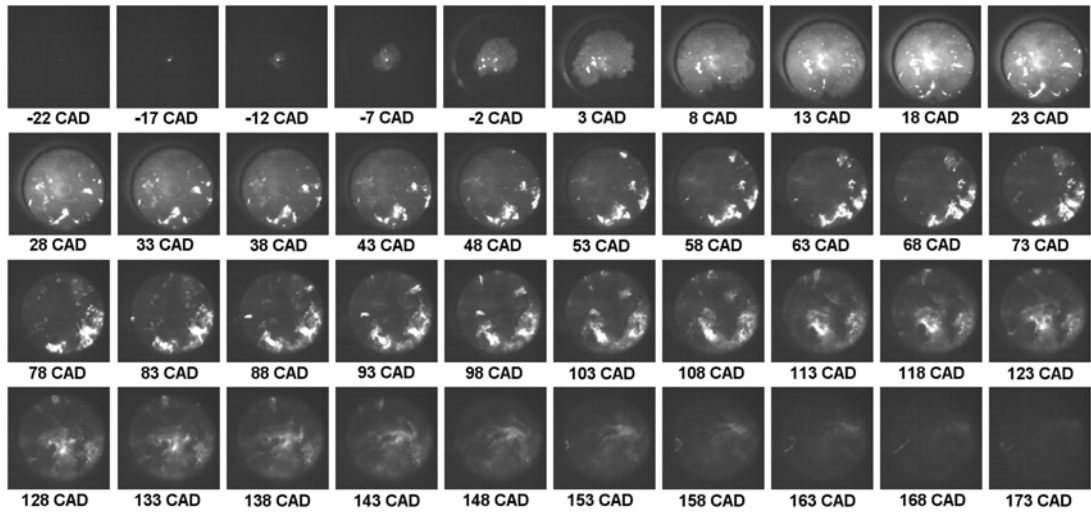
Figure 3.19: Typical sequence of crank-angle resolved images: closed valve (CV) injection strategy.
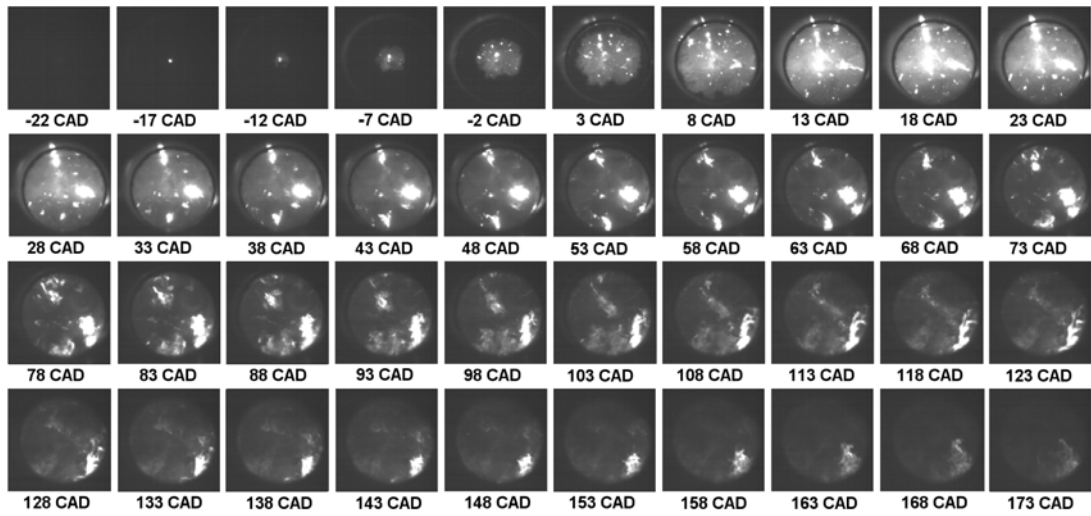
Figure 3.20: Typical sequence of crank-angle resolved images: open valve (OV) injection strategy.

ICA: Single cycle analysis. ICA is applied separately to each sequences consisting of $M = 80$ consecutive images. Each image is represented as a vector by concatenating its rows, and treated as a mixture $\mathbf{x}_i$. Then, the dimension of
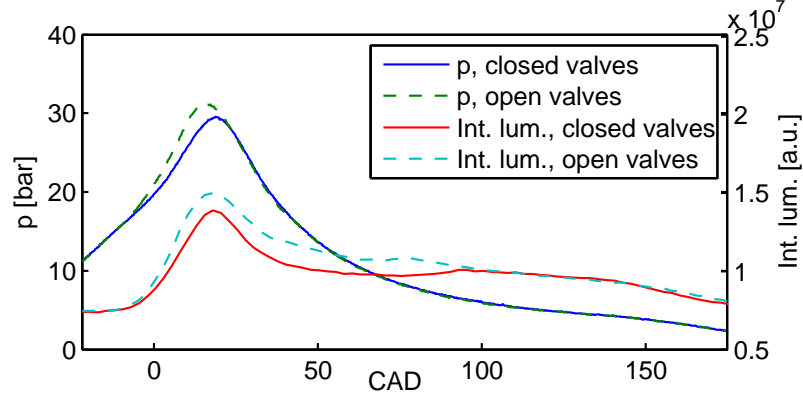
Figure 3.21: Typical in-cylinder pressure and integral luminosity for CV and OV injection strategy.

the original data is reduced, via discrete POD (equivalently SVD), to the number $k \ll n$ of components to be estimated. Both for the CV and OV injection strategy, we choose $k = 3$ modes, leading in terms of the so-called cumulative energy:

$$E_{POD,3} = \frac{\sum_{i=1}^{3} \lambda_i}{\sum_{i=1}^{M} \lambda_i} \approx 0.80$$

The leading three modes are found to retain about 80% of the total energy. The results of ICA performed on the cycles presented in Figure 3.19 and Figure 3.20 are presented in Figure 3.22a-c and Figure 3.22d-f, respectively. Due to the ambiguities of the ICA mixing model, there exists no intrinsic order in the components: in fact, as both $\mathbf{A}$ and $\mathbf{s}$ are unknown in Eq. (2.26), any source s_i can be always multiplied by an arbitrary scalar, α_i, and the corresponding column a_i of $\mathbf{A}$ divided by the same scalar.

In view of the dynamical analysis of the combustion process, the components are here displayed *in order of appearance*, while the time-dependent coefficients are normalized using maximum norm. More precisely, a *time centroid* is defined
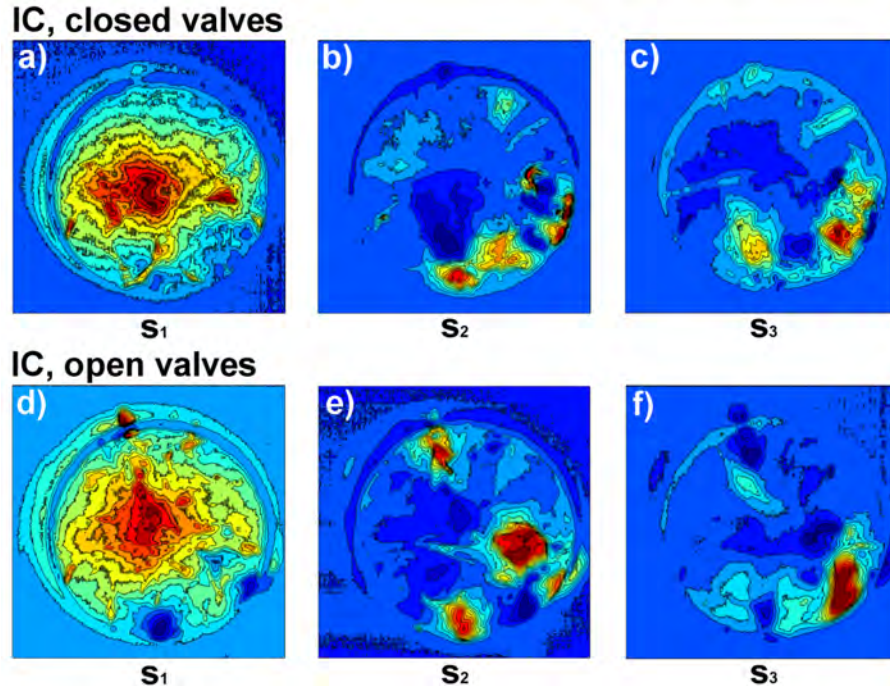
Figure 3.22: Independent components for CV (a-c) and OV injection strategy (d-f).

for each component, based on the time-dependent coefficient, as follows:

$$t_{ci} = \frac{\int_0^{2\pi} t|a_i(t)|dt}{\int_0^{2\pi} |a_i(t)|dt} \tag{3.8}$$

and then the components are ordered according to increasing t_{ci}. For both conditions, components s_1 (Figures 3.21a and 3.21d) represent predominantly the luminosity distribution related to ignition and propagation of the premixed flame front. The relevant coefficients (Figure 3.23), a_1, peak at 18 CAD, in correspondence of the integral luminosity peak. Components s_2 and s_3 represent the subsequent evolution of the luminosity field mostly due to the diffusion flames visible after the ignition of the fuel film deposited on the cylinder walls. Again, non-monotonic behaviour of the relevant coefficients, a_2 and a_3 (Figure 3.23), can be observed, which again peak at maximum luminosity of the burning fuel pockets, and tend
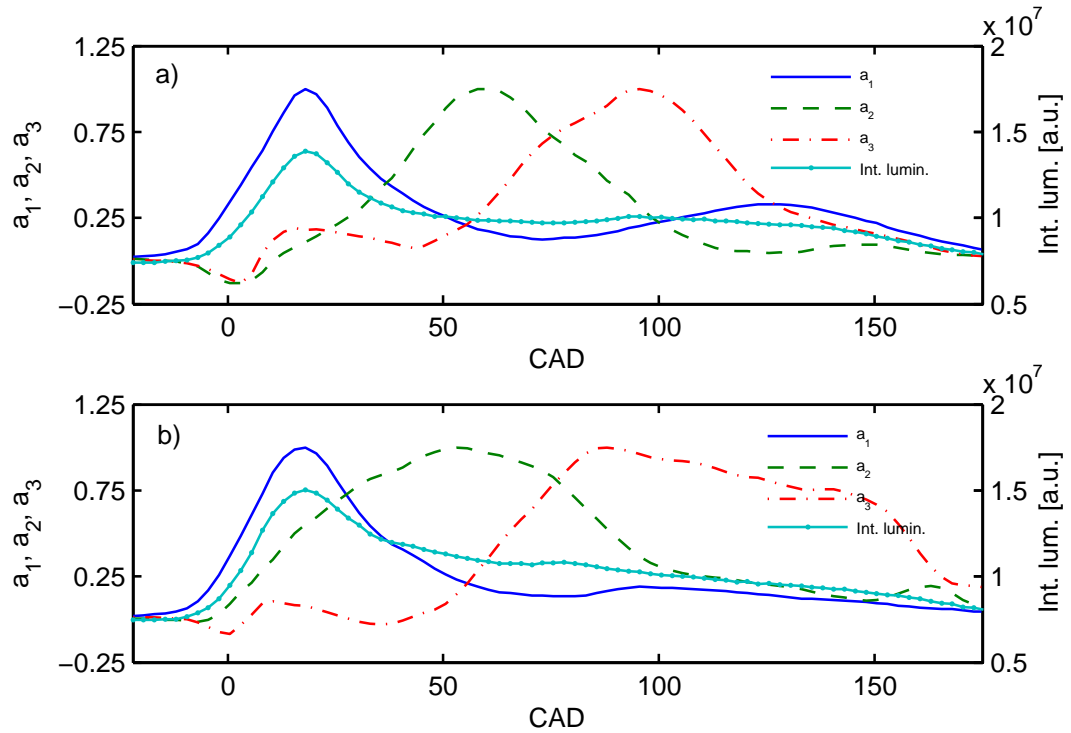
Figure 3.23: Coefficients and integral luminosity for CV (a) and OV injection strategy (b).

to decrease as they burn out. The thermal energy released at these times cannot be exploited in terms of mechanical work, and the inhomogeneities in the mixture fraction produce unburned hydrocarbons. In conclusion, in the analysis of a single cycle, ICA discriminates the most independent components, which are clearly separate in time, and reflect the spatial distribution of the high luminosity zones, whereas the corresponding coefficients characterize their time evolution.

ICA: cycle variability analysis. It is interesting to see how the components and their coefficients correlate among the cycles. The commonly used procedure is to cluster components sufficiently similar over the cycles, for example in terms of spatial correlation (Calhoun et al., 2009). Such an approach makes sense when

ICA is expected to determine spacewise similar components and their (different) time courses. Our case is perhaps opposite, aiming at characterizing the different space patterns of cyclic variations observed for timewise similar evolutions. Indeed, relatively high values of the 2D correlation coefficient are only found among components s_1 (varying from 0.89 to 0.97) for 10 successive cycles.

In fact, the first components describe the rather regular pattern of the flame front evolution. On the contrary, as expected, mean values of the 2D correlation coefficient of s_2 and s_3 are lower than 0.5. On the other hand, as well illustrated in Figure 3.24, the correlation of the corresponding time dependent coefficients is very high: the mean value of the coefficient of correlation is as high as 0.93 for a_2 and 0.91 for a_3. Hence, it is convenient to group the components according to the
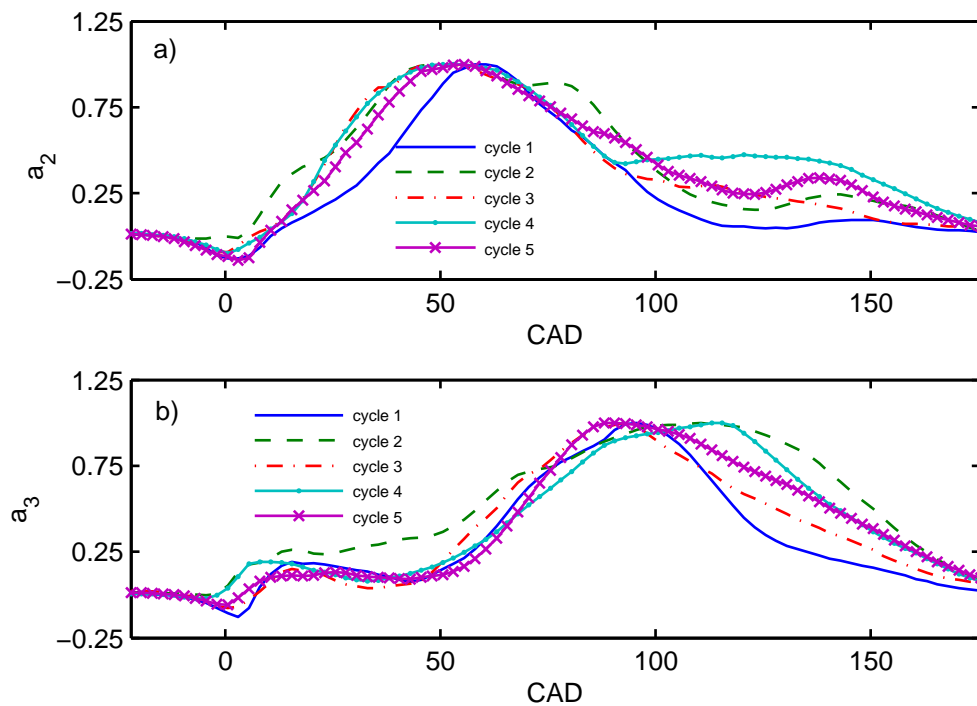
Figure 3.24: Coefficients of second (a) and third (b) components for five cycles (CV injection strategy).
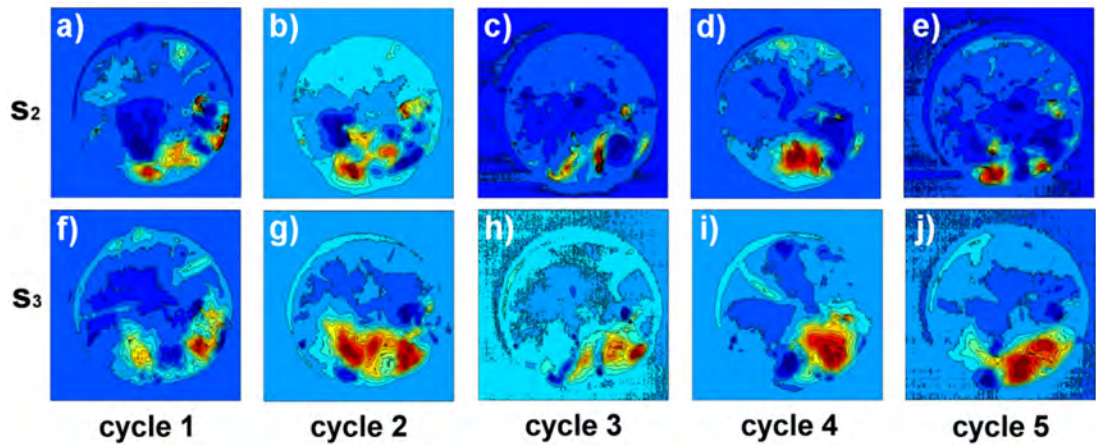
Figure 3.25: Second (a-e) and third (f-j) components for five cycles (CV injection strategy).

best correlated time-dependent coefficients, and then characterize cyclic variations by comparing spatial patterns in each group.

Figure 3.25 (five cycles, CV injection strategy) shows the erratic spatial patterns of s_2 and s_3 due to the strong spatial variability of the diffusion flames among the cycles. This is confirmed also by the *centroid of the luminosity* of the components (for 10 successive cycles, 3.26a): for component s_1, its position does not vary significantly over the cycles, whereas it scatters for s_2 and s_3, although with a general preference of the flame to evolve towards the intake valves. A similar trend is observed for OV injection strategy, with a consistent right shift compared to CV injection strategy (Fig. 3.26b). A much higher variability of the s_2 luminosity can be observed, whereas the centroid of s_3 is again rather regular, but not as centered as s_1. This means that, as the flame reaches the chamber wall, luminous combustion is more unstable for the OV injection strategy but gets more regular, with respect to the CV injection strategy, during the final phase.
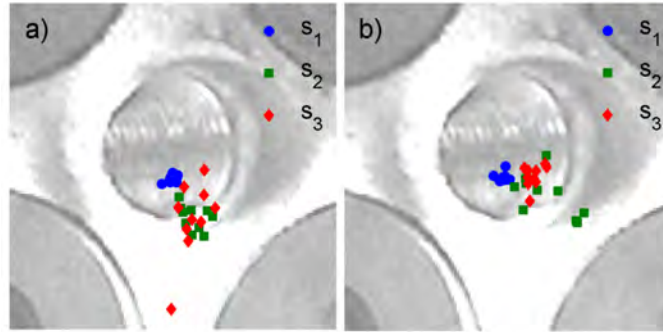
Figure 3.26: Centroid of the luminosity of the components for CV (a) and OV injection strategy (b).

Full ICA.   When ICA is applied on the original data characterized by a large number of observations (degrees of freedom), it gives as many components as the number of observations, most of which may be just random spurious source signals, physically inconsistent with the data set. On the other hand, data preprocessing by POD can be controversial: the number of sources to be determined, in many cases unknown, is arbitrarily set a priori. Furthermore, since POD is a lossy reduction technique, important information, though characterized by low energy, are lost. In order to evaluate the effects of POD lossy data preprocessing, we now assume that the mixing model is identifiable for $n = m$ (= 80 for each cycle) and thus ICA is applied to the whole original data set (Full ICA). The computed components are then ordered using Eq. (2.44). The leading components describe dominant spatio-temporal evolution of the luminosity in the combustion chamber, whereas the remainder are related to rather insignificant fluctuations and noise. The outcome of Full ICA is presented, for the CV case, in Figures 3.27 and 3.28.

The first dominant component (Fig. 3.27a) is clearly correlated with the s_1 obtained performing ICA on POD-reduced data (Fig. 3.22d), and so are the corresponding coefficients a_1 - solid line in Fig. 3.28 and Fig. 3.22b respectively. The value of the correlation coefficient for the latter is as high as 0.9728; in case of the
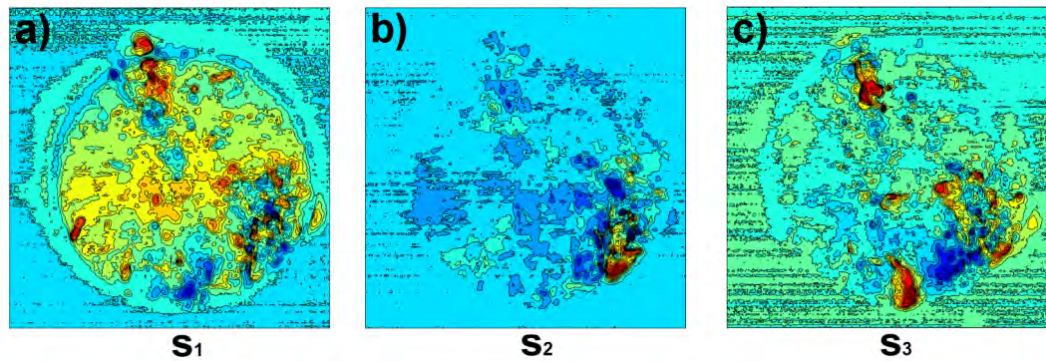
Figure 3.27: Full ICA: Dominant independent components (open valve injection).
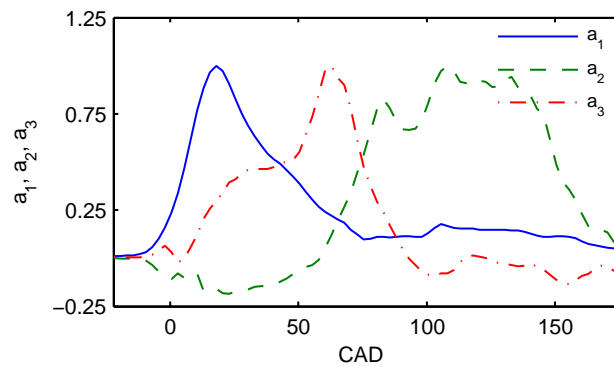
Figure 3.28: Full ICA: Dominant independent components (open valve injection).

components its lower but still relatively high, i.e. 0.7663. Similar affinity can be observed also when comparing successive ICs and corresponding coefficients obtained from reduced and original data. Interestingly, when employing the ordering established by Eq. (6) the third IC, in terms of temporal succession, is indexed as s_2 and the IC corresponding to the intermediate combustion as s_3.

3.1.5 Optical Flow application to analysis of the flame front propagation

This section shall be focused on the first attempt of application of optical flow technique to 2D images of turbulent flames. More details about optical flow estimations are reported in Section 2.4. Usually, velocity measurements of the flame front are provided by coupling PIV measurements, for the velocity field, and optical measurements of the flames. Thus, the complexity of performing these experimental measurements is rather high and requires the use of invasive diagnostic techniques, i.e. PIV needs the use of tracer particles. Therefore, the main scope of this section aims to introduce the application of the optical flow technique for the estimation of the relative motion of the flame front, like front of the burning gases. This is done by using only the luminosity emitted by combustion process, that is without the use of invasive diagnostic techniques, i.e. particle image velocimetry (PIV).

In this section, all of the experimental tests are performed at 2000 rpm with spark timing at -34 CAD. The intake air pressure and temperature are 1600 mbar and 298 K, respectively. The optical acquisitions were obtained by using a CMOS 16-bit high speed camera with spatial resolution of 1024×1024. To obtain the best match between spatial and temporal resolution, the image collection process clips a region of 895×496 pixels, allowing for a spatial resolution of around 0.11 mm/pixel, and employs a frame rate of 30000 fps which, for the engine operating at 2000 rpm, correspond to 0.4 CAD increments from frame to frame. The exposure time is 30 μs. During the experimental test, 500 images form 50 consecutive fired cycles were collected. Since the analysis was only focused on the flame kernel and its propagation, only the first 80 images of each cycle were considered. Besides, to avoid spurious results influenced by the reflection of the combustion light, a circular mask (centered x=452 and y=248 with radius r=224) frames the region of interest.

Recall that the optical flow constraint equation (see Section 2.4) is based on the assumption that the changes in the brightness of the image are only due to motion. Therefore, it is rather evident that the optical flow methods cannot be directly applied to flame images because the change of brightness in the image are due to both kinematic motion of the flame (flame front propagation) and the heat release rate. Since we are only interested in the motion of the flame front, it is possible to overcome this problem by means of binarization of the images. More precisely, in the case of binary images, the change of brightness are due only to the motion field.

The binarization of the images is performed by applying a proper threshold for the pixel value. Since, for the images acquired, typical pixel values (bit) of the flame front are rather close to those associated with thermal noise of the camera, the choice of such threshold is not easy. Therefore, after an analysis of the thermal noise of the camera, the threshold value of 5 bit. Figure 3.29 shows the binarization image for few snapshots. It can be noted as the binarization of the images by using a threshold value of 5 is able to show the flame front.

Now, the set of binarized images can be elaborated by optical flow algorithm. In this dissertation, the estimate of optical flow is carried out by using the algorithm proposed by Horn (1986), which minimizes the objective function of Eq. 2.73. The parameter α, which penalizes the regularization term, is fixed at 0.05.

Figure 3.30 shows the optical flow estimation at -18.4 CAD. It is possible to note as optical flow provides information about the local motion of the flame front. Additionally, the corrugated feature of the flame front, due to interaction between the turbulent eddies and flame front, determines a random distribution of the optical flow close to the flame front. For correctness, the local flame speed that will be estimated via optical flow method will have values between the laminar flame speed and turbulent flame speed because the spatial resolution of the camera is
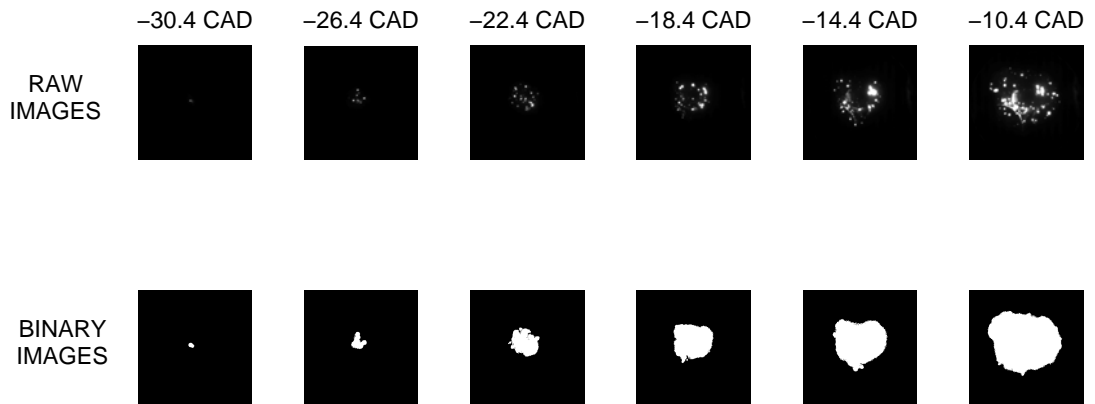
Figure 3.29: Images detected at various crack angles (top row) and the binary images (bottom row).

much higher than the flame front thickness. The velocity vectors non-null inside of the flame are not due to physical phenomena, but they are caused by the use of the regularization term employed in Eq. 2.73 in order to guarantee the uniqueness of the solution of the optimization problem. Furthermore, it is possible to note how the binarization of the images has allowed to avoid the problem due to the combustion of the fuel droplets, which would have been associated with high values of optical flow. To reduce the effects of the terms of regularization, it can be considered only the velocity vectors corresponding to the edge of the binary image, which can be considered a good approximation of the flame front.

Figure 3.31 reports the local flame front speed at various crack angle. At -30.4 CAD, close to spark timing, the local flame speeds of the flame kernel are rather constant, at about 5 m/s. Later, during the propagation of the flame kernel, the local flame speeds increase and assume a rather irregular distribution along the flame front. A statistical analysis of the flame front speed should be carried out in order to study the behaviour of the flame kernel during its propagation. For each crank angle, the spatial mean, μ_S, and the spatial standard variation, σ_S,
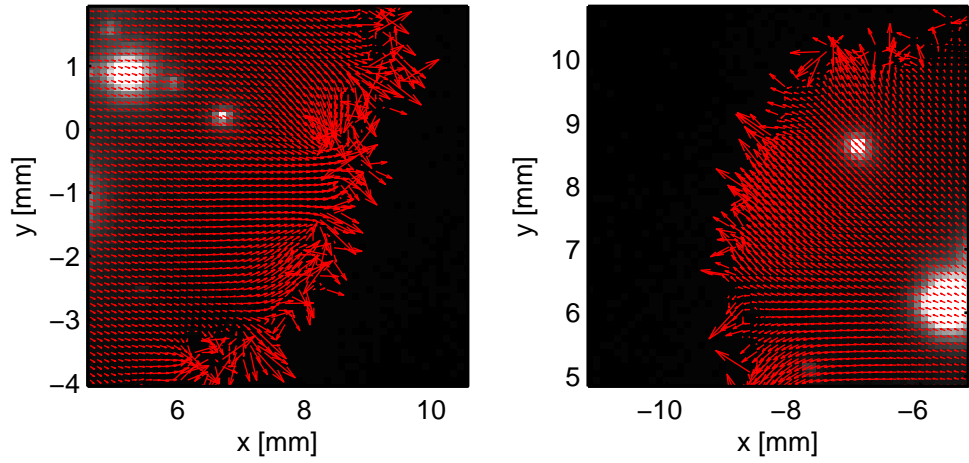
Figure 3.30: Optical flow field estimated at -18.4 CAD.
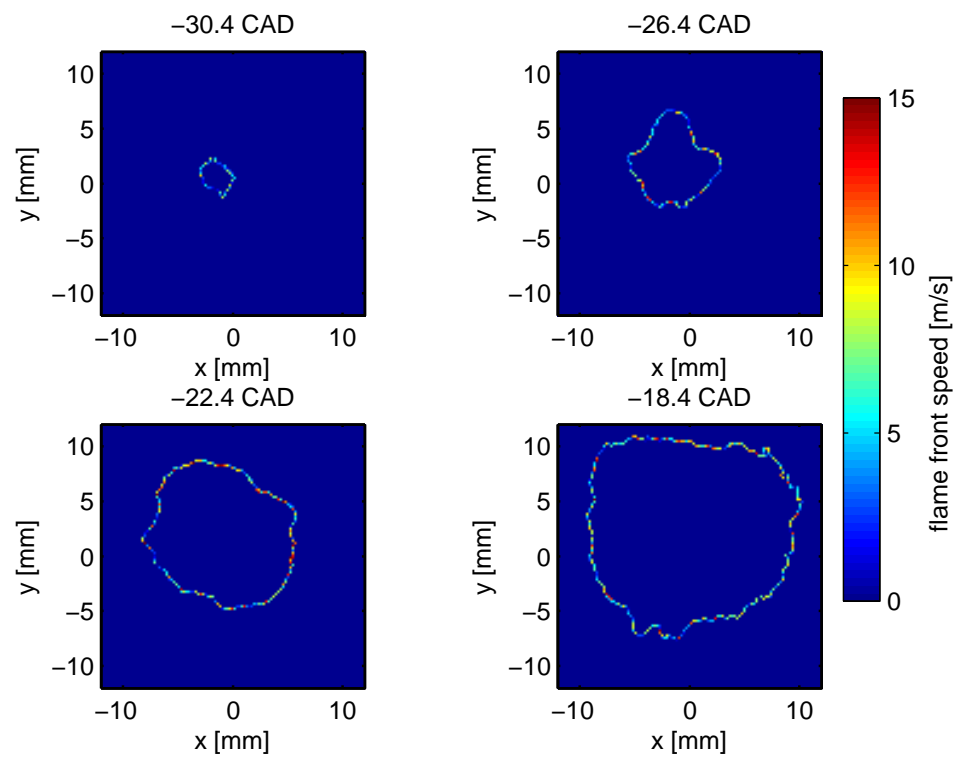
Figure 3.31: Optical flow field (absolute value) estimated at -18.4 CAD.

of the magnitude of the optical flow are estimated along the front flame for 50 consecutive fired cycles (Figure 3.32). Looking at Figure 3.32, it can be noted that the μ_S shows a rapid increase during the first 8 CAD after the spark timing. That is due to rapid corrugation of the flame front due to the interaction between the turbulent eddies and the flame front propagation. Spatial standard variation is calculated in order to provide information about the irregular distribution of the local flame speed along the flame front. Indeed, as it can be observed in Figure 3.32 (righ side), the mean value of σ_S increases rapidly during the first 8 CAD after the start of ignition until it stabilizes to about 3.5 m/s. Besides, the spatial dispersion of the local flame speeds along the flame front becomes stable after about the 8 CAD after SOI, whereas the spatial mean of local flame speed.

Finally, the application of optical flow techniques has provided useful information about the propagation of the flame front determining the local flame speeds at various crank angles.
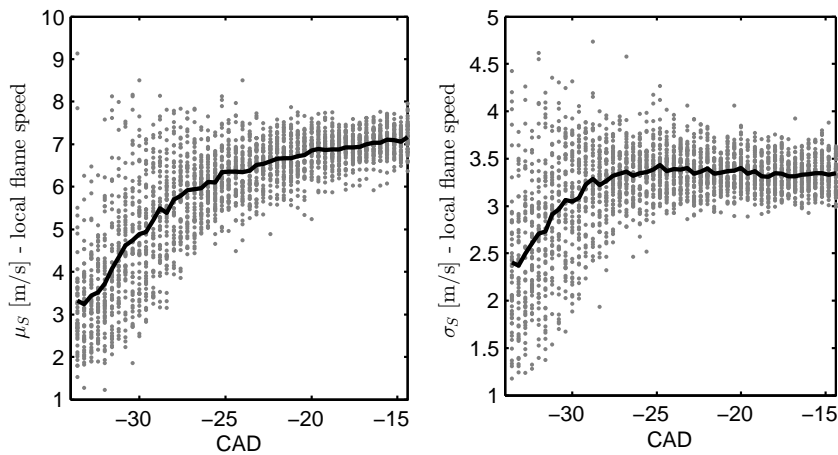
Figure 3.32: Scatter plots (dots) of the instantaneous spatial mean (left) and spatial standard variation (right) of the local flame speed and corresponding averages (solid line) over 50 consecutive fired cycles.

3.2 Diesel engine

This section reports the application of independent component analysis (ICA) to 2D images of combustion-related luminosity. The images are acquired from an optically accessible Diesel engine equipped with the common rail injection system and cylinder head of a most recent generation Euro 5 engine. The original data, from a sequence of crank-angle resolved images, are treated by ICA in order to identify leading independent structures. Two main independent components (IC) are extracted from sets of luminosity images, and the coefficients of the ICs are then used for further analysis, to study the transient during a single cycle, and for the assessment of cycle variability, along with data of dynamic in-cylinder pressure, rate of heat release and integral luminosity. In the analysis of a single cycle, the two independent components appear to be clearly separated and related to combustion events near the fuel jets and near the bowl walls respectively. The analysis over the cycles separates the mean combustion luminosity field at each crank angle from the random, erratic flame structures related to cycle variability. Quantitative analysis of the statistics of the two independent components confirms the lower variability of the jet flames and the high variability of combustion near the chamber walls. This is in agreement with the idea that the extensive impingement of the fuel sprays on to the piston bowl walls in modern, high-speed, direct injection Diesel engines is responsible for increase of unburned hydrocarbons and smoke emissions. The developed procedure, including the ICA, is fast and reliable and can be prospectively applied to many different optical engine configurations.

Table 3.3: Engine and injection system specifications.

Engine type	4-stroke single cylinder
Bore	8.5 cm
Stroke	9.2 cm
Swept volume	522 cm^3
Combustion bowl	21 cm^3
Vol. compression ratio	17.7:1
Injection system	Common Rail
Injector type	Solenoid driven
Number of holes	6
Cone angle of fuel jet axis	148°
Hole diameter	0.145 mm
Rated flow @ 100bar	40 cm^3/30s

3.2.1   Diesel engine: Experimental apparatus

The measurements were conducted in an optical Common Rail (CR) Diesel engine, consisting of a single-cylinder equipped with an injection system operating at a maximum pressure of 2000 bar. The injector is positioned along the cylinder axis, and features a single guide microsac nozzle. The injector is controlled by a fully flexible Electronic Control Unit (ECU) for combustion optimization. In order to obtain the same in-cylinder conditions of the real multi-cylinder engine, and to compensate lower compression ratio, typical of optical engines, an external air compressor has been used to supply pressurized intake air. On its way to the intake manifold, the air is filtered, dehumidified, and preheated.

A variable swirl actuator (VSA) system manages the air swirl in the intake manifold. Table reports engine and injection system specifications. All tests were

conducted at an engine speed of 1000 rpm, continuous-mode operation, using commercial Diesel fuel with a typical CR injection strategy of pre, main and post injections (PMP) in every cycle. The pre, main and post injections started at 9 CAD, 4 CAD and 11 CAD with duration of 400, 625 and 340 μs respectively, with injection pressure fixed at 600 bar and no EGR. Several images per cycle were acquired with a high-speed digital complementary metal oxide semiconductor (CMOS) camera, controlled by a trigger signal generated by a delay unit linked to the engine encoder, with a frame rate of 4 kHz and exposure time of 166 μs.

3.2.2 Experimental results

The experimental data set contains 888 images of the in-cylinder luminosity field, collected in sets of 24 from -4 CAD to 30.5 CAD over M= 37 consecutive fired cycles. The original spatial mesh of 529×147 is clipped to 120×120 pixels by framing the combustion chamber, and the original color pixels are grayscaled employing Bayer filter (Russ, 2011). Figure 3.33 shows images of combustion luminosity for the multiple injections in a cycle. First, luminous spots are observed around the injector nozzle at -2.5 CAD, due to ignition of the pre-injected fuel. The small amount of fuel mixes with a large quantity of air, burns in the cylinder and produces bright spots, due to pockets of fuel segregating in the chamber.

At 0.5 CAD, visible flames are mainly due to the main injection combustion. From 2 CAD to 5 CAD, combustion is present on all jets and in the vicinity of the chamber wall. As fuel along the jet axes is consumed, the combustion zone moves towards the bowl wall, burning the impinged fuel. At the end of combustion, (12.5 CAD) flames are mainly distributed near the walls. At 14 CAD, post injection jets are observed, autoigniting with a different behaviour: as it can be noted at 15.5 CAD, it occurs simultaneously along the whole jets, up to their tips, due to the high temperature near the chamber walls. The highest
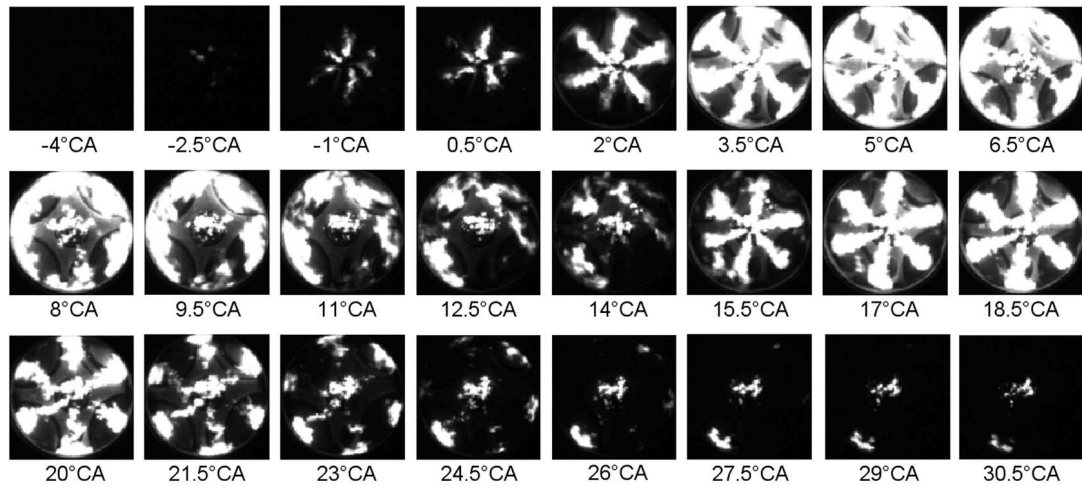
Figure 3.33: Sequence of crank-angle resolved combustion images.

post combustion luminosity is reached at 18.5 CAD. Figure 3.34a-j presents some images of combustion, acquired at several crank angles and for different combustion cycles, demonstrating the phenomenon of cycle-to-cycle variations. Not all jets burn with the same flame behaviour (Fig. 3.34a-c and 3.34g-j). During combustion development, flames are unevenly distributed along the jets axes. Figure 3.34d-f illustrate the start of post injection in a partly burning environment, where the irregular peripheral combustion influences the subsequent development of post-injection ignition.

3.2.3   ICA of crank angle resolved measurements

ICA is applied separately to each of the crank-angle resolved sequences of the 24 consecutive images of each cycle. In the procedure we assume that no geometric deformation affects our images over the crank angle, since photographs are taken from the bottom of the cylinder through a transparent piston. Figure 3.35 shows ICs y_1 and y_2, extracted from the cycle presented in Figure 3.33 and recognized as being related to the combustion along the fuel jets (Fig. 3.35a) and near the cham-
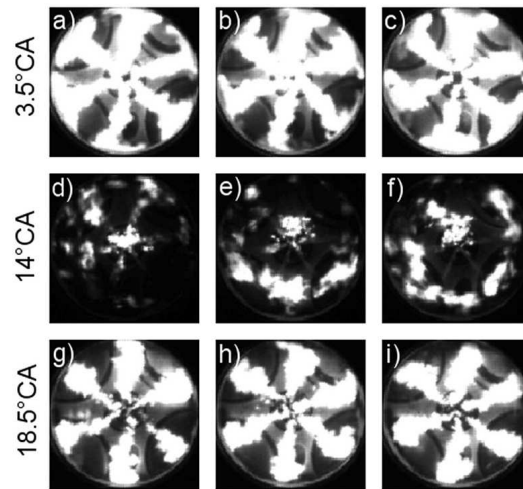
Figure 3.34: Sequence of crank-angle resolved combustion images.

ber walls (Fig. 3.35b) respectively. The swirl motion of the burning jets can be identified in the curved shape of the components jets in (Fig. 3.35a). For compari-
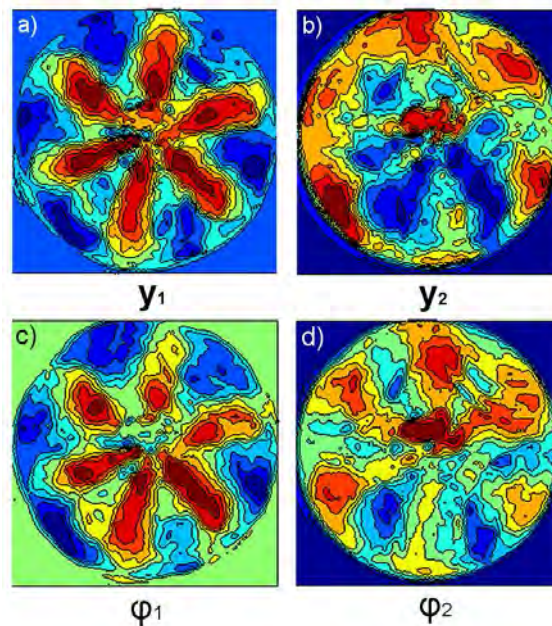
Figure 3.35: Two leading POD modes (a-b) and independent components (c-d) for the single cycle.
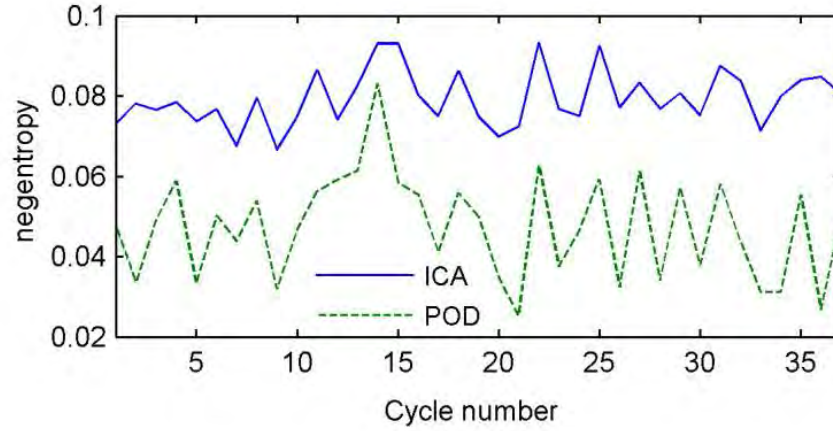
Figure 3.36: Negentropy computed for ICA and POD modes as a function of cycle number.

son, Fig. 3.35c and 3.35d report the POD spatial modes, which apparently do not separate completely the independent physical phenomena. A quantitative evaluation of the amount of information is provided by the negentropy, approximated as (Hyvärinen and Oja, 2000):

$$J(y) \approx \frac{1}{12}E\{y^3\}^2 + \frac{1}{48}\text{kurt}(y)^2 \tag{3.9}$$

where

$$J_{ICA} = J(y_1) + J(y_2); \qquad J_{POD} = J(\phi_1) + J(\phi_2) \tag{3.10}$$

is a normalized random variable. We now define Figure 3.36 shows that the negentropy is consistently higher for ICA than for POD, thus showing that ICA modes always carry a higher amount of information. It is interesting to see how time-dependent coefficients of the ICs correlate with combustion events. Figure 3.37a-b reports in-cylinder pressure, drive injector current, rate of heat release (ROHR) and integral rate of heat release for the analyzed combustion cycle. From the ROHR curve (Fig. 3.37b) start of combustion (SOC) of the various injections in the combustion chamber corresponds to those crank angles where the ROHR
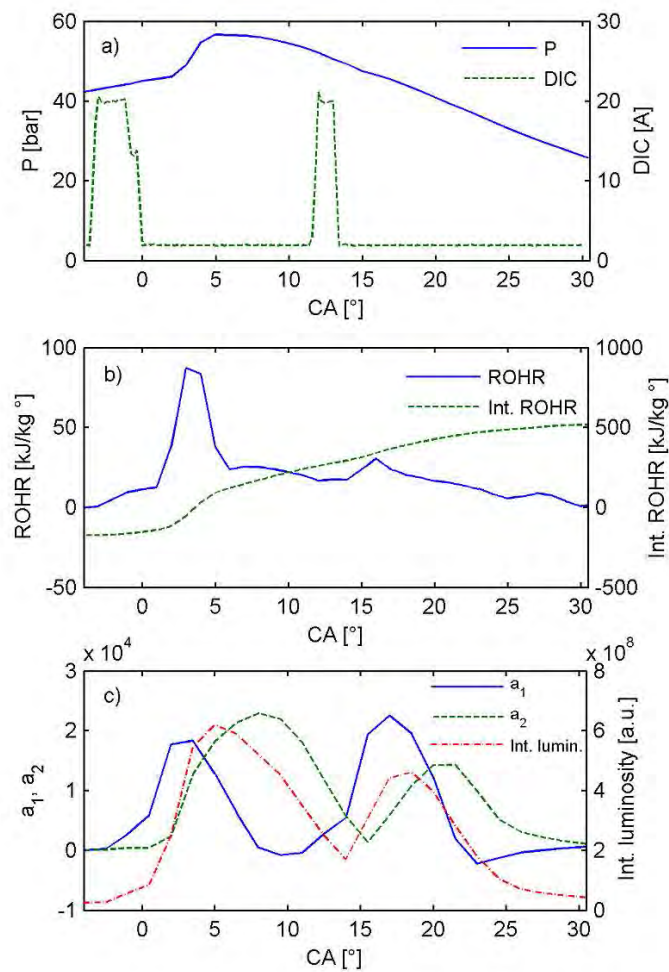
Figure 3.37: In-cylinder pressure and drive injector current (a), rate of heat release (ROHR) and integral ROHR (b), and ICs coefficients a_1 and a_2 , and integral luminosity (c) as a function of crank angle.

becomes positive or changes its slope, i.e. -4 CAD, 1 CAD, and 14 CAD respectively. Figure 3.37c shows the time-dependent coefficients of the components together with the integral flame luminosity. As it could be expected, the peaks of the coefficient a_1, of the component y_1, emerge at 3.5 CAD and 17 CAD, i.e. at the maximum luminosity of the regular combustion process near the fuel jets of the main and post injection. In conclusion, in the analysis of a single cycle, the most independent pair of components extracted by the ICA algorithm are clearly separated in time and clearly relate to combustion events near the fuel jets and near the bowl walls, respectively.

3.2.4 Cycle-to-cycle variation analysis

The same ICA procedure is applied separately for each data set collected at a specified crank angle in order to study the cycle-to-cycle variations. Figure 3.38 shows how ICA, applied over the cycles, permits to separate the mean combustion luminosity at each particular crank angle from the irregular flame structure related to cycle variability. The effectiveness of the extraction (Fig. 3.38a b and Fig. 3.38e f) is much better when the cycle-to-cycle variability is lower, i.e. for the crank angle values characterized by regular combustion process typical of the burning of the main and post injections along the jets. The separation is much worse when the cyclic variability is higher, i.e. at the end of main combustion when the flames move randomly near the bowl wall (Fig. 3.38c d) or towards the end of combustion, when several flames, which extinguish with irregular behaviour, are detected. This might indicate that there be more than two leading independent components in the process.

When looking at the cycle-dependent coefficients of the components presented in Figure 3.39 we can observe that the variation of coefficient for the ICs extracted at 3.5 CAD and 18.5 CAD (Fig. 3.39a and 3.39c, respectively) is substantially
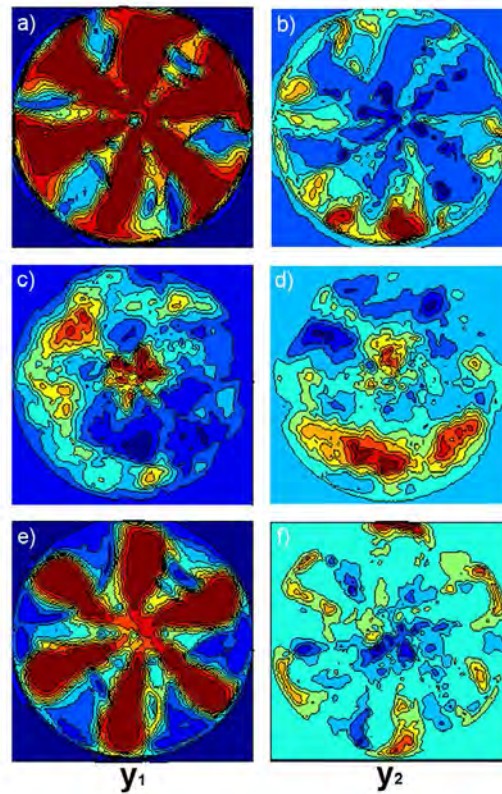
Figure 3.38: Independent components for the single crank angle positions: 3.5 CAD (a-b), 14 CAD (c-d) and 18.5 CAD (e-f).

lower than the variation of the coefficient a_1 of the first IC extracted at 14 CAD (Fig. 3.39b), i.e. the crank angle value for which both the integral luminosity and the morphology of the flame varies significantly over the cycles. The decreasing trend in the integral luminosity, specially seen for the crank angles at which the intensity is higher, is due to quartz window fouling over the cycles. To quantify the phenomenon of cycle to cycle variations observed in Fig. 3.34, we analyze now the coefficient of variation (CV), evaluated for the in-cylinder pressure and for the integral luminosity of the flame. Figures 3.40a-b show the average in-cylinder pressure, the drive injection current signal, the rate of heat release (ROHR), and its time integral, respectively. Two peaks, at 1 CAD and 5 CAD respectively,
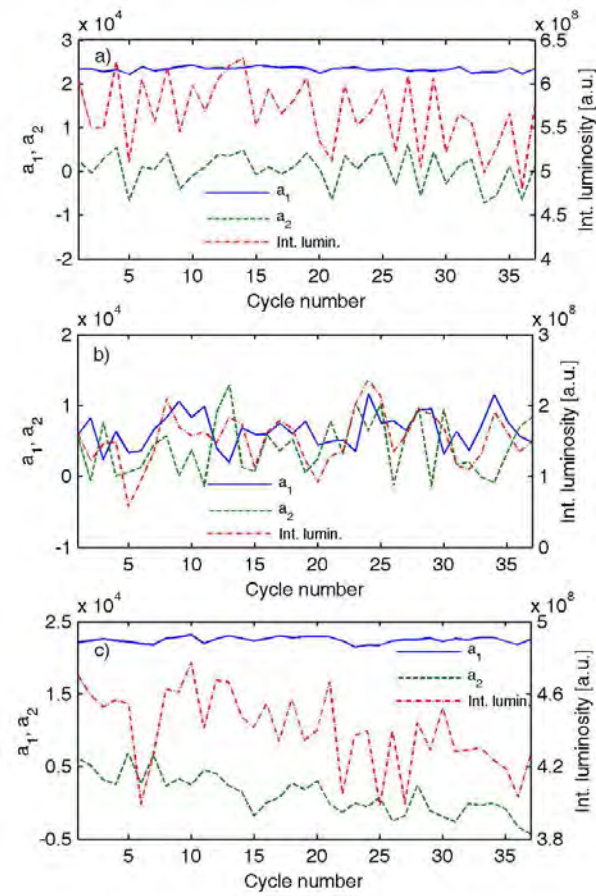
Figure 3.39: Coefficients y_1 and y_2 of the two independent components, and integral luminosity as a function of cycle number, for 3.5 CAD (a), 14 CAD (b) and 18.5 CAD (c).

emerge in the pressure CV (Fig. 3.40c), with the second one corresponding to the end of the injection, and to the minimum value of the CV. Then, the CV of the combustion pressure remains low and quite constant, since combustion of post injection fuel affects the pressure in the same way for all the cycles investigated. On the other hand, the CV of the luminosity field presents three distinct peaks, at 2.5, CAD, 14 CAD and 27.5 CAD, respectively (Fig. 3.39c). The first peak corresponds to the luminosity caused by the burning of the pilot injection fuel in

the centre of the bowl, under the nozzle tip. Subsequently, the burning of the main injection along the jet directions develops with a repeatable position of the flames and, thus, a minimum of the CV curve is detected. At the end of combustion of the main injection, flames move randomly near the bowl wall and the CV increases again and reaches its second peak at -14 CAD. The burning of the third injection again results in a regular combustion process and thus a second minimum value is found at -17 CAD. Lastly, several flames which extinguish with irregular behaviour are detected towards the end of combustion (27.5 CAD). A similar trend can be observed when looking at the CV evaluated for the coefficient of the first IC (Fig. 3.39d), a_1 , which peaks at -2.5 CAD and 14 CAD, where a rather irregular combustion process takes place and the separation between the repeatable and cycle-variable parts is less effective. Then, when the burning along the jets dominates, both for the main and post injection, the CV of a_1 achieves very low values since at these crank angles cycle-to-cycle variability is relatively low and the separation between the two independent components is much better: here again the first component represents in essence the average luminosity distribution whereas the second component represents the fluctuation and, of course, the coefficient of the average is almost constant over the cycles. Most interesting is the finding that the CV of a_2, related to combustion near the bowl walls, is at least one order of magnitude higher than the CV of a_1 . This is a quantitative confirmation of the fact that strong deviations from the ideal combustion process are located near the bowl walls. Variations in the mean ROHR are mainly associated with combustion variations near the walls of the bowl, also in accordance with the early correlation of the peak CV of a_2 (3.5 CAD) with the CV of pressure.

In summary, the main result of the analysis conducted over the cycles is the quantitative assessment of the statistics of the two independent components found, which confirms that the variability of combustion is low along the jets and high
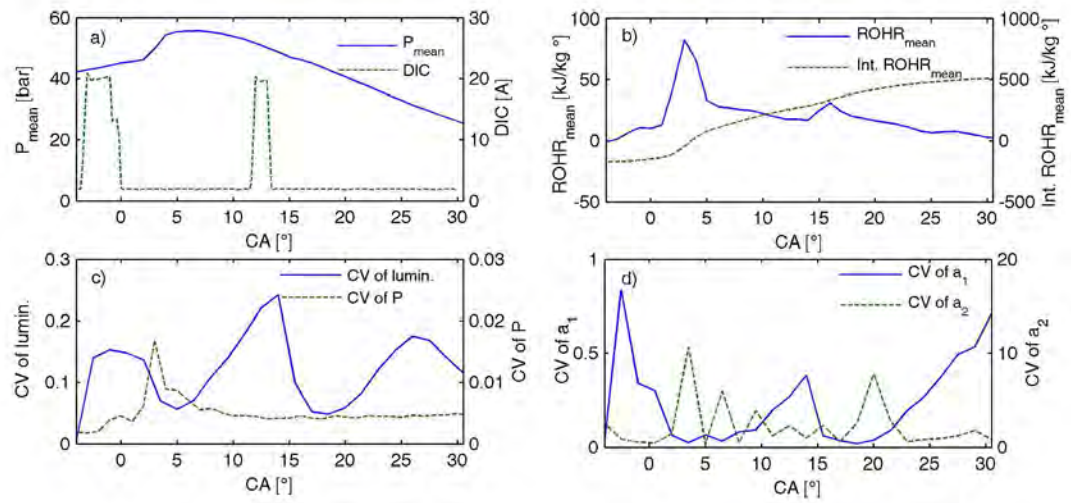
Figure 3.40: Average in-cylinder pressure and drive injector current (a), average rate of heat release (ROHR) and average integral ROHR (b), CV of the integral luminosity and of the in-cylinder pressure (c), and coefficient of variation of the ICs coefficients a_1 and a_2 (d) as a function of the crank angle.

near the chamber walls. It is important to note that sICA is spatially-distributed and thus the CV analysis describes the morphology of the flame structure.

Chapter 4

Analysis of OH* and OH-PLIF imaging of swirling spray flames far from and at extinction

4.1 Introduction

For systems having a dominant periodicity, as in thermoacoustically-excited flames, POD has also been used to reveal typical flame shapes and their connection with the acoustics (Davis et al., 2013) and the flow (Stöhr et al., 2012). POD has also been applied to chemiluminescence images to study the blow-off dynamics of stratified premixed flames (Kopp-Vaughan et al., 2013) and vortex shedding (Kostka et al., 2012). In simulations, POD has been used to represent DNS data (Danby and Echekki, 2006; Frouzakis et al., 2000) and for analysis of LES (Duwig and Fureby, 2007; Ayache and Mastorakos, 2013). The above references contain literature reviews on POD applications in flames and fluid mechanics and could be consulted for further background information.

Assuming that POD can be used to reveal structural changes in the flames as

operating conditions are altered, it is interesting to explore flame shapes at different degrees of extinction. Local extinction and global blow-off are very important topics in combustion. Cavaliere et al. (2013) used a swirl burner and compared the blow-off behaviour of methane premixed, methane non-premixed, and n-heptane spray flames. For all types of flame, the blow-off event (i.e. the slow reduction of flame area to zero) lasts a significant time (i.e. tens of ms) compared to the residence time in the burner, and before this process begins the flame seems stable. However, significant changes in flame shape are evident when one compares flames at operating conditions far from extinction and at the blow-off condition before the blow-off event (Cavaliere et al., 2013; Kariuki et al., 2012).

In this chapter, new experiments in the swirl burner of Cavaliere et al. (2013) are performed with a range of fuels including more volatile (ethanol) and less volatile (n-decane, n-dodecane), to represent with greater fidelity gas turbine combustors and to understand the effect of fuel volatility on flame blow-off behaviour. In particular, fast OH* chemiluminescence and OH-PLIF are used and the sequences of images are analysed with POD. Although OH* images have been analysed with POD before (Stöhr et al., 2012; Kostka et al., 2012; Davis et al., 2013; Kopp-Vaughan et al., 2013), POD's use on PLIF data is not available, with Ref. (Kariuki et al., 2012) being one of the first but applied to a laminar flame. The authors are not aware of POD analysis of OH* from spray swirl flames at blow-off, nor of POD analysis of OH-PLIF.

The specific objectives of work presented in this are: (i) to examine the performance of the POD technique for swirling, turbulent spray flames close to extinction; (ii) to examine differences in flame behaviour far from and close to extinction conditions; (iii) to reveal the dominant flame structures just before blow-off; and (iv) to reveal the differences and similarities among the different liquid fuels used. To study the statistical behaviour of the POD Modes, in terms of coherent and in-

coherent components, when the condition of the blow-off is approached, a method was adopted, proposed earlier by Bizon et al. (2009a) and based on a gaussianity index to classify the POD Mode as coherent or incoherent. This analysis was suggested since the blow-off condition can be considered as a qualitative change of the system state, hence also the statistical proprieties of the flame pattern are expected to change radically, so as the energy captured by coherent and incoherent components. In order to assess the POD Modes as coherent or incoherent, the Normality Test proposed by Shapiro-Wilk (Royston, 1982) is introduced, along with two new energy spectra based on statistical indexes are also introduced and employed to describe the statistical behaviour of the POD Modes when the blow-off condition is approached. Based on these spectra, parameters can be defined to capture the transition to blowoff and envisage the possibility of a safe near-blowoff operation.

4.2 Apparatus and image acquisition

A bluff-body swirl spray burner (Fig. 4.1) was used to stabilise liquid fuel flames far from and close to blow-off. The details of the burner can be found in Cavaliere et al. (2013); the same burner with a new atomizer that produces a spray for a range of liquid fuels has been used here. The fuels used were: ethanol, n-heptane, n-decane, and n-dodecane. The motivation is to examine the effects of fuel volatility on blow-off behaviour. N-decane and n-dodecane have very low volatility and this makes them relevant to aviation gas turbines that burn kerosene.
The flame conditions are summarized in Table 4.1.

For reaching the blow-off limit of the spray flame, the fuel flow rate is kept fixed, while gradually increasing the air flow rate in steps of approximately 2% (0.258 m/s) every 40 seconds until blow-off occurred, at which event the blow-off
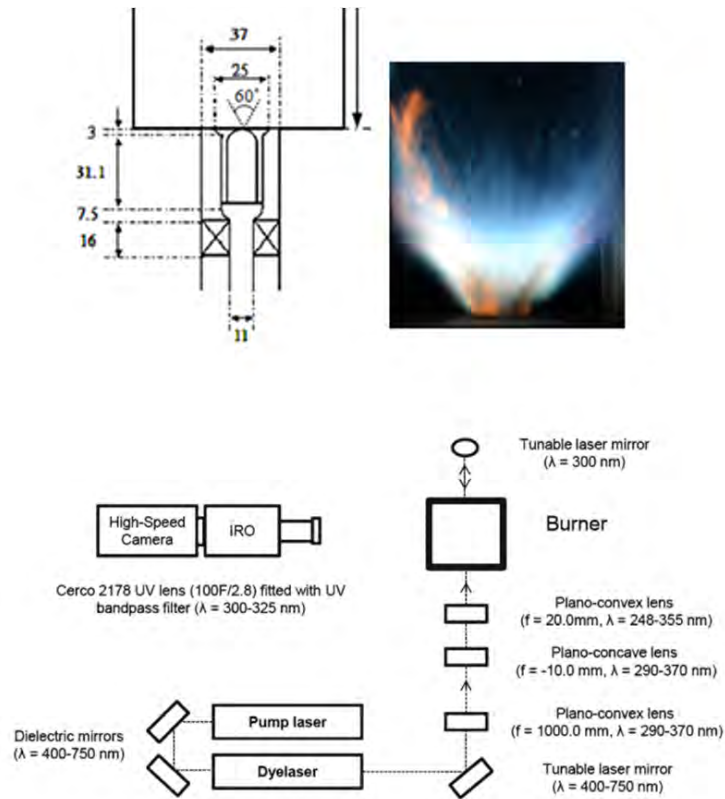
Figure 4.1: Burner schematic and a photograph of flame D1S1 (Upper) and OH-PLIF. Optical diagnostic system schematic (Lower).

velocity, UBO, was recorded. An average blow-off velocity of at least 5 individual UBO measurements under the same conditions was calculated and included in the table for each fuel flow rate. OH* chemiluminescence was line of sight measured, as an indicator of heat release of the flame, both at the stable case and at blow-off. OH-PLIF was captured separately to visualise the flame sheet structure. A similar diagnostic system was used in premixed flames by Kariuki et al. (2012) and non-premixed flames and heptane spray flames by Cavaliere et al. (2013) for flames close to blow-off. The OH-PLIF system consists of a high-repetition rate diode solid state laser (532 nm, Model JDSU Q201-HD), with a power of 14 W at 5 kHz and a pulse length of around 18 ns, and a SIRAH Credo high speed dye

Table 4.1: Test cases evaluated for various stable and blow-off conditions. Fuel mass flow rate is 0.27 g/s.

Fuel type	Name	Case	$U_{bulk}[m/s]$	$\phi_{overall}$
Ethanol	E1S1	Stable	17.1	0.19
	E1S2	Stable	20	0.16
	E1B1	Blow-off	21.6	0.15
n-Heptane	H1S1	Stable	17.1	0.32
	H1S2	Stable	20	0.27
	H1B1	Blow-off	22.8	0.24
n-Decane	D1S1	Stable	17.1	0.31
	D1S2	Stable	20	0.27
	D1B1	Blow-off	20.3	0.27
n-Dodecane	DD1S1	Stable	14.3	0.38
	DD1S2	Stable	17.1	0.32
	DD1B1	Blow-off	20.1	0.27

laser (Model 2400), with the output beam at 566 nm doubled by a BBO crystal. The output beam was tuned near 283 nm to excite the Q1 (6) line in the A1Σ - X2Π(1,0) band. The output power was 300 mW at 5 kHz (60 μ J/pulse). The laser beam was expanded into a sheet of around 0.23 mm thickness and 35 mm height using sheet optics. An IRO intensifier (LaVision, spectral range of 190-800 nm) was fitted with a UV filter (270-370 nm) for OH* and with a narrower filter (300-325 nm) for OH-PLIF. The intensifier was coupled with a Photron SA1.1 monochrome high speed CMOS camera with 1024 × 1024 pixel resolution up to 5.4 kHz. OH* chemiluminescence and OH-PLIF movies were captured at 5 kHz. 1000 images (0.2 s) were recorded per run. The OH* and OH-PLIF movies referred

to as E1B1, H1B1, D1B1, DD1B1 comprise only the part of the signal before the blow-off event, i.e. before the beginning of the disappearance of the flame; see Cavaliere et al. (2013) and Kariuki et al. (2012) for typical evolutions of the blow-off event.

4.3 Proper Orthogonal Decomposition

Given a data set $u_k(x)$, where x is the spatial variable and k is the snapshot (or temporal) index, the POD provides an optimal orthonormal basis function set, called the *POD Modes*, $\mathbf{\Phi} = \{\phi_1, \ldots, \phi_N\}$, such that the ensemble of the data can be expressed as a linear combination of these POD Modes. The data can be organized in the matrix of snapshots $\mathbf{U}$, that is:

$$\mathbf{U} = \begin{pmatrix} u(x_1, t_1) & \ldots & u(x_1, t_N) \\ \vdots & \ddots & \vdots \\ u(x_M, t_1) & \ldots & u(x_M, t_N) \end{pmatrix} \tag{4.1}$$

where M is the dimension of the discretized spatial domain, and N is the number of snapshots. When the number of the snapshots is much smaller than the dimension of the spatial discretization, $M \gg N$, it is useful to adopt the *method of snapshots* proposed by Sirovich (1987) that permits to express the POD basis functions (POD Modes) as linear combination of the snapshots.

$$\phi_i = \sum_{i=1}^{N} \psi_{ik} u_k(x) \tag{4.2}$$

where $\mathbf{\Psi} = \{\psi_1, \ldots, \psi_N\}$ is obtained by solving the eigenvalue problem $\mathbf{C\Psi} = \lambda\mathbf{\Psi}$ where

$$\mathbf{C} = \frac{1}{M-1}(\mathbf{U} - \overline{\mathbf{U}})^T(\mathbf{U} - \overline{\mathbf{U}}) = \frac{1}{M-1}\widetilde{\mathbf{U}}^T\widetilde{\mathbf{U}} \tag{4.3}$$

is the space correlation matrix centred on the mean component, which is also called covariance matrix. Then, $u(x, t)$ can be approximated by a linear combination of

the first K Modes

$$u(x,t) \approx c_0\phi_o(x) + \sum_{i=1}^{K} c_i(t)\phi_((x)$$ (4.4)

where $c_i(t)$ are the POD coefficients that can be calculated by projection of the data set onto the Modes. Mode 0, $\phi_0(x)$, multiplied by its coefficient c_0, is the mean field of the snapshots ($\overline{u} = c_0\phi_0$). The i-th eigenvalue,λ_i, represents the energy captured by the i-th POD Mode about the data set. Usually, the POD Modes are ordered according to decreasing magnitude of their corresponding eigenvalues (real, positive).

We define the *relative energy* captured by the k-th Mode, e_k, and the cumulative energy spectrum of the POD Modes, E_{K_POD}, respectively as

$$e_k = \frac{\lambda_k}{\sum_{i=1}^{N}\lambda_i} \qquad E_{K,POD} = \frac{\sum_{i=1}^{K \leq N}\lambda_i}{\sum_{i=1}^{N}\lambda_i}$$ (4.5)

The resulting eigenvalue problem can be solved by using the Matlab routine "eigs", based on ARPACK, a collection of Fortran77 subroutines designed to solve large scale eigenvalue problems. Since the temporal variable appears only in the POD coefficients, and the spatial variable appears only in the POD Modes, it can be said that the Modes carry information on the spatial features, whereas the coefficients describe the temporal features. In this work, POD has been used to extract and analyze the dominant structures from the ensemble of collected images, both OH* chemiluminescence and OH-PLIF, during the experiments described previously. The originally acquired frames were 1024x1024 pixels but, to reduce the computational cost they were cropped to the region of interest (831x365). The time series of the POD coefficients were normalized to have unit energy (or standard deviation one), that is

$$\varsigma_i(t) = c_i(t)/\sqrt{\lambda_i}$$ (4.6)

Subsequently, Power Spectral Density (PSD) and Cumulative Spectral Power (CSP) of the normalized POD coefficients were estimated. Welch's method with a Bartlett-

Hanning window (Welch, 1967) was employed to estimate the PSD. Since the POD coefficients were normalized to have unit energy and the data set was centred to have null mean, $\int_0^{+\inf} PSD_i(f)df = 1$ for all normalized POD coefficients, where f is the frequency. The analysis of the PSD of the POD coefficients can reveal any periodic features and the frequency content of the associated POD Mode.

4.4 Methods for the coherent-incoherent analysis

4.4.1 Analysis based on kurtosis and skewness

Bizon et al. (2009b) proposed a method to extract the coherent and incoherent components of the fluctuation of the luminosity field of the combustion process in an optically accessible internal combustion engines. Such method is built according to the Karhunen-Loève theorem (Loève, 1978), in that the fluctuations can be considered as realizations of a centred stochastic process in some compact set Ω satisfying generic regularity proprieties; hence, it admits an orthogonal decomposition wherein the coefficients are pairwise uncorrelated random variables. In fact, POD is the empirical version of the KL transform. Particularly, this method starts from computing skewness, γ_1, and kurtosis, β_2, for each POD coefficient, namely

$$\gamma_{1,i} = \frac{\overline{(c_i)^3}}{\sigma_i^3}; \qquad \beta_{2,i} = \frac{\overline{(c_i)^4}}{\sigma_i^4} \tag{4.7}$$

where σ_i is the standard deviation of c_i. . It is well known that the values of skewness and kurtosis for a Gaussian distribution are respectively 0 (because the Gaussian pdf is symmetric) and 3, as a measure of Gaussianity, Bizon et al. (2009a). proposed the quantity ρ_i defined as:

$$\rho_i = \sqrt{(\gamma_{1,i})^2 + (\beta_{2,i} - 3)^2} = \sqrt{(\gamma_{1,i})^2 + (\beta_{2,i}^*)^2} \tag{4.8}$$

where $\beta_{2,i} = (\beta_{2,i} - 3)$ is the *excess of kurtosis*. Subsequently, the POD Modes are reordered according to decreasing values of rho.

After that, it is possible to choose a threshold value, ρ_{th}, for ρ, and to identify S Gaussian (incoherent) coefficients, that is the subset, Coh , of the POD coefficients with $\rho_i \leq \rho_{th}$,

$$Coh = \{i = 1, 2, \ldots, N : \rho_i \leq \rho_{th}\} \tag{4.9}$$

and S-N non-Gaussian (coherent) coefficients, that is the subset, $Incoh$, of the POD coefficients with $\rho_i > \rho_{th}$,

$$Incoh = \{i = 1, 2, \ldots, N : \rho_i > \rho_{th}\} \tag{4.10}$$

Then, the incoherent component, w, will be obtained as linear combination between the S Gaussian coefficients and the corresponding POD Modes, that is:

$$w = \sum_{i \in Incoh} c_i(t)\phi_i(x) \tag{4.11}$$

Similarly, the coherent component, z, will be given as linear combination of the S-N non-Gaussian coefficients and corresponding POD Modes, that is:

$$z = \sum_{i \in Coh} c_i(t)\phi_i(x) \tag{4.12}$$

As a result, considering the reordering based on ρ , the ensemble of the snapshots can be also written as

$$u(x,t) = \overline{u} + \tilde{u} = \overline{u} + (w + z) \tag{4.13}$$

In this paper the distribution of energies captured by the POD Modes versus ρ, namely, the distribution of the POD Modes in the $\rho - e_K$ *plane*, , will be called *energy spectrum based on ρ*.Moreover, the cumulative energy spectrum based on ρ is given by

$$E_\rho(\rho) = \frac{\sum_{i \in P} \lambda_i}{\sum_{i=1}^{N} \lambda_i} \qquad P = \{i = 1, 2, \ldots, N : \rho_i \leq \rho\} \tag{4.14}$$

Finally, by choosing $\rho = \rho_{th}$ in Eq. (4.14), it is evident that $E_\rho(\rho)$ can be interpreted as the amount of coherent energy captured by POD Modes as function of ρ_{th}.

4.4.2 Analysis based on the Shapiro-Wilk test

Another way to discriminate the Gaussian and non-Gaussian POD coefficients is given by using a class of methods of statistical inference, known as hypothesis tests. A hypothesis test is a method that verifies if the null hypothesis (example, the sample is extracted from a Gaussian population) can be accepted (or rejected), with a given level of significance (α). In our case, the normality tests are interesting because they allow to classify the POD coefficients as Gaussian or non-Gaussian by testing the following two hypotheses:

1. null hypothesis (H_0), the data sample is extracted from a Gaussian population;

2. alternative hypothesis (H1), the data sample is not extracted from a Gaussian population.

An approach commonly adopted for the testing process of a hypothesis test is based on computing the p-value (Learning, 2011) The p-value is defined as *the probability, calculated assuming that the null hypothesis is true, of obtaining a value of the test statistic at least as contradictory to H_0 as the value calculated from the available sample* .

Briefly, the hypothesis tests are conducted via three steps, i.e:

1. Estimate the value of the *test statistic* for each POD coefficient.

2. Compute of the *p-value* associated to the test statistic.

3. Compare the *p-value* with the chosen significance level. Then, if the *p-value* is lower than the significance level, the null hypothesis (H_0) is rejected in favour of H_1; otherwise it is accepted.

Usually, when the null hypothesis is accepted, it is also said that the test statistic is significant. Besides, an interpretation about the p-value of a hypothesis test is the

following: the p-value can be considered as a measure of the amount of statistical evidence that supports the null hypothesis (Learning, 2011). Thus, in the case of normality test, wherein the null hypothesis (H_0) assumes that the sample is extracted from a Gaussian population, it is possible to interpret the *p-value* as a measure of the statistical evidence that the sample is extracted from a Gaussian population. Particularly, in case of a normality test, the higher the *p-value*, the greater the statistical evidence that the sample belongs to a Gaussian population. Finally, the coherent and incoherent components are provided by the following equations:

$$w = \sum_{i \in Incoh} c_i(t)\phi_i(x) \qquad Incoh = \{i = 1, 2, \ldots, N : (p_{value})_i \geq \alpha\} \qquad (4.15)$$

$$z = \sum_{i \in Coh} c_i(t)\phi_i(x) \qquad Coh = \{i = 1, 2, \ldots, N : (p_{value})_i < \alpha\} \qquad (4.16)$$

Bizon et al. (2010a) were the first authors to use a Normality hypothesis test (D'Agostino-Pearson Normality test (D'Agostino and Pearson, 1973)) to discriminate the Gaussian component from the non-Gaussian component of the fluctuations of the luminosity field of the combustion process occurring in an internal combustion engine. In this work, the Shapiro-Wilk normality test is used instead. In order to obtain a better understanding of the underlying phenomena in terms of coherent and incoherent features, we introduce two new spectra based on p-value. Particularly, $E_{p-value}$ will denote the *cumulative energy spectrum of the POD Modes based on p-value* and is given by:

$$E_{p-value}(p_{value}^*) = \frac{\sum_{i \in P} \lambda_i}{\sum_{i=1}^{N} \lambda_i} \qquad P = \{i = 1, 2, \ldots, N : (p_{value})_i \leq p_{value}^*\} \quad (4.17)$$

This spectrum can also be viewed as the amount of energy captured by the coherent POD Modes obtained by employing the Shapiro-Wilk Normality Test with

a level of significance $\alpha = p^*_{value}$. It should be noted that the method based on Shapiro-Wilk normality test can also be extended to other hypothesis tests known in literature.

4.5 POD Analysis: results and discussion

In this Section, the POD results are discussed. Flames far from extinction and the flames immediately before the extinction transient are chosen. First, the results for n-decane are shown, as representative of all flames and in order to emphasize the behaviour of a low-volatility fuel due to its relevance to gas turbines. The following discussion focuses on: (i) the basic structure of the flame; (ii) its temporal evolution; (iii) the difference between the flames, which reveals the "footprint" of blow-off in this geometry. The presentation follows with a sample of similar results from the other fuels (ethanol, n-heptane, n-dodecane) to examine how the fuel volatility affects the flame behaviour, as revealed in the POD analysis. Finally, POD analysis using the Gaussian/non-Gaussian component separation and the corresponding reconstructions are discussed.

4.5.1 n-Decane

OH* results. Figure 4.2 shows the mean image (Mode 0) and the first five POD Modes from the OH* for D1S1. Mode 1 highlights a roughly antisymmetric pair of heat release fluctuations about the flame axis. Since the POD reconstruction is given by a linear combination of the POD Modes with the modal coefficients, and given that the POD coefficients have mean value 0, it is possible to say that the first Mode reveals a transverse oscillating motion of the flame. A similar conclusion can be drawn by looking at Modes 1 of D1S2 (Fig. 4.3) and D1B1 (Fig. 4.4). These dominant structures cannot be seen as easily in the raw OH* images (Figs. 4.5-4.7,

upper row) due to the underlying small-scale fluctuations, but are shown in the reconstructed movie (Figs. 5-7; middle row) with mean image (Mode 0; constant in time) and the first Mode, which represents the principal left/right oscillation. The reconstructed movies for the blow-off condition (Fig. 7, middle and lower rows), in particular, show that almost half of the flame may be completely quenched during this transverse motion.

Looking at Modes for D1S1 (Fig. 4.2). Mode 2 can be associated to the turnover of the flame from a central zone, which is related to a compact flame, to lateral regions, which are related to flames localized along the spray. This Mode therefore can be thought of as a standing oscillation, where the central region reacts less intensely when the outer region reacts more intensely. Modes 3 and 4 can be associated to axial oscillation. Mode 5 presents spatial features more complex than the previous Modes. Similar comments can to be made for the Modes of flames D1S2 (Fig. 4.3) and D1B1 (Fig. 4.4). Figures 4.5-4.7 (lower row) show snapshots obtained by reconstruction of the data with the mean image and the first 5 Modes. It is evident that the reconstruction of the data with the first few POD Modes has allowed the filtering of the spatial features of small scale, so that it has been possible to visualise better the dominant shapes. Looking at Modes 1 to 3 for D1B1 (Fig 4.4) together and the reconstructed movie suggests that at the blow-off condition, the flame seems to have a wedge-like shape that rotates. The clarity of this motion from the reconstructed POD snapshots, and the difference between the stable flame and the one at extinction, demonstrates the power of POD to extract the dominant features of the OH* movies.

Figure 4.8 reports the spectra of cumulative energy. It appears that when the blow-off condition is approached, the energy of the Modes of low order increases. Therefore, the first 50 POD Modes for the operating conditions D1S1, D1S2 and D1B1 have cumulative energy respectively of 77.47%, 79.89% and 82.88%, while
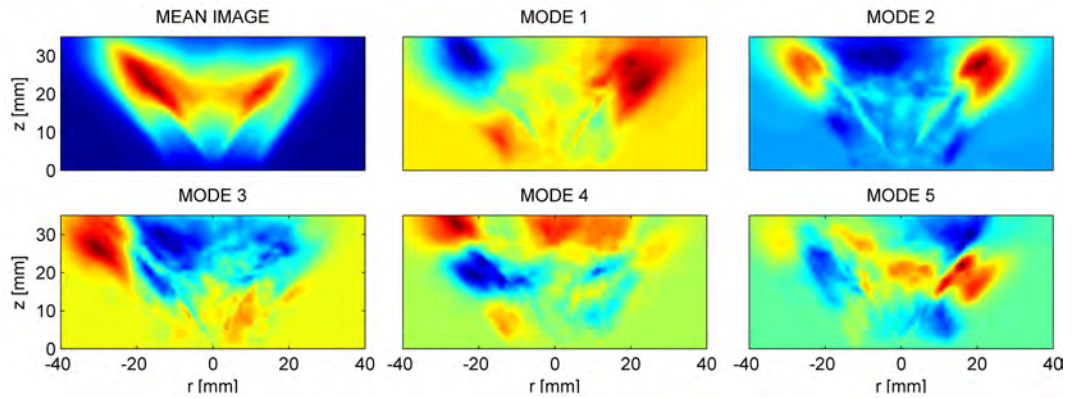
Figure 4.2: Mean image and the first 5 POD Modes from OH*, Flame D1S1.
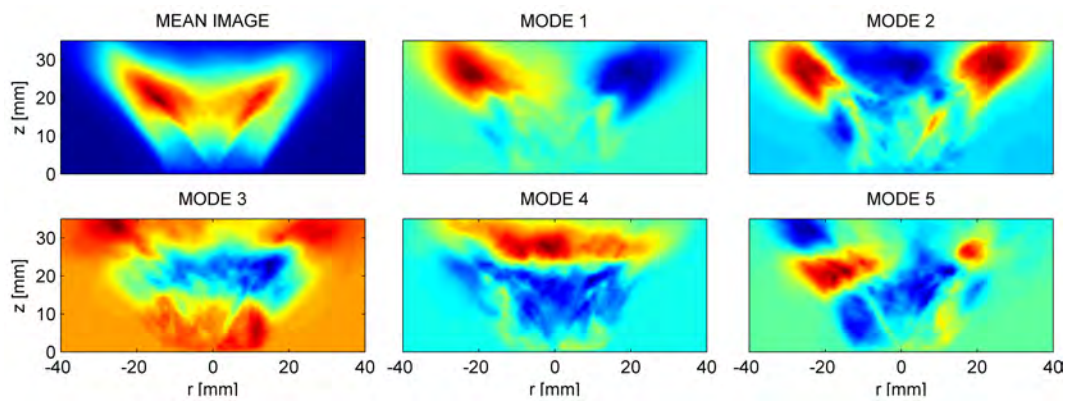
Figure 4.3: Mean image and the first 5 POD Modes from OH*, Flame D1S2.
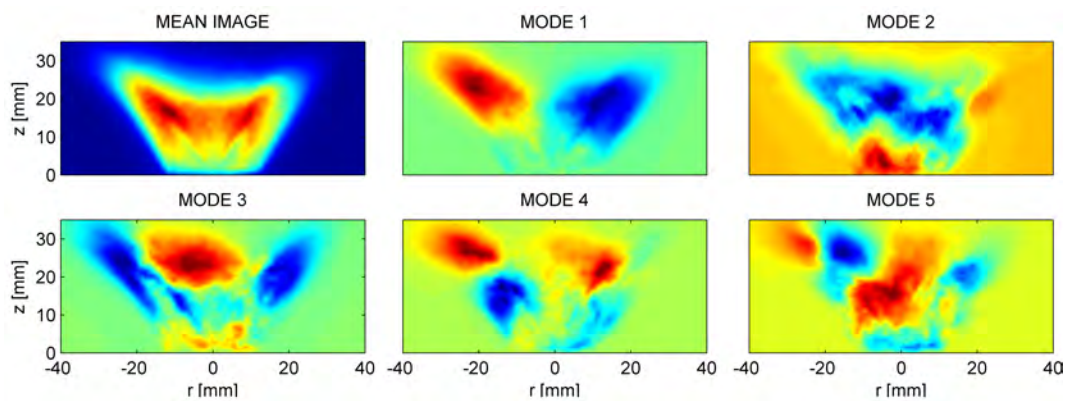
Figure 4.4: Mean image and the first 5 POD Modes from OH*, Flame D1B1.
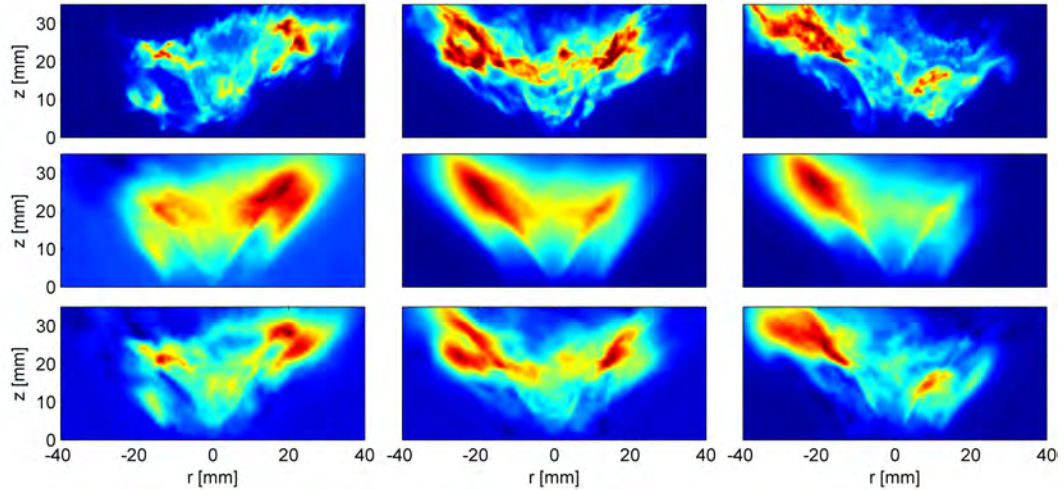
Figure 4.5: Flame D1S1. (Upper) Snapshots from raw OH* movie. Snapshots at the same times from reconstructed OH* movie using (middle) the mean and Mode 1 only and (lower) the mean and Modes 1 to 5.
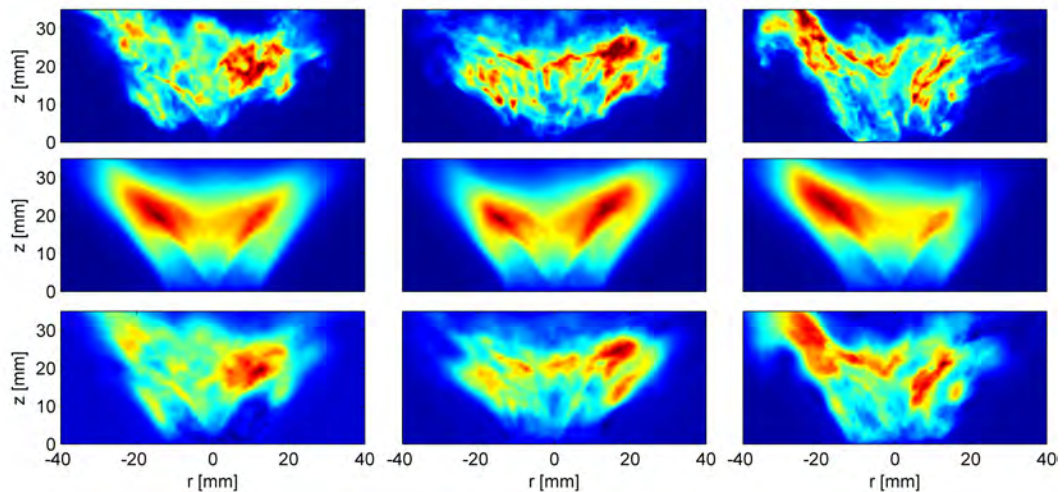
Figure 4.6: Flame D1S2. (Upper) Snapshots from raw OH* movie. Snapshots at the same times from reconstructed OH* movie using (middle) the mean and Mode 1 only and (lower) the mean and Modes 1 to 5.
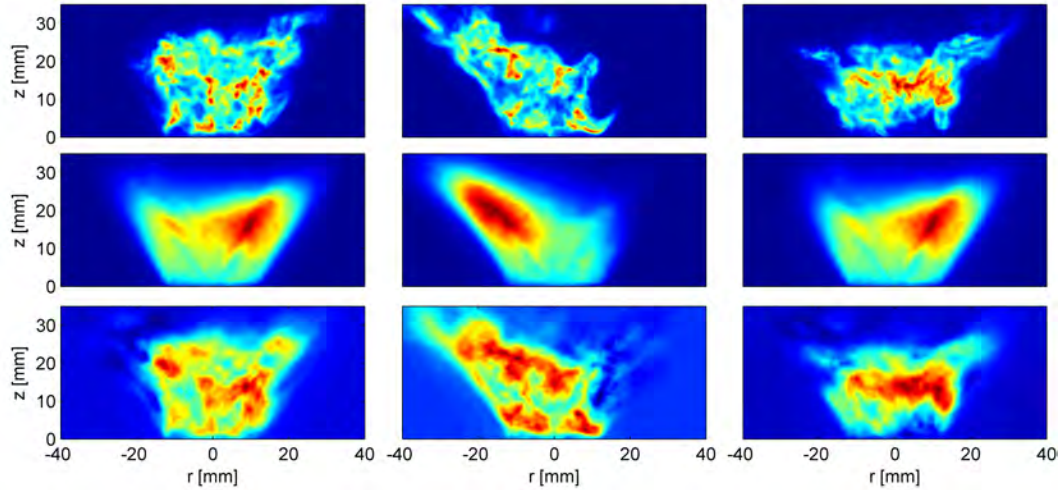
Figure 4.7: Flame D1S2. (Upper) Snapshots from raw OH* movie. Snapshots at the same times from reconstructed OH* movie using (middle) the mean and Mode 1 only and (lower) the mean and Modes 1 to 5.
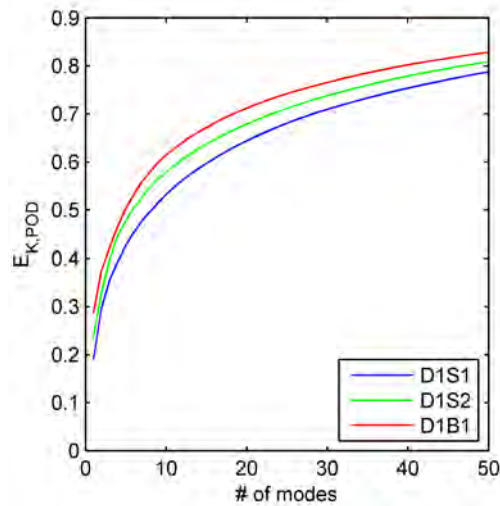
Figure 4.8: Cumulative energy spectrum of the POD Modes of OH* chemiluminescence and OH-PLIF for flames of n-decane.
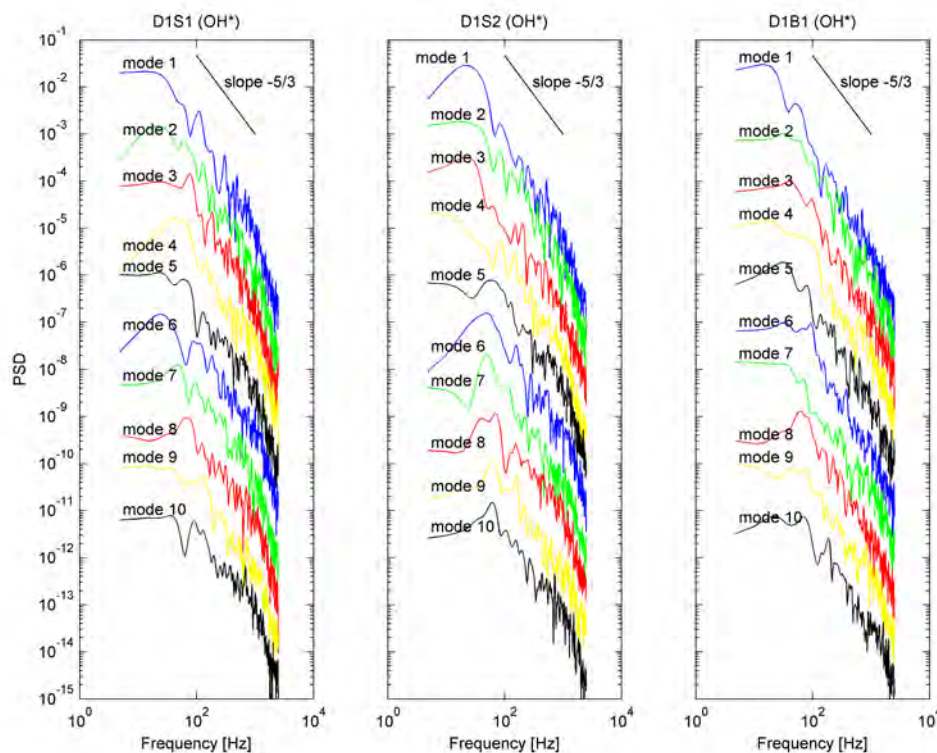
Figure 4.9: Flames of n-decane. PSD of POD coefficients from Modes 1 to 10 of OH*.

the first 5 Modes contain about 41.45 % of the energy for D1S1 and about 50.36 % for D1B1; this is probably related to the more pronounced Mode 1 for the blow-off condition that contains 28.69% for D1B1 and 17.88% for D1S1.

Figure 4.9 shows the PSD of the first 10 normalized POD coefficients (the PSDs were shifted along the y-axis for clarity) for flames D1S1, D1S2 and D1B1. Many POD Modes contain a broad peak between about 30 and 60 Hz and occasionally its harmonics. This result reveals the dynamics, in terms of frequency, of the flame. For flame D1S1, the transverse Mode (Mode 1) does not show a strong peak in its PSD, although a clear motion is seen (e.g. Figs. 4.2, 4.3), while the coefficients of
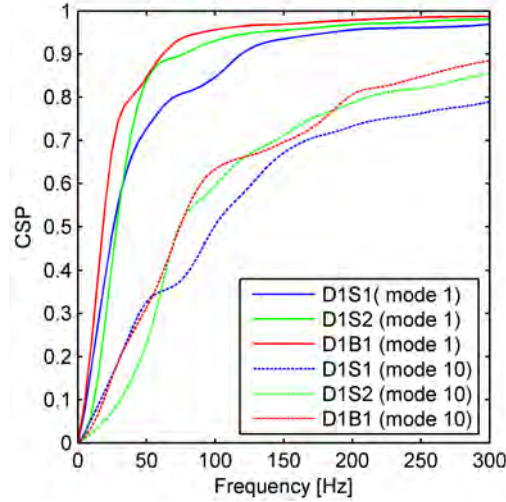
Figure 4.10: Flames of n-decane. CSP of POD coefficients of Modes 1 and 10 of OH*.

the higher Modes tend to have such broad peaks: 24.4 Hz for Modes 2 (turn-over motion) and 5 and the harmonic at 48.8 Hz for Modes 3 and 4. For flame D1S2, Mode 1 (transverse fluctuation) and Mode 3 (axial fluctuation) show a strong peak in at 24.4 Hz. For the flame at blow-off (D1B1), where a significant part of the flame has been quenched (Fig. 4.4), the absence of a peak in the PSD of the coefficients of Mode 1 suggests that there is no strong periodicity associated with this flame motion, this can be associated to the unstable dynamic of the flame. The axial and standing Modes (Modes 2-3), however, have broad spectral peaks at 48.8 Hz. It is interesting that these spectral peaks depend little on the flow velocity. In the absence of detailed velocity information the origin of these heat release fluctuations cannot be inferred further. LES of swirling flames (see, for instance (Frouzakis et al., 2000; Duwig and Fureby, 2007) and references therein) often show similar peaks in the POD coefficients attributed to precessing vortex cores (PVC) or other vortical motions; the Strouhal numbers of the present peaks though are too low compared to the o(1) Strouhal number usually reported for
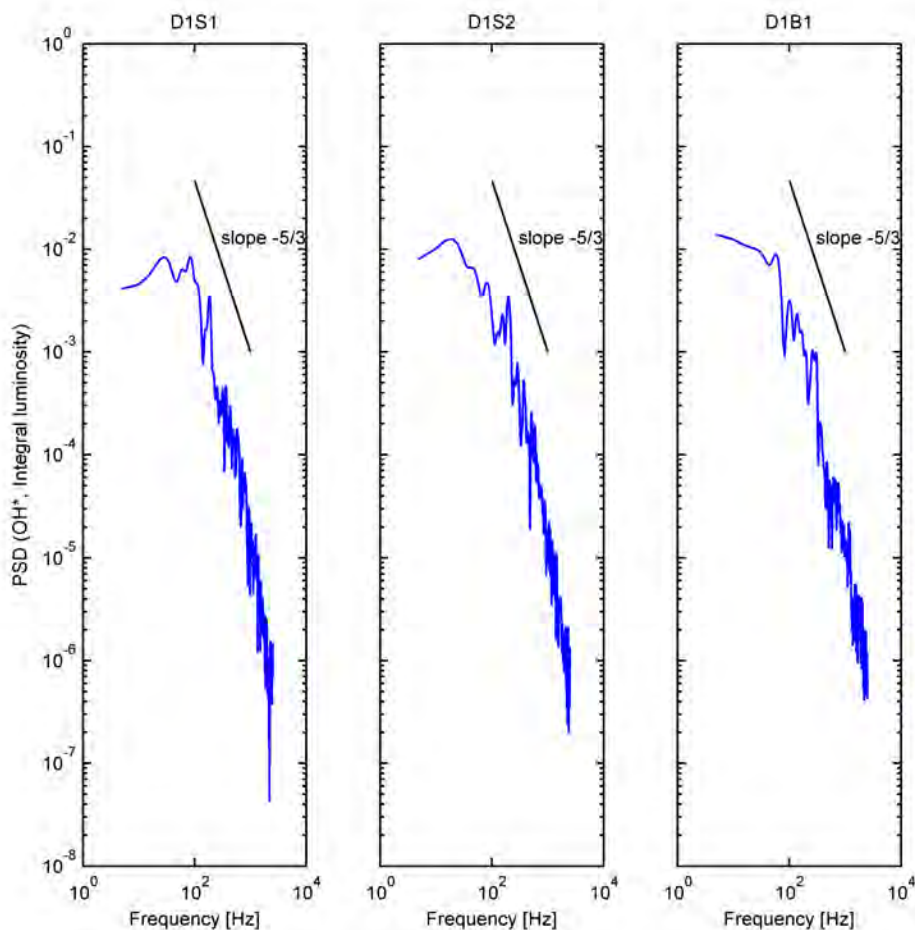
Figure 4.11: Flames of n-decane. PSD of the integral luminosity OH*.

PVC (Duwig and Fureby, 2007).

All PSDs include a portion with a -5/3 decay, typical of the energy spectrum of turbulence, and the OH* shows a sharper drop-off after about 1 kHz (Fig. 4.9). Figure 4.10 shows the CSPs (cumulative spectral power) of the POD coefficients of the Modes 1 and 10 for all operating conditions. It is evident that the higher the Mode order, the higher the contribution of energy at the high frequencies. Furthermore, it is interesting to see as the CSP of the first Mode, which captures
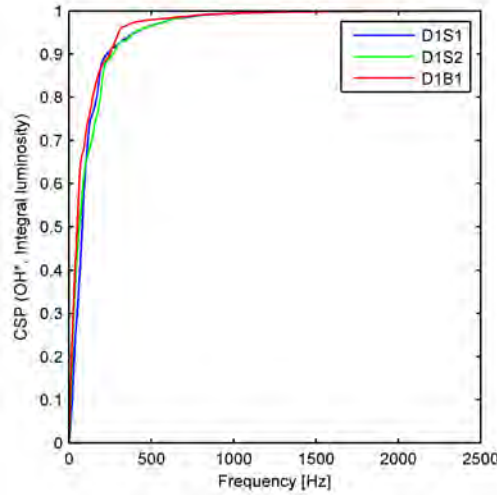
Figure 4.12: Flames of n-decane. CSP of the integral luminosity OH*.

the highest energy, changes when the blow-off condition is approached. Particularly, it is possible to note that, when the blow-off condition is approached, the energy captured by Mode 1, at low frequencies, increases. In addition, the higher the POD Mode order, the higher the contribution of the high frequency motions to the POD coefficients fluctuations (Figs. 4.9 and 4.10). For D1B1, the coefficients of Mode 1 do not have any significant content above 100 Hz, due to the pronounced slow transverse motion, while the flame far from extinction (D1S1) has higher frequency content.

Figures 4.11 and 4.12 show the PSD and CSP of the spatial integral of OH* for the flames D1S1, D1S2 and D1B1. The PSD of the spatial integral OH* for flame D1S1 shows two peaks at 24.41 Hz and 83 Hz; for flame D1S2, the PSD of spatial integral OH* signal shows only a peak at 19.53 Hz. Instead, there is no peak in the PSD of the integral OH* when the blow-off condition is approached. Therefore, it can be thought that such change is due to a qualitative change of the operating condition. Also all PSDs of the spatial integral OH* include a portion with a -5/3 decay, typical of the energy spectrum of turbulence. Furthermore, it

is possible to see that the CSP of the integral OH* follows the same trend of the CSP of the first POD Mode as the blow-off condition is approached. Hence, it is possible to say that at blow-off the flame is characterized from slower dynamics than at stable conditions.

OH-PLIF results. The instantaneous OH-PLIF images reveal the following (Figs. 4.14-4.15, upper row). First, there are two branches of the flame, the inner one roughly aligned with the spray, and the outer one roughly aligned with the annular air jet. The outer flame is lifted more often than the inner one, even for the flame condition far from blow-off. Second, the blow-off condition (D1B1) shows a severely fragmented flame with only small flame elements visible. Third, the stable flames D1S1 (Fig. 4.13, upper row) and D1S2 (Fig. 4.14, upper row) also shows a discontinuous OH zone, but the number of holes in the OH sheet seems smaller. Finally, at blow-off there are often flame fragments residing along the bluff body surface. Similar observations were made for the heptane flame (Cavaliere et al., 2013), although the present n-decane flame shows a more pronounced signal along the spray, which could partly be due to greater interference by fuel fluorescence. Figs. 4.16-4.18 show the mean and first 5 POD Modes respectively for flames D1S1, D1S2 and D1B1. It is possible to note as the mean component changes severely the morphology as the blow-off is approached. Specifically, for flame D1S1 (Fig. 4.16), the mean component show that the flame is localized mainly along the jet axis, drawing a wedge-shaped reaction zone close to bluff-body. The mean component of flame D1S2 (Fig. 4.17), show a wide reaction zone far from bluff-body due to the higher bulk air velocity. Finally, for the flame at the blow-off D1B1 (Fig. 4.18), the mean component shows a feature more compacted and closer to bluff-body, this is in agreement with that obtained from OH* data.
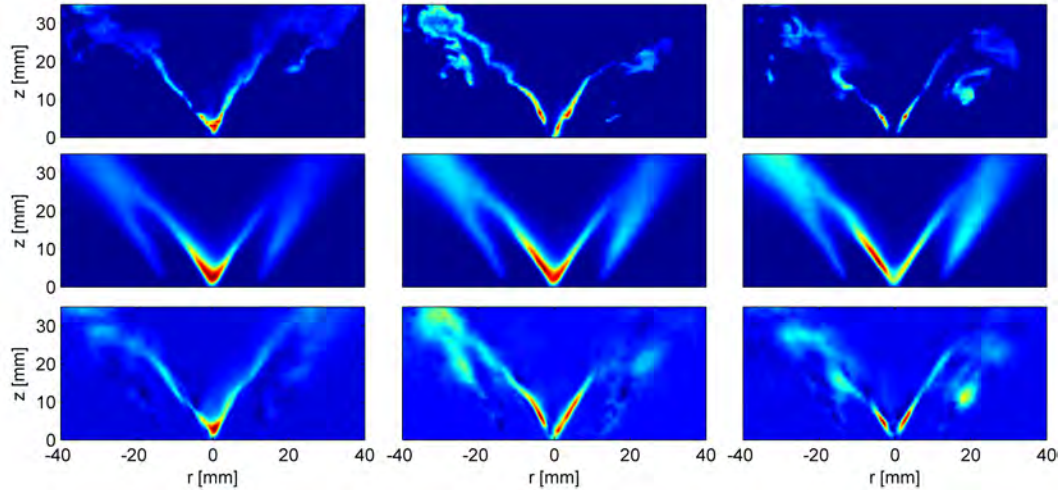
Figure 4.13: Flame D1S1. (Upper) Snapshots from raw OH-PLIF movie. Snapshots at the same times from reconstructed OH* movie using (middle) the mean and Mode 1 only and (lower) the mean and Modes 1 to 20.
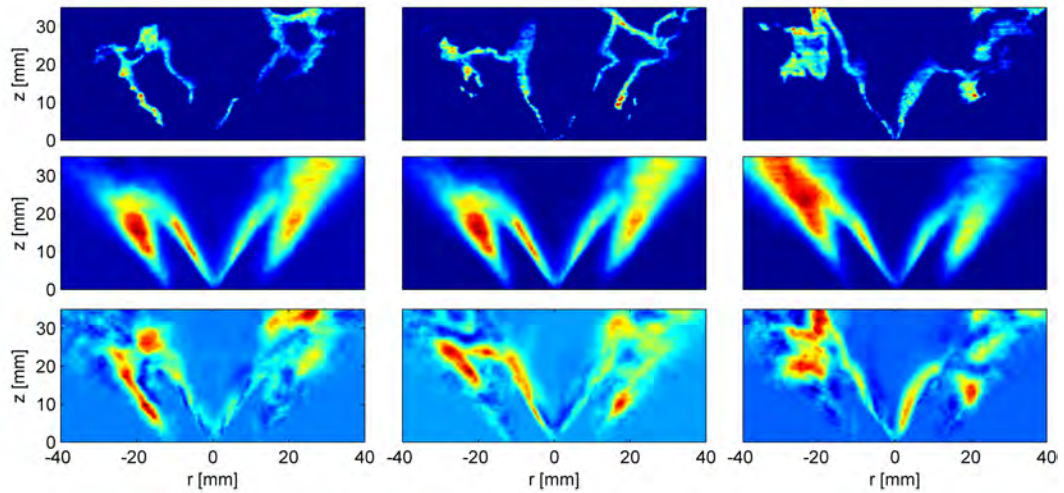
Figure 4.14: Flame D1S2. (Upper) Snapshots from raw OH* movie. Snapshots at the same times from reconstructed OH* movie using (middle) the mean and Mode 1 only and (lower) the mean and Modes 1 to 20.
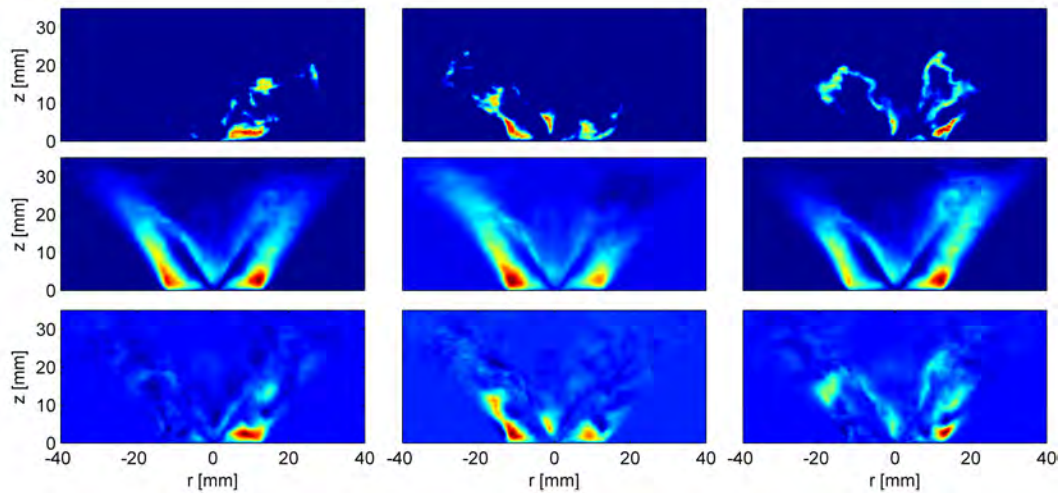
Figure 4.15: Flame D1S2. (Upper) Snapshots from raw OH* movie. Snapshots at the same times from reconstructed OH* movie using (middle) the mean and Mode 1 only and (lower) the mean and Modes 1 to 20.
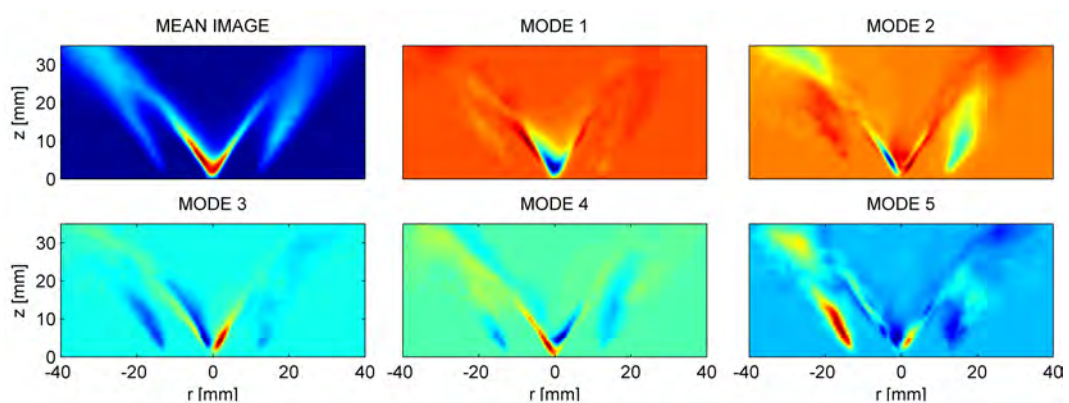
Figure 4.16: Mean image and the first 5 POD Modes from OH-PLIF, Flame D1S1.
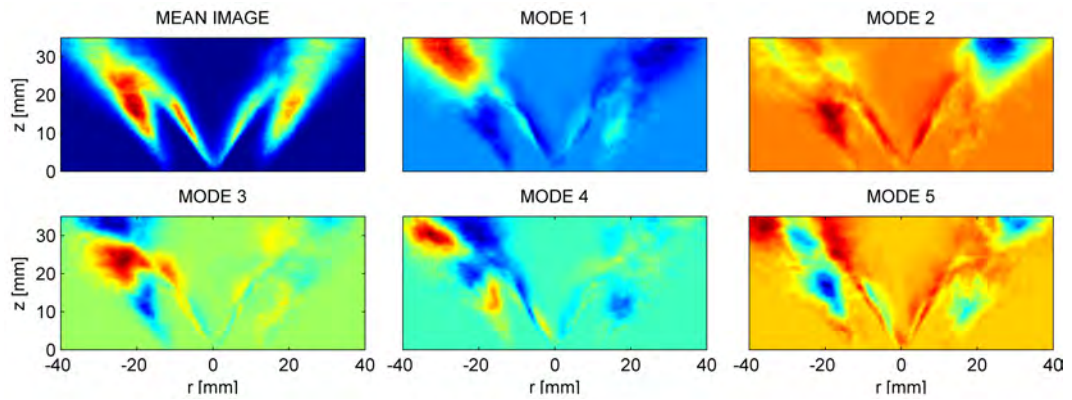
Figure 4.17: Mean image and the first 5 POD Modes from OH-PLIF, Flame D1S2.
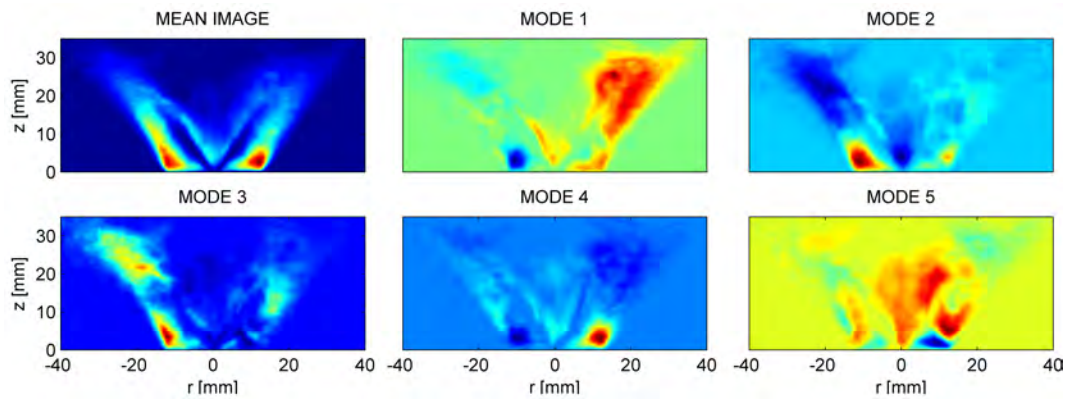
Figure 4.18: Mean image and the first 5 POD Modes from OH-PLIF, Flame D1B1.
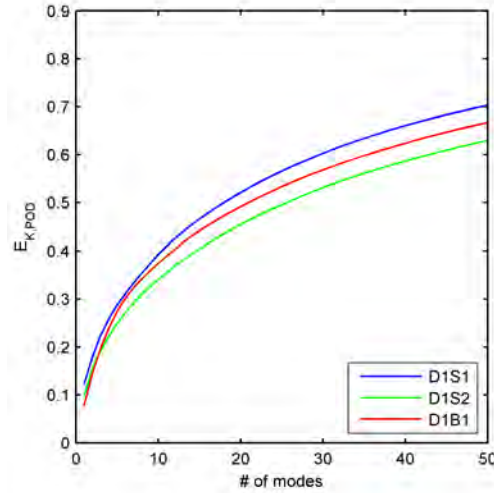
Figure 4.19: Cumulative energy spectrum of the POD Modes of OH* chemiluminescence and OH-PLIF for flames of n-decane.

The POD energy spectrum for the PLIF images (Fig. 4.19) shows that a larger number of Modes is needed to represent the same percentage of energy than for OH* and that the differences between the flames are smaller. So, to reach 50% of the energy, in OH-PLIF we require more than 20 Modes, which is to be contrasted to the 5 Modes needed in OH*. Besides, there is no clear trend between the cumulative energy spectra and the operating conditions. This result suggests that such spectrum should not be employed to build a detection algorithm for the operating condition.

In addition, the PSD of the POD coefficients (Fig. 4.20) shows broad peaks at the same frequency range than the OH*, but there is significantly more high-frequency content, with the -5/3 slope extending now to the Nyquist frequency of the present acquisition system (2.5 kHz). The spectra show no evidence of the sharper drop-off at 1 kHz observed in the OH*. This may be associated with the intrinsic averaging performed in the line-of-sight chemiluminescence imaging that
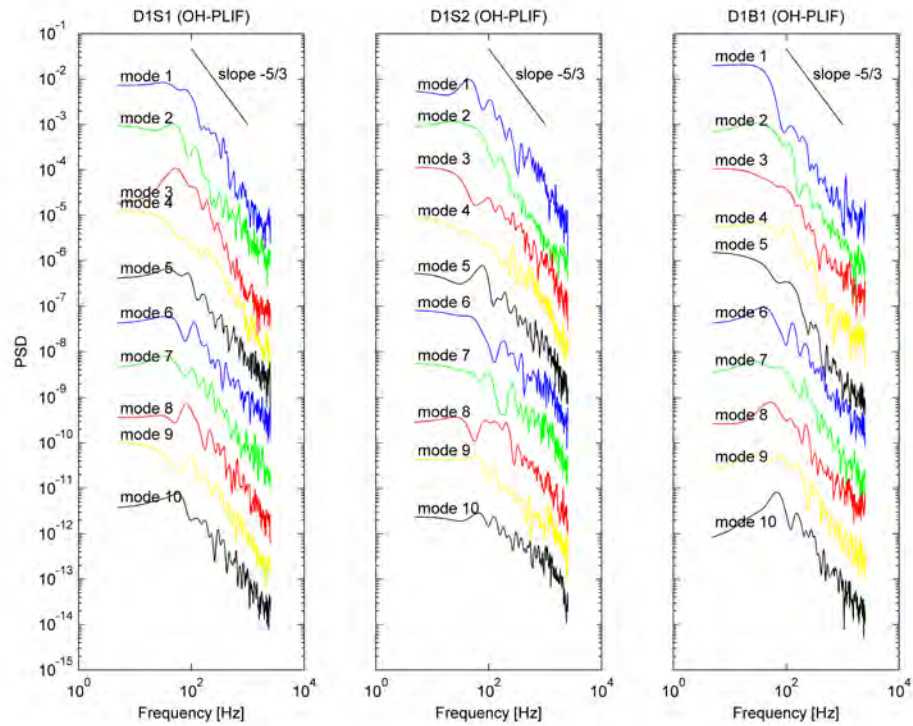
Figure 4.20: Flames of n-decane. PSD of the integral luminosity OH-PLIF.

would tend to smear the small scale motion.

For flame D1S1, Mode 1 (Fig. 4.16) suggests that when there is significant OH at the fuel injector (the apex of the inner conical flame), the rest of the flame shows less OH and vice versa. An alternative interpretation is that when the flame is attached at the corner of the bluff body, it tends to lift from the nozzle. There is a mild peak at 29.3 Hz associated with this motion. Mode 2 shows that when one side lifts-off the corner of the bluff body, the other side tends to remain attached. Mode 3 - 5 show flame features close to the corner; furthermore, Mode 4 shows that the left-right oscillation of the flame near the corner presents no peak in the PSD coefficient. This suggests that the dynamics of the flame pattern presents no stable left-right oscillations. Mode 5 shows the flame pattern regarding

the up-down oscillations with a middle frequency peak at 43.95 Hz. Coming to Flame D1S2, if we compare it to flame D1S1, the mean suggests that the flame is localized farther from the bluff-body; furthermore, the spatial distribution of the OH radical is wider. Modes 1-5 show few component of the fluctuation of the flame. Particularly, Modes 1 and 2 can be associated with the transverse fluctuation of the flame, and Modes 3 and 4 show a anti-symmetric fluctuation along the jet. A strong peak at 43.95 Hz occurs for Mode 1, which is associated with the transverse fluctuation of the flame. Since Mode 1 captures the most amount of energy, this result reveals that the flame D1S2 has a dominant dynamic at 43.95 Hz.

The D1B1 flame remains more attached to the corners of the bluff body (Fig. 4.18). Mode 1 seems similar to the corresponding OH* Mode (Fig. 4.5), showing an increase of OH on one side when the other side has a reduction in OH. A strong peak at 29.3 Hz, similar to D1S1, is associated with this structure. Mode 2 shows an axial movement so that when the flame tends to be lifted from the corners, it remains attached to the nozzle at r=0. Higher Modes (not shown here) show a behaviour characterised by anti-symmetric lift-off (one side remains attached while the other lifts-off) and flame breaks (when the left outer flame has extinction, the right outer flame does not). Mode 2 and 4 show respectively the axial movement of the flame regarding the right and left side of the combustor; since that the Mode 3 is characterized by a frequency peak at 43.95 Hz, this helps to highlight the anti-symmetric behaviour of the flame when the blow-off condition is approached.

The reconstructed snapshots using the mean and Mode 1 only (Figs. 4.13-4.15, middle row) do not reveal the lift-off of the outer flame. However, the reconstructed snapshots using the mean and Modes 1 to 20 (Figs. 4.13-4.15, lower row) reproduce the lift-off. For flame D1B1 in particular, the fragmentation and lift-off seen in the original (Fig. 4.15, upper) is also seen in the reproduction using Modes 1-20
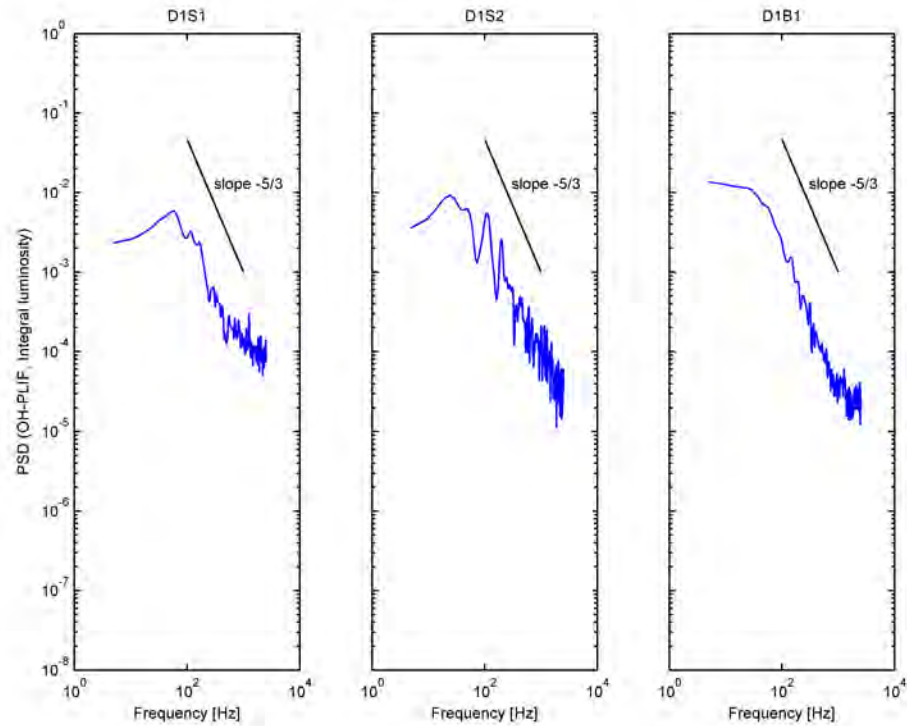
Figure 4.21: Flames of n-decane. PSD of the integral luminosity OH-PLIF.

(Fig. 4.15, lower). Note that it was necessary to include many Modes to achieve a representative reconstruction, due to the broader energy content distribution of the POD Modes in OH-PLIF compared to the OH*. Exploring how many (or which) Modes are needed to reproduce particular features of the OH-PLIF movie can help identify the underlying mechanisms.

Figures 4.21 and 4.22 show respectively the PSD and CSP of the spatial integral of OH-PLIF for the flames D1S1, D1S2 and D1B1. For the flame D1S1, the PSD of the spatial integral OH-PLIF show a strong peak at 58.59 Hz; for flame D1S2, the PSD of spatial integral OH-PLIF signal shows a peak at 24.41 Hz and 117.2 Hz. Conversely, there is no peak in the PSD of the integral OH-PLIF when the blow-off condition is approached. In addition, when the blow-off is approached,
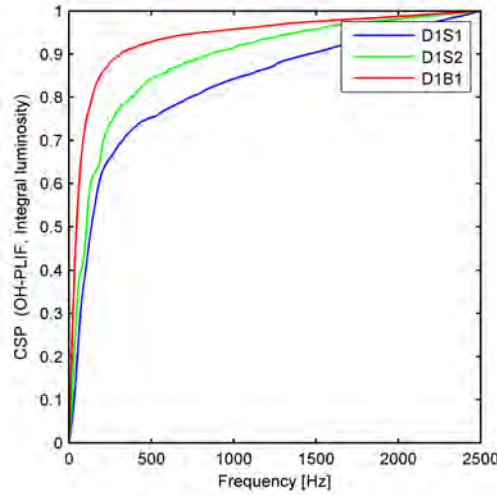
Figure 4.22: Flames of n-decane. CSP of the integral luminosity OH-PLIF.

all PSDs tend to include a portion with -5/3 decay, typical of the spectrum of turbulent energy. Looking at CSP (Fig. 4.22) it is possible to note a clear trend on the operating condition; in particular, the amount of energy captured at low-frequencies increases as blow-off is approached. This result suggests that the blow-off is characterized by slower dynamics. Finally, the analysis suggests that the footprint of extinction in the present n-decane swirl flame, as seen from line-of-sight OH* images, is the emergence of a wedge-shaped reaction zone, with about one half of the flame quenched, that slowly rotates. From the perspective of planar OH-PLIF, global blow-off is manifested by anti-symmetric lift-off from the corners of the bluff-body, and with severe fragmentation of the inner and outer parts of the flame. For OH*, only Mode 1 is sufficient to recover the flame motion before blow-off, whereas OH-PLIF needs about 20 Modes to be properly represented.

4.5.2   n-Dodecane

OH* results.   Figure 4.23 shows the mean image (Mode 0) and first five POD Modes from the OH* for DD1S1. Mode 1 highlights roughly flame features on the left-side, whereas Mode 2 shows roughly the same structure on right-left. Looking at Modes 1 and 2, and considering the POD coefficients and the POD Mode proprieties, it is possible to think that the first two POD Modes represent respectively the main heat release fluctuations along the jet axes. This behaviour is completely different from what observed with D1S1 (n-decane). Looking at Modes 1 and 2 for flames DD1S1 (Fig. 4.23) and DD1S2 (Fig. 4.24), it can be observed strong morphological changes for the two stable operating conditions. Particularly, Mode 1 of flame DD1S2 (Fig. 4.24) shows a rough antisymmetry of the heat release fluctuations about the axis; furthermore, it is possible to say that Mode 1 represents the transverse fluctuations of the flame, whereas Modes 1 and 2 of DD1S1 can be associated to the fluctuations of the flame along the jet axes. Mode 2 of flame DD1S2 (Fig. 4.24) shows features of the flame concerning the up-down fluctuation, which do not appear in the first POD Modes of flame DD1S1. Mode 3 of flame DD1S1 (Fig. 4.24) shows a more complicated feature than first and second Mode. Particularly, Mode 3 shows an asymmetry of the flame turn-over motion from lateral zones to central zone. Modes 4 and 5 (Fig. 4.24) show more complex features than previous Modes. Instead, for flame DD1S2, Mode 3 (Fig. 4.24) shows a clear feature that can be associated with the flame turn-over motion from lateral zones to central zone.

Figure 4.25 shows the mean and the first 5 POD Modes for the operating condition close to blow-off (DD1B1). Particularly, Modes 1 and 2 show both flame pattern that can be associated with the transverse fluctuation of the heat release. Mode 3 shows a flame pattern that can be associated with the turn-over motion of the flame from lateral zones to central zone. Modes 4-5 show more complex
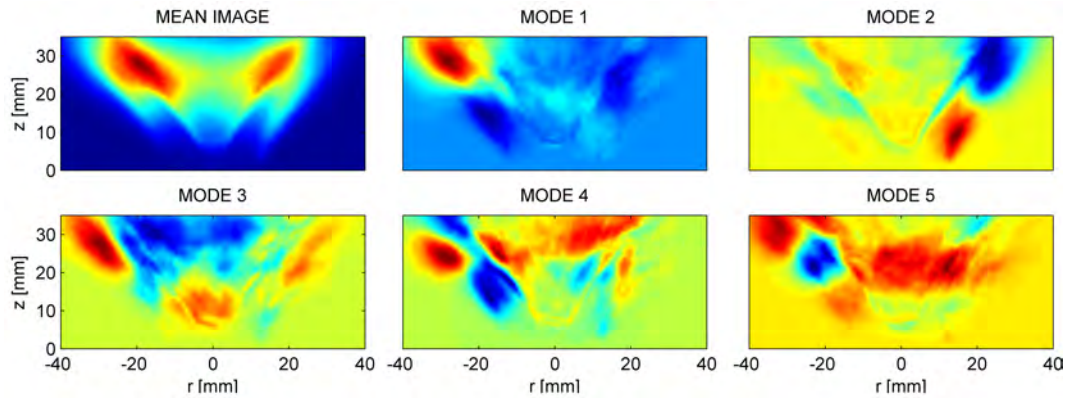
Figure 4.23: Mean image and the first 5 POD Modes from OH*, Flame DD1S1.
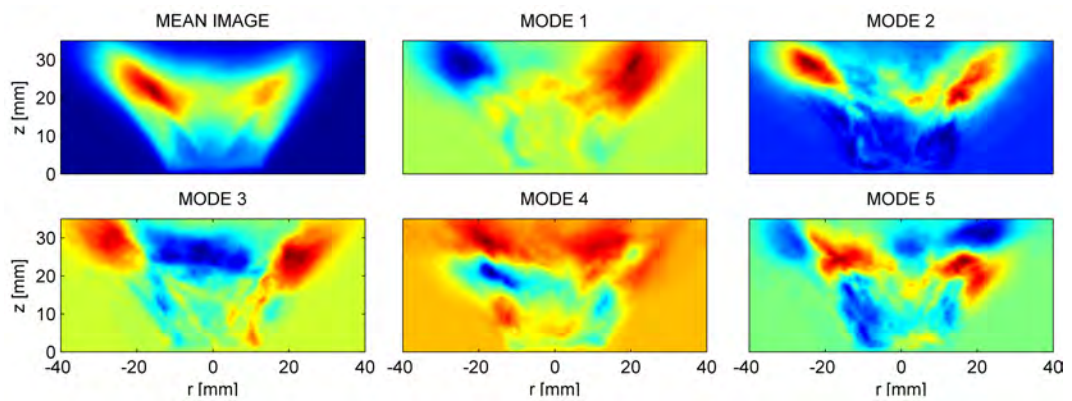
Figure 4.24: Mean image and the first 5 POD Modes from OH*, Flame DD1S2.
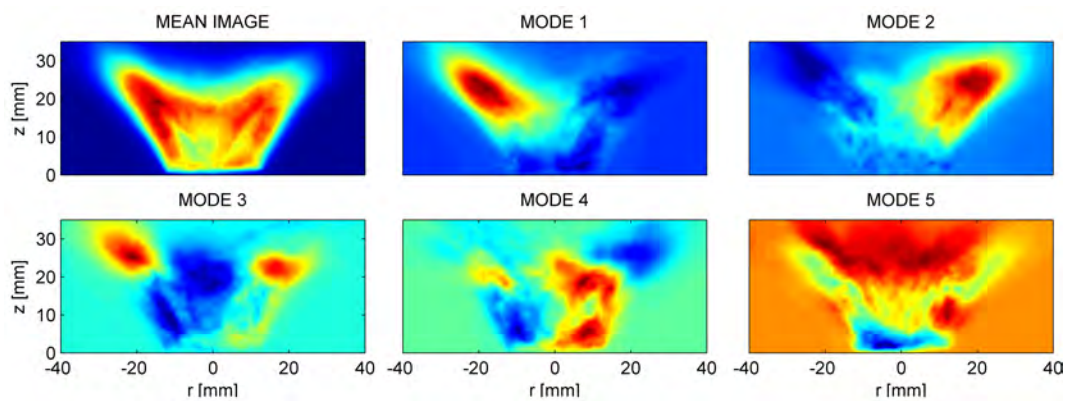
Figure 4.25: Mean image and the first 5 POD Modes from OH*, Flame DD1B1.
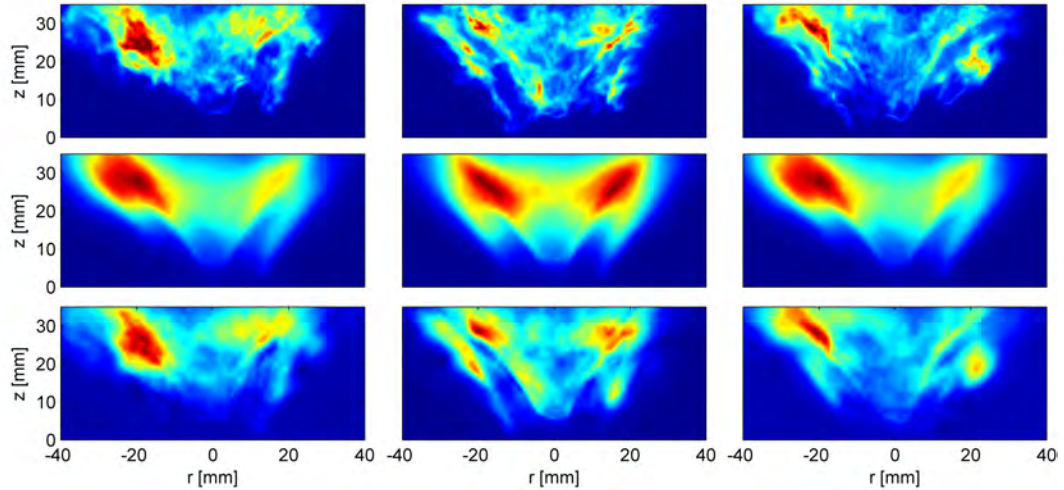
Figure 4.26: Flame DD1S1. (Upper) Snapshots from raw OH* movie. Snapshots at the same times from reconstructed OH* movie using (middle) the mean and Mode 1 only and (lower) the mean and Modes 1 to 5.
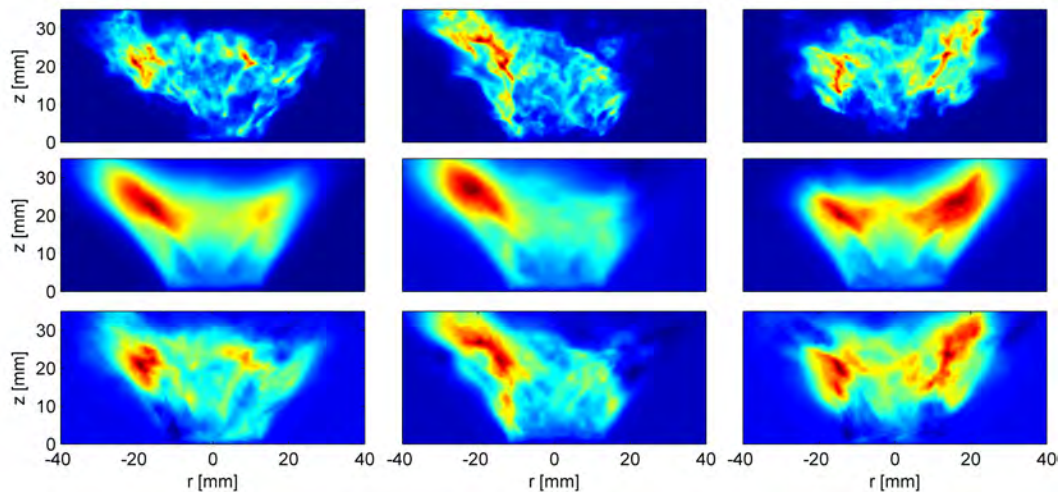
Figure 4.27: Flame DD1S2. (Upper) Snapshots from raw OH* movie. Snapshots at the same times from reconstructed OH* movie using (middle) the mean and Mode 1 only and (lower) the mean and Modes 1 to 5.
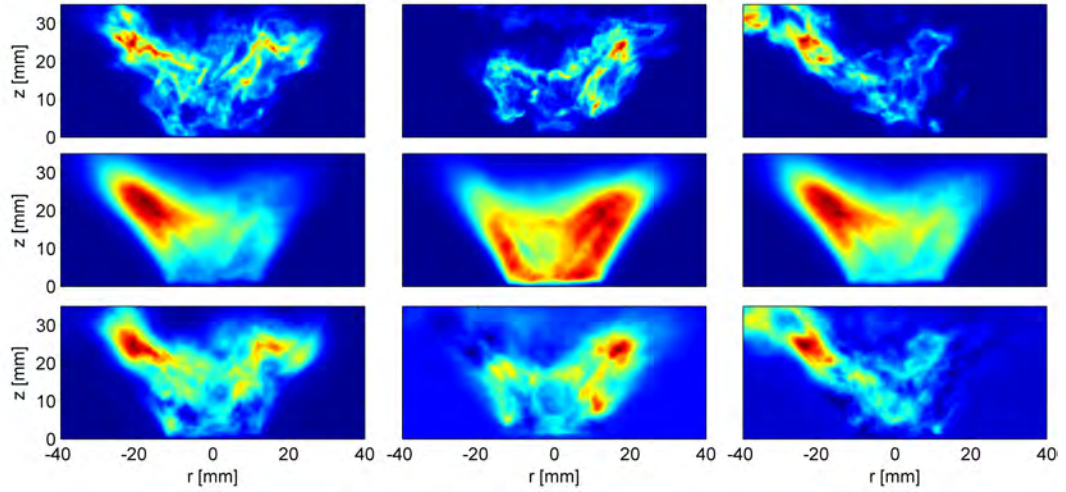
Figure 4.28: Flame DD1B1. (Upper) Snapshots from raw OH* movie. Snapshots at the same times from reconstructed OH* movie using (middle) the mean and Mode 1 only and (lower) the mean and Modes 1 to 5.
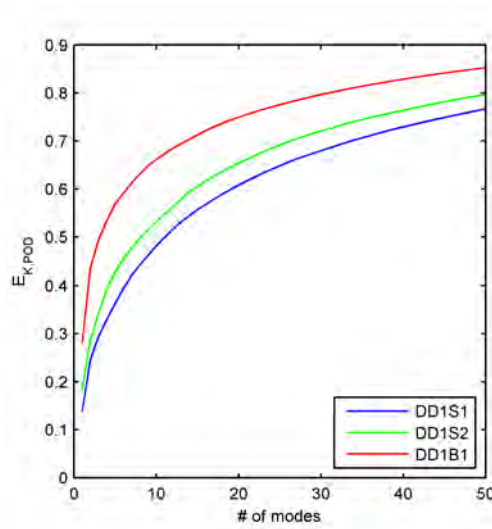
Figure 4.29: Cumulative energy spectrum of the POD Modes of OH* chemiluminescence and OH* for flames of n-dodecane.
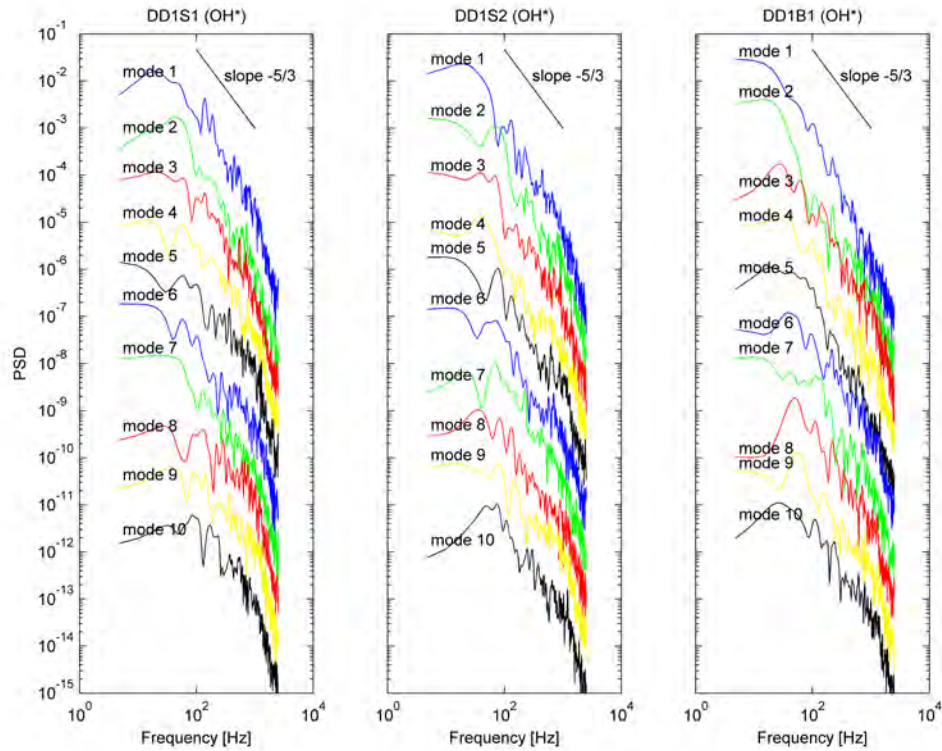
Figure 4.30: Flames of n-dodecane. PSD of POD coefficients from Modes 1 to 10 of OH*.

features. By comparing the first 5 Modes of all operating conditions (Fig 4.23 - 4.25), it is possible to note that Modes 1 and 2 show strong changes of their morphologies as the blow-off is approached. This result indicates the occurrence of a qualitative change in the state of the system (from stable flame to unstable flame).

It is evident that the snapshots reconstructed using the mean and the first POD Mode (Figs 4.26-4.28) allow the filtering of the small scale features, highlighting the zone where the combustion reactions are more present. Focusing on the reconstructed data by using the mean and the first POD Mode (Fig 4.26-4.28, middle rows) for the three flames DD1S1, DD1S2 and DD1B1, it is possible to observe as
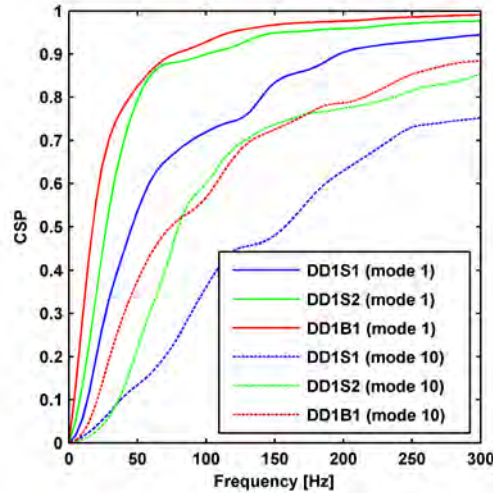
Figure 4.31: Flames of n-decane. CSP of POD coefficients of Modes 1 and 10 of OH*.

the right/left fluctuations are always captured from first Mode. The reconstructions of the same flames made by using the mean and first 20 POD Modes (Fig. 4.26-4.28, bottom rows) show a good description of the morphological features of the flames. Moreover, looking at the mean and the first Mode for each n-dodecane flame, it is possible to observe that the flame becomes more and more compact as the blow-off condition is approached. Identical considerations were obtained for the n-decane flame.

For flame DD1S1, the mean and the fluctuation captured respectively 47% and 53% energy of the overall data-set. Figure 4.29 reports the cumulative energy spectra. It appears that, when the blow-off condition is approached, the energy of the Modes of low order increases. Therefore, the first 50 POD Modes for the operating conditions DD1S1, DD1S2 and DD1B1 have cumulative energy respectively of 76.67%, 79.68% and 85.27%, while the energy captured by first 5 Modes for DD1S1, DD2S2 and DD1B1 are respectively of 36.27%, 42.61% and 56.88%. It is possible to say that there is a trend of the spectrum of cumulative energy
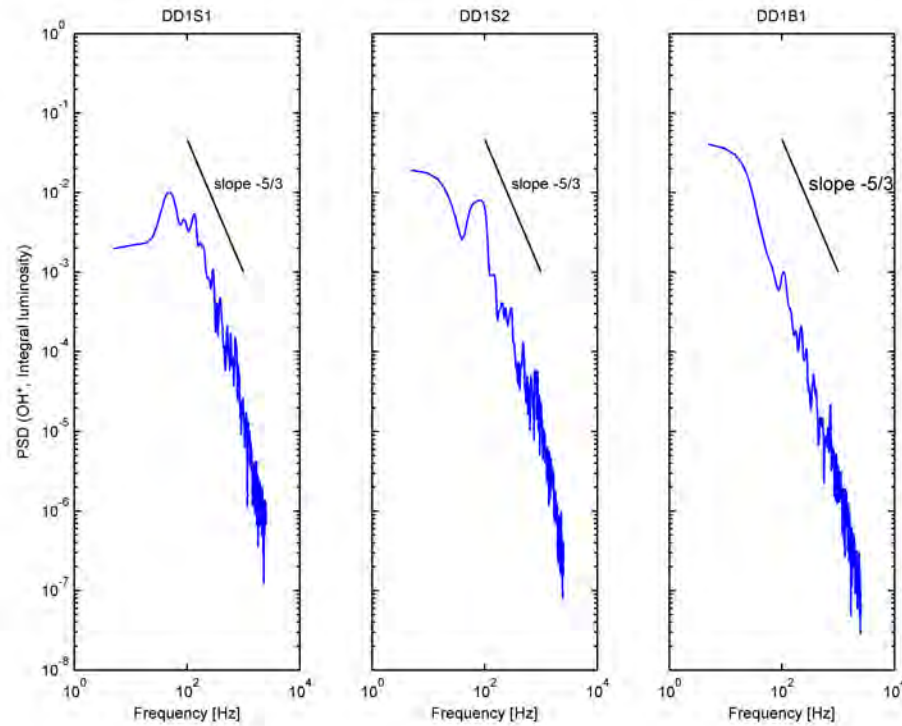
Figure 4.32: Flames of n-dodecane. PSD of the integral luminosity OH*.

when the blow-off condition is approached. This result is in good agreement with that obtained for the n-decane flames. As in the previous case (n-decane flames), Figure 4.30 shows the PSDs for the first 10 normalized POD coefficients (the PSDs were shifted along the y-axis). It can be observed that all PSDs include a portion with a -5/3 decay, typical of the energy spectrum of turbulence. For flame DD1S2, Mode 1 (transverse fluctuation) has a broad peak at 19.53 Hz, Mode 3 (turn-over motion) has a peak at 24.41 Hz; whereas, Mode 2 (axial fluctuation) does not show any relevant peak in the PSD of the coefficient. For flame DD1B1, where a significant part of the flame is quenched (Fig. 4.25), the absence of a peak in the PSD of the coefficient of Mode 1 suggests that there is no strong periodicity associated with this flame motion.
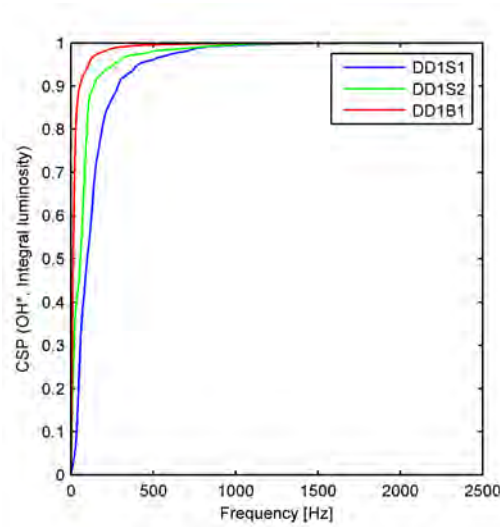
Figure 4.33: Flames of n-dodecane. CSP of the integral luminosity OH*.

Figure 4.31 shows the CSPs (cumulative spectral power) of the POD coefficients of Modes 1 and 10 for all operating conditions. It is evident that the higher the Mode order, the higher the contribution of energy at the high frequencies. Furthermore, it is interesting to see as the CSP of the first Mode, which captures the highest energy, changes when the blow-off condition is approached. Particularly, it is possible to note when the blow-off condition is approached, the energy captured by Mode 1 at low frequencies, increases (Fig. 4.30). This result also suggests that the flame during the blow-off condition is characterized by slower dynamics.

PSDs of the spatial integral OH* for the flames DD1S1 and DD1S2 (Fig. 4.32) show respectively frequency peaks at 48.83 Hz and 83.01 Hz; instead, there is no peak in the PSD of the integral OH* when the blow-off condition is approached. Therefore, it can be thought that such change is due to a qualitative change in the state of the system. Furthermore, it is possible to highlight as the CSP of the integral OH* (Fig. 4.33) shows a trend on the operating condition similar to that reported from the CSP of the first POD Mode (Fig. 4.31). Once more, this result confirms that the operating condition close to blow-off is characterized by slower

dynamics.

OH-PLIF results.   Figure 4.34 shows the mean image (Mode 0) and first five POD Modes from the OH-PLIF for DD1S2. Mode 1 suggests that when the flame is attached to the corner of the bluff body, it tends to lift from the nozzle. Besides, Mode 1 suggests also the component in phase between up/down and left right oscillations. Mode 2 can be associated to transverse oscillations of the flame. In addition, Mode 2 shows that when one side lifts-off the corner of the bluff body, the other side tends to remain attached. Mode 3 may be interpreted as the component of the flame motion from the lateral zones to the central zone. Modes 4 and 5 show a pattern more complex than previous, but it is possible to see that they still include some information about the transverse oscillation of the flame. Figure 4.35 shows the mean component (Mode 0, constant in time) and the first 5 POD Modes for the flame DD1B1. Comparing the mean component of the flames DD1S2 and DD1B1, it is possible to say that when the blow-off condition is approached, the reactive zone is closer to the bluff-body. This component provides no information about the dynamics of the flame and its own possible characteristic patterns. Modes 1 and 2 can be associated with the transverse (left/right) oscillation of the flame, respectively far and close to the bluff-body. Mode 4 can be associated with the turnover of the flame from a central zone to lateral zones. Modes 3 and 5 show more complex features.

The POD energy spectrum for the PLIF images (Fig. 4.38) shows that a larger number of Modes is needed to capture the same percentage of energy than for OH*, and that the flames are smaller. Moreover, it is important to note that it is needed to include many Modes to achieve a representative reconstruction due to the broader energy content distribution of the POD Modes in OH-PLIF
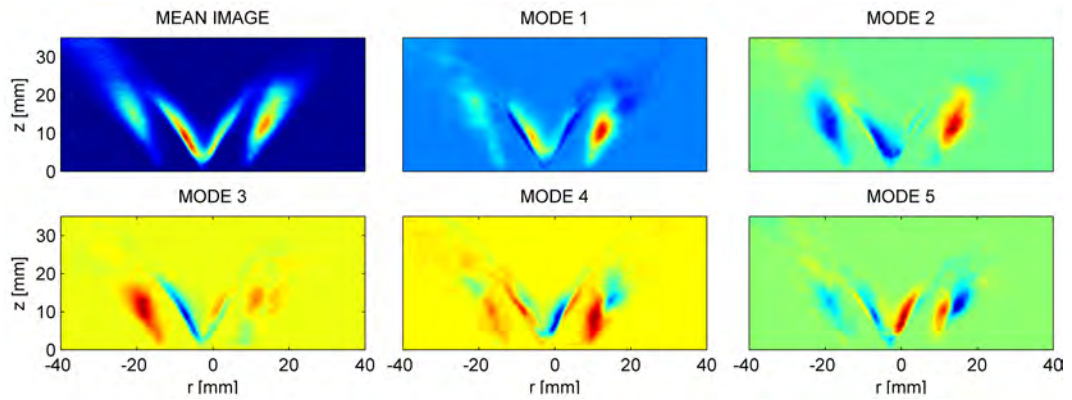
Figure 4.34: Mean image and the first 5 POD Modes from OH-PLIF, Flame DD1S2.
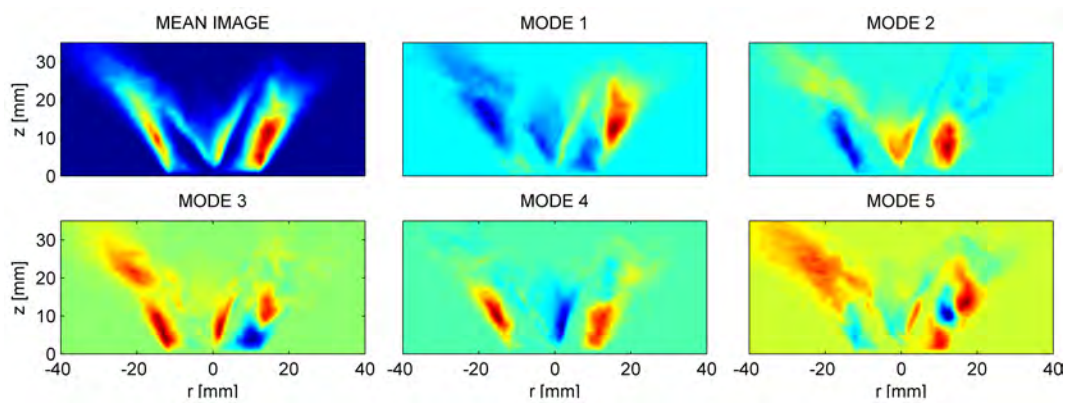
Figure 4.35: Mean image and the first 5 POD Modes from OH-PLIF, Flame DD1B1.
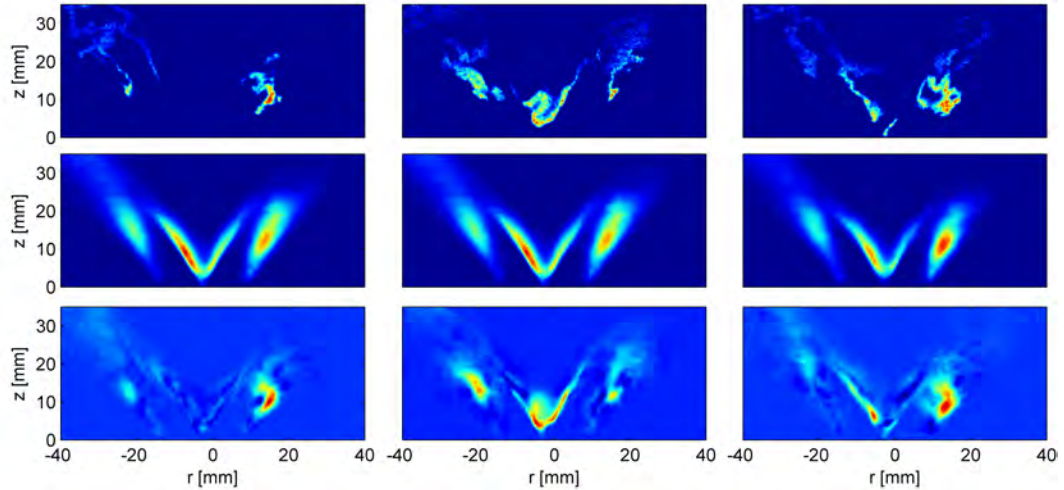
Figure 4.36: Flame DD1S2. (Upper) Snapshots from raw OH-PLIF movie. Snapshots at the same times from reconstructed OH* movie using (middle) the mean and Mode 1 only and (lower) the mean and Modes 1 to 20.
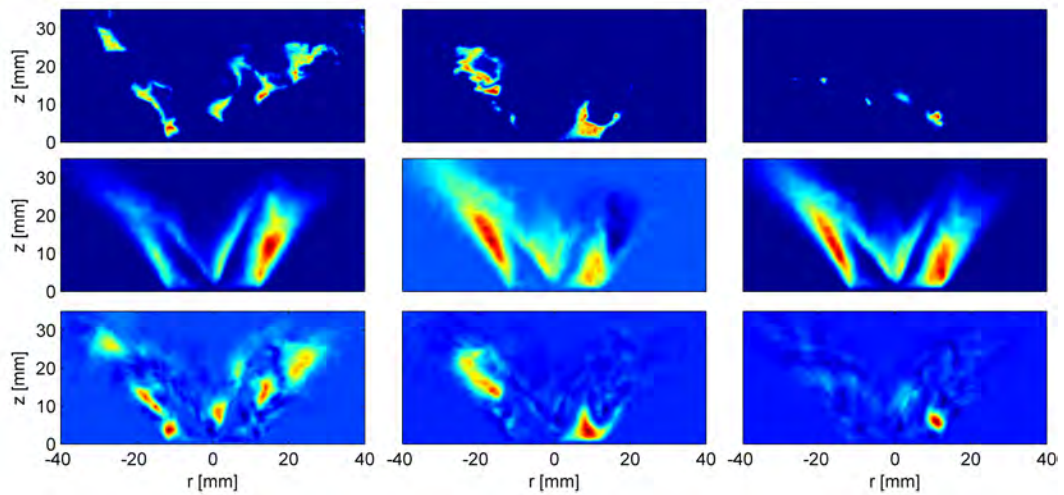
Figure 4.37: Flame DD1S2. (Upper) Snapshots from raw OH-PLIF movie. Snapshots at the same times from reconstructed OH* movie using (middle) the mean and Mode 1 only and (lower) the mean and Modes 1 to 20.
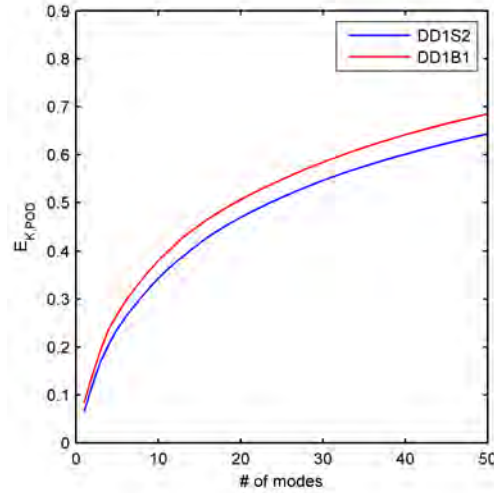
Figure 4.38: Cumulative energy spectrum of the POD Modes of OH-PLIF chemiluminescence.

compared to the OH*. Exploring how many (or which) Modes are needed to reproduce particular features of the OH-PLIF movie can help identify the underlying mechanisms. Figures 4.36 and 4.58 show, respectively for the flames DD1S2 and DD1B1, few snapshots of the OH-PLIF signal of the detected images (upper row), reconstructed images using the mean and the first POD Mode (middle row) and reconstructed images using the mean and the first 50 Modes POD (bottom row). It is possible to see as the first POD Modes capture the features of the large scales. It is possible to note that the energy spectrum of the POD Modes has a clear trend when the blow-off condition is approached; namely, the percentage of energy captured by first POD Modes for the operating condition close to blow-off condition (DD1B1) is higher than for the operating condition far from blow-off. This result suggests that POD can be used to develop a detector of the occurrence of blow-off conditions.

Figure 4.39 shows the PSD of the normalized first 10 POD coefficients (the PSDs were shifted along the y-axis) include a portion with a -5/3 decay, typical of the
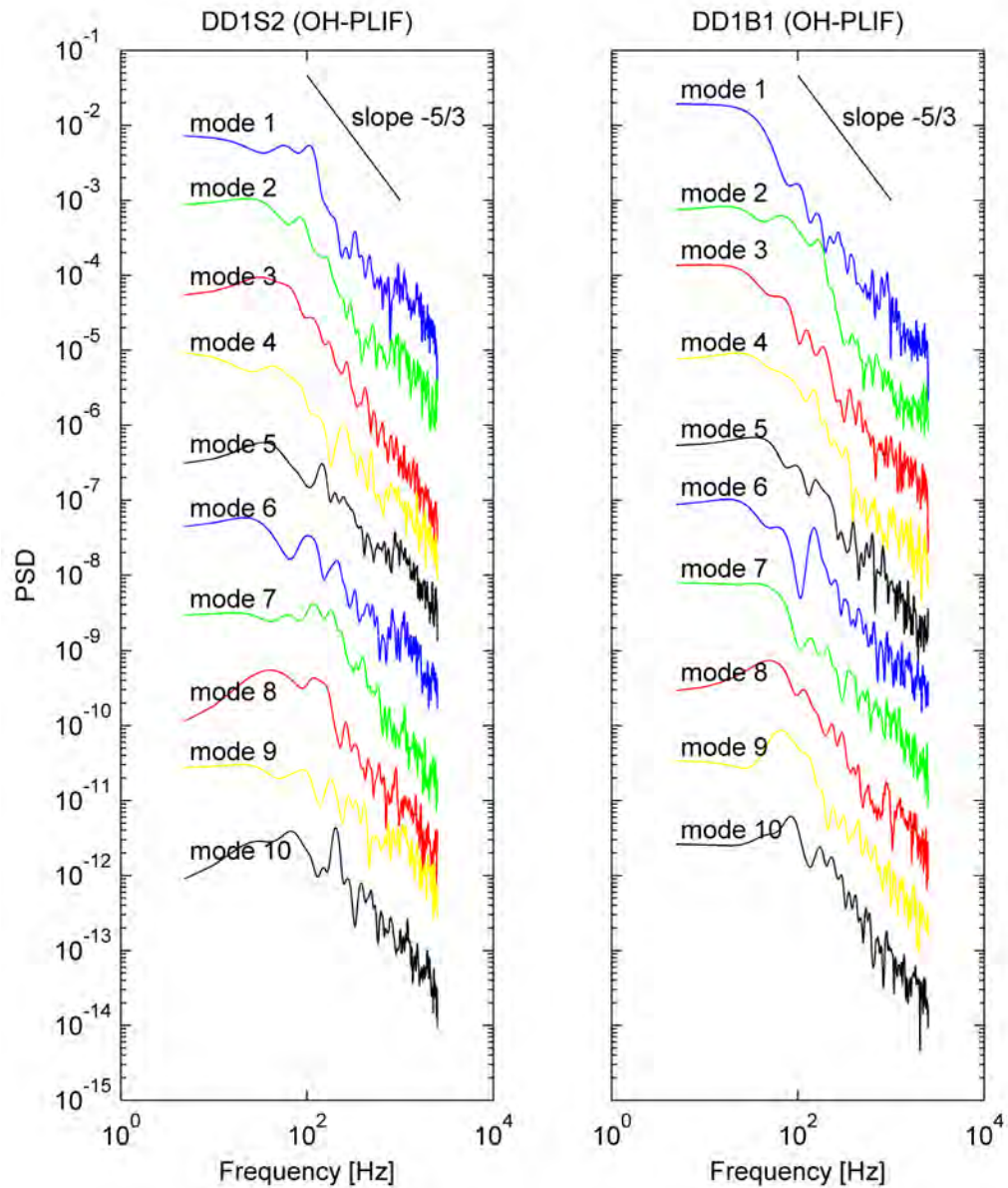
Figure 4.39: Flames of n-dodecane. PSD of POD coefficients from Modes 1 to 10 of OH-PLIF.

energy spectrum of turbulence, and the OH-PLIF shows a sharper drop-off after about 1 kHz (Fig. 4.39). For flame DD1S1, Mode 1 shows no dominant peak,
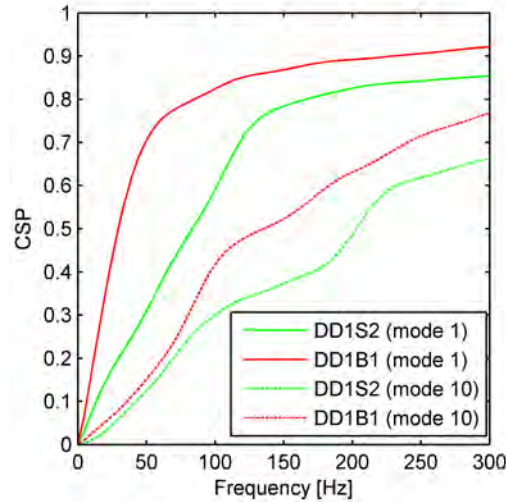
Figure 4.40: Flames of n-dodecane. CSP of POD coefficients of Modes 1 and 10 of OH-PLIF.

whereas Mode 2 shows a strong peak at 19.53 Hz. Recalling that the second POD Mode was associated with the left/right fluctuation of the flame, it is possible to say that such fluctuation is characterized by a dominant frequency around 19.53 Hz. For flame DD1B1, Mode 1 presents a strong peak at 24.41 Hz, and Mode 2 shows strong peaks at 19.53 Hz and 63.48 Hz. Since the morphology of Modes 1 and 2 can be associated with transverse oscillations respectively far and close to bluff-body, it is possible to say that the dynamics of the transverse motion "far" from the bluff-body presents a dominant frequency at 24.41 Hz. Instead, the transverse motion of the flame "close" to bluff-body presents two characteristic frequencies at 19.53 Hz and 63.48 Hz. As previously mentioned, Mode 4 can be associated with the turnover of the flame from a central zone to lateral zones. Figure 4.40 shows the CSP of the normalized POD coefficients regarding Modes 1 and 10 for flames DD1S2 (far from blow-off) and DD1B1 (close to blow-off). As for the OH* signal, there is a clear trend of both Modes 1 and 10 when the condition of blow-off is approached; in particular, when the blow-off condition is approached,

the percentage of energy captured by the low frequencies increases. Moreover, the same considerations made for the OH* data can be made here: namely, the condition close to blow-off is characterized by a slower dynamics than it is far from blow-off.

4.5.3   Ethanol

OH* results   Figures 4.41-4.43 show respectively the mean component and the first 5 POD Modes from the OH* of E1S1, E1S2 and E1B1. Observing the mean components of the three flames (E1S1, E1S2 and E1B1), it can be noted that the flame is closer and closer to bluff-body when the operating condition is closer and closer to blow-off condition. This result is in good agreement with that obtained byCavaliere et al. (2013). Looking at Modes 1 for the flames E1S1 and E1S2 respectively in the Figs. 4.41 and 4.42, it is possible to say that they draw flame patterns that can be associated with the transverse fluctuation of the heat release. Instead, Mode 1 of the flame E1B1 (Fig. 4.43), which represents the operating condition close to blow-off, can be associated to the axial fluctuation (up-down fluctuation) of the heat release. Thus, when the operating condition approaches to blow-off condition, the morphology described by the first POD Mode changes strongly; namely, the first POD Mode can be associated to transverse fluctuations of the flame during the operating conditions far from the blow-off condition; whereas, when the blow-off condition is approached, Mode 1 is associated to the axial fluctuation. Since the first POD Mode captures the biggest energy, it is possible to think that the operating conditions far from blow-off are dominated by transverse fluctuations of the heat release, whereas the operating conditions close to blow-off are dominated by axial (up-down) fluctuation of the heat release. Modes 2 of E1S1 (Fig. 4.41) and E1S2 (Fig. 4.42) both represent a flame pattern that can be associated to the axial fluctuation of the heat release; whereas, Mode 2
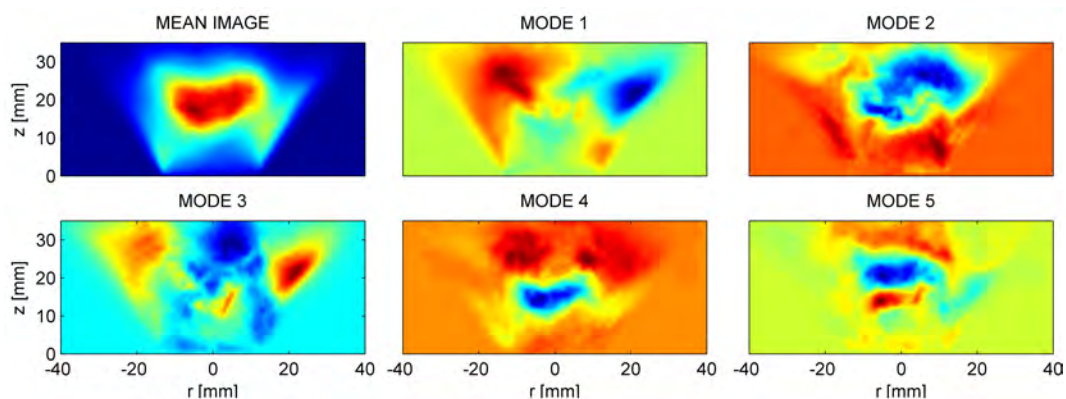
Figure 4.41: Mean image and the first 5 POD Modes from OH*, Flame E1S1.
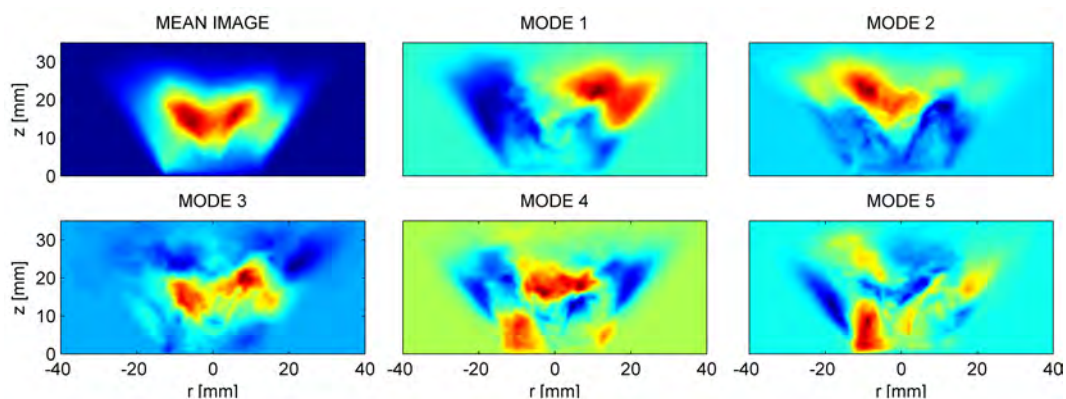
Figure 4.42: Mean image and the first 5 POD Modes from OH*, Flame E1S2.

of E1B1 (Fig. 4.44) represents a flame pattern which identifies the transverse fluctuation of the heat release. Therefore, when the operating condition approaches to blow-off, the morphological features of the fluctuation of the heat release changes from a pattern describing the axial fluctuation to another describing the transverse fluctuation of the heat release.

Looking at the POD modes of S1 (Fig. 4.41), it can be possible to say that Mode 3 shows a flame pattern that can be associated to the turnover of the flame from a central zone, which is related to a compact flame, to lateral zones, which are related to flames localized along the spray. Mode 4 shows another pattern that
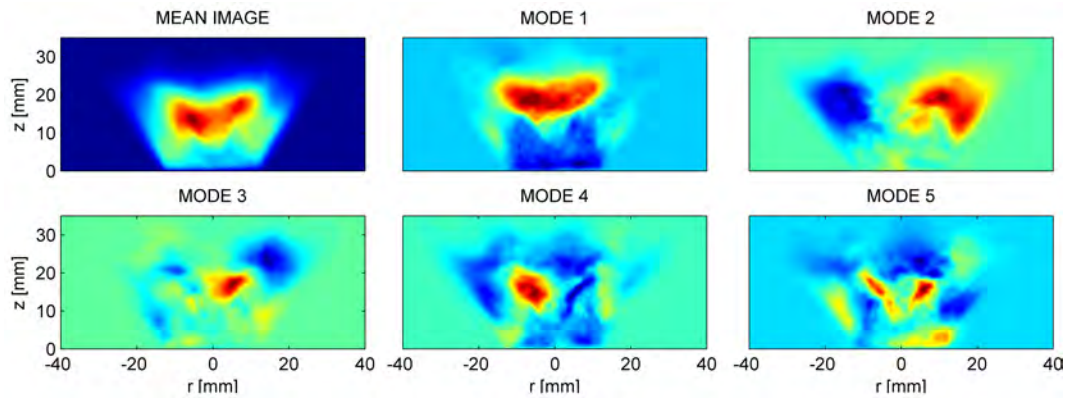
Figure 4.43: Mean image and the first 5 POD modes from OH*, Flame E1B1.
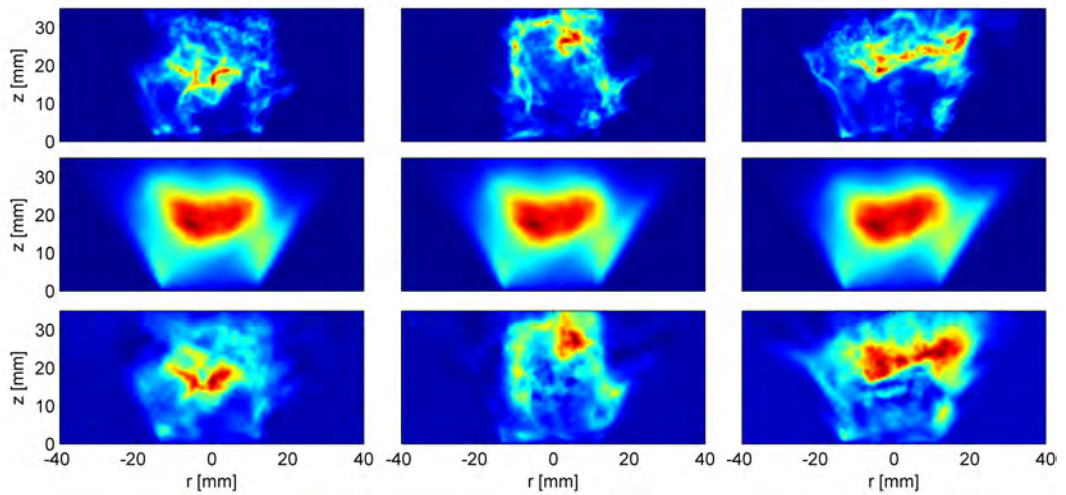
Figure 4.44: Flame E1S1. (Upper) Snapshots from raw OH* movie. Snapshots at the same times from reconstructed OH* movie using (middle) the mean and mode 1 only and (lower) the mean and modes 1 to 5.
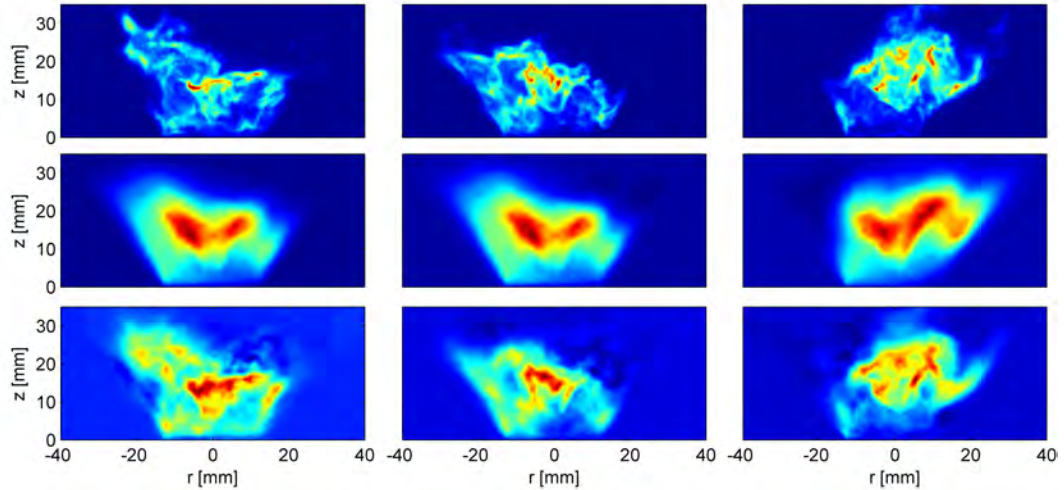
Figure 4.45: Flame E1S2. (Upper) Snapshots from raw OH* movie. Snapshots at the same times from reconstructed OH* movie using (middle) the mean and mode 1 only and (lower) the mean and modes 1 to 5.
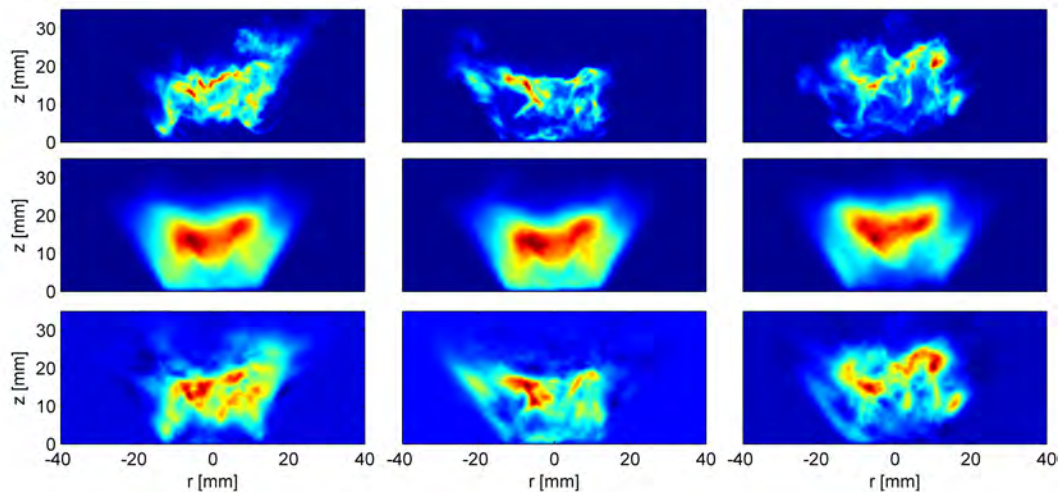
Figure 4.46: Flame E1B1. (Upper) Snapshots from raw OH* movie. Snapshots at the same times from reconstructed OH* movie using (middle) the mean and mode 1 only and (lower) the mean and modes 1 to 5.
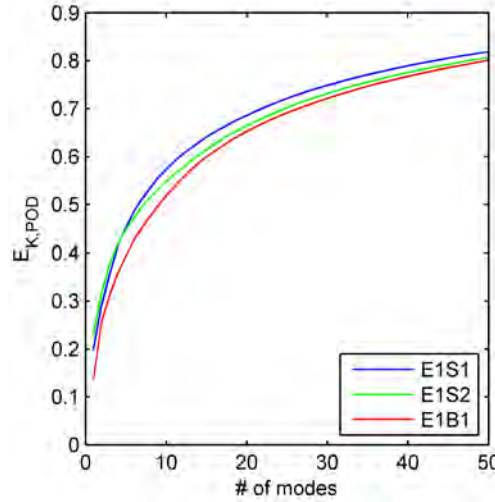
Figure 4.47: Cumulative energy spectrum of the POD modes of OH* chemilumi-nescence and OH-PLIF for flames of ethanol.

can be associated to the up/down fluctuation of the heat release. Mode 5 shows a feature that can be associated to effect of the convective flux on the flame pattern. In addition, Mode 5 is characterized by length scale smaller than in the previous modes: this is due to fact that the energies captured by the large scales is higher than the corresponding for small scales. Looking at Mode 3 of E1S2 (Fig. 4.42), it is possible to make the same considerations made for Mode 4 of E1S2; namely, it is possible to associate this mode to the axial (up-down) fluctuation of the heat release. Mode 4 of E1S2 can be associated with the turnover of the flame from a central zone to lateral zones, similarly to Mode 3 of E1S1. Mode 5 represents a more complex feature with respect to the previous modes, and by a a lower amount of energy captured. Looking at Modes 3-5 of E1B1 (Fig. 4.43), it is possible to highlight no feature that can be associated to any particular physical phenomena, because that modes are characterized by features that are morphologically too complex.

Similarly to the previous fuels analysed, it is possible to note as the dominant

structures cannot be easily seen from the raw OH* images (Figs 4.44-4.46), due to the overlying of the small-scale fluctuations. Nevertheless, they are shown in reconstructed snapshots with image mean (Mode 0; constant in time) and first POD mode (middle row), and with the first 5 POD Modes (lower row). Once more, it is noted as the reconstruction of the snapshots by using the first POD modes allows the filtering of the small scale features, highlighting the zones where the combustion reactions are more present. Looking at the reconstructed data using the mean and first POD mode for three flames E1S1, E1S2 and E1B1, it is possible to note as the more reactive zones are captured by the mean component and first 5 Modes. Moreover, it is possible to observe as the reconstructed snapshots with the mean component and only first POD Mode highlight the reactive zone that becomes more and more compact, while the operating condition is closer and closer to blow-off.

Figure 4.47 reports the cumulative energy spectra. It appears that, when the blow-off condition is approached, the energy captured by the low order Modes increases. In fact, the first 50 most energetic POD modes for the operating conditions E1S1, E1S2 and E1B1 capture 81.92%, 80.72% and 80.11% respectively of the total energy. Although the cumulative energy captured by the first 50 POD modes are roughly similar, it can observed a clear trend between the cumulative energy spectrum, $E_{K,POD}$, and the operating condition; in particular, when the blow-off is approached, the energy captured by the first modes increases. It is remarked that this trend is opposite to that shown for the flames of n-decane and n-dodecane.

Figure 4.48 reports the PSDs of the first 10 POD coefficients for the flames E1S1, E1S2 and E1B12. It is possible to see once more that the PSDs of the POD coefficients include a portion with a -5/3 decay, typical of the inertial range of the energy turbulence spectrum. For flame E1S1 (stable operating condition), the
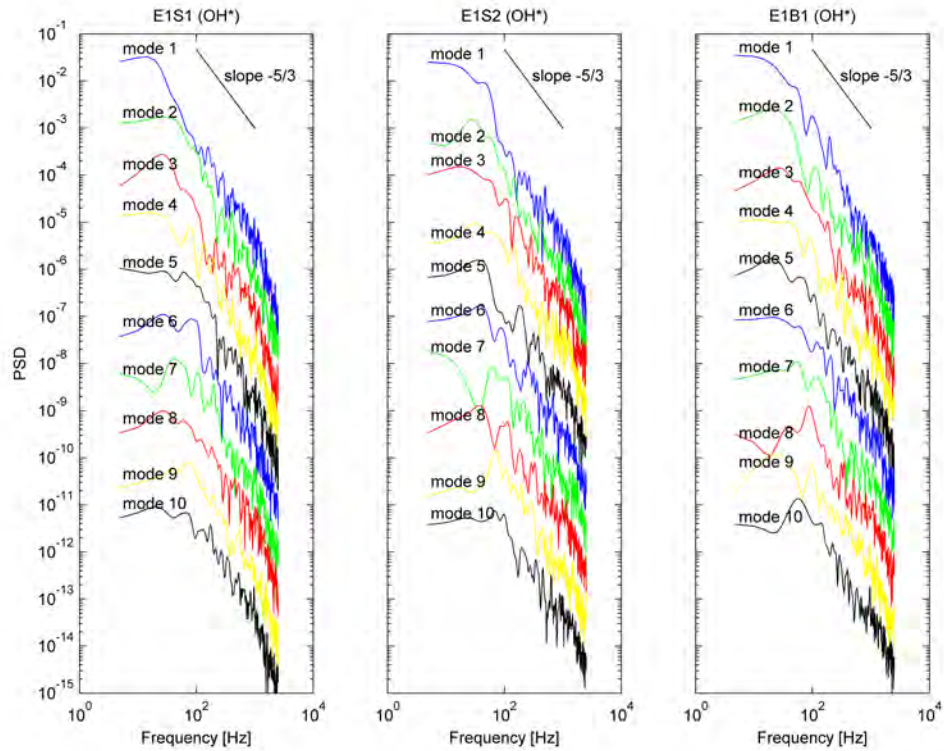
Figure 4.48: Flames of ethanol. PSD of POD coefficients from modes 1 to 10 of OH*.

first 3 modes show dominant peaks respectively at 14.65 Hz, 34.18 Hz and 24.41 Hz. Since that the first and second Modes can be associated respectively with the left/right and up/down oscillations of the flame, it is possible to say that the up/down (axial) and left/right (transverse) oscillations are characterized by dominant frequencies respectively at 14.65 Hz and 34.18 Hz. For flame E1S2, the first Mode shows no dominant peaks in its PSD. The cut-off frequency is about 100 Hz. Since the first Mode of E1S2 can be associated with the transverse fluctuation of the flame, it is possible to conclude that the transverse fluctuation is characterized by frequencies lower than 100 Hz. The PSDs concerning modes 2 and 4 (of E1S2) both show a dominant peak at 29.3 Hz. Since modes 2 and 4 can be associated
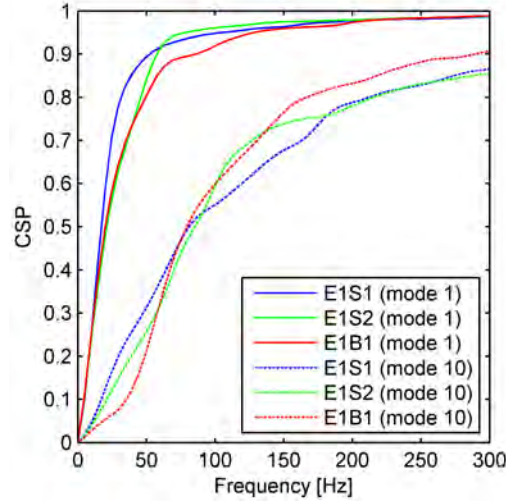
Figure 4.49: Flames of ethanol. CSP of POD coefficients of modes 1 and 10 of OH*.

respectively with the axial fluctuation and the turn-over of the flame, we may say that both dynamic behaviours have the same characteristic frequency at 29.3 Hz. For flame E1B1 (close to blow-off), Mode 1 shows no dominant peak and a cut-off frequency of about 29.3 Hz, which is associated with the axial fluctuation of the heat release rate. Mode 2, which was associated with the transverse fluctuation, shows a peak at 19.53 Hz with a broad band. Hence, the transverse and axial fluctuations become respectively slower and faster when the blow-off is approached. Besides, for flame E1S1 and E1S2, the turn-over feature is characterized by frequency peaks respectively at 24.41 Hz and 29.3 Hz. Instead, for flame E1B1 (close to blow-off), no feature was found to be connected to the flame turn-over motion from central zone to lateral zones. This can suggest that, during blow-off, the flame is fragmented into small reactive zones close to the bluff-body.

Figure 4.49 shows the normalized CSPs (cumulative spectral power) of the POD coefficients of the Modes 1 and 10 for all types of flames. Once more, it is evident that the higher the Mode order, the higher the contribution of energy at the high
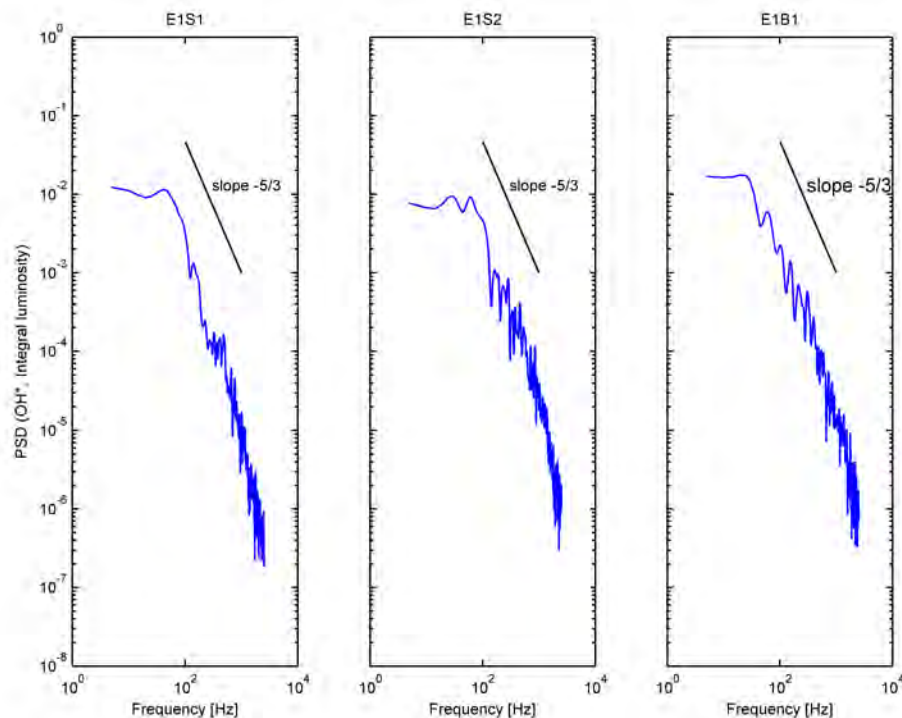
Figure 4.50: Flames of ethanol. PSDs of the integral luminosity OH*.

frequencies. Besides, it is interesting to note that the energy captured at the low frequencies by Mode 1 (which captures the largest overall energy) decreases (Figure 4.49) as the blow-off condition is approached. Hence, it can be thought that the flame approaching blow-off is characterized by faster dynamics.

Figures 4.50 and 4.51 report the PSDs and CSPs respectively for the spatial integral OH* signal for flames E1S1, E1S2 and E1B1. PSDs of integral OH* show one peak at 43.95 Hz for E1S1, two peaks at 29.3 Hz and 58.6 Hz (second harmonic) for E1S2, and no peak for the operating condition close to blow-off. Therefore, blowoff is announced by a distinct qualitative change in the combustion process. In contrast with the CSP of Mode 1, no trend between the CSP of the spatial integral OH* and the operating condition is observed.
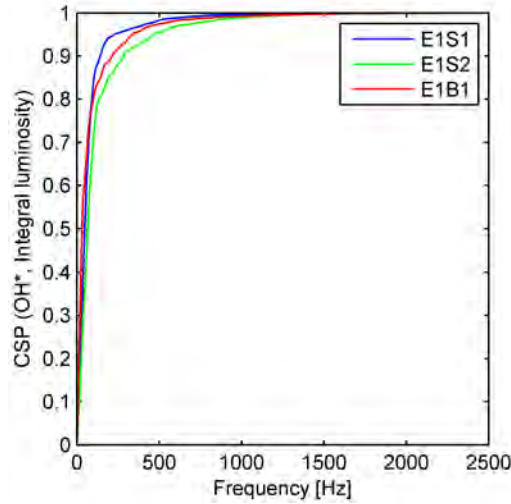
Figure 4.51: Flames of ethanol. CSPs of the integral luminosity OH*.

Finally, it is worth noting that all trends found for the ethanol flame are opposite to those found for n-decane and n-dodecane flames. This result might be due to the lower volatility of the ethanol that influences the mixing and the dynamics of the combustion, but further studies are necessary to better elucidate the relevant mechanism.

OH-PLIF results. Figures 4.52-4.54 show the mean component and the first 5 POD Modes from the OH-PLIF of E1S1, E1S2 and E1B1 respectively. Focusing on the mean components of the three flames (E1S1, E1S2 and E1B1), it can be noted that, when the operating condition is approaching blow-off condition, the flame is closer and closer to the bluff-body. Furthermore, the flame size decreases when the flow condition is approaching blow-off. This result is in agreement with that obtained previously, although less marked.

For flame E1S1 (Fig. 4.52), Mode 1 shows a pattern that can be associated with the transversal oscillation of the flame. Modes 2 - 5 shows pattern more complicated
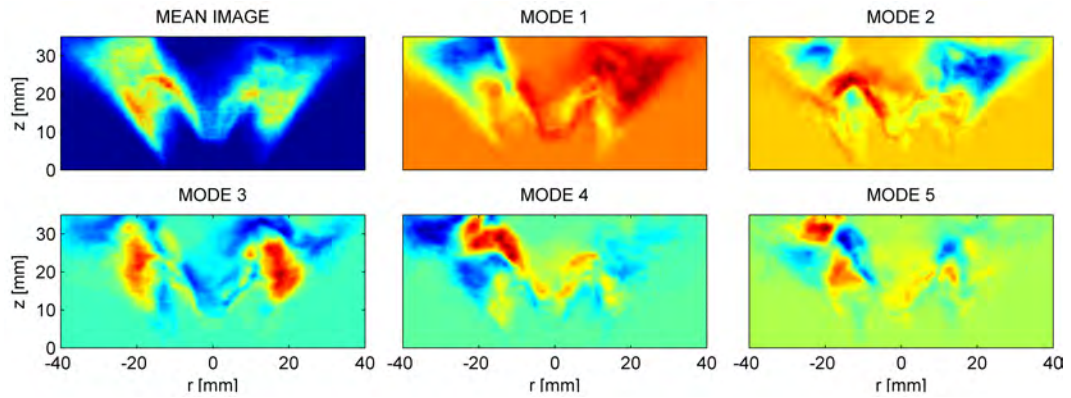
Figure 4.52: Mean image and the first 5 POD modes from OH-PLIF, Flame E1S1.

that cannot be associated with any clearly identifiable phenomena. Regarding flame E1S2 (Fig. 4.53), Mode 1 highlights a feature that can be associated with the lateral reactive zone localized on left-side; Mode 2 shows the dominant component of the transversal oscillation. Modes 3-5 shows more complex features than previous Modes, but it can be possible to see some feature along the jet axis. Finally for flame E1B1 (Fig. 4.54), Modes 1 and 2 can be associated respectively with transverse and axial oscillations of the fluctuation of the OH-PLIF field. Modes 3-5 show patterns more complex than previous, hard to identify. Once more, by comparing the mean components of E1S1, E1S2 and E1B1, it can be possible to note that the mean component becomes more and more symmetric when the operating condition is closer and closer to blow-off.

Figures 4.55-4.57 show, respectively for flames E1S1, E1S2 and E1B1, few snapshots from the raw PLIF-OH movie (top row) and the corresponding POD reconstructions obtained using the mean and first 5 POD Modes (middle row), and the mean and first 20 POD Modes (bottom row). As in the previous cases, POD is able to extract the dominant features. Obviously, the reconstruction obtained using the mean component and first 20 POD Modes provides more details on the morphology of the flame than the reconstruction obtained using the mean and first
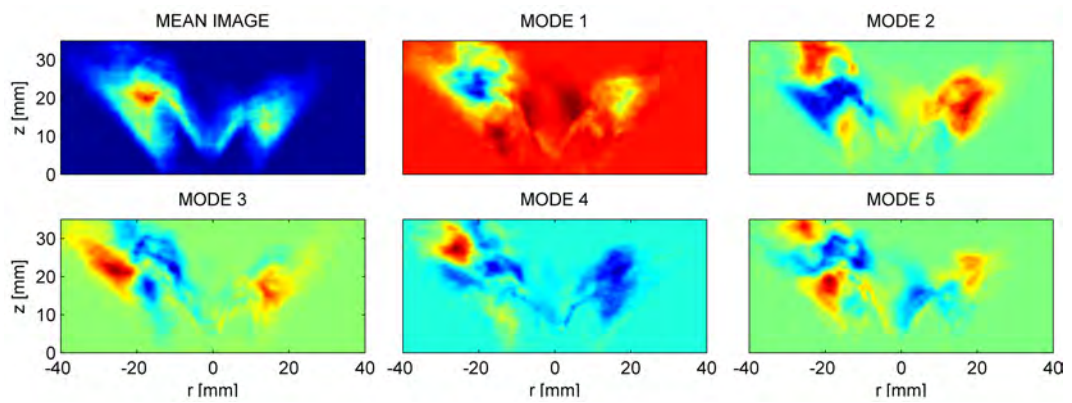
Figure 4.53: Mean image and the first 5 POD modes from OH-PLIF, Flame E1S2.
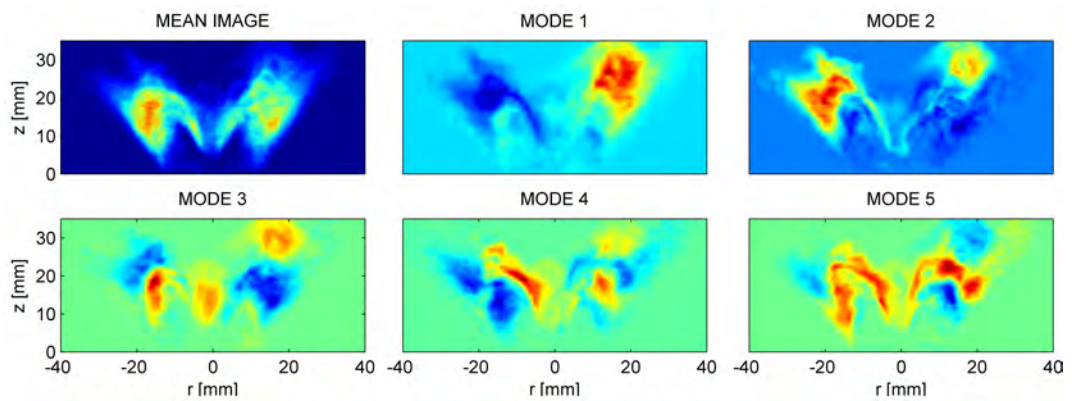
Figure 4.54: Mean image and the first 5 POD modes from OH-PLIF, Flame E1B1.
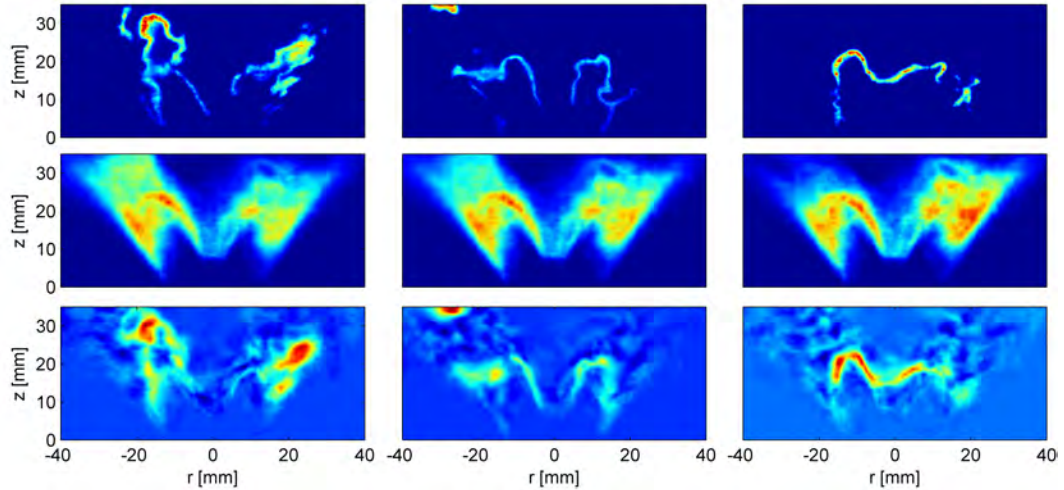
Figure 4.55: Flame E1S1. (Upper) Snapshots from raw OH-PLIF movie. Snapshots at the same times from reconstructed OH* movie using (middle) the mean and mode 1 only and (lower) the mean and modes 1 to 20.
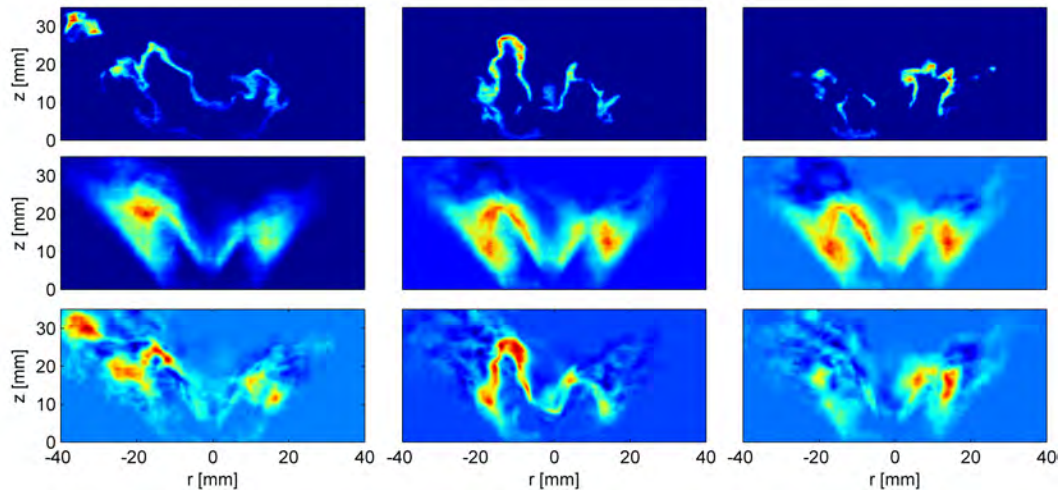
Figure 4.56: Flame E1S2. (Upper) Snapshots from raw OH-PLIF movie. Snapshots at the same times from reconstructed OH* movie using (middle) the mean and mode 1 only and (lower) the mean and modes 1 to 20.
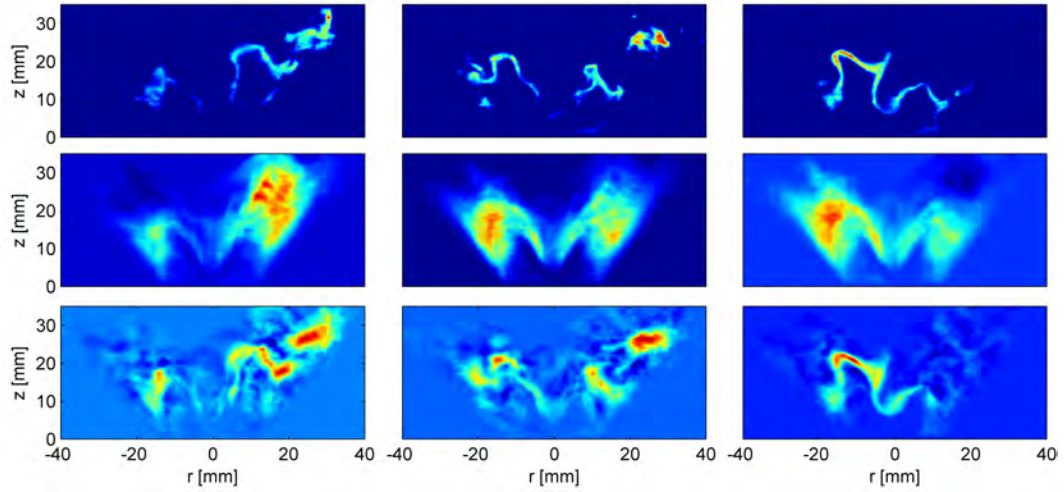
Figure 4.57: Flame E1B1. (Upper) Snapshots from raw OH-PLIF movie. Snapshots at the same times from reconstructed OH* movie using (middle) the mean and mode 1 only and (lower) the mean and modes 1 to 20.
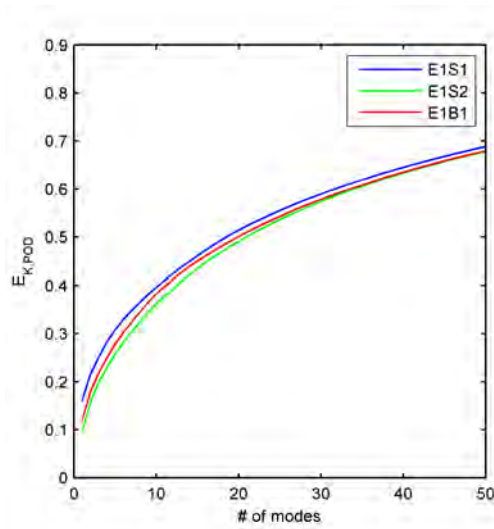
Figure 4.58: Cumulative energy spectrum of the POD modes of OH-PLIF. Flames of ethanol.
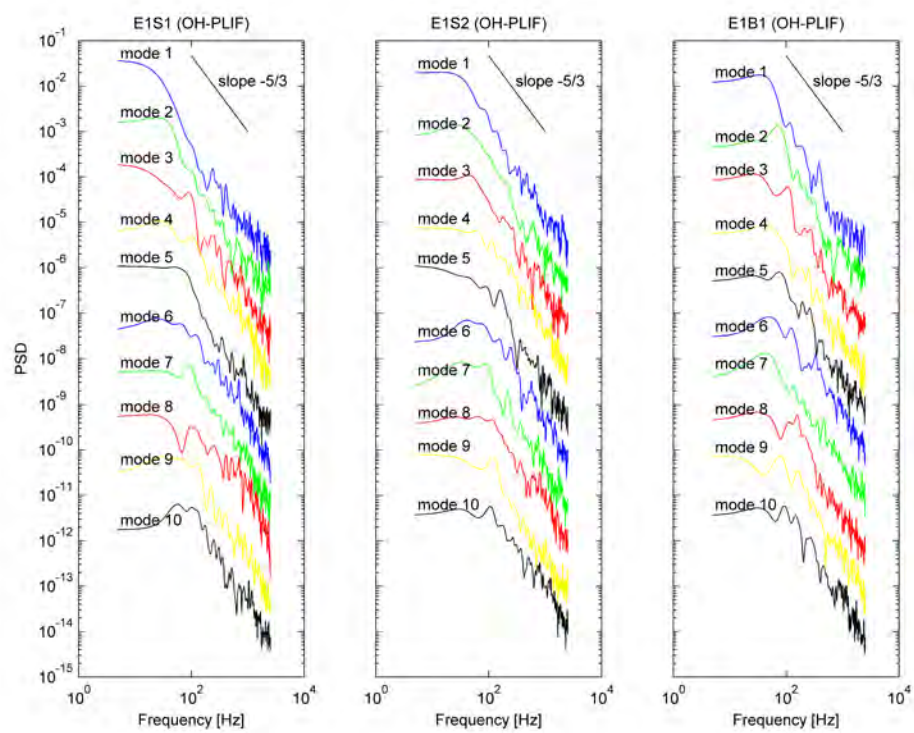
Figure 4.59: Flames of ethanol. PSD of POD coefficients from modes 1 to 10 of OH-PLIF.
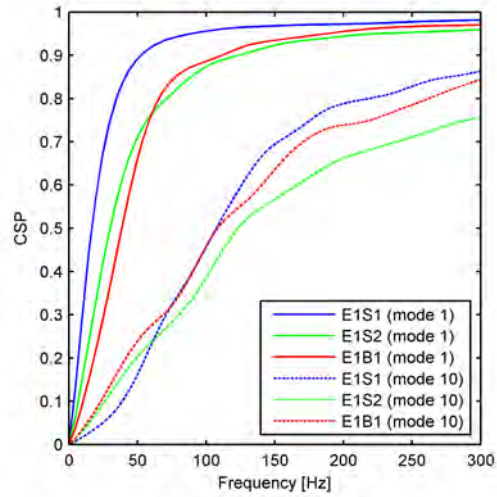
Figure 4.60: Flames of ethanol. CSP of POD coefficients of modes 1 and 10 of OH-PLIF.
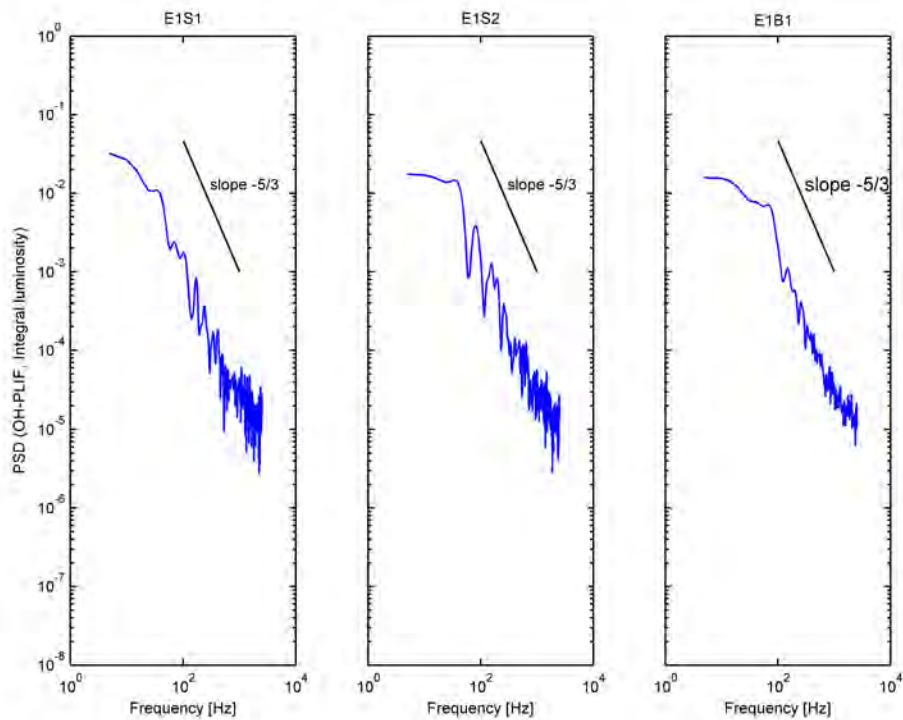
Figure 4.61: Flames of ethanol. PSD of the integral luminosity OH-PLIF.
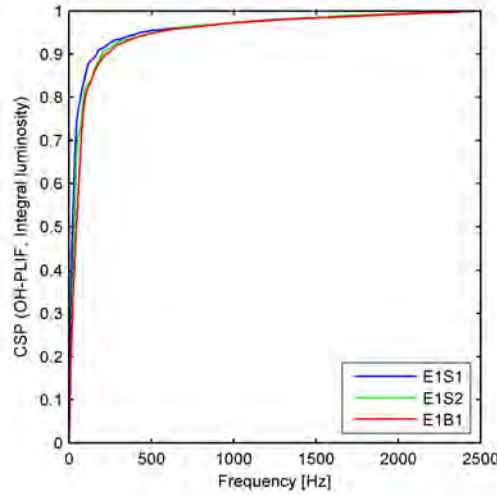
Figure 4.62: Flames of ethanol. CSP of the integral luminosity OH-PLIF.

5 POD Modes.

Figure 4.58 reports the cumulative energy spectra (Eq. (4.5)) for all operating conditions. It is interesting to highlight that no clear trend can be observed between the cumulative energy spectra and the corresponding operating conditions. The cumulative energy spectra for the flames of ethanol are roughly similar.

As in the previously cases, the PSDs (Fig. 4.59) of the first normalized 10 POD coefficients (the PSDs were shifted along the y-axis) include a portion with a -5/3 decay, typical of the energy spectrum of turbulence. It is possible to see that the bandwidth of the first POD is wider and wider when the operating condition is closer and closer to blow-off. In addition, the PSD of Mode 1 shows a peak (100 Hz) only for the blow-off (E1B1). Mode 2 shows bandwidth behaviour similar to Mode 1, but its PSD shows dominant peaks in every operating conditions analysed. Particularly, the PSD of Mode 2 shows dominant peaks at 24.41 Hz, 29.3 Hz and 73.24 Hz, for flames E1S1, E1S2 and E1B1 respectively. Besides, it is possible to highlight that the highest peak of the PSD of Mode 2 occurs during the operating condition close to blow-off. This suggests that the flame is characterized by

periodic fluctuations before its extinction.

Figure 4.60 shows the normalized CSP of the coefficients of Modes 1 and 10 for the flame E1S1, E1S2 and E1B1. It is possible to note that a clear trend between the CSP of Mode 1 and operating condition is shown for frequencies lower than 60 Hz. This result suggests that the dynamics of the flame becomes faster and faster when the operating condition is approaching blow-off.

Furthermore, Figure 4.60 shows clearly that the higher the POD Mode order, the higher the contribution of energy at high frequencies. Consequently, this suggests that they may be associated with the fast components of the flame pattern. Figure 4.61 and 4.62 show the PSDs and CSPs of the integral luminosity of the OH-PLIF signal for the flames E1S1, E1S2 and E1B1. The PSD of the integral OH-PLIF show no dominant peak for all flames, instead it is possible to note that the cut-off frequency increases when the operating condition approaches blow-off: this may be due to the faster dynamics. Furthermore, it is possible to see that the CSP of the integral OH-PLIF follows the same trend of the CSP of the first POD Mode when the blow-off condition is approached. Hence, it is possible to say that the blow-off is characterized from faster dynamics than the stable operating conditions. Finally, both results obtained from the PSD and CSP analysis are in agreement with those obtained from the analysis carried on the OH* data.

4.5.4   n-Heptane

OH* results.   Figures 4.63-4.65 show respectively the mean component and the first 5 POD Modes from the OH* of H1S1, H1S2 and H1B1. Observing the mean components of the three flames (H1S1, H1S2 and H1B1), it can be noted that the flame is closer and closer to bluff-body when the operating condition is closer and closer to blow-off condition. It is evident that this behaviour is similar to that of

flame analysed in the previous sections.

Looking at Modes 1 for the flames H1S1, H1S2 and H1B1, it is possible to note that they draw flame patterns that can be associated with the transverse fluctuation of the heat release rate. Thus, the feature associated with Mode 1 does not change when the operating condition is approaching blow-off. Modes 2 and 4 for flame H1S1 (Fig. 4.63) can be associated with the axial fluctuation of the flame. Mode 3 can be associated with the turn-over of the flame from a central zone to lateral zones. Mode 5 shows a pattern more complex than previous, mainly due to the interaction between turbulent small scales and the flame front. For flame H1S2 (Fig. 4.64), Mode 2 shows a pattern that can be associated with the turn-over motion of the flame from a central zone to lateral zones; Modes 3-5 can be associated with the components of the axial fluctuation of the flame. For flame H1B1 (Fig. 4.65), Modes 2, 4 and 5 show different patterns that can be associated with the different components of the axial fluctuation of the flame; instead, Mode 3 can be associated with the turn-over of the flame from a central zone to lateral zones. By comparing the results obtained for flame H1S1, H1S2 and H1B1, it is evident when the operating condition approaches blow-off (H1B1), it is possible to observe a morphologic change of the first 5 POD Modes. Nevertheless, it is necessary to highlight that such change is less marked than with the fuels analysed in previous sections. Figures 4.66-4.68 report respectively for flames H1S1, H1S2 and H1B1, three snapshots from raw data (upper row) and the corresponding POD reconstructions obtained using the mean component and first 1 POD Modes (middle row), and using the mean component and first 5 POD Modes (lower row). It is possible to note once again how POD is a useful technique in order to filter the small-scale features, consequently it allows to highlight the dominant features of the flame.

Figure 68 shows the cumulative energy spectra captured by the POD Modes
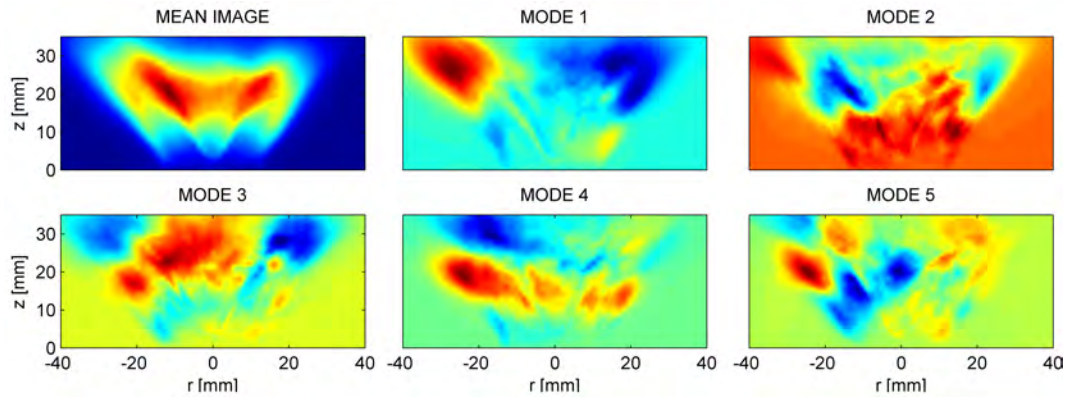
Figure 4.63: Mean image and the first 5 POD Modes from OH*, Flame H1S1.
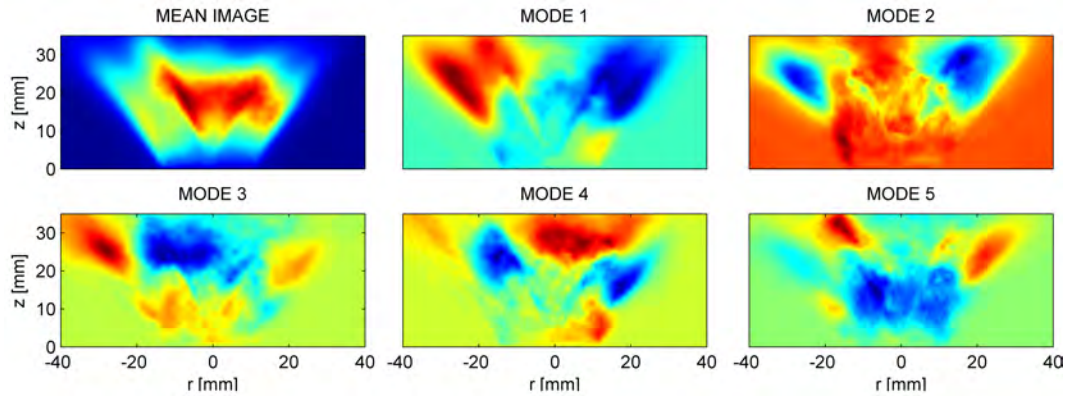
Figure 4.64: Mean image and the first 5 POD Modes from OH*, Flame H1S2.

for flames H1S1, H1S2 and H1B1. It is interesting to note that a clear trend exists between cumulative energy spectrum and the operating condition. In other words, when the operating condition approaches blow-off, the energy captured by low order Modes increases.

Figure 4.70 shows the PSDs of the normalized POD coefficients for H1S1, H1S2 and H1B1. As in the previous cases, the PSDs of the POD coefficients show a range with slope -5/3 [dB/decade], that is typical of the turbulent energy spectrum. Looking at the PSD of the coefficient of the first POD Mode, it is possible to observe that no dominant peak (dominant frequency) occurs for any operating
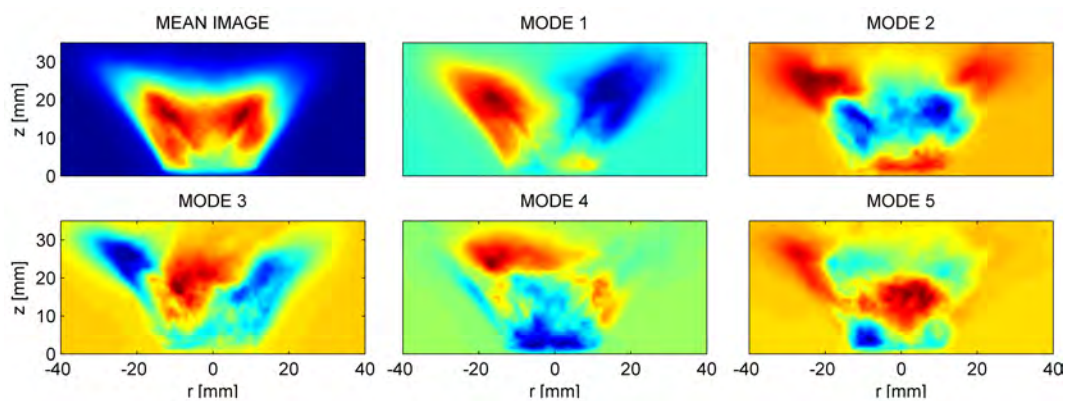
Figure 4.65: Mean image and the first 5 POD Modes from OH*, Flame H1B1.
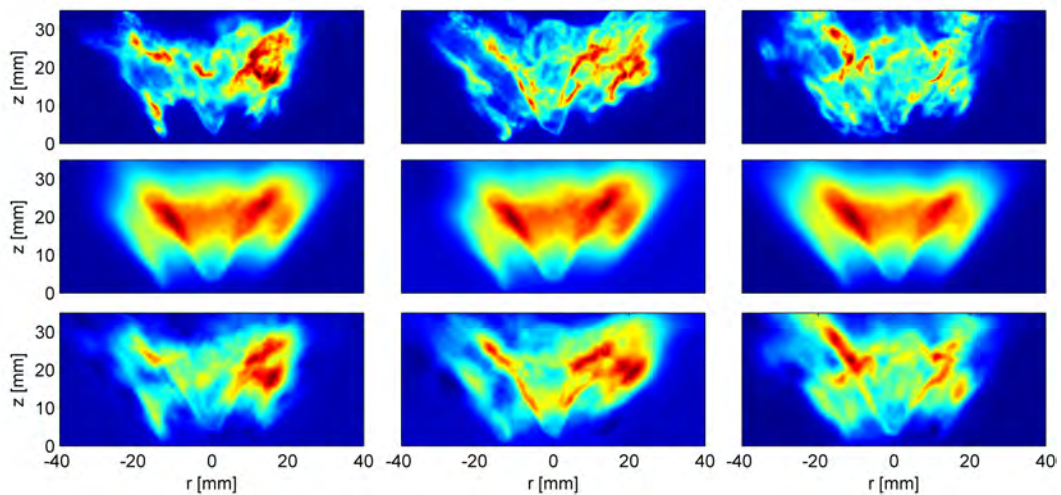
Figure 4.66: Flame H1S1. (Upper) Snapshots from raw OH* movie. Snapshots at the same times from reconstructed OH* movie using (middle) the mean and Mode 1 only and (lower) the mean and Modes 1 to 5.
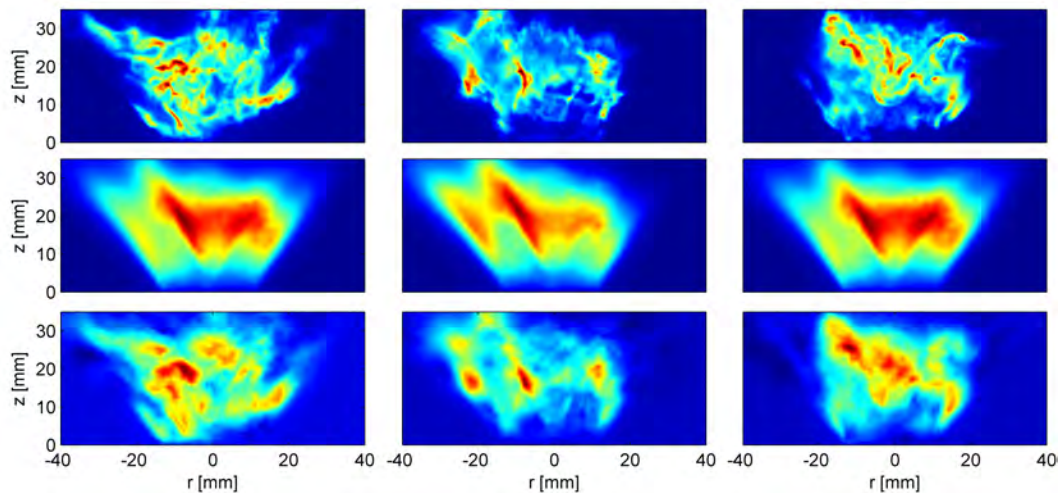
Figure 4.67: Flame H1S2. (Upper) Snapshots from raw OH* movie. Snapshots at the same times from reconstructed OH* movie using (middle) the mean and Mode 1 only and (lower) the mean and Modes 1 to 5.
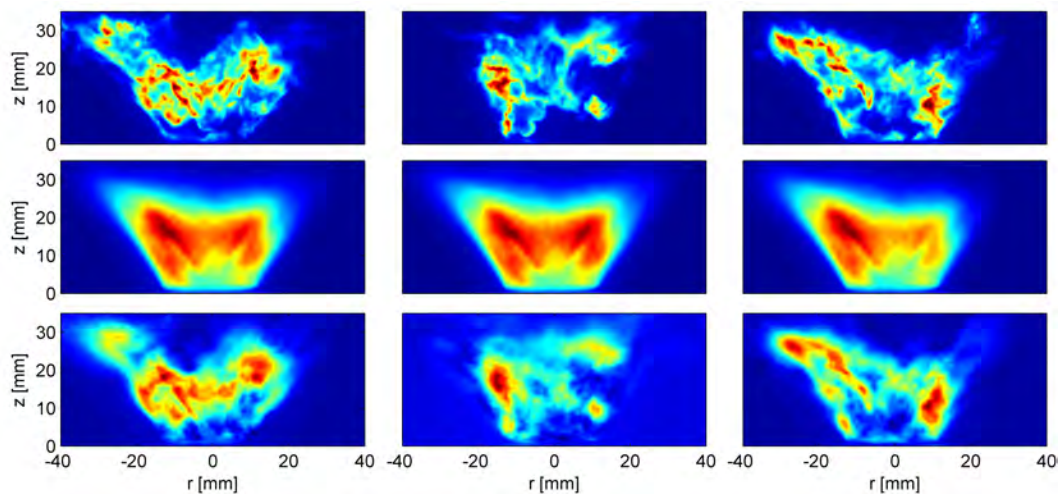
Figure 4.68: Flame H1B1. (Upper) Snapshots from raw OH* movie. Snapshots at the same times from reconstructed OH* movie using (middle) the mean and Mode 1 only and (lower) the mean and Modes 1 to 5.
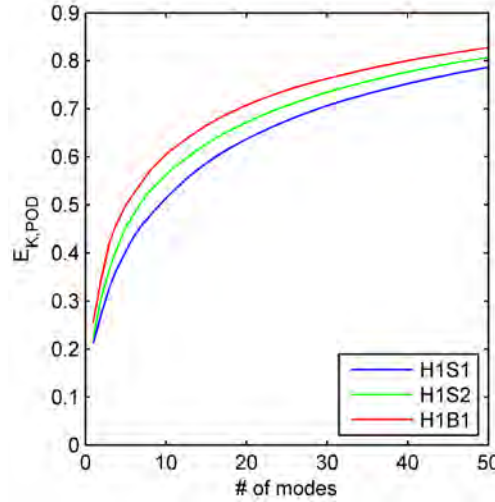
Figure 4.69: Cumulative energy spectrum of the POD Modes of OH* chemiluminescence and OH-PLIF for flames of n-heptane.

conditions analysed. In addition, it is possible to note that the cut-off frequency increases when the operating condition is approaching blow-off. Reminding that Mode 1 has been associated with the transverse fluctuation for all operating conditions analysed, it is possible to say that the axial fluctuation have a frequency band lower than 100 Hz. For flame H1S1, the PSD of the coefficient of Mode 2, which was associated with axial fluctuation, shows a strong peak at 53.71 Hz and a weak peak at 107.4 Hz (first harmonic of 53.71 Hz). Both Modes 3 and 5 show a dominant frequency at 34.18 Hz. Since Modes 3 and 5 were associated with the turn-over motion of the flame, it is possible to say that such phenomena presents a dominant frequency at 34.18 Hz. For the flame H1S2, Modes 2 and 4 show dominant peaks respectively at 39.06 Hz and 53.71 Hz. Since both Modes 2 and 4 can be associated with the axial (up/down) fluctuation, it is possible to say that such fluctuations are characterized by dominant frequencies at 39.06 Hz and 53.71 Hz. For flame H1B1 (operating condition close to blow-off), the frequency analysis of the POD coefficients highlights as Mode 2 shows no dominant peak in frequency,
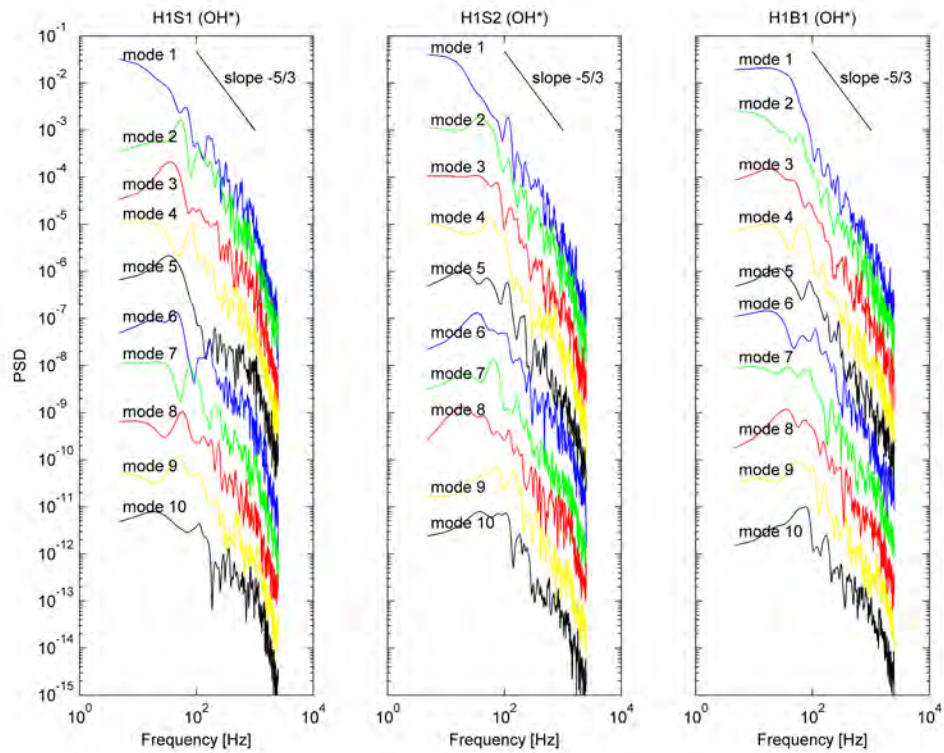
Figure 4.70: Flames of heptane. PSD of POD coefficients from Modes 1 to 10 of OH*.

Mode 3 shows a weak peak at 19.53 Hz, Mode 4 shows two peaks at 14.65 Hz and 63.48 Hz, and Mode 5 shows two peaks at 29.3 Hz and 87.9 Hz (third harmonic of 29.3 Hz). Since Mode 4 can be associated with the axial fluctuation of the heat release, it is possible to say that the dynamic of such fluctuation is characterized by dominant frequencies of 14.65 Hz and its third harmonic. Since Mode 3 can be associated with the flame turn-over from central zone to lateral zones, it is possible to say that such phenomenon is characterized by dominant frequency at 19.53 Hz. Figure 4.71 shows the CSPs of the normalized POD coefficients of Modes 1 and 10 for flames H1S1, H1S2 and H1B1. Once more, it is evident that the higher the Mode order, the higher is the contribution of energy at the high frequencies. Look-
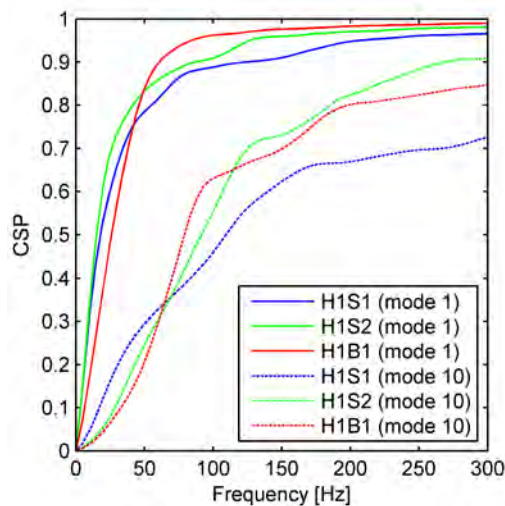
Figure 4.71: Flames of heptane. CSP of POD coefficients of Modes 1 and 10 of OH*.
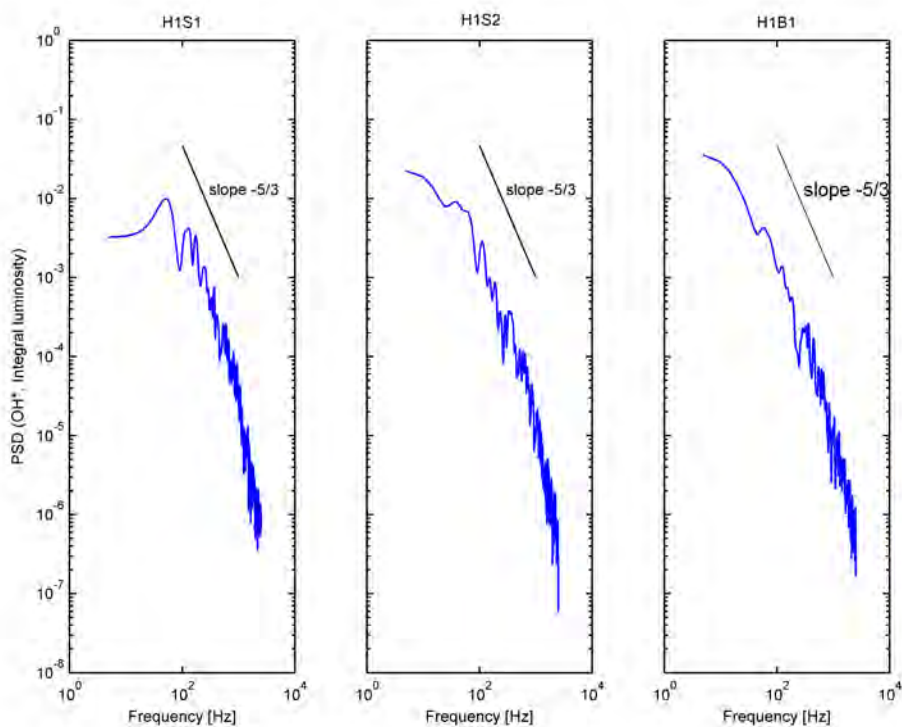
Figure 4.72: Flames of heptane. PSDs of the integral luminosity OH*.
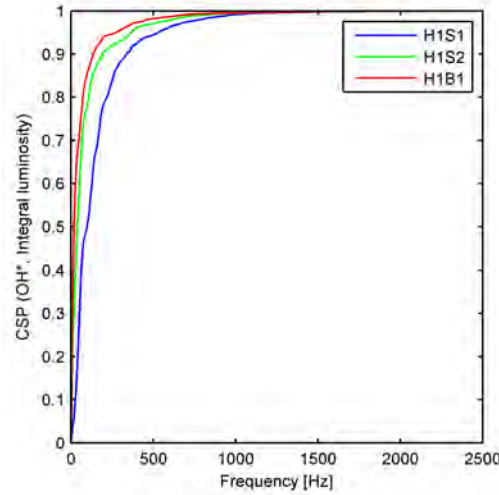
Figure 4.73: Flames of heptane. CSPs of the integral luminosity OH*.

ing at the CSPs of Mode 1 for all operating condition investigated, it is possible to note a clear trend between the operating condition and the energy of the first Mode captured by low frequencies (<500 Hz). This trend highlights that, when blow-off is approached, the energy captured by the first Mode at low frequencies decreases. Hence, it is possible to say that the n-heptane flame during the blow-off conditions is characterized by faster dynamics than stable conditions (H1S1 and H1S2).

Figures 4.72 and 4.73 show the PSDs and CSPs of the spatial integral of OH* (marker of the integral heat release rate) for flames H1S1, H1S2 and H1B1. It is possible to note that the PSD of the integral OH* for flame H1S1 shows a frequency peak at 53.71 Hz. Indeed, no peak is found in the PSDs of integral OH* for flames H1S2 and H1B1. Hence, it is possible to say that the integral heat-release rate tends to assume a less and less periodic behaviour while operating condition is approaching blow-off. Moreover, it is possible to note, when blow-off is approached, that the cut-off frequency of the heat-release rate decreases. Looking at the CSPs of the integral OH*, it can be seen that there exists a relation between

the CSP and the operating condition. Specifically, when the operating condition approaches blow-off, the amount of energy captured by the low frequencies gets higher and higher. Hence, it is possible to note that blow-off is characterized by faster dynamics than stable conditions (H1S1 and H1S2). Therefore, this result is in agreement with the result obtained from the analysis carried out on the first POD Modes. Finally, the change of the spectral information is due to a qualitative change of the operating condition (from stable condition to unstable condition).

OH-PLIF results.   Figures 4.74 and 4.75 show the mean component and the first 5 POD Modes from the OH-PLIF respectively for flames H1S1 and H1B1. Focusing on the mean components of these flames, it can be noted that the size of flame H1B1 (close to blow-off) is slightly smaller than the size of flame H1S1. Besides, it can also be noted that flame H1B1 is slightly closer to the bluff-body than flame H1S1. For flame H1S1 (Fig. 4.74), Mode 1 shows a pattern that can be associated with the transversal oscillation of the flame. Modes 2 and 3 draw patterns that can be associated with the fluctuation of the flame along the jet axis. Mode 4 shows a pattern that can be associated with combustion phenomena that occurs simultaneously in both left and right sides of the spatial domain. Similarly to Modes 2 and 3, Mode 5 shows a pattern that can be associated with the axial fluctuation but with a more complex feature. For flame H1B1 (close to blow-off, Fig. 4.75), Mode 1 clearly shows a feature that can be associated with the transverse fluctuation of the flame. Mode 2 shows a pattern that can be associated with the turn-over of the flame from lateral zones to a central zone. Modes 3-5 show components of the axial fluctuation on the left side but with more complex features. By comparing the first 2 POD Modes of flames H1S1 (Fig. 4.74) and H1B1 (Fig. 4.75), it can be seen that meaningful changes do not
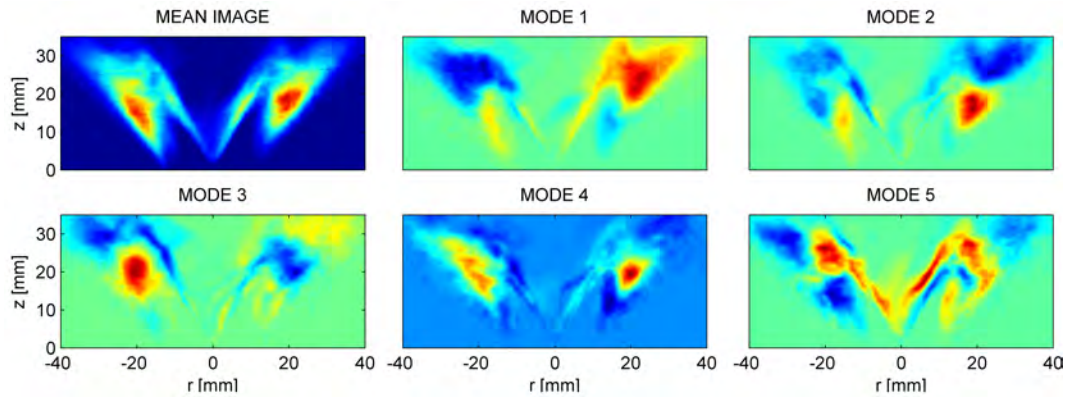
Figure 4.74: Mean image and the first 5 POD modes from OH-PLIF, Flame H1S1.
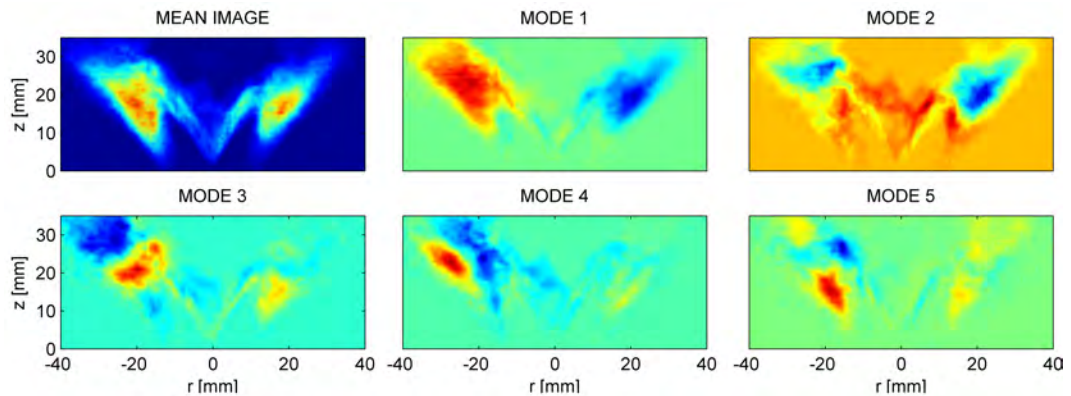
Figure 4.75: Mean image and the first 5 POD modes from OH-PLIF, Flame H1B1.

occur between flames H1S1 (stable) and H1B1 (unstable). Instead, Modes 3-5 show meaningful changes when blow-off is approached. It is possible to highlight that the behaviour of the n-heptane flame is meaningfully different from the other previous fuels analysed.

Figures 4.76 and 4.77 show, for flames H1S1 and H1B1 respectively, few snapshots from the raw PLIF-OH movie (upper row) and the corresponding POD reconstructions obtained using the mean and first 5 POD Modes (middle row), and the mean and first 20 POD modes (lower row). As in the previous cases, once
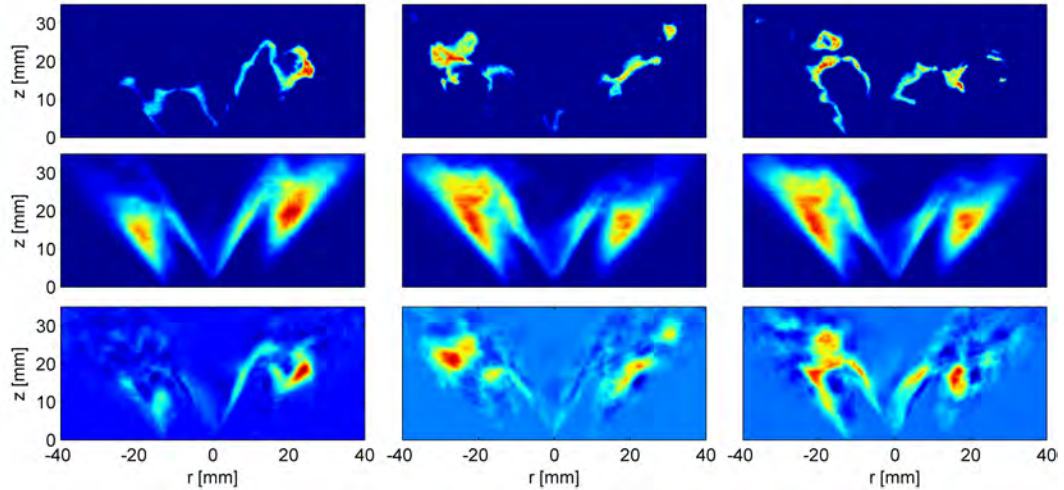
Figure 4.76: Flame H1S1. (Upper) Snapshots from raw OH-PLIF movie. Snapshots at the same times from reconstructed OH* movie using (middle) the mean and mode 1 only and (lower) the mean and modes 1 to 20.
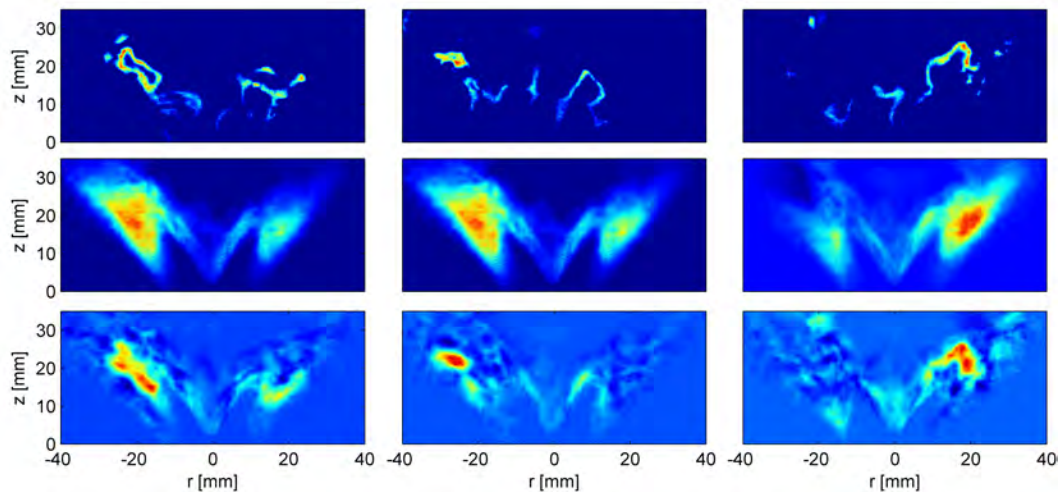
Figure 4.77: Flame H1B1. (Upper) Snapshots from raw OH-PLIF movie. Snapshots at the same times from reconstructed OH* movie using (middle) the mean and mode 1 only and (lower) the mean and modes 1 to 20.
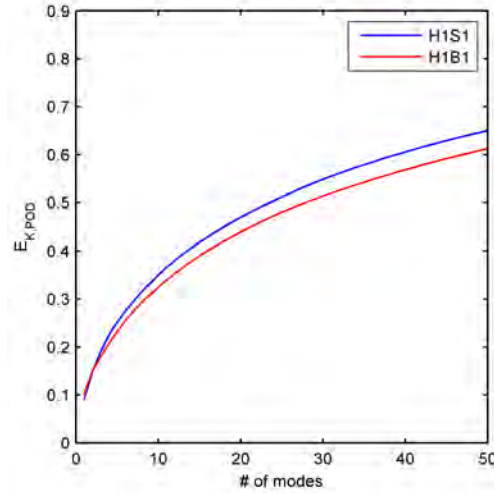
Figure 4.78: Cumulative energy spectrum of the POD modes of OH-PLIF. Flames of heptane.

more the ability emerges of POD to extract the dominant features. In fact, the reconstruction obtained using the mean component and first 20 POD modes provides more details on the morphology of the flame than the reconstruction obtained using the mean and first 5 POD Modes. Figure 4.78 shows the cumulative energy spectra captured by POD Modes for flames H1S1 and H1B1. It is interesting to note, when the blow-off condition is approached, that the energy captured by low order Modes decreases. Hence, the dominant features of H1B1 are less coherent than those of H1S1.

In order to study the dynamic of the n-heptane flame far and close to blow-off conditions, the PSDs of the normalized POD coefficients were analysed. Therefore, Figure 4.79 shows the PSDs of the first 10 normalized POD coefficients (the PSD were shifted along the y-axis to improve the representation) which include a portion at high frequencies with a -5/3 decay, typical of the energy spectrum of turbulence within inertial range. For the flame H1S1, it is possible to note that the PSD of Mode 1 (transverse fluctuation) shows a strong peak at about 34.18
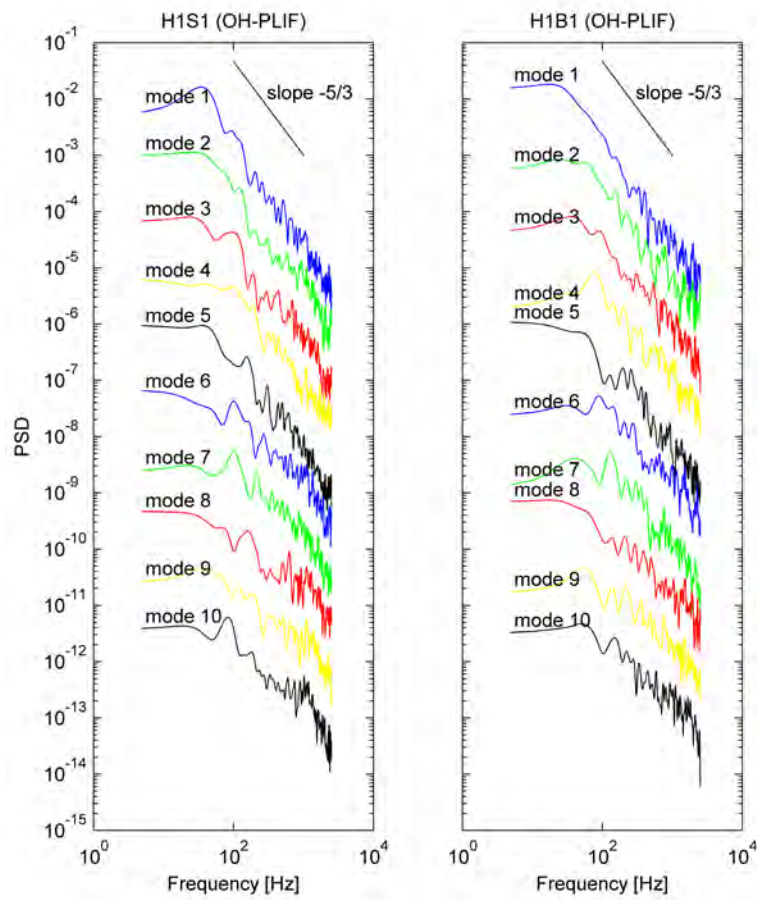
Figure 4.79: Flames of heptane. PSD of POD coefficients from modes 1 to 10 of OH-PLIF.
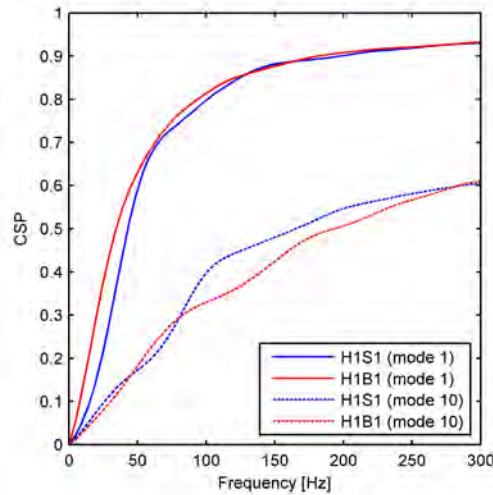
Figure 4.80: Flames of heptane. CSP of POD coefficients of modes 1 and 10 of OH-PLIF.

Hz. In addition, it can be noted that, when the operating condition approaches blow-off, Mode 1 shows no dominant frequency. As a consequence of this result, it is possible to identify a qualitative change of the state of the burner by monitoring the PSD of POD Mode 1. Looking at the PSD of other POD Modes, it is possible to note that a -5/3 decay occurs for frequencies higher than 100 Hz.

Figure 4.80 shows the normalized CSPs of the coefficients for Modes 1 and 10. In contrast to the results obtained for the previous fuels, wherein the CSP of the first POD Mode shows a clear trend with the operating condition, in the case of n-heptane there is no trend of the CSP of the first POD Mode with the operating conditions. Figures 4.81 and 4.82 show respectively PSDs and CSPs relative to spatial integral of the OH-PLIF signal for flames H1S1 and H1B1. For both flames H1S1 and H1B1, the PSDs of the integral OH-PLIF signal show a peak about at 90 Hz. Therefore, it is possible to note that the bandwidth of the integral OH-PLIF is about 100 Hz. Similarly to what was obtained for the first POD Mode, there is no clear trend between the CSP of the integral OH-PLIF signal and the operating
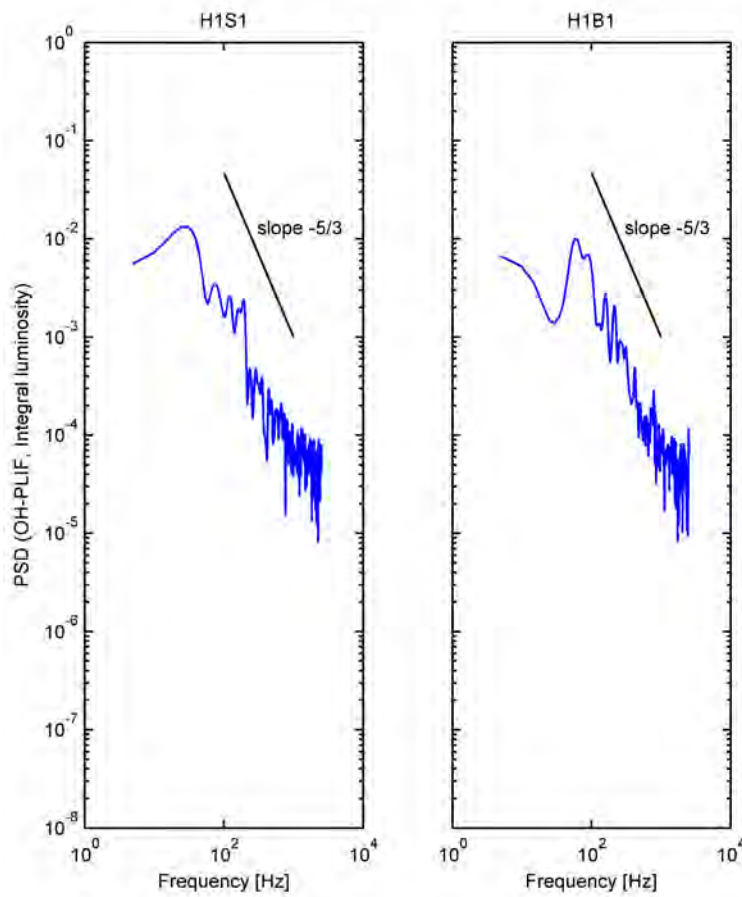
Figure 4.81: Flames of heptane. PSD of the integral luminosity OH-PLIF.
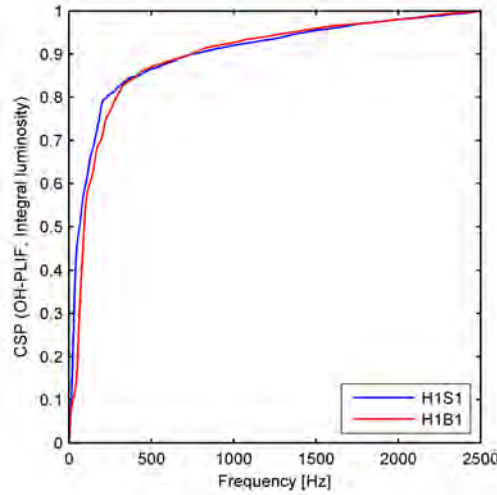
Figure 4.82: Flames of heptane. CSP of the integral luminosity OH-PLIF.

conditions.

4.6 Coherent-Incoherent component analysis

In this section, the study of the coherent (non-Gaussian) and incoherent (Gaussian) components is developed and discussed for every flame studied in the previous section. This analysis is a new tool to analyse experimental data in order to improve the knowledge of the differences in the underlying phenomena between stable conditions and blow-off. Besides, in order to verify the accuracy of the analysis, both the method of separation of coherent and incoherent components proposed by (Bizon et al., 2009a), and that based on Shapiro-Wilk normality test, which is presented for the first time in this work, are employed to extract the coherent and incoherent components from OH* and OH-PLIF imaging swirling spray flames far from and at blow-off.
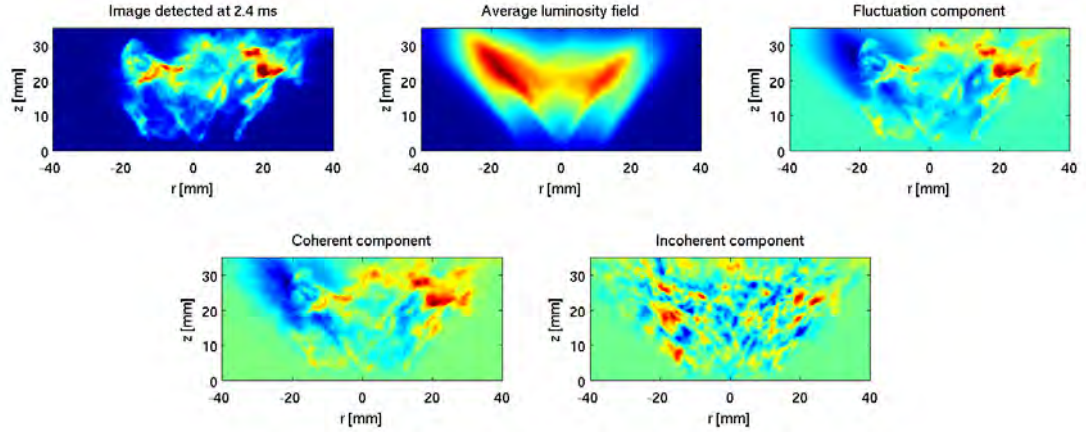
Figure 4.83: Flames of D1S1. Coherent-incoherent decomposition of a OH* snapshot.

4.6.1 n-Decane

OH* results. The fluctuations of OH* for D1S1, D1S2 and D1B1 were studied by means of the coherent-incoherent component analysis by using both methods based on ρ and Shapiro-Wilk normality test. The reconstructed movies of the coherent and incoherent fluctuation are given as supplementary material.

Firstly, the coherent-incoherent analysis carried out with the method based on ρ index is discussed. For flame D1S1, Figure 4.83 shows the mean, the fluctuation, the coherent and incoherent components of OH* obtained by using the method based on ρ . It is possible to see as the large-scale features of the fluctuation belongs to the coherent (non-Gaussian) component, and the small-scale features belong to the incoherent (Gaussian) component. It is necessary to recall that in this method POD modes are reordered according to increasing ρ.

It is interesting to view as the energies captured by the POD modes are distributed along ρ . Therefore, Figure 4.84 shows the scatter plots concerning the energy spectra based on ρ for flames D1S1, D1S2 and D1B1. Looking at these spectra, it is possible to observe as such energy spectra (Fig. 4.84) are localized
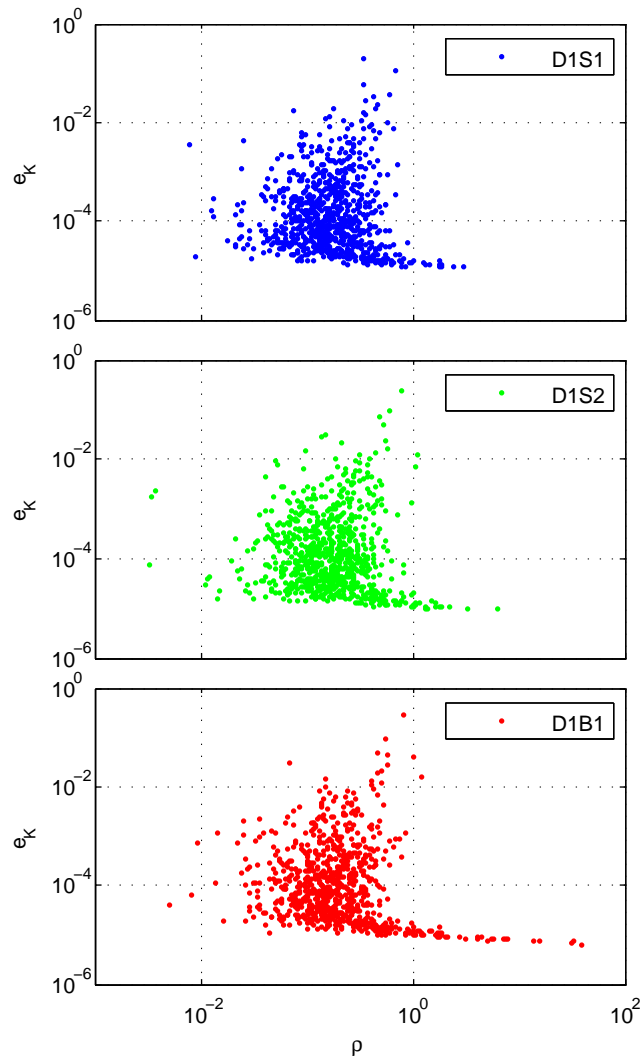
Figure 4.84: Flames of D1S1. Distribution of the energies captured by the POD modes along ρ.

inside a bounded region of the plane. For both flames D1S1 and D1S2 (stable conditions), it is interesting to observe as the shapes of these regions (in the plane) look roughly alike. Conversely, the energy spectrum based on rho for flame D1B1 (close to blow-off), shows a branch at low energy (low luminosity) that can be associated with the extinction phenomena of the flame, which are characterized by low intensity of OH*. It is possible to note that such branch is characterized by high ρ . This result suggests that the extinction phenomena are characterized by non-Gaussian behaviours.

By applying a threshold value to ρ_{th}, it is possible to classify the POD Modes as Gaussian ($\rho_{th} \leq \rho$) or non-Gaussian ($\rho_{th} > \rho$). Subsequently, it is possible to reconstruct the coherent and incoherent components using Eqs (4.11)-(4.12). Furthermore, it is interesting to show the amount of incoherent (or coherent) energy as function of ρ. This last information is given from the cumulative energy spectrum based on ρ, E_ρ (Eq. (4.14)). Figure 4.85 shows E_ρ for the flames D1S1, D1S2 and D1B1. It is possible to note a clear trend between E_ρ and the operating conditions. Particularly, it can be noted that, when the operating condition approaches blow-off, the coherent energy increases. This means that the fluctuation of the OH* field assumes a less Gaussian behaviour at blow-off. This result can be explained by the fact that the flame, during stable operating conditions, assumes a stochastic behaviour similar to that of the flow, which is strongly turbulent. Indeed, it is known from the literature that, for high Reynolds number flows, the fluctuations of the velocity field are usually assumed to be Gaussian. On the other hand, the coherent energy, which represents the amount of energy captured by non-Gaussian modes, becomes higher and higher as the operating condition is closer and closer to blow-off. Hence, it is possible to conclude that the OH* signal assumes a behaviour far from Gaussian for operating conditions close to blow-off. Moreover, as it was shown from OH-PLIF measurements, it is necessary to remember that
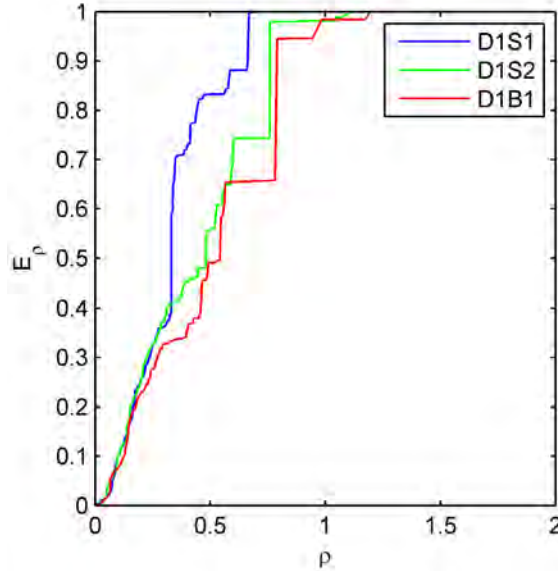
Figure 4.85: Flames of n-decane (OH*). Cumulative energy spectra based on ρ.

blow-off, before extinction, is characterized by a fragmented flame that will tend to extinction. As a result, this suggests that fragmented flames assume statistical behaviour far from Gaussian.

By applying the method of classification based on Shapiro-Wilk normality test to classify the POD modes as coherent and incoherent, it is expected that the same conclusion obtained from the method proposed by Bizon et al. (2009a). Figure 4.86 shows the distribution of the energies captured by the POD Modes on the p-values obtained from Shapiro-Wilk normality test, respectively for flames D1S1, D1S2 and D1B1. Recalling that the p-value can be considered as a measure of the statistical evidence that the sample does not satisfy the null hypothesis; hence, in our case, it is extracted from a non-Gaussian population. The energy spectra based on the Shapiro-Wilk test (Fig. 4.86) provide useful information about the phenomena investigated. Indeed, it is possible to show as the most energetic POD modes has a behaviour strongly non-Gaussian (very low p-values). The data are
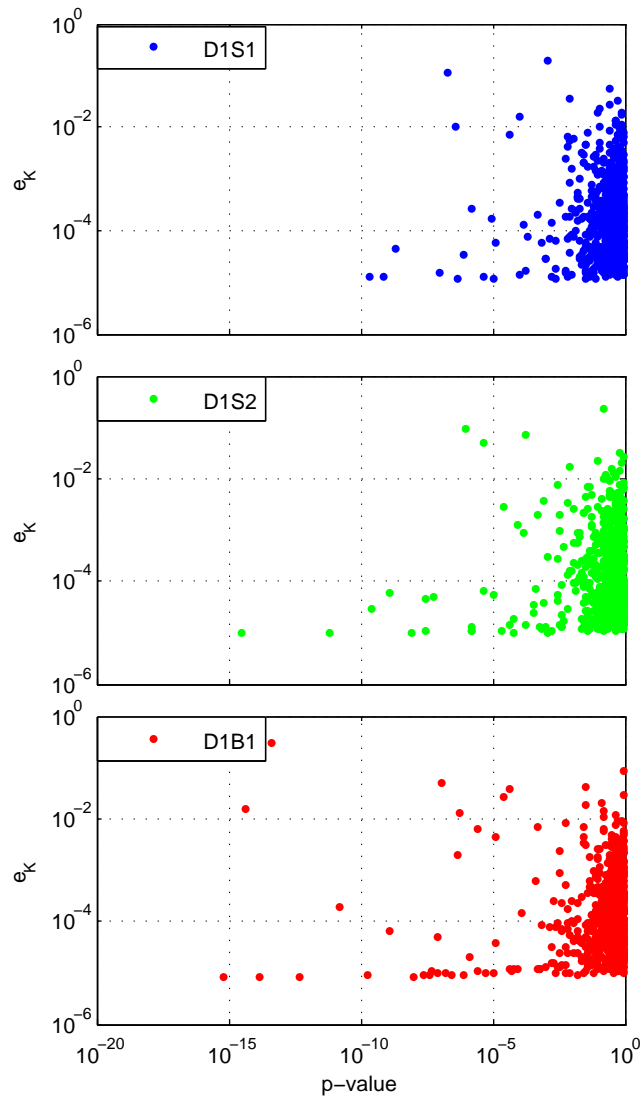
Figure 4.86: Flames of D1S1 (OH*). Distribution of the energies captured by the POD modes along p-value.
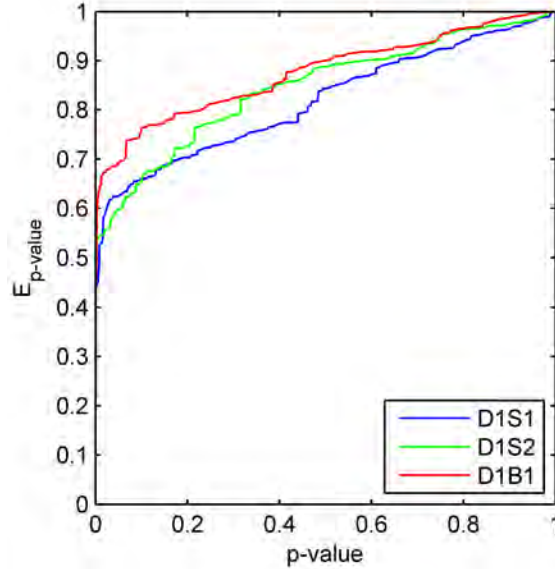
Figure 4.87: Flames of n-decane (OH*). Cumulative energy spectra based on
p-value.

thus investigated by using the cumulative energy spectrum based on Shapiro-Wilk
normality test, $E_{p-value}$ (Eq. (4.15)). Figure 4.87 shows the cumulative energy
spectra based on Shapiro-Wilk for flames D1S1, D1S2 and D1B1. It is possible to
note that a clear trend exists between these spectra and the operating conditions.
As introduced in Section 4.4.2, the cumulative energy spectrum based on Shapiro-
Wilk test (Eq. (4.15)) makes it possible to show the energy captured by coherent
component as a function of the p-value.

It is then possible to classify the POD modes as coherent and incoherent by
choosing an appropriate threshold (level of significance, α) for the p-value. Sub-
sequently, POD modes having a p-value lower than the level of significance will
be classified as coherent, otherwise they will be classified as incoherent modes.
Table 4.2 reports the percentages of coherent and incoherent energies at the most
common level of significance for all flames investigated by means of OH* mea-

Table 4.2: OH* measurements. Energies captured by the coherent component at three values of significance.

OH*	D1S1	D1S2	D1B1
α	Coherent Energy	Coherent Energy	Coherent Energy
0.01	52.77%	62.53%	65.89%
0.05	54.49%	59.81%	65.89%
0.1	64.60%	69.08%	76.36%
OH*	DD1S1	DD1S2	DD1B1
α	Coherent Energy	Coherent Energy	Coherent Energy
0.01	43.09%	48.61%	74.65%
0.05	55.25%	62.09%	81.62%
0.1	57.89%	69.35%	84.98%
OH*	H1S1	H1S2	H1B1
α	Coherent Energy	Coherent Energy	Coherent Energy
0.01	40.11%	52.90%	64.17%
0.05	52.33%	57.39%	65.99%
0.1	59.35%	60.92%	69.63%
OH*	E1S1	E1S2	E1B1
α	Coherent Energy	Coherent Energy	Coherent Energy
0.01	66.33%	59.37%	59.29%
0.05	72.37%	65.57%	64.77%
0.1	77.70%	73.02%	68.01%
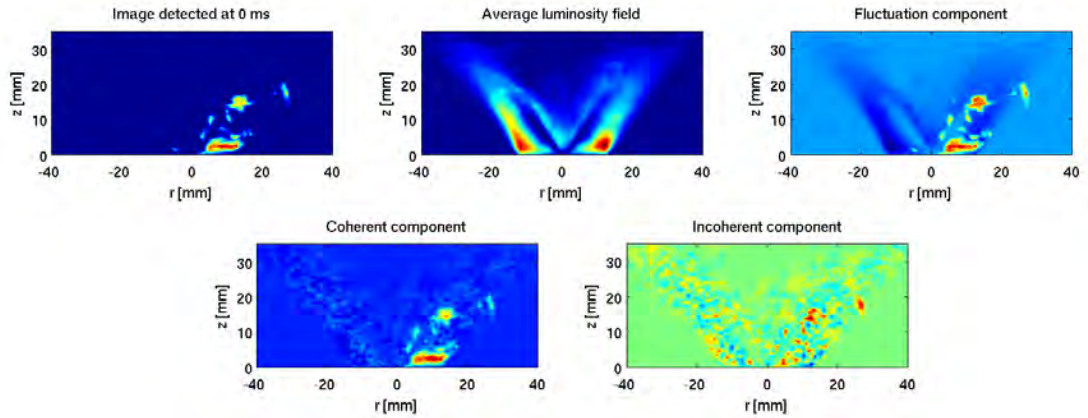
Figure 4.88: Flames of D1B1. Coherent-incoherent decomposition of a OH-PLIF snapshot.

surements. Hence it is evident that, when the operating condition is approaching blow-off, the energy captured by the coherent component gets higher.

OH-PLIF results. Similarly to OH* data, incoherent/coherent analysis is carried out for the OH-PLIF data for flames D1S1, D1S2 and D1B1. Recalling that OH-PLIF data are relative to a flame sheet, the influence of the turbulent field on the flame is much evident. Figure 4.88 shows a raw snapshot, the mean, the fluctuation, coherent and incoherent components of OH-PLIF for D1B1. It is possible to see as the large-scale features of the fluctuation are captured by the coherent (non-Gaussian) component, and the small-scale features are captured by the incoherent (Gaussian) component. Figure 4.89 shows the scatter plots concerning the energy spectra based on ρ for flames D1S1, D1S2 and D1B1. Looking at these spectra, it is possible to observe that they draw bounded regions inside the $\rho - e$ plane. Moreover, it is interesting to note how the shapes of the regions relative to D1S1 and D1S2 (stable operating conditions) are roughly similar. Moreover, it is possible to note that flame D1B1 (blow-off) draws, inside the $\rho - e$ plane, a zone
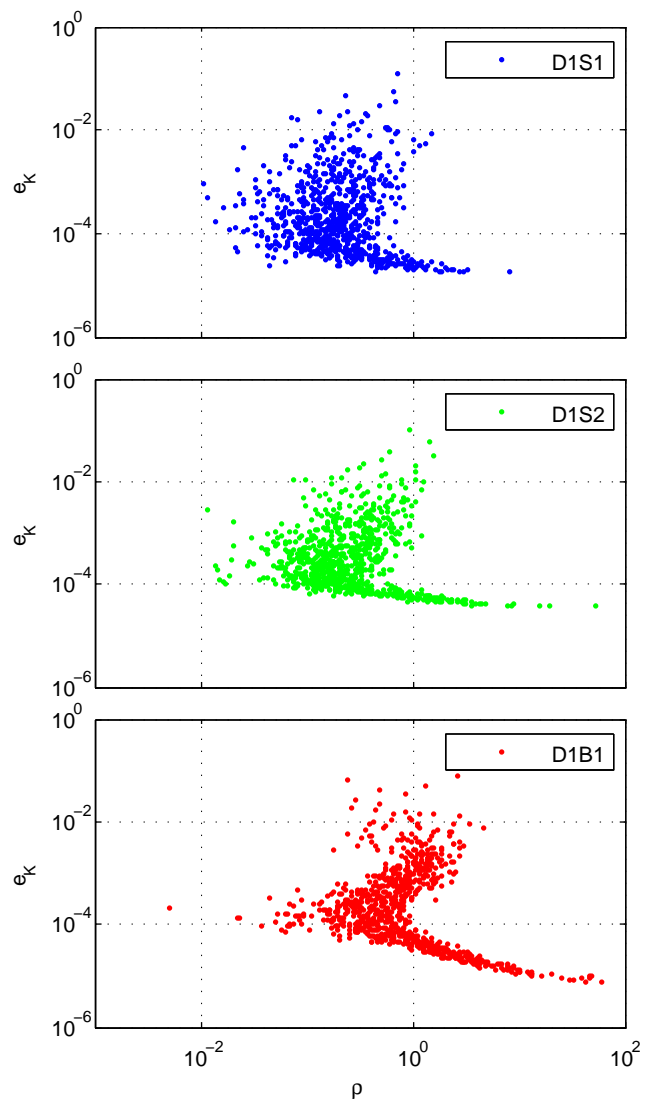
Figure 4.89: Flames of D1S1 (OH-PLIF). Distribution of the energies captured by the POD modes along ρ.
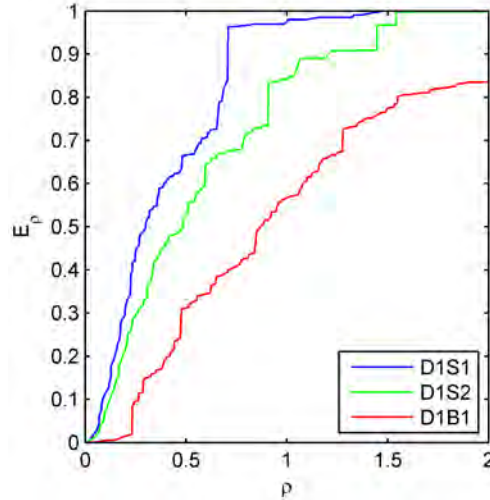
Figure 4.90: Flames of n-decane (OH-PLIF). Cumulative energy spectra based on ρ.

localized at ρ values higher than the stable flames. Besides, it is possible to notice when the operating condition is closer and closer to blow-off, the branch of POD modes at low energy and high ρ values becomes more and more marked; in other words, the number of POD modes, which belong to such branch, increases.

In order to study the amount of energy captured by the coherent and incoherent components, the cumulative energy spectra based on ρ, E_ρ , are studied (Figure 4.90) for all n-decane flames. It is of interest to note how these spectra show a clear trend on the operating condition; specifically, when the blow-off is approached, the energy captured by the coherent component increases. This result suggests that the fluctuation of the flame front assumes a less Gaussian statistical behaviour. In addition, this last result is in good agreement with that obtained from the OH* data; hence, the same considerations can be made.

For flames D1S1, D1S2 and D1B1, Figure 4.91 shows the distributions of the energy captured by each POD mode along p-values obtained by evaluating the statistical test proposed by Shapiro (1965). Fig. 4.92 shows the cumulative energy
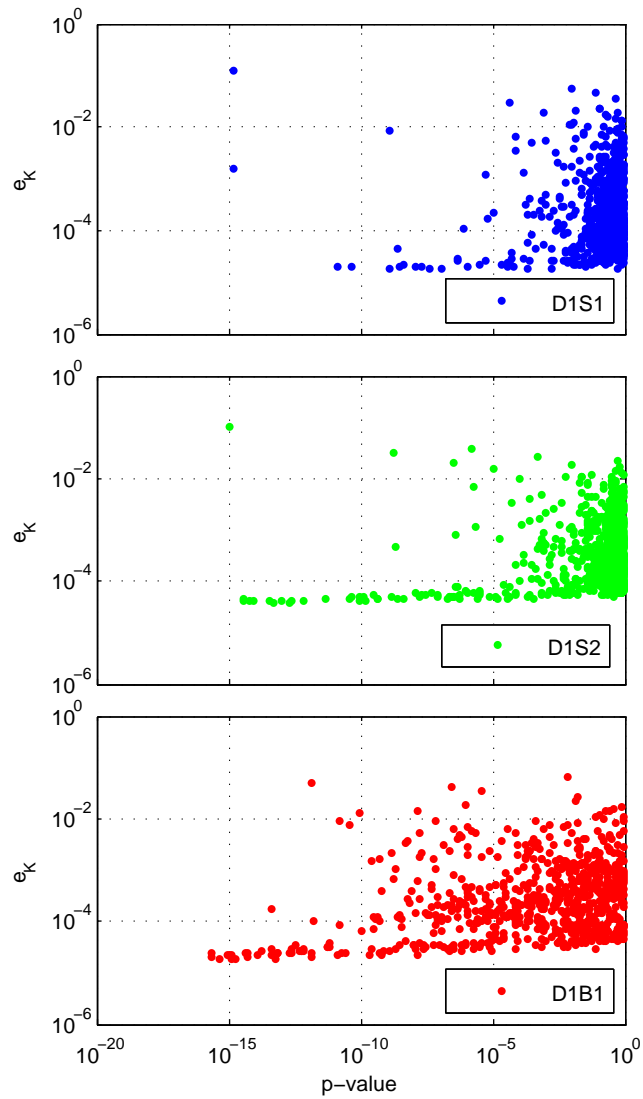
Figure 4.91: Flames of D1S1 (OH-PLIF). Distribution of the energies captured by the POD modes along p-value.
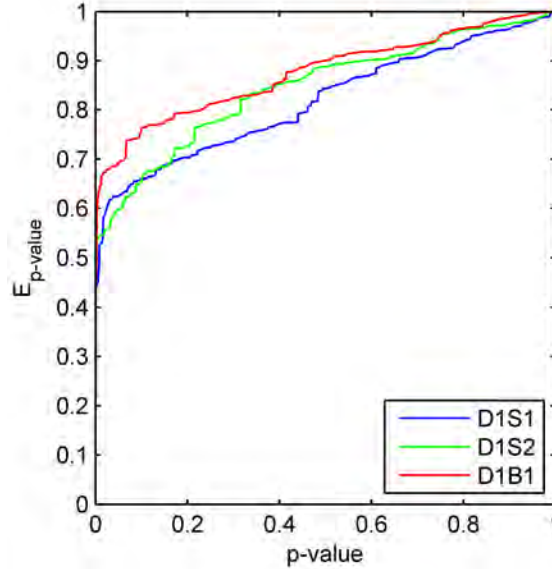
Figure 4.92: Flames of n-decane (OH-PLIF). Cumulative energy spectra based on p-value.

spectra based on Shapiro-Wilk test for the OH-PLIF signals relative to flames D1S1, D1S2 and DDB1. Also in this case, it is possible to note as the energy captured by the coherent component is higher and higher, when the operating condition is closer and closer to blow-off. Besides, it is possible to note as the spectra based on the p-value show a clearer trend than that based on ρ (Bizon et al., 2009a). At a fixed level of significance, it is possible to reconstruct the coherent and incoherent components of the data by using Eqs (4.14)-(4.15).

Once more, it is possible to classify the POD modes as coherent or incoherent, through the choice of a proper level of significance for Shapiro-Wilk normality test. For all investigated flames, Table 4.3 reports the energy captured by coherent and incoherent components at the most common level of significance. It is possible to say that the statistical behaviour of the n-decane flame at the blow-off (D1B1) is more Gaussian than the stable operating conditions (D1S1 and D1S2).

Table 4.3: OH-PLIF measurements. Energies captured by the coherent component at three values of significance.

OH-PLIF	D1S1	D1S2	D1B1
α	Coherent Energy	Coherent Energy	Coherent Energy
0.01	41.60%	45.12%	74.90%
0.05	48.62%	55.91%	89.54%
0.1	53.43%	59.88%	90.99%
OH-PLIF	DD1S1	DD1S2	DD1B1
α	Coherent Energy	Coherent Energy	Coherent Energy
0.01	-	28.88%	54.44%
0.05	-	38.33%	66.66%
0.1	-	43.87%	70.39%
OH-PLIF	H1S1	H1S2	H1B1
α	Coherent Energy	Coherent Energy	Coherent Energy
0.01	40.59%	-	69.51%
0.05	53.74%	-	78.47%
0.1	59.66%	-	82.41%
OH*	E1S1	E1S2	E1B1
α	Coherent Energy	Coherent Energy	Coherent Energy
0.01	57.67%	70.97%	71.31%
0.05	64.87%	77.42%	80.31%
0.1	69.40%	84.65%	87.80%

Hence, once more, it is possible to highlight that, when the operating condition approaches blow-off, the coherent energy increases. Then, at blow-off, the fluctuation of the flame front (OH-PLIF signal) is characterized by a less Gaussian behaviour. This result can be due to fact that the flame, during stable operating conditions, assumes a statistical behaviour similar to that of the flow, which is strongly turbulent. Indeed, for high Reynolds flows, the fluctuations of the velocity field are usually assumed to be Gaussian. Therefore, the coherent energy, which represents the amount of energy captured by non-Gaussian modes, is higher and higher as the blow-off condition is approached. As a result, this suggests that fragmented flames, which occur during the blow-off, have statistical behaviour far from Gaussian.

4.6.2 Other fuels

OH* results The coherent-incoherent component analysis was also carried out on the OH* chemiluminescence measurements for n-dodecane (DD1), n-heptane (H1) and ethanol (E1) flames. Moreover, we should recall that OH* is know as a marker of the heat release rate.

For the n-dodecane flames (DD1), Figures 4.93 and 4.94 show the energy spectra and cumulative energy spectra based on method proposed by Bizon et al. (2009a). By comparing these spectra, it is possible to note that the n-dodecane flames (DD1) are roughly similar to n-decane flames (D1). Particularly, when the operating condition is closer and closer to blow-off, the energy captured by coherent component is higher and higher. This result is in good agreement with that obtained for the n-decane flames. Besides, in reference to Fig. 4.93, the shapes of the regions associated to the flames of n-dodecane have morphologies similar to those of n-decane flames. Indeed, as for n-decane flames, the n-dodecane flames

show a branch at low energy and high ρ. Such branch is more and more evident, when the operating condition is approaching to blow-off (DD1B1). Looking at the cumulative energy spectra based on ρ for the n-dodecane flames (D1), it is possible to note that a clear trend exists between the operating condition and the cumulative energy spectra correspond to that obtained for the n-decane flames in the previous section. Figure 4.94 shows the cumulative energy spectra based on p-value (method based on Shapiro-Wilk normality test). Once again, it is possible to notice that a trend exists between the cumulative energy spectra and the operating conditions, and it is similar to that regarding of the n-decane flames. As a result, this suggests that the n-dodecane (DD1) and n-decane (D1) flames have roughly similar statistical behaviours.

For the n-heptane flame (H1). Figures 4.95 and 4.96 show respectively the energy spectra and the cumulative spectra energy based on ρ. By comparing the energy spectra based on ρ for the n-heptane flames and that regarding the previous flames, it is possible to note little dissimilarity among the shapes of the regions spanned by the points. Particularly, for flame H1B1, the branch at low energy and high is shorter and less marked than those of the flames DD1S1 and DD1S2. In addition, n-heptane flames show also a trend between the operating conditions and the length of such branch, localized at low-energy and high ρ , but it is less marked than those obtained for D1 and DD1 flames. Looking at the cumulative energy spectra based on ρ (Fig. 4.96), no trend is shown between the cumulative energy spectrum and operating condition. This result is completely different than those obtained from previous fuels analysed.

Recall that the Shapiro-Wilk test is one the most powerful normality tests. Thus, for flames H1, in order to prove the correctness of the result obtained by method based on ρ , the coherent-incoherent analysis is also carried out by using the method of classification based on Shapiro-Wilk normality test. Therefore, Figure
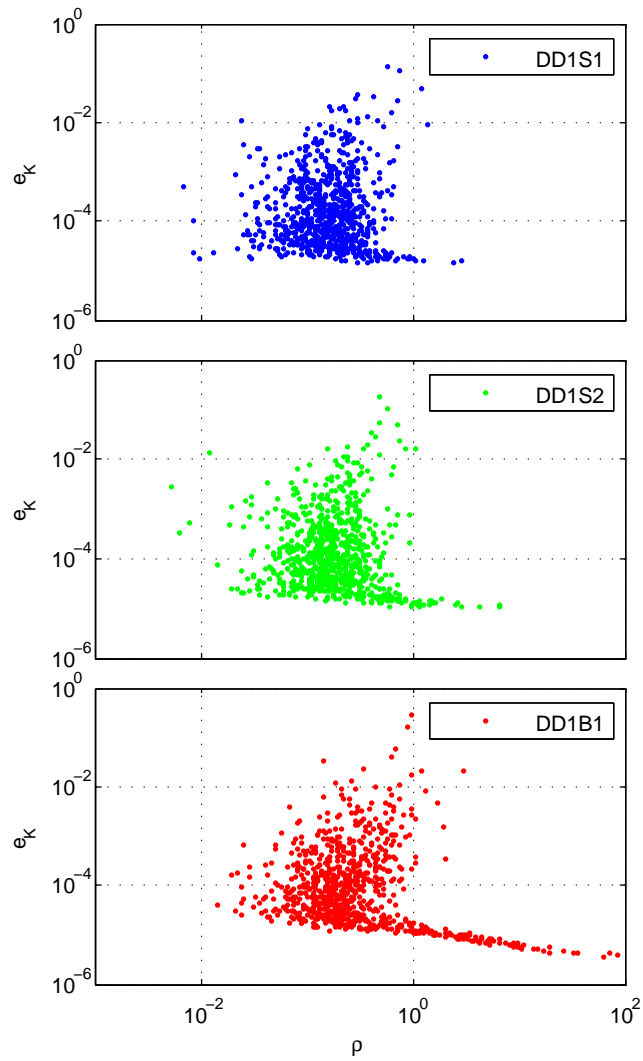
Figure 4.93: Flames of n-dodecane (OH*). Distribution of the energies captured by the POD modes along ρ.
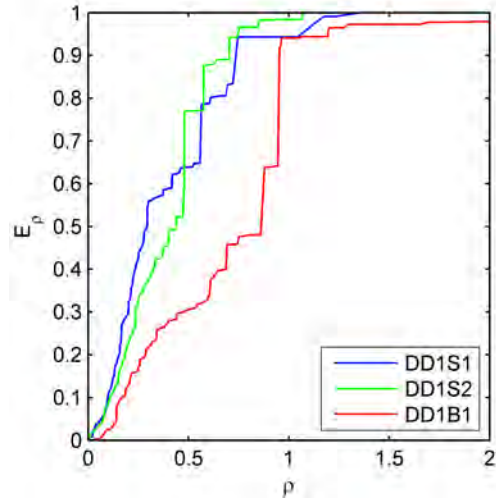
Figure 4.94: Flames of n-dodecane (OH*). Cumulative energy spectra based on ρ.

4.97 shows the cumulative energy spectra based on p-value for flames H1. By observing these spectra at the most common levels of significance (1%, 5%, 10%) (Table 4.2), it is possible to note that a clear trend exists between the amounts of energy captured by coherent and incoherent components respectively, and the behaviour of the flame. Particularly, when the operating condition is approaching blow-off, the amount of energy captured by the coherent component is higher and higher. This last result is in agreement with the results obtained for flames of n-decane and n-dodecane. In this case, the method based on Shapiro-Wilk test has been more powerful than the method based on ρ.

Finally, OH* data for ethanol flames are studied through the coherent-incoherent analysis. Figures 4.98 and 4.99 show energy spectra and cumulative energy spectra based on ρ for the flames E1S1, E1S2 and E1B1. In this case, the regions spanned by points of the energy spectra based on for E1S1, E1S2 and E1B1 identify (Fig. 4.98). By comparing the energy spectra based on ρ for the n-ethanol flames and those regarding the previous flames, it is possible to note few differences among the shapes of the regions spanned by the points. Firstly, for the flame E1, the
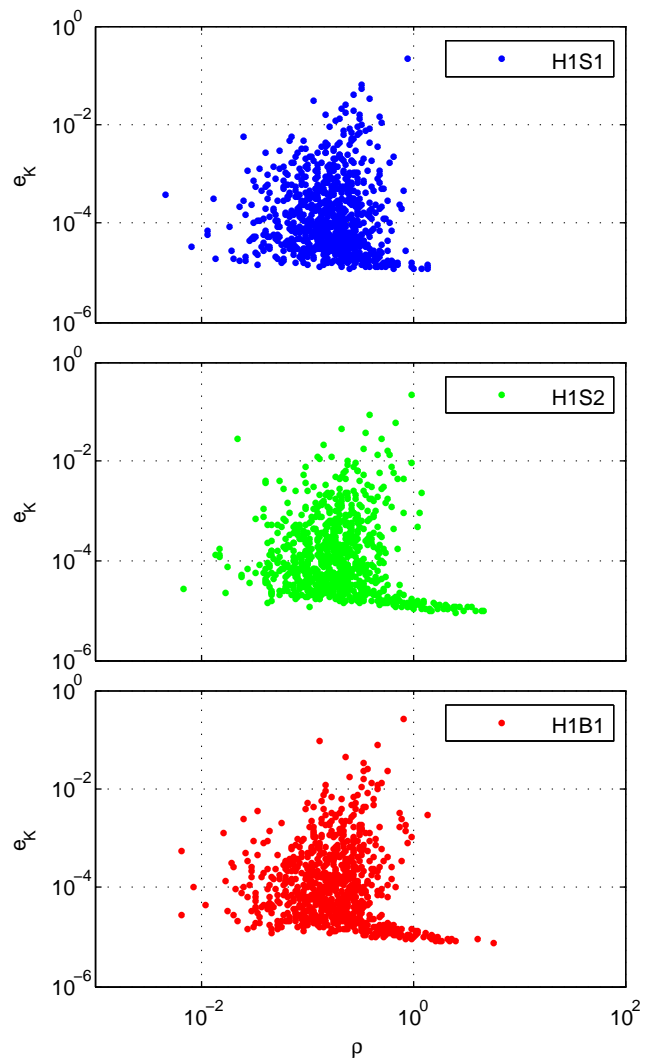
Figure 4.95: Flames of n-heptane (OH*). Distribution of the energies captured by the POD modes along ρ.
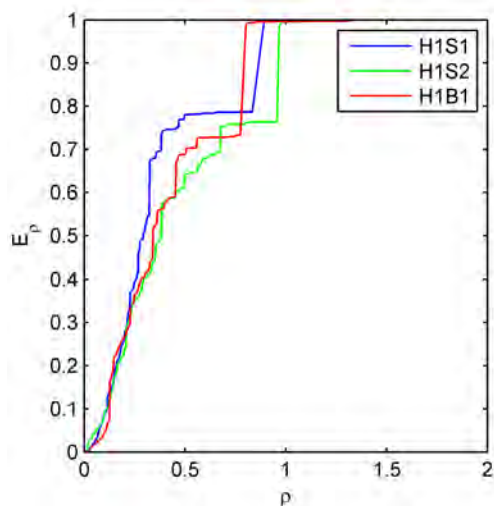
Figure 4.96: Flames of n-heptane (OH*). Cumulative energy spectra based on ρ.
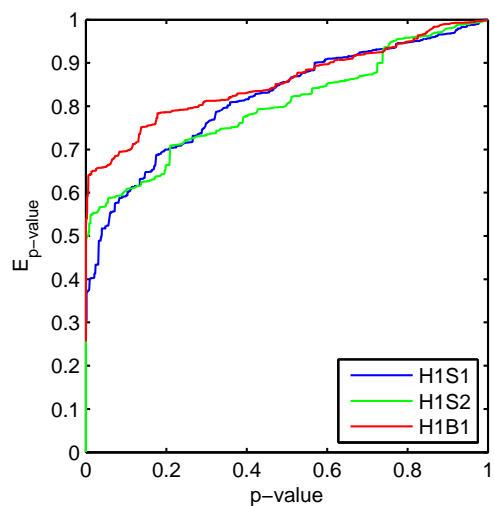
Figure 4.97: Flames of n-heptane (OH*). Cumulative energy spectra based on p-value.
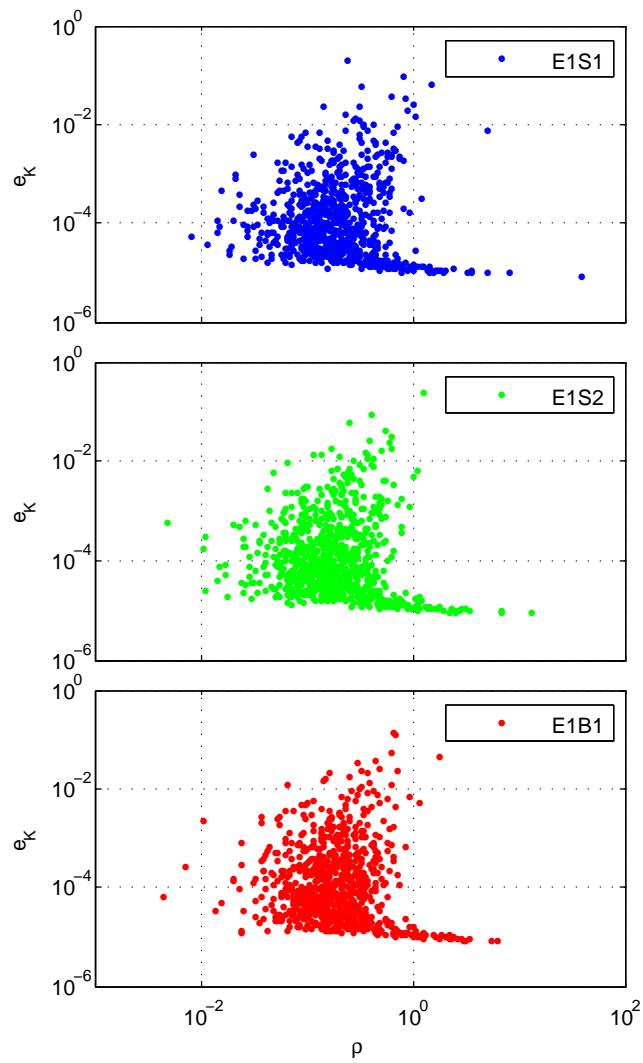
Figure 4.98: Flames of ethanol (OH*). Distribution of the energies captured by the POD modes along ρ.
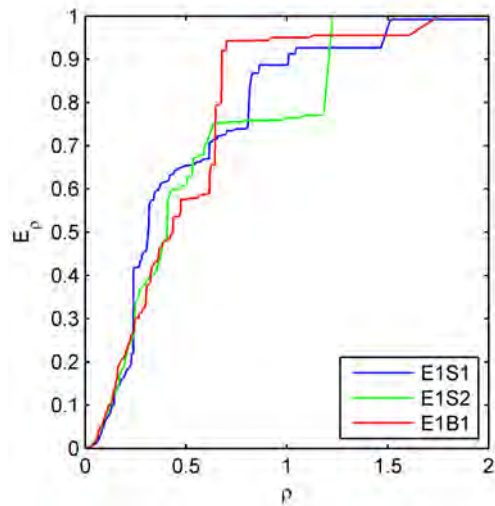
Figure 4.99: Flames of ethanol (OH*). Cumulative energy spectra based on p-value.
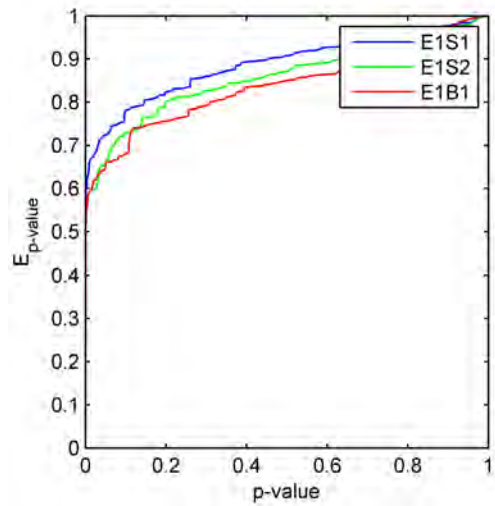
Figure 4.100: Flames of ethanol (OH*). Cumulative energy spectra based on p-value.

branch at low energy and high ρ occurs for all operating conditions; conversely to the previous flames studied. Secondly, the length of this branch decreases as the blow-off condition is approached. Looking at cumulative spectra based on ρ , no trend occurs in these spectra. Then, the method based on Shapiro-Wilk test should be able to find any useful statistical feature that can be used for the classification of the operating condition.

Figure 4.100 shows the cumulative energy spectra based on p-value for the flames of ethanol (E1S1, E1S2 and E1B1). Wherein, it can be seen that a clear trend occurs between the cumulative energy spectra and the operating condition. Particularly, it is clear that the flame becomes more and more incoherent as the blow-off condition is approached. In other words, this means that the ethanol flame close to blow-off, E1B1, is more Gaussian than flames E1S1 and E1S2, with regard to stable conditions. It is interesting to highlight that this result is in opposition to those obtained for the previous fuels. As a result, regarding to OH* measurements, when the operating condition approaches to blow-off, the heat release of ethanol flame (E1) assumes a statistical behaviour in opposition to that of the other fuels analysed (D1, DD1, H1).

OH-PLIF results. The coherent-incoherent component analysis was also carried out on the OH-PLIF measurements for n-dodecane (DD1), n-heptane (H1) and ethanol (E1) flames. It is necessary to recall that the OH-PLIF signal is a marker of the instantaneous flame front; for this reason, the results of this subsection will concern the flame front. For OH-PLIF data, Figures 4.101-4.103 show respectively the energy spectra based on ρ for flames DD1, H1 and E1. Also for these flames, it is possible to note that the shapes of the region spanned by points in the $\rho - e$ plane (Figs 4.101-4.103), are roughly similar to those obtained for the corresponding OH* measurement. Besides, the branch of points at low energy and
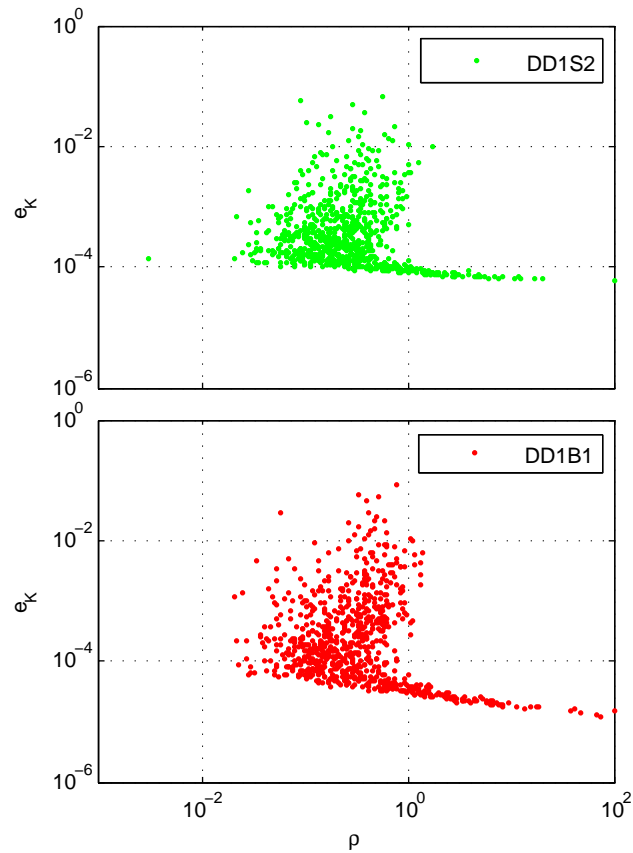
Figure 4.101: Flames of n-dodecane (OH-PLIF). Distribution of the energies captured by the POD modes along ρ.

high ρ occurs regularly for OH-PLIF data as well. As in the previous section, in order to extract clearer information from data, the spectra E_ρ are estimated and studied. Then, Figures 4.104-4.106 show respectively the spectra E_ρ for flames DD1, H1 and E1. Looking at the cumulative energy spectra E_ρ (Figs 4.104-4.106) obtained from OH-PLIF measurements, it is possible to highlight that they show trend similar to that obtained for flames D1. This result suggests that the flame front assumes behaviour less and less Gaussian as the blow-off is approached, independently from the fuel used. This result is very useful in order to individuate a proper control parameter for the developing of robust controller based on optical
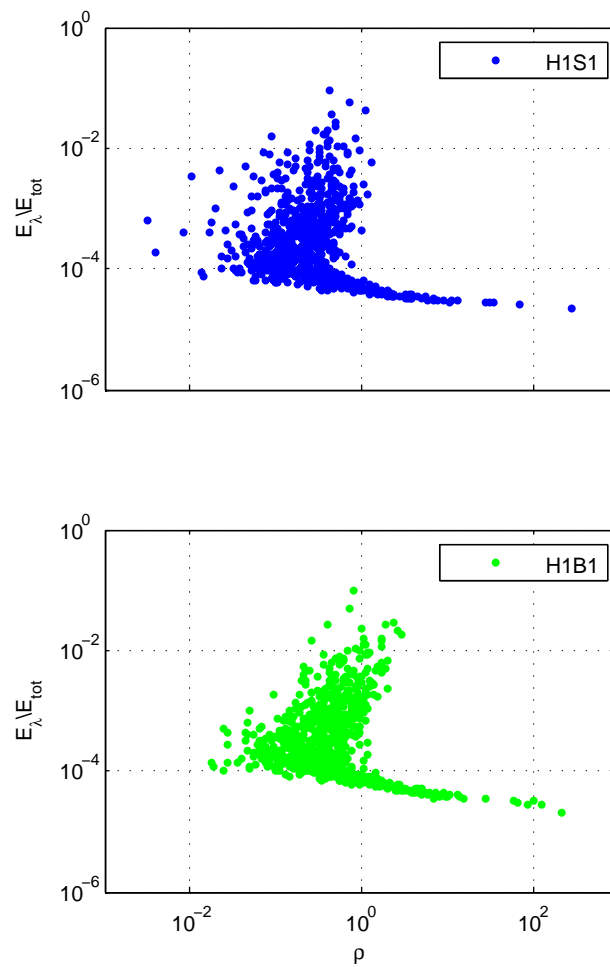
Figure 4.102: Flames of n-heptane (OH-PLIF). Distribution of the energies captured by the POD modes along ρ.
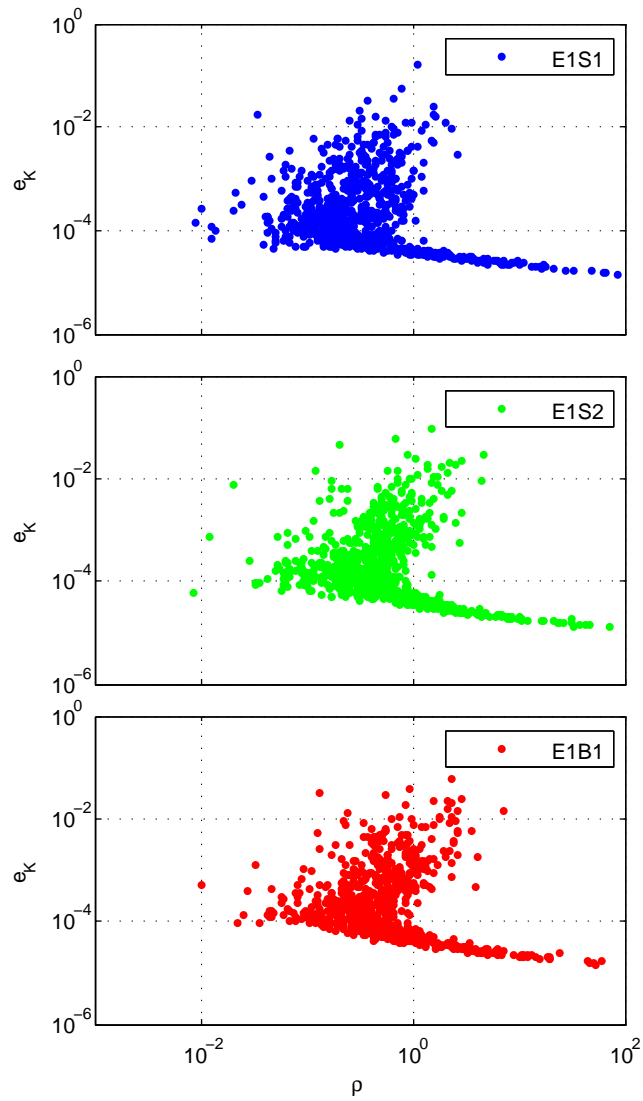
Figure 4.103: Flames of ethanol (OH-PLIF). Distribution of the energies captured by the POD modes along ρ.
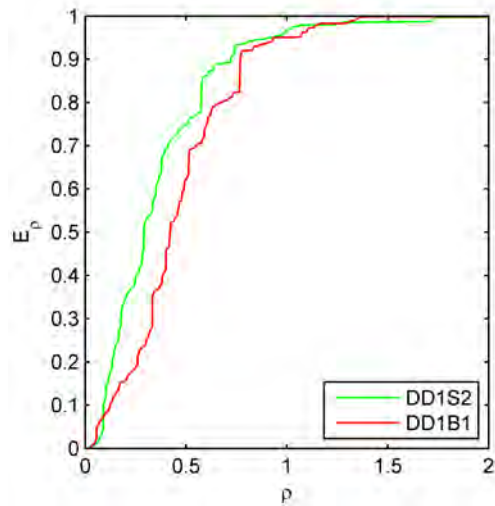
Figure 4.104: Flames of n-dodecane (OH-PLIF). Cumulative energy spectra based on ρ.
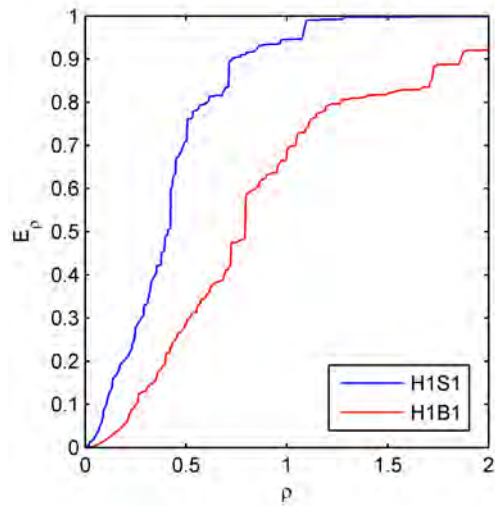
Figure 4.105: Flames of n-heptane(OH-PLIF). Cumulative energy spectra based on ρ.
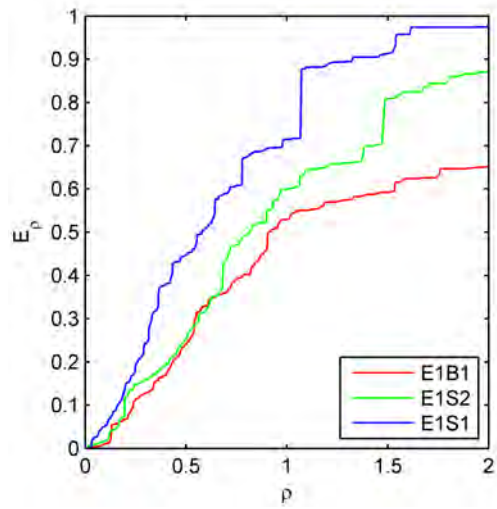
Figure 4.106: Flames of ethanol (OH-PLIF). Cumulative energy spectra based on ρ.
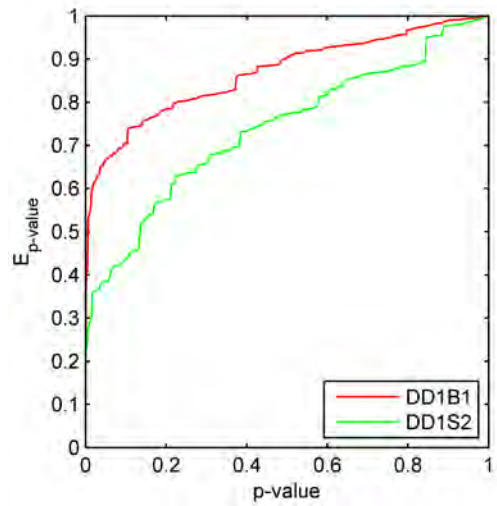
Figure 4.107: Flames of n-dodecane (OH-PLIF). Cumulative energy spectra based on p-value.
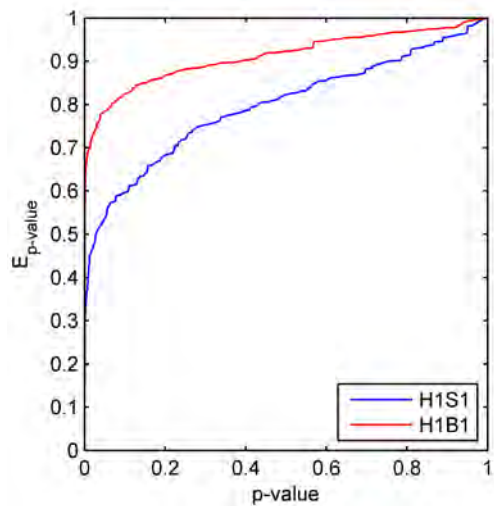
Figure 4.108: Flames of n-heptane (OH-PLIF). Cumulative energy spectra based on p-value.
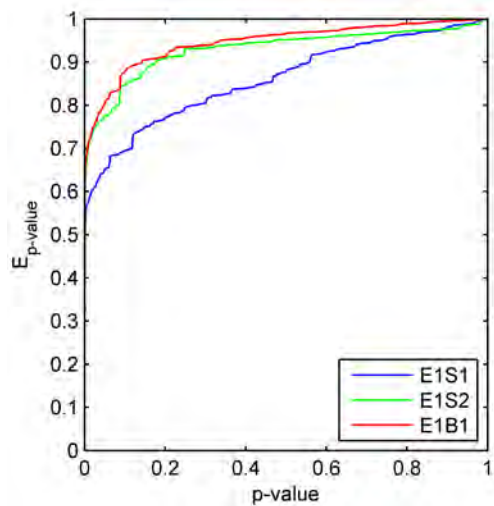
Figure 4.109: Flames of ethanol (OH*). Cumulative energy spectra based on p-value.

diagnostic techniques. The coherent-incoherent component analysis has also been carried out by means of the method of classification based on Shapiro-Wilk test. Figures 4.107-4.109 show the cumulative energy spectra based on p-value. Once again, for all fuels analysed, it is possible to observe a clear trend between the cumulative energy spectra and the operating conditions. Particularly, it is possible note that the flame is more and more coherent when the operating condition is closer and closer to blow-off. Since results are in good agreement with those obtained from the analysis carried out through the method based on ρ proposed by Bizon et al. (2009b), this suggests that the coherent-incoherent analysis is a good tool in order to characterize the combustion processes from statistical point of view (Gaussian and non-Gaussian components).

Chapter 5

DMD applications

This section is focused on the application of Dynamic Mode Decomposition to PIV measurements of high Reynolds and high swirl number flow in order to extract the dominant dynamics, in terms of frequency and growth rate, of the turbulent flow investigated in terms.

5.1 DMD Analysis of experimental PIV Data of a Swirled Jet

Swirl flows are widely used in several technical applications such as cyclone separators, gas turbine combustors, hybrid rockets etc. (Gupta, 1984). For example, in combustion processes the high turbulence levels and the recirculating flow observed at high swirl levels greatly improve reactants mixing and flame stability, while allowing the reduction of pollutant emissions. Improvement in these technical applications requires a deeper understanding of the dynamics of swirling flows, whose features are still debated by the scientific community. One peculiar phenomenon of swirl flows is the so-called Precessing Vortex Core (PVC). The PVC occurs in high Reynolds and swirl number flows and is characterized by the reg-

ular precession of the large-scale vortical structure typical of swirling jets around the geometrical axis of symmetry (Gupta, 1984). An analysis of the 3D and unsteady flow structure of the PVC can be found in the experimental works of Cala (2004), Cala et al. (2006) and Shtork et al. (2007), while a review of PVC instability in swirl combustion systems can be found in Syred (2006). In this section, it will be discussed the application of Dynamic Mode Decomposition (DMD) to PIV measurements of a swirled jet in order to identify and characterize the dominant dynamic components of the system.

5.1.1   Experimental setup

The investigated flow is a turbulent free swirling jet of air at ambient pressure and temperature. The swirl generator was of axial plus-tangential entry type characterized by four axial and four tangential air inlets. A converging nozzle of exit radius $R = 12$ mm was located vertically on top of the swirl generator. A circular pipe having an inner radius $R_{inj} = 6$ mm was located coaxially to the swirl generator and used for flow seeding. Its exit section was set at about 26 Rinj below the nozzle exit. A schematic view of the nozzle is shown in Figure 5.1, while a detailed drawing of the swirl generator is reported in Martinelli (2007). The total air flow rate and the swirl strength were regulated by controlling the flow rates in the seeding system, the axial and the tangential entries by using thermal mass flowmeters whose error was estimated around $\pm 1\%$ of the full scale. The seeding system generates oil droplets with an estimated diameter of about 1-2 m. The maximum measurable frequency of the flow fluctuations, limited by the inertia of the tracer particles, was estimated to be around 12.7 kHz, while the Stokes number estimation allowed to assume that the centrifugal effect on tracer particles was negligibly small Martinelli (2007). PIV measurements were performed using a high speed double pulsed Nd:YLF laser operating at 527 nm.
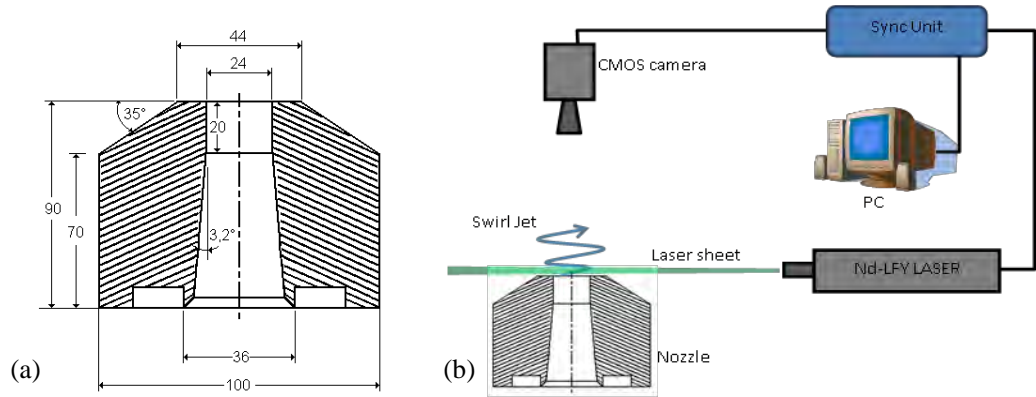
Figure 5.1: Schematic of the nozzle, all dimension in mm (a). Sketch of the experimental set-up (b).

Double images were acquired with a CMOS (Dantec NanoSense MKIII) cross-correlation PIV camera with a full resolution of 1280×1024 pixels. The spatial resolution in the direction normal to the measurement plane was estimated from the average thickness of the laser sheet, which was about 1 mm. The laser sheet was located normally to the nozzle axis and at about 1 mm above the nozzle exit, (see Figure 5.1). At the investigated swirl and Reynolds numbers (Re = 244400) the jet exhibits a Precessing Vortex Core (PVC) with a frequency of about 486 Hz (Martinelli, 2012), thus, to fulfill the Nyquist-Shannon sampling theorem, PIV images were acquired at about three time the PVC frequency, i.e. 1500 double images/s, while the interframe time was set to 10 μs. The camera operates at the (reduced) resolution of 640×640 pixels corresponding to a field of view of about 33×33 mm^2 and a magnification of 0.305.

PIV images were processed by means of the Dantec software. The size of the interrogation area was set to 32×32 pixels corresponding to a spatial resolution of about 1.2 mm. An overlap of 50% was used. The velocity maps were vector-validated basing on the cross-correlation peak height ratio and on the velocity magnitude. The statistical error relative to the mean value of the velocity is
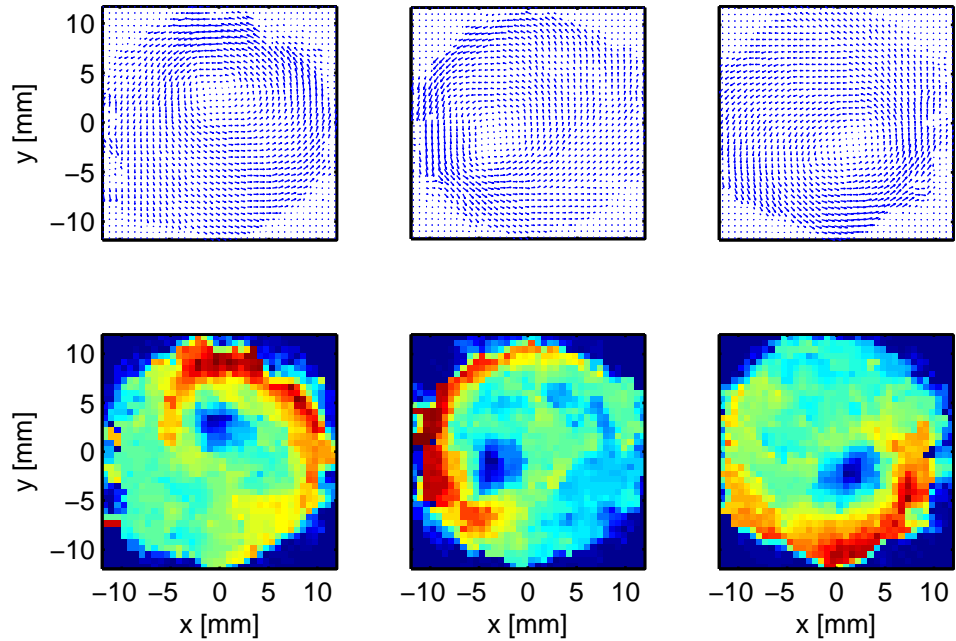
Figure 5.2: Representative snapshots of the arrow field velocity maps (top) and
their moduli shown as scalar fields (bottom).

estimated to be less than 3% for the 1000 couples of images acquired.

5.1.2   DMD analysis

Figure 5.2 shows representative snapshots of the PIV velocity field, with clear
evidence of the PVC. DMD applied to the PIV data elucidates the dynamics
connected with vortex motion and other transient phenomena. Figure 5.3 reports,
in the complex plane, the spectrum of the companion matrix $\mathbf{S}$ (Eq. (2.54)),
where it is seen that all eigenvalues tend to localize close to the unit circle. Figure
5.3 (left) shows the eigenvalues of $\mathbf{S}$. As expected, there are many complex and
conjugate eigenvalues, due to the oscillating dynamics. The radius of each data
marker corresponds to the square amplitude of the mode, i.e. the amount of kinetic
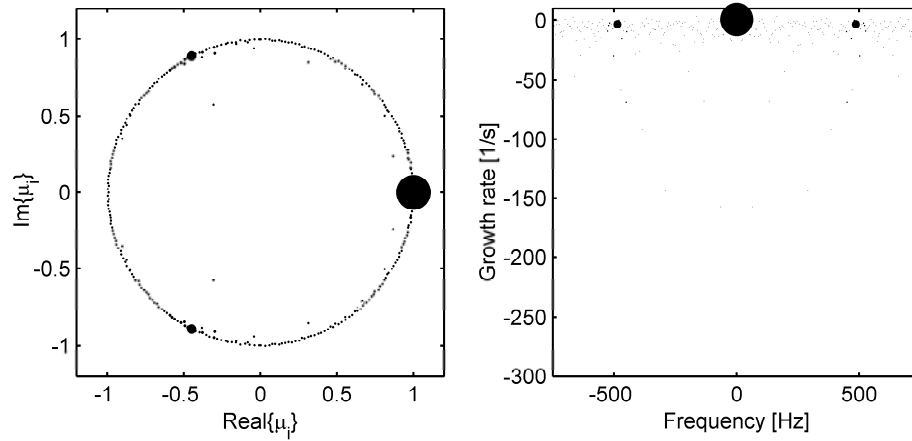
Figure 5.3: DMD analysis using the last 300 snapshots. (Left) Scatter plots of
the eigenvalues of **S**. (Right) Scatter plots of the normalized growth rates versus
normalized frequencies for all dynamic modes. In both scatter plots, size of the
circle denote the amount of energy captured by dynamic mode.

energy of the flow captured by the dynamic mode. Most of the kinetic energy of the
flow is captured by mode DM0, namely the mean component, and by one pair of
complex-conjugate modes, DM2 and DM2* , associated with the main precessing
vortex. a magnification of 0.305. In order to analyse transient phenomena that
may be captured by the PIV dataset, DMD was carried out on different numbers
of snapshots, namely for different observation times. Particularly, two ensembles
of snapshot were studied by DMD. The first set is made up of 1000 snapshots (i.e.
the entire sequence of snapshots), and the second one is made up of the last 300
snapshots of the entire sequence. Figures 5.4 and 5.5 show the amplitude spectra
of the dynamic modes relating to the two sequences of 1000 snapshots and 300
snapshots, respectively. It is possible to notice that the dynamic mode DM1 occurs,
with significant amplitude, only for the case of 1000 snapshots, namely when the
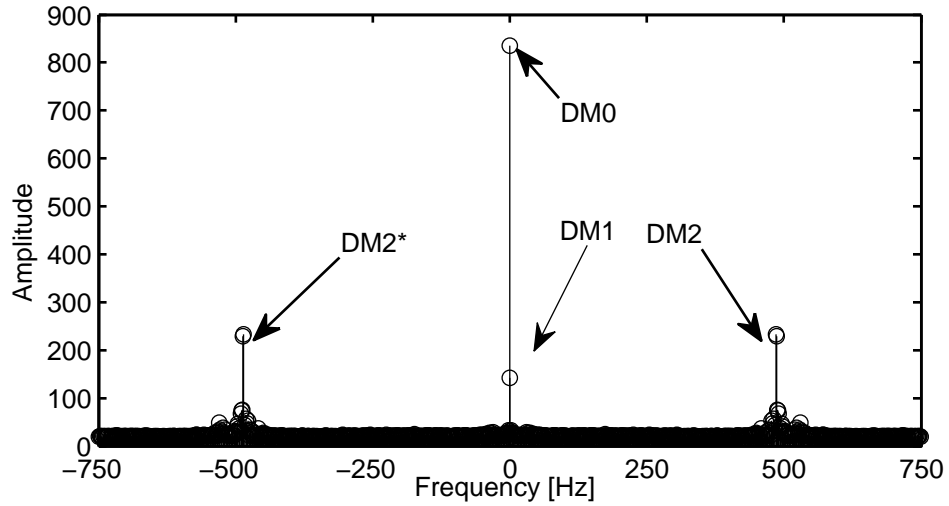
Figure 5.4: Amplitudes of the DMD modes for 1000 snapshots.
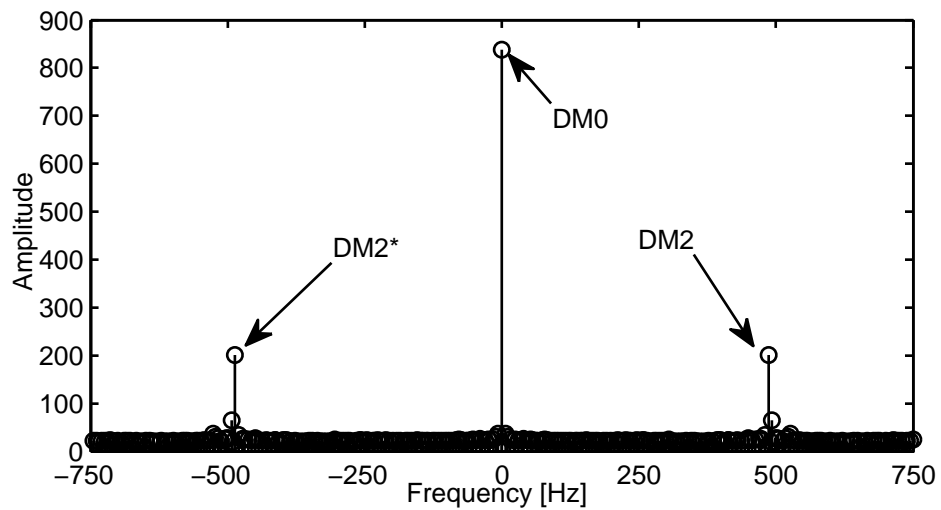
Figure 5.5: Amplitudes of the DMD modes for 300 snapshots.

time interval includes the early transient. Indeed, DM1 is not observed for the
sequence made of the last 300 snapshots. Figure 5.6 shows the spatial features
associated with dynamic modes DM0 and DM1. Since DM0 has both zero growth
rate and zero frequency, DM0 is associated with the mean component. Mode DM1

has significant values of amplitude and growth rate, therefore it is associated with a
transient phenomenon. Precisely, the growth rate of DM1 is about -7.95 s^{-1}, which
corresponds to a half-time of about 175.3 ms, and to about 20% of the amplitude of
the mean component. For these reasons, DM1 can be considered as a marker of the
transient condition of the system. In Figure 5.6 we look at the morphology of the
first four modes. We see that DM0 is axisymmetric as it should be, dealing with a
conical swirled jet. DM1 is roughly axisymmetric as well, and peaks near the edge
of the jet. This indicates that the main transient component of the flow is related
to viscous phenomena that decay in amplitude whilst maintaining axisymmetric
structure. The spiral patterns of the paired modes associated with the precessing
vortex are also reported. In Figures 5.3 it is possible to see a cloud of minor modes
in a neighbourhood of the normalized frequencies of the pair of dominant conjugate
modes associated with the precessing vortex, however only one dominant pair of
dynamic modes (DM2, DM2*) are related to the precessing vortex, with frequency
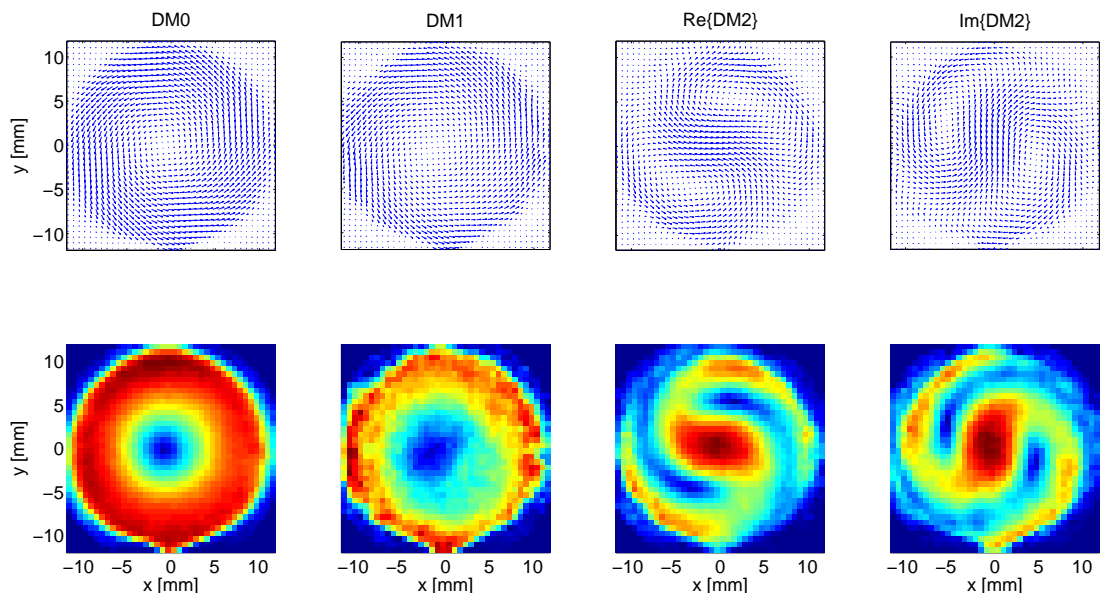
Figure 5.6: Amplitudes of the DMD modes for 300 snapshots.

of 486 Hz for both samples. DM1, detected as the second largest in the set of first 1000 snapshots, disappears in the set of last 300 snapshots. The mean component (DM0) and the precessing vortex (DM2 and DM2*) are identified by the three largest circles in Figure 5.3 and the three highest spikes in Figures 5.4 and 5.5, and are present in both spectra, the one obtained by 1000 snapshots and the one obtained by using the last 300 only. Finally, since all growth rates are negative, or, equivalently, the eigenvalues of $\mathbf{S}$ are less than unity in absolute value, the dynamics of the system can be considered stable. In other words, all dynamic mode have a stable behaviour.

Conclusions

The development and the applications of the numerical techniques presented in this thesis were focused on:

- the analysis of the cycle-to-cycle variations in optically accessible engines in terms of luminosity and morphological features of the flames,

- the analysis of the characteristic features of swirl spray flames of various liquid fuels (ethanol, heptane, decane, dodecane) at conditions far from and close to blow-off.

Chapter 3 was focused on the analysis of flame images acquired from a port-fuel injection spark-ignition (PFI SI) engine and a Diesel engine. With regards to PFI-SI, cycle-resolved images of the combustion were acquired for two injection strategies: closed valve (CV) injection and open valve (OV) injection. The analysis of the cycle variations were carried out either on global indexes (in-cylinder pressure, integral luminosity and centroid of the luminosity field) and in terms of morphological features. Cycle-to-cycle variations analysis carried out on the global indexes has shown that CV injection strategy exhibits higher variability than OV injection strategy.

The analysis of cycle variations in terms of dominant features of the flames was carried out by applying Proper Orthogonal Decomposition (POD) and Independent

Component Analysis (ICA). POD has permitted to analyze the cycle variations
through the coefficient of variation of the POD coefficients (CoV_{POD}), which takes
into account both the variations for the luminous intensities and of the morpholo-
gies of the flames. Besides, it was shown that the most energetic POD modes iden-
tify and separates the dominant features connected to normal combustion (flame
front propagation) and the irregular combustion due to the diffusion-controlled
combustion of liquid fuel deposited on the intake valves and chamber combustion.
ICA has allowed to extract the independent spatial structures of the flames for both
CV and OV operating conditions. Spatial independent components and their coef-
ficients are first extracted from sets of luminosity images, and then used to identify
leading structures and to study the transient behaviour of the combustion process.
The three components identified from the combustion images are representative of
ignition and radial-like flame propagation (first component), and erratic luminous
combustion (second and third component) occurring subsequently. A set of cycle-
resolved sequences has been analysed in terms of cycle variation, by making use of
the statistics of the coefficients of the independent components. It is seen that the
second and third ICs represent the dominant morphology of the cyclic variations,
and the corresponding coefficients represent the magnitude and the time evolu-
tion of such variations. Fluctuations in the luminosity field are mainly ascribed to
combustion of fuel pockets.

With regards to flame images collected from an optical Diesel engine, ICA has
allowed to identify the independent components that describe the combustion pro-
cess. Two independent components were sought and found, as emerging from the
analysis, related to combustion along the fuel jets and near the bowl walls respec-
tively. The former present low variability over the cycles, the latter high variability.
This confirms quantitatively that strong deviations from the ideal combustion pro-
cess are located near the bowl walls.

Application of the optical flow (OF) technique has allowed to estimate the motion
field associated with the propagation of the flame front, more precisely burned gas
front, from the spark to the chamber wall. OF proves to be a useful tool, able to
extract information on the dynamic of the flame, provided that consecutive image
sequences sufficiently time-resolved are available. The motion field of the flame
front was analysed in terms of spatial average and spatial standard variation of the
local speed of the flame front. The spatial average velocity can be interpreted as a
global measure of the propagation of the front flame, whereas the spatial standard
deviation of the local flame speed can be interpreted as a global measure of the
interaction between the turbulent eddies and the flame front.

In chapter 4, POD has been used for the analysis of 5 kHz OH* chemiluminescence
and OH-PLIF images from ethanol, n-heptane, n-decane, and n-dodecane swirl-
stabilised spray flames far from and close to blow-off, to examine how the flame is
modified at extinction conditions and how the large-scale features of the blow-off
process may be detected before complete extinction. The analysis has allowed to
identify for each flame and each operating condition the dominant structures of
the flame (POD modes). The most meaningful dominant features extracted by
POD are:

- transverse oscillations of the flame due to interaction between the swirl mo-
  tion and flame front;

- axial oscillations of the flame due to the convective axial flow;

- motion of turn-over of the flames due to interaction of the flame and recir-
  culation zones induced by the use of a bluff-body.

From the POD analysis it is seen that flames becomes more and more compact
when the operating condition approaches blow-off.

The dynamics of the dominant features of the flames were studied by applying the
Fourier analysis to the POD coefficients, which captured all the temporal infor-
mation. From this analysis is emerged that all the power spectra densities (PSDs)
of the POD coefficients include a portion with a -5/3 decay, which is typical of
the turbulent energy spectrum in the inertial subrange. This result validates that
the acquired data take into account the effects of the turbulence on the flame.
From the Fourier analysis (PSD and CSP) is is seen that the flames of n-heptane,
n-decane and n-dodecane at blow-off are characterized by slower dynamics; in-
stead, the flame of ethanol is characterized by faster dynamics. This result might
be due to the lower volatility of the ethanol that influences the mixing and the
dynamics of the combustion, but further studies are necessary to better elucidate
the relevant mechanism. The statistical behaviour of the flames was analysed via
the coherent (non-Gaussian) and incoherent (Gaussian) analysis. Coherent and
incoherent analyses were carried out by using two method of separation:

- the method based on kurtosis and skewness;

- the method based on the Normality Test of Shapiro-Wilk, which is introduced
  in this thesis.

Coherent-incoherent analyses carried out on OH-PLIF measurement has shown
that the flame front assumes less and less Gaussian behaviour as the blow-off is
approached, independently from the fuel used. This result is very useful in order
to individuate a proper control parameter, i.e. the percentage of coherent energy
at fixed level of significance, for the development of a robust controller to prevent
blow-off, based on advanced optical measurements.

Chapter 6 reports an application of Dynamic Mode Decomposition to PIV mea-
surements from a swirled jet flow. DMD has allowed to identify the features of

the precessing vortex in terms of frequency, growth rate and morphology (spatial pattern described by the dynamic modes), and even allowed to identify the feature associated with a transient phenomenon. On account of the determined eigenvalues, the system can be considered dynamically stable.

The study of future works should be focused on the development of these techniques in order to extract useful information. Both POD and ICA are shown to be powerful numerical tools, able to extract useful information from a huge amount of data. Particularly, the modal decomposition methods (ICA,DMD and POD) may be employed for the development of empirical models that may be employed to describe the propagation of the flame kernel in spark-ignition engines, whereas DMD can be employed on time-resolved image sequences of turbulent flames to extract the dominant dynamics of stationary and non-stationary flames.

Bibliography

A. Albarbar, F. Gu, and A.D. Ball. Diesel engine fuel injection monitoring using acoustic measurements and independent component analysis. *Measurement*, 43 (10):1376 – 1386, 2010. ISSN 0263-2241. doi: http://dx.doi.org/10.1016/j. measurement.2010.08.003.

Kozo Aoki, Masayasu Shimura, Shinichi Ogawa, Naoya Fukushima, Yoshitsugu Naka, Yuzuru Nada, Mamoru Tanahashi, and Toshio Miyauchi. Short- and long-term dynamic modes of turbulent swirling premixed flame in a cuboid combustor. *Proceedings of the Combustion Institute*, 35(3):3209 – 3217, 2015. ISSN 1540-7489. doi: http://dx.doi.org/10.1016/j.proci.2014.10.003.

Simon Ayache and Epaminondas Mastorakos. Investigation of the tecflam non-premixed flame using large eddy simulation and proper orthogonal decomposition. *Flow, Turbulence and Combustion*, 90(2):219–241, 2013. ISSN 1386-6184. doi: 10.1007/s10494-012-9428-6.

J.L. Barron, D.J. Fleet, and S.S. Beauchemin. Performance of optical flow techniques. *International Journal of Computer Vision*, 12(1):43–77, 1994. ISSN 0920-5691. doi: 10.1007/BF01420984.

G. Berkooz, P. Holmes, and J. L. Lumley. *Annual Review of Fluid Mechanics*, 25: 539–575, 1993. ISSN 0066-4189. doi: 10.1146/annurev.fl.25.010193.002543.

K. Bizon, G. Continillo, K.C. Leistner, E. Mancaruso, and B.M. Vaglieco. Pod-based analysis of cycle-to-cycle variations in an optically accessible diesel engine. *Proceedings of the Combustion Institute*, 32(2):2809 – 2816, 2009a. ISSN 1540-7489. doi: http://dx.doi.org/10.1016/j.proci.2008.08.010.

K. Bizon, G. Continillo, S. Lombardi, S.S. Merola, P. Sementa, C. Tornatore, and B.M. Vaglieco. Analysis of flame kinematics and cycle variation in a port fuel injection spark ignition engine. *SAE International Journal of Engines*, 2(2): 443–451, 2010a. doi: 10.4271/2009-24-0057.

K. Bizon, G. Continillo, E. Mancaruso, S.S. Merola, and B.M. Vaglieco. Pod-based analysis of combustion images in optically accessible engines. *Combustion and Flame*, 157(4):632 – 640, 2010b. ISSN 0010-2180. doi: http://dx.doi.org/10.1016/j.combustflame.2009.12.013.

Katarzyna Bizon and Gaetano Continillo. Spectral reduction on empirically derived orthogonal basis of the dynamical model of a circulating fluidized bed combustor. In Jacek Jeżowski and Jan Thullie, editors, *19th European Symposium on Computer Aided Process Engineering*, volume 26 of *Computer Aided Chemical Engineering*, pages 931 – 935. Elsevier, 2009. doi: http://dx.doi.org/10.1016/S1570-7946(09)70155-5.

Katarzyna Bizon and Gaetano Continillo. Reduced order modelling of chemical reactors with recycle by means of pod-penalty method. *Computers Chemical Engineering*, 39(0):22 – 32, 2012. ISSN 0098-1354. doi: http://dx.doi.org/10.1016/j.compchemeng.2011.10.001.

Katarzyna Bizon, Gaetano Continillo, Simona S. Merola, and Bianca M. Vaglieco. Reconstruction of flame kinematics and analysis of cycle variation in a spark ignition engine by means of proper orthogonal decomposition. In Jacek JeÅ¼owski

and Jan Thullie, editors, *19th European Symposium on Computer Aided Process Engineering*, volume 26 of *Computer Aided Chemical Engineering*, pages 1039 – 1043. Elsevier, 2009b. doi: http://dx.doi.org/10.1016/S1570-7946(09)70173-7.

Katarzyna Bizon, Simone Lombardi, Gaetano Continillo, Ezio Mancaruso, and Bianca Maria Vaglieco. Analysis of diesel engine combustion using imaging and independent component analysis. *Proceedings of the Combustion Institute*, 34 (2):2921 – 2931, 2013. ISSN 1540-7489. doi: http://dx.doi.org/10.1016/j.proci. 2012.08.004.

Jean-Paul Bonnet and Joel Delville. Review of coherent structures in turbulent free shear flows and their possible influence on computational methods. *Flow, Turbulence and Combustion*, 66(4):333–353, 2001. ISSN 1386-6184. doi: 10. 1023/A:1013518716755.

J.P. Bonnet, D.R. Cole, J. Delville, M.N. Glauser, and L.S. Ukeiley. Stochastic estimation and proper orthogonal decomposition: Complementary techniques for identifying structure. *Experiments in Fluids*, 17(5):307–314, 1994. ISSN 0723-4864. doi: 10.1007/BF01874409.

J. Borèe. Extended proper orthogonal decomposition: a tool to analyse correlated events in turbulent flows. *Experiments in Fluids*, 35(2):188–192, 2003. ISSN 0723-4864. doi: 10.1007/s00348-003-0656-3.

C.E. Cala, E.C. Fernandes, M.V. Heitor, and S.I. Shtork. Coherent structures in unsteady swirling jet flow. *Experiments in Fluids*, 40(2):267–276, 2006. ISSN 0723-4864. doi: 10.1007/s00348-005-0066-9.

Fernandes E.C. Heitor M.V. Shtork S.I. Cala, C.E. Lda analysis of pvc-central recirculation zone interaction in a model vortex burner. In *12th Int. Symp. On Applications of Laser Techniques, Lisbon*. Lisbon, July 2004.

Vince D. Calhoun, Jingyu Liu, and Talay Adali. A review of group ica for fmri data and ica for joint inference of imaging, genetic, and erp data. *NeuroImage*, 45(1, Supplement 1):S163 – S172, 2009. ISSN 1053-8119. doi: http://dx.doi. org/10.1016/j.neuroimage.2008.10.057. Mathematics in Brain Imaging.

D.E. Cavaliere, J. Kariuki, and E. Mastorakos. A comparison of the blow-off behaviour of swirl-stabilized premixed, non-premixed and spray flames. *Flow, Turbulence and Combustion*, 91(2):347–372, 2013. ISSN 1386-6184. doi: 10. 1007/s10494-013-9470-z.

Xu Chen, Pascal Zillé, Liang Shao, and Thomas Corpetti. Optical flow for incompressible turbulence motion estimation. *Experiments in Fluids*, 56(1):8, 2015. ISSN 0723-4864. doi: 10.1007/s00348-014-1874-6.

J. H. Citriniti and W. K. Greorge. Reconstruction of the global velocity field in the axisymmetric mixing layer utilizing the proper orthogonal decomposition. *Journal of Fluid Mechanics*, 418:137–166, 9 2000. ISSN 1469-7645. doi: 10. 1017/S0022112000001087.

R.B. D'Agostino and E.S. Pearson. Tests of departure from normality. empirical results for the distribution of b2 and b1. *Biometrika*, 60:613–622, 1973.

Sean J. Danby and Tarek Echekki. Proper orthogonal decomposition analysis of autoignition simulation data of nonhomogeneous hydrogen-air mixtures. *Combustion and Flame*, 144(1-2):126 – 138, 2006. ISSN 0010-2180. doi: http://dx.doi.org/10.1016/j.combustflame.2005.06.014.

D.W. Davis, P.L. Therkelsen, D. Littlejohn, and R.K. Cheng. Effects of hydrogen on the thermo-acoustics coupling mechanisms of low-swirl injector flames in a model gas turbine combustor. *Proceedings of the Combustion Institute*, 34(2):

3135 – 3143, 2013. ISSN 1540-7489. doi: http://dx.doi.org/10.1016/j.proci. 2012.05.050.

C. Duwig and C. Fureby. Large eddy simulation of unsteady lean stratified premixed combustion. *Combustion and Flame*, 151(1-2):85 – 103, 2007. ISSN 0010-2180. doi: 10.1016/j.combustflame.2007.04.004.

J. Eriksson and V. Koivunen. Identifiability, separability, and uniqueness of linear ica models. *Signal Processing Letters, IEEE*, 11(7):601–604, July 2004. ISSN 1070-9908. doi: 10.1109/LSP.2004.830118.

R. Everson and L. Sirovich. Karhunen-loeve procedure for gappy data. *J. Opt. Soc. Am. A*, 12:1657–1664, 1995.

Marie Farge, Kai Schneider, and Nicholas Kevlahan. Non-gaussianity and coherent vortex simulation for two-dimensional turbulence using an adaptive orthogonal wavelet basis. *Physics of Fluids*, 11(8):2187–2201, 1999. doi: http://dx.doi.org/ 10.1063/1.870080.

C.E. Frouzakis, Y.G. Kevrekidis, J. Lee, K. Boulouchos, and A.A. Alonso. Proper orthogonal decomposition of direct numerical simulation data: Data reduction and observer construction. *Proceedings of the Combustion Institute*, 28(1):75 – 81, 2000. ISSN 1540-7489. doi: http://dx.doi.org/10.1016/S0082-0784(00) 80197-6.

Mark N. Glauser and William K. George. Application of multipoint measurements for flow characterization. *Experimental Thermal and Fluid Science*, 5(5):617 – 632, 1992. ISSN 0894-1777. doi: http://dx.doi.org/10.1016/0894-1777(92) 90018-Z. Special Issue on Experimental Methods in Thermal and Fluid Science.

S. V. Gordeyev and F. O. Thomas. Coherent structure in the turbulent planar jet.

part 1. extraction of proper orthogonal decomposition eigenmodes and their self-similarity. *Journal of Fluid Mechanics*, 414:145–194, 7 2000. ISSN 1469-7645. doi: 10.1017/S002211200000848X.

A. Greenbaum. *Iterative Methods for Solving Linear Systems*. SIAM, 1997.

Lilley D.G. Syred N. Gupta, A.K. *Swirl Flows.* Abacus Press, Tunbridge Wells, UK, 1984.

Lumley J.L. Berkooz G. Rowley C.W. Holmes, P. *Turbulence, Coherent Structures, Dynamical Systems and Symmetry.* Cambridge University Press, second edition, 1996. ISBN 978-1-107-00825-0.

Berthold K. P. Horn and Brian G. Schunck. Determining optical flow. *ARTIFICAL INTELLIGENCE*, 17:185–203, 1981.

Berthold K.P. Horn. *Robot Vision.* MIT Electrical Engineering and Computer Science. The MIT Press, mit press ed edition, 1986. ISBN 0262081598,9780262081597.

A. Hyvarinen. Fast and robust fixed-point algorithms for independent component analysis. *Neural Networks, IEEE Transactions on*, May 1999.

A. Hyvärinen and E. Oja. Independent component analysis: algorithms and applications. *Neural Networks*, 13(4-5):411–430, 2000. ISSN 0893-6080. doi: http://dx.doi.org/10.1016/S0893-6080(00)00026-5.

T. Ito, Y. Tsuji, H. Nakamura, and Y. Kukita. Application of ultrasonic velocity profile meter to vortex shedding and empirical eigenfunctional analysis. *Experiments in Fluids*, 31(3):324–335, 2001. ISSN 0723-4864. doi: 10.1007/s003480100291.

James Kariuki, James R. Dawson, and Epaminondas Mastorakos. Measurements in turbulent premixed bluff body flames close to blow-off. *Combustion and Flame*, 159(8):2589 – 2607, 2012. ISSN 0010-2180. doi: http://dx.doi.org/10.1016/j.combustflame.2012.01.005. Special Issue on Turbulent Combustion.

Kristin M. Kopp-Vaughan, Trevor R. Jensen, Baki M. Cetegen, and Michael W. Renfro. Analysis of blowoff dynamics from flames with stratified fueling. *Proceedings of the Combustion Institute*, 34(1):1491 – 1498, 2013. ISSN 1540-7489. doi: http://dx.doi.org/10.1016/j.proci.2012.06.074.

Stanislav Kostka, Amy C. Lynch, Bethany C. Huelskamp, Barry V. Kiel, James R. Gord, and Sukesh Roy. Characterization of flame-shedding behavior behind a bluff-body using proper orthogonal decomposition. *Combustion and Flame*, 159(9):2872 – 2882, 2012. ISSN 0010-2180. doi: http://dx.doi.org/10.1016/j.combustflame.2012.03.021.

South-Western Cengage Learning, editor. *Statistics for Management and Economics,*, 2011.

J.T.C. Liu. Contributions to the understanding of large-scale coherent structures in developing free turbulent shear flows. volume 26 of *Advances in Applied Mechanics*, pages 183 – 309. Elsevier, 1988. doi: http://dx.doi.org/10.1016/S0065-2156(08)70289-8.

Xianhua Liu, Robert B. Randall, and Jérôme Antoni. Blind separation of internal combustion engine vibration signals by a deflation method. *Mechanical Systems and Signal Processing*, 22(5):1082 – 1091, 2008. ISSN 0888-3270. doi: http://dx.doi.org/10.1016/j.ymssp.2007.11.011.

M. Loève. *Probability Theory*, volume 2. Springer-Verlag, berlin, germany edition, 1978.

J. L. Lumley. The structure of inhomogeneous turbulence. In A. M. Yaglom and V. I. Tatarski, editors, *Atmospheric Turbulence and Wave Propagation*, pages 166–178, Nauka, Moscow, 1967.

J. L. Lumley. *Stochastic tools in turbulence.* Dover Publications, INC., 2007.

Cozzi F. Coghe A. Martinelli, F. Phase-locked analysis of velocity fluctuations in a turbulent free swirling jet after vortex breakdown. *Experiments in Fluids*, 53(2):437–449, 2012. ISSN 0723-4864. doi: 10.1007/s00348-012-1296-2. URL `http://dx.doi.org/10.1007/s00348-012-1296-2`.

Olivani A. Coghe A. Martinelli, F. Experimental analysis of the precessing vortex core in a free swirling jet. *Experiments in Fluids*, 42(6):827–839, 2007. ISSN 0723-4864. doi: 10.1007/s00348-006-0230-x. URL `http://dx.doi.org/10.1007/s00348-006-0230-x`.

Igor Mezić. Analysis of fluid flows via spectral properties of the koopman operator. *Annual Review of Fluid Mechanics*, 45(1):357–378, 2013. doi: 10.1146/annurev-fluid-011212-140652.

Nathan E. Murray and Lawrence S. Ukeiley. An application of gappy pod. *Experiments in Fluids*, 42(1):79–91, 2007. ISSN 0723-4864. doi: 10.1007/s00348-006-0221-y.

B.W. van Oudheusden, F. Scarano, N.P. van Hinsberg, and D.W. Watt. Phase-resolved characterization of vortex shedding in the near wake of a square-section cylinder at incidence. *Experiments in Fluids*, 39(1):86–98, 2005. ISSN 0723-4864. doi: 10.1007/s00348-005-0985-5.

Franck Richecoeur, Layal Hakim, Antoine Renaud, and Laurent Zimmer. Dmd algorithms for experimental data processing in combustion. *Proceeding of the 2012 Summer Program*, pages 459–468, 2012.

Clarence W. Rowley, Igor Mezić, Shervin Bagheri, Philipp Schlatter, and Dan S. Henningson. Spectral analysis of nonlinear flows. *Journal of Fluid Mechanics*, 641:115–127, 12 2009. ISSN 1469-7645. doi: 10.1017/S0022112009992059.

J.P. Royston. An extension of shapiro and wilk's w tes for normality to large sample. *Journal of the Royal Stiatistical Society: Series C (Applied Statistics)*, 31:115–124, 1982.

J.C. Russ. *The image processing handbook*. CRC Press, Boca Raton, USA, 6th edition, 2011.

Alexander Sakowitz, Mihai Mihaescu, and Laszlo Fuchs. Effects of velocity ratio and inflow pulsations on the flow in a t-junction by large eddy simulation. *Computers & Fluids*, 88(0):374 – 385, 2013. ISSN 0045-7930. doi: http://dx.doi.org/10.1016/j.compfluid.2013.10.001.

Louis L Scharf. The {SVD} and reduced rank signal processing. *Signal Processing*, 25(2):113 – 133, 1991. ISSN 0165-1684. doi: http://dx.doi.org/10.1016/0165-1684(91)90058-Q.

Peter J. Schmid. Dynamic mode decomposition of numerical and experimental data. *Journal of Fluid Mechanics*, 656:5–28, 8 2010. ISSN 1469-7645. doi: 10.1017/S0022112010001217.

Peter J. Schmid and J. Sesterhenn. Dynamic mode decomposition of numerical and experimental data. *Bull. Amer. Phys. Soc.*

P.J. Schmid, L. Li, M.P. Juniper, and O. Pust. Applications of the dynamic mode decomposition. *Theoretical and Computational Fluid Dynamics*, 25(1-4): 249–259, 2011. ISSN 0935-4964. doi: 10.1007/s00162-010-0203-9.

Abu Seena and Hyung Jin Sung. Dynamic mode decomposition of turbulent cavity flows for self-sustained oscillations. *International Journal of Heat and Fluid Flow*, 32(6):1098–1110, 2011. doi: http://dx.doi.org/10.1016/j.ijheatfluidflow. 2011.09.008.

Wilk M.B. Shapiro, S.S. An analysis of variance test for normality (complete samples). *Biometrika*, 52:591–611, 1965.

S.I. Shtork, C.E. Cala, and E.C. Fernandes. Experimental characterization of rotating flow field in a model vortex burner. *Experimental Thermal and Fluid Science*, 31(7):779 – 788, 2007. ISSN 0894-1777. doi: http://dx.doi.org/10.1016/ j.expthermflusci.2006.08.008.

Lawrence Sirovich. Turbulence and the dynamics of coherent structures. 2. symmetries and transformations. *Quarterly of Applied mathematics*, 45(3):573–582, 1987.

Micheal Stöhr, Isaac Boxx, Campbell D. Carter, and Wolfgang Meier. Experimental study of vortex-flame interaction in a gas turbine model combustor. *Combustion and Flame*, 159(8):2636 – 2649, 2012. ISSN 0010-2180. doi: http://dx.doi.org/10.1016/j.combustflame.2012.03.020. Special Issue on Turbulent Combustion.

James V. Stone. *Independent Component Analysis. A Tutorial Introduction.* The MIT Press, Cambridge, USA, 2004.

Nicholas Syred. A review of oscillation mechanisms and the role of the precessing vortex core (pvc) in swirl combustion systems. *Progress in Energy and Combustion Science*, 32(2):93 – 161, 2006. ISSN 0360-1285. doi: http: //dx.doi.org/10.1016/j.pecs.2005.10.002.

Cheng Tan, Lijun Xu, Xiaomin Li, and Yong Yan. Independent component analysis-based fuel type identification for coal-fired power plants. *Combustion Science and Technology*, 184(3):277 – 292, 2012. doi: 10.1080/00102202.2011. 635613.

S. Tirunagari, V. Vuorinen, O. Kaario, and M. Larmi. Analysis of proper orthogonal decomposition and dynamic mode decomposition on les of subsonic jets. *CSI Journal of Computing*, 1:2–19, 2012.

Bau III David Trefethen, Lloyd N. *Numerical linear algebra.* Society for Industrial and Applied Mathematics, 1997. ISBN 0898713617.

A.R. Webb. *Statistical Pattern Recognition.* John Wiley & Sons, Ltd., second edition, 2002.

P.D. Welch. The use of fast fourier transform for the estimation of power spectra: A method based on time averaging over short, modified periodograms. *IEEE Trans. Audio Electroacoustics*, AU-15:70–73, 1967.

C.G. Wu, Y.C. Liang, W.Z. Lin, H.P. Lee, and S.P. Lim. A note on equivalence of proper orthogonal decomposition methods. *Journal of Sound and Vibration*, 265(5):1103 – 1110, 2003. ISSN 0022-460X. doi: http://dx.doi.org/10.1016/S0022-460X(03)00032-4.

Edmond HaoCun Wu, Philip L. H. Yu, and Wai Keung Li. An independent component ordering and selection procedure based on the MSE criterion. In Justinian P. Rosca, Deniz Erdogmus, José Carlos Príncipe, and Simon Haykin, editors, *Independent Component Analysis and Blind Signal Separation, 6th International Conference, ICA 2006, Charleston, SC, USA, March 5-8, 2006, Proceedings*, volume 3889 of *Lecture Notes in Computer Science*, pages 286–294. Springer, 2006. doi: 10.1007/11679363_36.